

# **FINITE STRIP MODELING OF THIN- WALLED MEMBERS**

by

Zhanjie Li

A dissertation submitted to Johns Hopkins University in conformity with the  
requirement for the degree of Doctor of Philosophy

Baltimore, Maryland

September 2011

@2011 Zhanjie Li

All rights reserved

## Abstract

Under load thin-walled members potentially have cross section instability (i.e., local and/or distortional) in addition to global instability (Euler buckling) of the member. To assess the stability of thin-walled members requires advanced tools, such as the finite strip (FSM) and/or finite element methods (FEM). However, commonly available FSM solutions are only applicable to simply supported ends, while FEM analysis, using plate or shell elements for both elastic buckling and nonlinear collapse analyses, is limited by the subjective and laborious nature required in identifying the characteristic local, distortional, and global buckling modes.

In this thesis new FSM implementation is developed to account for general end boundary conditions: pin-pin, fixed-fixed, fixed-pin, fixed-free, and fixed-guided and these solutions are used to extend the constrained Finite Strip Method (*c*FSM). The full derivation for a FSM stability solution that applies to general end boundary conditions is provided. Verification problems are provided against eigenbuckling shell finite element analysis solutions implemented in ABAQUS. Particular attention is paid to the number of longitudinal terms required, spring modelling, and the possibility of an element-wise FSM. In addition, the existing *c*FSM solutions for pin-pin boundary conditions are recast into the new generalized notation for general end boundary conditions. Formulation of the constraint matrices that form the basis for modal decomposition and identification in *c*FSM is provided with full derivation. Orthogonalization and normalization of the bases are discussed in detail. Recommendations are provided regarding the choice of basis and normalization.

To address issues in shell FEM solutions for linear elastic buckling analysis, an automatic mode identification method is proposed which uses a special system of modal base functions, referred to as the *c*FSM base functions. After extrapolating the *c*FSM base functions to the FEM context, a sizeable minimization problem is completed for assigning the contributions to the fundamental buckling deformation classes. Modal identification results of FEM solutions are validated against FSM solutions. A set of generalized *c*FSM base functions are proposed to handle all end boundary cases, such as mixed boundary conditions and semi-rigid boundary conditions. Moreover, modal identification for collapse analysis of thin-walled members modelled using material and geometric nonlinear shell finite element analysis is studied. The method enables the quantification of failure modes and tracks the evolution of the buckling classes up to and through collapse.

For design purposes, application of *c*FSM and modal identification with the Direct Strength Method is proposed. Conclusions and recommendations for future research are provided.

Advisor: Professor Benjamin W. Schafer

Readers: Professor Takeru Igusa

Professor James K. Guest

## **Acknowledgements**

The author wants to thank several people who made this research possible during the past four years.

First of all, I want to express my great gratitude and very sincere thanks to my advisor, Professor Ben Schafer. His expertise, enthusiastic guidance, and encouragement stimulated my research work for the past four years through all the stages of my doctoral studies. Professor Schafer is not only a great mentor in research but also in life. I can never thank him enough.

I also would like to thank Professor Takeru Igusa and Professor James Guest for serving on my doctoral committee and for their review and suggestions on this work. I also want to thank Professor Narutoshi Nakata who served as alternative on my doctoral committee and also my GBO committee. In addition, I want to thank Professor Lori Graham-Brady who also served on my GBO committee. Their help and kindness are truly appreciated.

Besides, I wish to specially thank Professor S ndor d ny at Budapest University of Technology and Economics for his continuous effort through our collaboration on this cutting-edge research topic.

Through my four years in the department of Civil Engineering at Johns Hopkins University, a lot of former and current fellow student gave me so much help. I want to give them my sincere appreciation for their friendship and the many valuable discussions, especially, the “gangs” of the thin-walled research group, Cris Moen, Yared Shifferaw, Mina Seif, Vahid Zeinoddini, Luiz Vieira, Kara Peterman, Jiazheng Leng, Stefan Szyniszewski, Deniz Ayhan, Hannah Blum, Peng Liu, Tian Gao and visiting scholars

from my alma mater, Professor Jinghai Gong and Guozhi Qiu. I will cherish all the joyful moments I shared with you guys for the rest of my life.

There are lots of friends at Johns Hopkins University who gave me significant support and numerous advice. Particularly, the time we spend together during the spare time keep my life colorful in the USA.

Finally, I want to thank my wife Juan Chen and our families for their continuous encouragement, tenacious support, enormous patience, and invaluable sacrifice. I know they will always behind me as my safe harbor no matter how fierce and difficult the future will be.

It is always worth marking everything in life; especially when the surprising new life comes along like a miracle just walks in. At the graduation time, our first baby is coming to the world in January 2012. This makes me truly grateful of life.

*With all the loves to Juan and our new baby*

## Preface

This dissertation is submitted to the Johns Hopkins University for the degree of Doctor of Philosophy. The work described in the dissertation was carried out by the author as a graduate student in the Department of Civil Engineering from Sep. 2007 to Aug. 2011 under the guidance of Professor Ben Schafer.

The author claims that the work presented in the dissertation is original with proper references to acknowledge any information or ideas from other resources during the course of this research. Several supporting papers which are based on the work presented in the dissertation have been published in conjunction with Professor Ben Schafer and other coauthors as listed:

1. Li, Z., Schafer, B.W. (2009) “*Finite strip stability solutions for general boundary conditions and the extension of the constrained finite strip method.*” 12<sup>th</sup> International Conf. on Civil, Structural and Environmental Engineering Computing (CC-2009), Funchal (Madeira), Portugal. Published in Trends in Civil and Structural Computing, Ed. Topping et al., Saxe-Colburg Publications, pp. 103-13
2. Li, Z., Schafer, B.W. (2010) “*The constrained finite strip method for general end boundary conditions.*” Structural Stability Research Council - Proceedings of the 2010 Annual Stability Conference, Orlando, FL, USA; 573-591
3. Li, Z., Schafer, B.W. (2010) “*Buckling Analysis of Cold-Formed Steel Members with General Boundary Conditions using CUFSM: Conventional and Constrained Finite Strip Methods.*” 20<sup>th</sup> International Specialty Conference on Cold-Formed Steel Structures, St. Louis, MO

4. Li, Z., Schafer, B.W. (2010) “*Application of the finite strip method in cold-formed steel member design.*” *Journal of Constructional Steel Research*. 66(8-9): p. 971-980
5. Li, Z., Hanna, M.T., Ádány, S., Schafer, B.W. (2010) “*Impact of Basis, Orthogonalization, and Normalization the constrained Finite Strip Method for Stability Solutions of Open Thin-walled Members.*” *Thin-Walled Structures*, 49 (9), pp. 1108-1122
6. Li, Z., Joó, A.L., Ádány, S., Schafer, B.W. (2011) “*Approximate modal identification in nonlinear collapse analysis of thin-walled members.*” *Structural Stability Research Council - Proceedings of the 2011 Annual Stability Conference, Pittsburg, PA, USA; May 10-14*
7. Li, Z., Joó, A.L., Ádány, S., Schafer, B.W. (2011) “*Modal identification for finite element models of thin-walled members.*” *Proceedings of the 6th Intl. Conf. on Thin-Walled Structures, Sept. 5-7, Timisoara, Romania*

# Table of Contents

List of Figures .....	xiv
List of Tables .....	xx
Chapter 1 Introduction .....	1
1.1 Cold-formed steel members .....	1
1.2 Numerical modeling of elastic buckling analysis .....	3
1.2.1 Finite Strip Method .....	4
1.2.2 Constrained Finite Strip Method .....	7
1.2.3 Generalized Beam Theory .....	8
1.2.4 Finite Element Method .....	9
1.3 Design methods .....	10
1.3.1 Effective Width Method .....	10
1.3.2 Direct strength method .....	11
1.4 Motivation .....	14
1.5 Outline of thesis .....	17
Chapter 2 Conventional finite strip method for general end boundary conditions .....	20
2.1 Introduction .....	20
2.2 Finite strip method .....	21
2.2.1 Degree of freedoms and shape functions .....	21
2.2.2 Elastic stiffness matrix .....	22
2.2.3 Geometric stiffness matrix .....	25
2.2.4 Assembly .....	27
2.2.5 Stability solution .....	28
2.3 Validation studies for finite strip solution .....	29

2.3.1	Plate studies: comparison to classical solution .....	29
2.3.2	Plate studies: comparison to finite element solution.....	31
2.3.3	Member studies .....	38
2.4	Signature curve and general finite strip method solution.....	45
2.5	Longitudinal terms .....	50
2.6	Spring modeling .....	55
2.6.1	Spring stiffness in FSM .....	55
2.6.2	Analytical solution for global buckling .....	56
2.6.3	Comparison with shell FEM .....	68
2.7	Element-wise finite strip method .....	72
2.8	Summary .....	75
Chapter 3 Constrained finite strip method for general end boundary conditions .....		77
3.1	Introduction .....	77
3.2	Buckling mode definition.....	78
3.3	Notations and framework of constrained finite strip method.....	80
3.4	Derivations of constraint matrix $R$ .....	83
3.4.1	Derivation of $R_{GD}$ .....	83
3.4.2	Derivation of $R_L$ .....	93
3.4.3	Derivation of $R_{ST}/R_O$ .....	94
3.5	Bases.....	96
3.5.1	Natural basis.....	96
3.5.2	Modal basis .....	98
3.5.3	Summary of the bases .....	100
3.6	Normalizations .....	101

3.7	Modal decomposition.....	102
3.8	Modal Identification.....	108
3.9	Recommendation of basis, normalization, and summation of participation options.....	114
3.10	Summary.....	115
Chapter 4 Modal Identification for elastic buckling FE analysis .....		117
4.1	Introduction .....	117
4.2	Extrapolation of cFSM base function to FEM context .....	118
4.3	Identification Method.....	119
4.3.1	Minimization problem .....	119
4.3.2	Participation evaluation .....	120
4.3.3	Error estimation .....	121
4.4	Numerical studies: FSM-like boundary conditions.....	121
4.4.1	Finite element modeling .....	122
4.4.2	<i>Associated</i> base function.....	124
4.4.3	Generalized base function.....	134
4.4.4	Comparison of participations between associated and generalized base functions.....	142
4.5	Numerical studies: arbitrary boundary conditions .....	146
4.5.1	Semi-rigid end boundary conditions.....	147
4.5.2	Mixed end boundary conditions.....	155
4.6	Numerical studies: partially restrained members .....	158
4.7	Numerical studies: unidentical mesh.....	165
4.8	Numerical studies: member with holes .....	167
4.9	Summary .....	169

Chapter 5 Modal identification for nonlinear FE collapse analysis.....	171
5.1 Introduction .....	171
5.2 Differences compared to elastic buckling analysis .....	172
5.2.1 Eigenbuckling identification.....	172
5.2.2 Nonlinear collapse analysis.....	173
5.3 Linear elastic static analysis.....	174
5.4 Modeling parameters for nonlinear collapse analysis .....	178
5.4.1 Element and Mesh.....	179
5.4.2 Boundary conditions .....	179
5.4.3 Material model .....	180
5.4.4 Imperfections .....	180
5.4.5 Solution control.....	180
5.5 Modal identification of FEM nonlinear collapse analysis .....	181
5.5.1 Cross-sections under study .....	181
5.5.2 Modal identification: perfectly initial geometry (no initial imperfection)	182
5.5.3 Modal identification: models with initial imperfections.....	185
5.6 Discussion .....	192
5.7 Summary .....	193
Chapter 6 Design applications of the finite strip method and modal identification .....	195
6.1 Introduction .....	195
6.2 Two step method based on signature curve .....	196
6.2.1 Problem statement.....	196
6.2.2 Proposed solution.....	198
6.3 Method based on FSM solution of general boundary conditions.....	199

6.3.1	Conventional FSM solution .....	199
6.3.2	Method with modal identification.....	200
6.3.3	Alternative way implemented by modal decomposition .....	201
6.4	Method based on FEM for general boundary conditions.....	202
6.4.1	Traditional observation method .....	203
6.4.2	Method with Modal identification .....	203
6.5	Numerical examples.....	204
6.5.1	FSM-like boundary condition cases.....	204
6.5.2	Partially-restrained beam cases.....	208
6.6	Discussions.....	210
6.7	Summary .....	211
Chapter 7 Summary and recommendations .....		212
7.1	Summary .....	212
7.2	Recommendations for future research.....	216
References.....		218
Appendix A: Integrals from $I_1$ to $I_5$ .....		222
Appendix B: CUFSM v4 .....		225
B.1	Flow charts of the program .....	225
B.2	Screen shots of the program .....	227
B.3	Codes.....	233

## List of Figures

Figure 1-1 A variety of cold-formed steel cross sections [3].....	2
Figure 1-2 Commonly used cold-formed steel shapes [3] .....	3
Figure 1-3 Typical FEM versus FSM mesh for thin-walled lipped channel .....	5
Figure 1-4 The cross-section stability “signature curve” from an FSM solution .....	6
Figure 1-5 Failure modes in the test (Courtesy of Yu and Schafer [44]) .....	15
Figure 2-1 Coordinates, Degree of Freedom, and loads of a typical strip [46] .....	21
Figure 2-2 Buckling coefficients of plates in compression with varying end conditions.	31
Figure 2-3 Buckling coefficients FEM and FSM results, C-C, s-s.....	32
Figure 2-4 Buckling mode shapes of FEM and FSM at $L/b=5$ , C-C, s-s .....	33
Figure 2-5 Buckling coefficients FEM and FSM results, C-C, c-c .....	33
Figure 2-6 Buckling mode shapes of FEM and FSM at $L/b=5$ , C-C, c-c.....	34
Figure 2-7 simply supported on unloaded edges (s-s), various boundary conditions on loaded edges.....	36
Figure 2-8 clamped on unloaded edges (c-c), various boundary conditions on loaded edges .....	38
Figure 2-9 Stability under compression for a 350S162-43 with clamped ends.....	40
Figure 2-10 Mode shapes for a 350S162-43 in compression with clamped ends .....	41
Figure 2-11 Stability in major-axis bending for a 350S162-43 with clamped ends .....	42
Figure 2-12 Mode shapes for a 350S162-43 in major-axis bending with clamped ends..	43
Figure 2-13 Stability in minor-axis bending for a 350S162-43 with clamped ends.....	43
Figure 2-14 Mode shapes for a 350S162-43 in minor-axis bending with clamped ends .	44
Figure 2-15 Stability solutions of SSMA 400S162-68 under major-axis bending for S-S .....	47

Figure 2-16 Stability solutions of SSMA 400S162-68 under major-axis bending for C-C .....	49
Figure 2-17 Stability solutions of SSMA 400S162-68 under major-axis bending for both S-S and C-C combined.....	50
Figure 2-18 Participation of longitudinal terms at $L/b=5$ .....	51
Figure 2-19 Participation of the longitudinal terms .....	54
Figure 2-20 FSM and analytical solutions of the column with/without springs for S-S ..	59
Figure 2-21 FSM and analytical solutions of the column with/without springs for C-C .	60
Figure 2-22 FSM and analytical solutions of the column with/without springs for S-C..	60
Figure 2-23 FSM and analytical solutions of the column with/without springs for C-F..	61
Figure 2-24 FSM and analytical solutions of the column with/without springs for C-G .	61
Figure 2-25 Illustration of cross section and springs .....	63
Figure 2-26 FSM and analytical solution of column for S-S with/without springs.....	66
Figure 2-27 FSM and analytical solution of column for C-C with/without springs.....	66
Figure 2-28 FSM and analytical solution of column for S-C with/without springs .....	67
Figure 2-29 FSM and analytical solution of column for C-G with/without springs.....	67
Figure 2-30 FSM and analytical solution of column for C-F with/without springs .....	68
Figure 2-31 Continuous springs in the member length.....	69
Figure 2-32 FSM and FEM solutions of column for C-C with/without springs.....	70
Figure 2-33 Buckling mode shapes of FEM and FSM at $L=2.42m$ .....	70
Figure 2-34 FSM and FEM solutions of beam member with springs for C-C .....	71
Figure 2-35 FSM and FEM buckling mode shapes at $L=2.42m$ .....	72
Figure 2-36 Pre-buckling stress distribution in FSM and FEM for spring modeling.....	72
Figure 2-37 uniform boundary conditions and element-wise boundary conditions at the ends .....	73
Figure 2-38 Stability solution of FSM and FEM for mixed end boundary conditions.....	74

Figure 2-39 Stress distribution of plates with mixed end boundary conditions .....	75
Figure 3-1 Node classification and numbering scheme .....	81
Figure 3-2 Cross-section model for enforcement of Criterion #2.....	86
Figure 3-3 Warping vectors of four global modes.....	92
Figure 3-4 FSM and pure <i>c</i> FSM solutions against GBT solutions.....	103
Figure 3-5 Modal decomposition of <i>c</i> FSM.....	106
Figure 3-6 Buckling modes of the conventional FSM and <i>c</i> FSM .....	107
Figure 3-7 Sensitivity of modal identification to $L^1$ and $L^2$ norm in signature curve .....	113
Figure 4-1 Dimension of the cross section and discretization .....	123
Figure 4-2 FE buckling modes for selected cases.....	124
Figure 4-3 FEM base functions for different boundary conditions .....	125
Figure 4-4 Critical loads, participations, and identification error of FE solution of FSM-like S-S boundary conditions .....	127
Figure 4-5 Critical loads, participations, and identification error of FE solution of FSM-like C-C boundary conditions .....	128
Figure 4-6 Critical loads, participations, and identification error of FE solution of FSM-like S-C boundary conditions.....	129
Figure 4-7 Critical loads, participations, and identification error of FE solution of FSM-like C-G boundary conditions.....	130
Figure 4-8 Critical loads, participations, and identification error of FE solution of FSM-like C-F boundary conditions.....	131
Figure 4-9 Higher mode shapes of FE solution of FSM-like S-S boundary.....	131
Figure 4-10 FEM deformed shapes compared with identified mode shapes from <i>c</i> FSM for some selected modes (add C-F #3) .....	133
Figure 4-11 Participations and identification error of FE solution of FSM-like C-C by S-S <i>c</i> FSM base function .....	136
Figure 4-12 Participations and identification error of FE solution of FSM-like S-C by S-S <i>c</i> FSM base function .....	136

Figure 4-13 Participations, and identification error of FE solution of FSM-like C-G by S-S cFSM base function .....	136
Figure 4-14 Participations and identification error of FE solution of FSM-like C-F by S-S cFSM base function .....	136
Figure 4-15 Longitudinal field diagram: (a) C-F&F-C m=1; (b) S-S m=1,2,...,10 .....	138
Figure 4-16 S-S, C-F, and F-C of m=1, G1, D1, L1 .....	139
Figure 4-17 Participations and identification error of FE solution of FSM-like C-C by generalized base function.....	141
Figure 4-18 Participations and identification error of FE solution of FSM-like S-C by generalized base function.....	141
Figure 4-19 Participations, and identification error of FE solution of FSM-like C-G by generalized base function.....	141
Figure 4-20 Participations and identification error of FE solution of FSM-like C-F by generalized base function.....	141
Figure 4-21 Semi-rigid boundary condition cases .....	147
Figure 4-22 Modal identification of semi-rigid case I .....	149
Figure 4-23 Boundary conditions and springs in FEM model.....	150
Figure 4-24 Modal identification of semi-rigid case II - partially restrained at the end as a whole.....	150
Figure 4-25 FEM and approximated mode shapes for selected modes .....	151
Figure 4-26 Boundary conditions and springs in FEM model.....	152
Figure 4-27 Modal identification of semi-rigid case II - partially restrained at four corners .....	152
Figure 4-28 FEM and approximated mode shapes for selected modes .....	153
Figure 4-29 Boundary conditions and springs information in FEM model.....	154
Figure 4-30 Modal identification of semi-rigid case III .....	154
Figure 4-31 FEM and approximated mode shapes for selected modes .....	155
Figure 4-32 Mixed boundary cases.....	156

Figure 4-33 Modal identification of mixed boundary case a.....	157
Figure 4-34 Modal identification of mixed boundary case b.....	157
Figure 4-35 Modal identification of mixed boundary case c.....	158
Figure 4-36 FEM mode shapes for selected modes .....	158
Figure 4-37 Partially restrained simply supported beam .....	159
Figure 4-38 Modal identification of beam without springs .....	161
Figure 4-39 Modal identification of beam with weak springs.....	162
Figure 4-40 Modal identification of beam with practical springs.....	163
Figure 4-41 Selected buckling modes.....	164
Figure 4-42 springs effects on buckling behavior by FSM.....	165
Figure 4-43 Modal identification of unidentical mesh .....	166
Figure 4-44 Selected buckling mode shapes of irregular mesh model .....	167
Figure 4-45 Hole location and size and column boundary conditions (mm).....	168
Figure 4-46 Modal identification of column with rectangular holes .....	168
Figure 4-47 Selected buckling mode shapes for column with holes .....	169
Figure 5-1 Warping functions of $G$ space.....	175
Figure 5-2 Warping functions of $D$ space.....	176
Figure 5-3 Deformed shapes of major-axis bending warping functions for S-S and C-C .....	177
Figure 5-4 Deformed shapes of symmetric distortional warping functions for S-S and C-C .....	178
Figure 5-5 Dimensions of cross sections (mm) and mesh .....	182
Figure 5-6 Local dominant model.....	188
Figure 5-7 Distortional dominant model.....	190
Figure 5-8 Local-distortional interacted model .....	191

Figure 6-1 Cross-section models and dimensions for use in FSM analyses..... 197

Figure 6-2 Signature curve augmented with pure mode *c*FSM solution and illustration of the proposed FSM@*c*FSM- $L_{cr}$  solution to identifying non-unique minima..... 199

## List of Tables

Table 3-1 Mode classification.....	80
Table 3-2 Summary of the bases.....	100
Table 3-3 A summary of normalized subspaces .....	104
Table 3-4 Participation of G, D, L and ST for C-C boundary conditions, vector norm .	110
Table 3-5 Participation of G, D, L and ST for C-C boundary conditions, work norm...	114
Table 4-1 Participations and errors of FE solution of FSM-like S-S boundary conditions by base functions with different longitudinal terms .....	132
Table 4-2 Participations and critical loads of FEM and FSM solutions .....	134
Table 4-3 Modal identification differences by generalized base functions relative to those by associated base functions for C-C.....	143
Table 4-4 Modal identification differences by generalized base functions relative to those by associated base functions for C-F .....	143
Table 4-5 Participations of FEM solution by associated and generalized base functions .....	146
Table 5-1 Participations of eigenmode and nonlinear collapse models.....	183
Table 5-2 Imperfection cases and their peak loads .....	186
Table 6-1 Characteristic buckling modes of FSM by different methods .....	205
Table 6-2 Characteristic buckling modes of FEM by different methods.....	206
Table 6-3 Nominal strengths of the columns by FSM solutions .....	207
Table 6-4 Nominal strengths of the columns by FEM solutions .....	207
Table 6-5 Identified characteristic buckling modes for all three cases.....	209
Table 6-6 Nominal strengths of the beams .....	210

## **Chapter 1 Introduction**

### **1.1 Cold-formed steel members**

As one of the two primary constructional steel types, cold-formed steel is widely used as secondary load-carrying members in tall buildings such as roof and floor decks, steel joists, wall panels, window frame and entrance structures, etc. [1] or even as primary load-carrying members in low-rise and modest midrise buildings. Cold-formed steel members are usually created by the working of sheet steel using stamping, rolling, or presses to deform the sheet into a usable product [2]. As the name indicates, different from the other steel construction material - hot-rolled steel, the manufacturing of cold-formed steel products occurs at room temperature. The material is plastically deformed to shape, thus the material's yield strength increases along with residual stresses and strains, while ductility decreases modestly [3].

One of the distinct characteristics of cold-formed steel is the variety of cross section shapes. Due to the relatively easy method of manufacturing, the cross section can be formed into any desired shape to accommodate the demands of optimized design in structural applications for economical purposes. Figure 1-1 shows an assembly of cold-formed steel cross section shapes used in practice. Some typically used cross section shapes are shown in Figure 1-2.

Cold-formed steel also offers many other advantages including lightness, high strength and stiffness, ease of prefabrication and mass production, uniform quality, fast

and easy installation, and economy in transportation and handling. Therefore, cold-formed steel members have been widely used in buildings, bridges, storage racks, grain bins, car bodies, railway coaches, highway products, transmission towers, transmission poles, drainage facilities, various types of equipment and others [3].

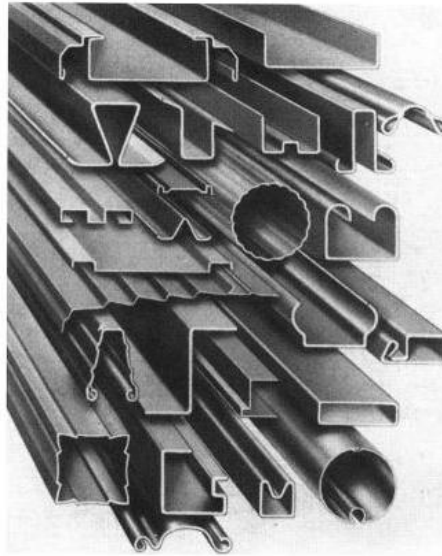


Figure 1-1 A variety of cold-formed steel cross sections [3]

Cold-formed steel has taken upon a significant market share among construction materials because of its advantages and the industry-wide support provided by various organizations that promote cold-formed steel research and products, including codes and standards development that is supervised by the American Iron and Steel Institute (AISI) [4].

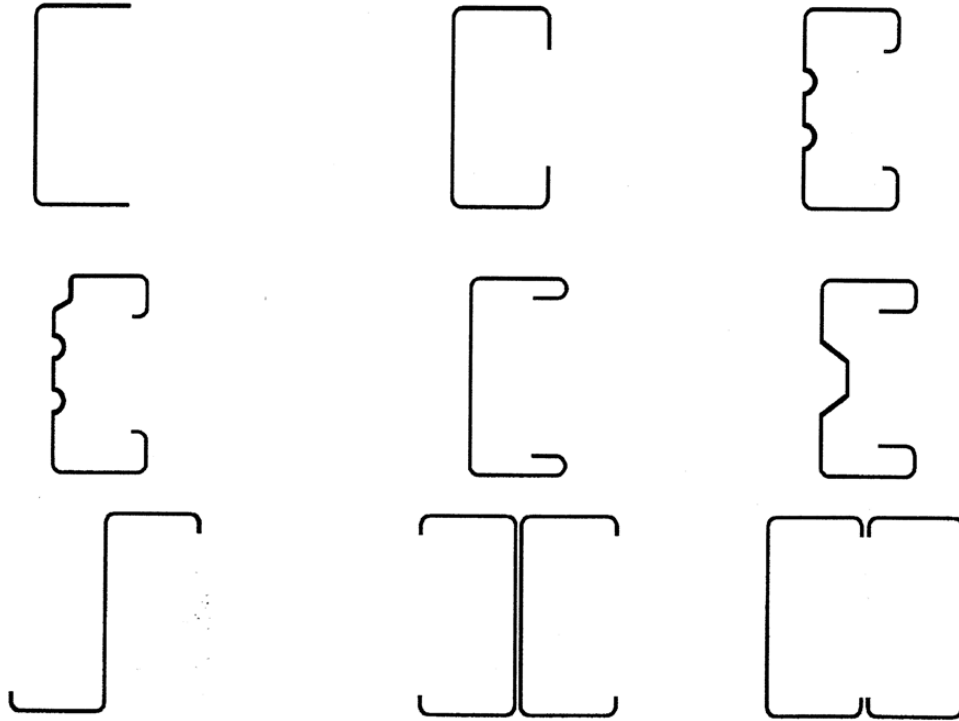


Figure 1-2 Commonly used cold-formed steel shapes [3]

## 1.2 Numerical modeling of elastic buckling analysis

Due to the high slenderness ratio of each individual component comprising a thin-walled member, it is common that these thin members buckle at a stress level less than the yield point if they are subjected to loading cases that may generate compression stress in the cross section. Thus, buckling phenomena are paid special attention to in the design of thin-walled structures.

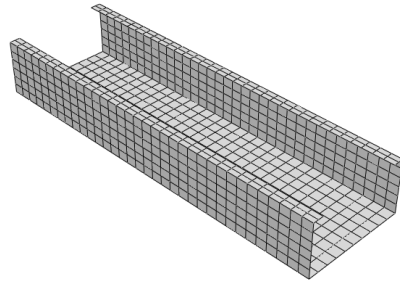
Current design specifications (e.g., for cold-formed steel) [4-6] all tackle the strength prediction in member design from the investigation of the elastic buckling based on rational analyses (numerical or analytical), then employ empirical equations based on experimental data to predict the design strength of the member. The prediction of the elastic buckling plays a central role in the design procedure. In particular, for open cross-section cold-formed steel members (e.g., C, Z, hat, etc.), usually, three basic classes of

buckling may be encountered: local (plate), distortional, and global (Euler) buckling. As reflected in current design specifications, each buckling mode is treated individually because of their significantly different post-buckling behavior, further some modes are considered interactively since they may be coupled with one another.

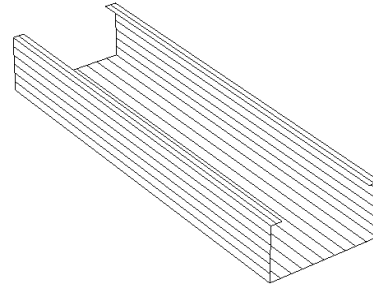
Many analysis methods for elastic buckling prediction are also available, such as the Finite Element Method (FEM), Finite Strip Method (FSM), constrained Finite Strip Method (cFSM), Generalized Beam Theory (GBT), and analytical solutions. Analytical solutions, based on simplified models, e.g., for distortional buckling [7-10], are inherently limited in their applicability and so can never provide the general methodology sought here. Thus, the focus of this research is on the aforementioned numerical methods.

### **1.2.1 Finite Strip Method**

The idea behind the finite strip method is to reduce the number of partial differential equations that must be solved when modeling. The reduction is achieved by assuming the separation of variable approach can be applied in expressing the interpolation functions of the unknown displacement [11]. More specifically, instead of discretizing the member in the longitudinal direction, FSM uses specially selected shape functions to interpolate the longitudinal field, while common polynomial shapes are still used for the transverse field, as is common in FEM. Therefore, a thin-walled cross-section is discretized into a series of longitudinal strips (or elements) opposite to finite element discretization, see Figure 1-3. Some obvious limitations of FSM are that the cross section has to be uniform along the length and depending on the formulation the application is only suitable to prismatic cross sections.



(a) FEM mesh



(b) FSM mesh

Figure 1-3 Typical FEM versus FSM mesh for thin-walled lipped channel

Since the longitudinal field is interpolated by longitudinal shape functions, the choice of suitable interpolation functions for a strip play a key role in the application of FSM. There are several options available as interpolation functions dependent on the boundary conditions as well as the nature of the problem. For instance, functions sought from the vibration eigenfunctions are commonly used, which is a combination of continuously differentiable harmonic and hyperbolic series that are chosen to satisfy the end boundary conditions of the strip. Consequently, the stiffness matrices can be formulated explicitly without numerical integration, and the FSM is often referred to as the semi-analytical finite strip method. Similarly, employing only trigonometric functions (e.g., [12]) satisfying the boundary conditions a priori is proven to be effective as well. Other shape functions such as buckling eigenfunctions from the mode shape, exponential functions, and decaying power series [11] are all valid choices. In addition, spline functions [13] and computed shape functions [14] have further increased the flexibility in the choice of interpolation functions especially in dealing with multi-span or column-supported structures. Once the displacement field has been fully defined, the traditional formulation of the stiffness matrices (elastic and geometric stiffness) can be performed based on the selected plate theory (Kirchhoff or Mindlin).

The semi-analytical finite strip method was originally developed by Cheung for the stress analysis of a plate in bending [15]. Cheung further extended the method by including the membrane deformation in addition to the plate bending [16]. Later, the semi-analytical FSM has been applied by many researchers to vibration and stability analysis in many structural applications such as shell structures [17, 18], bridges [16, 19, 20], and tall building [21-23].

In stability analysis, for examining instabilities in a thin-walled member under longitudinal stress (axial, bending, and/or warping torsion), the semi-analytical FSM has been widely used. In particular, the application to members with simply supported ends results in an efficient solution and the “signature curve” of the stability of a member in terms of buckling half-wavelength vs. buckling load as shown in Figure 1-4 for example, as popularized by Hancock [24] and implemented in the open source program CUFSM [25].

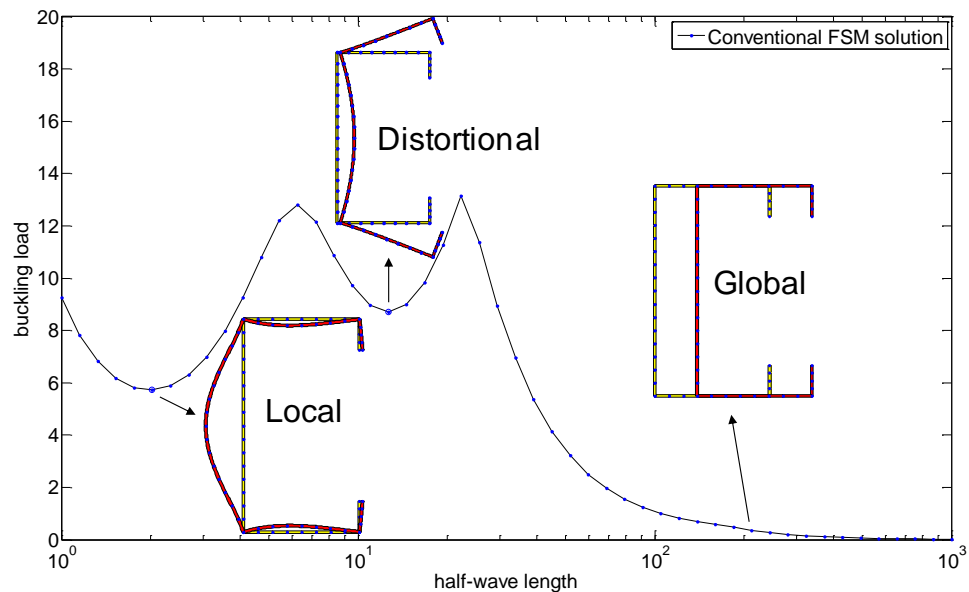


Figure 1-4 The cross-section stability “signature curve” from an FSM solution

Minima in the signature curve, as shown in Figure 1-4, indicate the lowest critical load at which a particular buckling mode occurs, and also the half-wavelength at which that mode will repeat within any physical member length. Traditionally, the first minimum is local buckling, the second distortional buckling, and global buckling is identified in the descending branch of the curve at a longer half-wavelength equal to the global unbraced length of the member.

Therefore, even though the finite element method has dominated computational structural analysis, the finite strip method continues to have its role due to its own merits such as ease of modeling and computational efficiency.

### 1.2.2 Constrained Finite Strip Method

The constrained FSM (*cFSM*) was originally derived from the semi-analytical FSM by Ádány and Schafer [25-28]. The key feature of *cFSM* is that based on mechanical criteria [26, 28], the general displacement field  $d$  (or buckling mode  $\phi$ ) may be separated into  $G$ ,  $D$ ,  $L$ , and  $ST/O$  subspaces corresponding to the Global, Distortional, Local and Shear and Transverse extension or Others deformation modes. Mathematically, any general displacement field may be written as:

$$d = R_M d_M \quad (1-1)$$

where  $R_M$  is the constraint matrix for the selected modal space(s) and  $d_M$  is the resulting deformations within that space. Note, the subscript  $M$  refers to the modal space ( $G$ ,  $D$ ,  $L$ ,  $ST/O$  or any combination thereof).  $R_M$  is obtained through exploiting the mechanical criteria of  $G$ ,  $D$ ,  $L$ , and  $ST/O$ .

There are two primary capabilities of *c*FSM: (1) *modal decomposition*: stability solutions can be forced into selected deformation modes, e.g. focusing only on distortional buckling; and (2) *modal identification*: general stability solutions from FSM can be classified into several fundamental modal bases, e.g. identifying the contribution of local and distortional buckling for a selected FSM solution.

### **1.2.3 Generalized Beam Theory**

Generalized Beam Theory (GBT) is an extension of classical beam theory that enriches the displacement degrees of freedom enabling cross-section distortion and local plate bending. The development of the theory has been pioneered by Professor R. Schardt and his colleagues at the University of Darmstadt in Germany, then greatly extended to linear elastic [29] and second-order analysis including cross-section distortion to application of buckling problems and general second-order problems [30] by Davies, et.al. Later, Silvestre and Camotim extended GBT to arbitrary orthotropic materials [31, 32] and formalized the method [33] to a wide number of applications [34-37]. The method has been implemented in a user-friendly code GBTUL [35].

The application of GBT stems from its cross sectional analysis as given in [31, 32] and this leads to the definition of several cross section deformation modes: axial extension, major/minor axis bending, torsional, distortional, and local-plate modes. With the cross-section deformation modes in place, the modal selection for the next-step member analysis is possible similar to the selection of modal space,  $M$  (Eq. 1-1). Then, the solution of the buckling problem involves solving a coupled system of eigenvalues based on the GBT equilibrium equations. This can be performed in two methods: 1) an analytical method that, similar to FSM, uses trigonometric function to represent the

longitudinal field; or 2) an FEM-based method that discretizes the member into elements along the length. Currently, application of the analytical method is limited to simply-supported boundary conditions. After solving the eigenvalue problem, the critical loads and buckling modes can be investigated. Modal participation of included cross-section deformation modes can be identified as well.

It is worth noting here that although GBT and cFSM begin from different backgrounds, the two methods use similar mechanical definitions for the three basic buckling mode classes (cross-section deformation modes), i.e. local, distortional, and global, and thus lead to very similar solutions [38].

#### 1.2.4 Finite Element Method

With the advances in computational resources, shell finite element analysis has been increasingly used in the stability analysis of thin-walled structures. The ability to handle arbitrary boundary conditions, explicitly consider moment gradient, appropriately take account of shear effects, and handle members with varying cross sections along the length (like holes) make the use of FEM exclusively attractive.

Usually, there are two steps to performing an elastic buckling analysis with the geometry, material property, boundary conditions, and reference loading defined in the FEM model. First, a linear perturbation static analysis is solved to find the stress distribution in the model based on the reference loading. Second, with the stress distribution the geometric stiffness matrix can be formulated and the stability equilibrium equation can be obtained as:

$$([K] - \lambda [K_{g, \sigma, ref}]) \phi = 0 \quad (1-2)$$

where,  $[K]$  is the elastic stiffness matrix, and  $[K_g]_{\sigma, \text{ref}}$  is the geometric stiffness matrix at the reference loading state. Eigenvalue  $\lambda$  is the critical buckling load and eigenvector  $\phi$  is the associated buckling mode.

FEM is not often used by designer because of the overhead in initiating the model and the fact that it cannot uniquely identify the buckling modes. These drawbacks are the primary reason for the popularity of FSM in this field.

### **1.3 Design methods**

In current cold-formed steel design specifications, e.g., in North America, two basic design methods for cold-formed steel members are available: the Effective Width Method and the Direct Strength Method (DSM). The Effective Width Method performs a reduction of the plates that comprise a cross-section based on the stability of the individual plates, while DSM performs a similar reduction, but based on the full cross-section stability; in either local, distortional, and/or global buckling modes. In essence the essential difference is the replacement of plate stability with member stability that includes plate buckling.

#### **1.3.1 Effective Width Method**

Normally, for a “stiffened plate”, i.e., one which is restrained along both the loaded and unloaded sides does not collapse when the buckling stress is reached. Instead, additional load can still be carried by the plate after buckling by means of transverse stresses. This phenomenon is termed “postbuckling reserve”.

For the “stiffened plate”, the stress distribution in the longitudinal direction is not uniform due to the reduced rigidity in the center of the plate as it buckling (deforms) out-

of-plane. The maximum stress will increase over the buckling stress up to the yield stress at the supported sides, then the plate fails. The load can be assumed to be carried by a fictitious width, which is subjected to a uniformly distributed stress  $f_{\max}$ , which is the edge stress, and assumed equals to the yield stress at maximum capacity. This is the effective width concept, first introduced by von Karman et al. [39] and later modified by Winter [40]. This has become the key to the design of cold-formed steel members from the first AISI specification in 1946 to the latest 2007 NAS specification.

For complex cross sections, the effective width should be determined for each compression portion and the strength of the section can be calculated based on the effective cross section.

However, from a theoretical point of view, this is a largely simplified method. First, it focuses on the membrane and neglects the bending. Second, it does not take into consideration of the variation along the length associated with the buckling shape and also the variation in the thickness. Third, due to the imperfection, the stress distribution is not uniform even before the buckling occurs.

### **1.3.2 Direct strength method**

Although the Effective Width Method has been adopted in many specifications worldwide and proven to be reliable, there are two major drawbacks that make it highly undesirable. One, the Effective Width Method treats the elements of the whole cross section independently, so the interaction between elements has been totally ignored. Two, when the section becomes more complex or optimized with additional edge and/or immediate stiffeners, the computation of the Effective Width Method becomes unduly complicated and time-consuming.

Therefore, a new design method – Direct Strength Method (DSM) has been proposed by Schafer and Peköz [41, 42] to overcome these problems and adopted in specification [4]. The new method avoids the calculation of effective width and uses strength curves instead. The elastic buckling loads are obtained based on the entire member, for instance from FSM solutions, instead of individual elements/plates. DSM is based on the same empirical assumption as the effective width method, that the nominal strength is a function of elastic buckling load and yield stress of the material. The equations of DSM were calibrated against a large amount of experimental data (similar to the Effective Width Method, in fact many of the same experiments were employed).

Specifically, according to DSM, if all the elastic instabilities for the gross section, i.e. local, distortional, and global buckling loads (or moments), have been determined and also the squash load (or yield moment) that causes the cross-section to yield, then the strength can be directly determined by predicting the load (or moment) capacities separately for Global (*G*), Local (*L*), and Distortional (*D*) buckling. The relevant DSM formulae in the specification [8] are recalled here in condensed form.

The nominal axial strength,  $P_n$ , is the minimum of the individual predicted capacities:

$$P_n = \min(P_{ne}, P_{n\ell}, P_{nd}) \quad (1-3)$$

where, the nominal axial strengths,  $P_{ne}$  for global buckling (flexural, torsional, or torsional-flexural buckling),  $P_{n\ell}$  for local buckling, and  $P_{nd}$  for distortional buckling are:

$$P_{ne} = \begin{cases} (0.658 \lambda_c^2) P_y & \text{if } \lambda_c \leq 1.5 \\ (0.877 \lambda_c^2) P_y & \text{if } \lambda_c > 1.5 \end{cases} \quad (1-4)$$

$$P_{n\ell} = \begin{cases} P_{ne} & \text{if } \lambda_\ell \leq 0.776 \\ (1 - 0.15(P_{cr\ell} / P_{ne})^{0.4}) (P_{cr\ell} / P_{ne})^{0.4} P_{ne} & \text{if } \lambda_\ell > 0.776 \end{cases} \quad (1-5)$$

$$P_{nd} = \begin{cases} P_y & \text{if } \lambda_d \leq 0.561 \\ \left(1 - 0.25(P_{crd}/P_y)^{0.6}\right) (P_{crd}/P_y)^{0.6} P_y & \text{if } \lambda_d > 0.561 \end{cases} \quad (1-6)$$

where,  $\lambda_c = \sqrt{P_y/P_{cre}}$ ,  $\lambda_\ell = \sqrt{P_{ne}/P_{cr\ell}}$ ,  $\lambda_d = \sqrt{P_y/P_{crd}}$ ,  $P_y = A_g F_y$ ,  $P_{cre}$ , minimum of the critical elastic column buckling load in flexural, torsional, or torsional-flexural buckling,  $P_{cr\ell}$ , critical elastic local column buckling load,  $P_{crd}$ , critical elastic distortional column buckling load,  $A_g$ , the gross area of the cross-section, and  $F_y$ , the yield stress.

The nominal bending strength,  $M_n$ , is the minimum of the individual capacities:

$$M_n = \min(M_{ne}, M_{n\ell}, M_{nd}) \quad (1-7)$$

where, the nominal bending strengths,  $M_{ne}$  for global buckling (lateral-torsional buckling),  $M_{n\ell}$  for local buckling, and  $M_{nd}$  for distortional buckling are:

$$M_{ne} = \begin{cases} M_{cre} & \text{if } M_{cre} < 0.56M_y \\ \frac{10}{9} M_y \left(1 - \left(\frac{10M_y}{36M_{cre}}\right)\right) & \text{if } 2.78M_y \geq M_{cre} \geq 0.56M_y \\ M_y & \text{if } M_{cre} > 2.78M_y \end{cases} \quad (1-8)$$

$$M_{cr\ell} = \begin{cases} M_{ne} & \text{if } \lambda_\ell \leq 0.776 \\ \left(1 - 0.15(M_{cr\ell}/M_{ne})^{0.4}\right) (M_{cr\ell}/M_{ne})^{0.4} M_{ne} & \text{if } \lambda_\ell > 0.776 \end{cases} \quad (1-9)$$

$$M_{nd} = \begin{cases} M_y & \text{if } \lambda_d \leq 0.673 \\ \left(1 - 0.22(M_{crd}/M_y)^{0.5}\right) (M_{crd}/M_y)^{0.5} M_y & \text{if } \lambda_d > 0.673 \end{cases} \quad (1-10)$$

where,  $\lambda_\ell = \sqrt{M_{ne}/M_{cr\ell}}$ ,  $\lambda_d = \sqrt{M_y/M_{crd}}$ ,  $M_y = S_f F_y$ ,  $M_{cre}$ , critical elastic lateral-torsional buckling moment,  $M_{cr\ell}$ , critical elastic local buckling moment,  $M_{crd}$ , critical elastic distortional buckling moment, and  $S_f$ , the gross section modulus referenced to the extreme fiber in the first yield.

Essentially, the use of column curves for global buckling is extended to local and distortional buckling instabilities with appropriate consideration of post-buckling reserve and interaction in these modes [42]. In particular, interaction between local and global buckling is included explicitly as shown in Eqs. (1-6) and (1-10).

#### **1.4 Motivation**

Design of cold-formed steel members requires careful examination of the elastic buckling loads for all the three buckling modes, global, local and distortional, that are commonly categorized. Current design specification, e.g. the Direct Strength Method [42, 43], aim to predict the ultimate strength in response to each mode as well as take into consideration the interaction of the modes. Therefore, finding the elastic buckling of a member under any loading and boundary condition, as input parameters for the Direct Strength Method, is a key step towards the final prediction of the ultimate strength.

To assess the stability of thin-walled members requires advanced tools to overcome the limitations in current numerical tools such as FSM and FEM. In particular, commonly available FSM solutions are only applicable to simply supported ends, while FEM analysis using plate or shell elements is limited by the subjective and laborious nature required in identifying the characteristic local, distortional, and global buckling modes.

Moreover, the development of the design equations for member design, in particular DSM, is based on the appropriate identification of the failure modes, e.g., as shown in Figure 1-5. Determination of the failure modes is complicated by potential failure mechanisms of material yielding, local buckling, distortional buckling, global buckling, and combinations thereof. To date, failure mode identification is investigated based on

subjective, and largely visual, engineering observations. Even for numerical simulations by nonlinear FEM analysis, since FEM itself provides no means of modal identification, failure modes are also judged by visual characterization. It is important to recognize that the underlying mechanisms of the member's failure are necessary for future specification development. Extensive nonlinear analysis incorporating geometric and material imperfections will be needed. A quantification method, similar to the strength prediction in the specification, is highly desirable to simplify the complicated behavior down to the fundamental buckling classes.



(a) Channel with sheathing



(b) Zed with sheathing

Figure 1-5 Failure modes in the test (Courtesy of Yu and Schafer [44])

The first step of this study is to develop a new FSM to account for general end boundary conditions: pin-pin, fixed-fixed, fixed-pin, fixed-free, and fixed-guided and use these solutions to extend the *c*FSM. The trigonometric longitudinal shape functions in [12] have been chosen over the spline shape functions for two reasons. First, the well-known signature curve is based on the trigonometric shape function (for simply-supported boundary conditions). Second, half-wavelength information of the buckling mode may still be easily evaluated with the trigonometric longitudinal shape functions.

The full derivation for a FSM stability solution that applies to general end boundary conditions is provided. The elastic and geometric stiffness matrices are provided in a general form with only specific integrals remaining boundary condition dependent. The new FSM has been implemented in a custom version of the finite strip program CUFSM as part of this thesis. Verification problems are provided against eigenbuckling shell finite element analysis solutions implemented in ABAQUS. Detailed theoretical background of modelling the springs in the new FSM solution is also provided. Particular attention has been paid to the number of longitudinal terms required in the analysis.

In addition, the developed solution provides a means to extend the constrained FSM, or *c*FSM, to the case of general end boundary conditions. The existing *c*FSM solutions for pin-pin boundary conditions are recast into the new generalized notation; specifically the constraint matrices for the Global, Distortional, Local, and Other (*G, D, L, ST/O*) deformation spaces are written in the generalized notation. Orthogonalization and normalization are discussed in detail. Recommendations are provided regarding the choice of basis and normalization. Full implementation of *c*FSM is enabled in a custom version of CUFSM (CUFSM v4).

To address the limits in modal identification in shell FEM solutions for linear elastic buckling analysis, an automatic mode identification method has been proposed which uses a special system of modal base functions, referred to as *c*FSM base functions. The modal identification method is enabled by creating a series of base functions within the fundamental buckling deformation classes that can then be compared to the general finite element displacements. The base functions are constructed using the constrained finite strip method (*c*FSM) for general end boundary conditions. A fairly sizeable minimization

problem is required for assigning the contributions to the fundamental buckling deformation classes. Modal identification results of FEM solutions are validated, and the applicability to arbitrary boundary conditions and members with perforations explored.

Moreover, the modal identification is extended to collapse analysis of thin-walled members modelled using material and geometric nonlinear shell finite element analysis. The method is able to (a) quantitatively associate failures with particular classes, e.g. state a model is a local failure, and (b) track the evolution of the classes, e.g., mixed local and distortional buckling leads to a distortional failure in a given model.

A conjugate goal of this study is to provide tools for elastic buckling analysis to aid the design procedure. For this purpose, application of the FSM and modal identification with the Direct Strength Method are discussed. As an ultimate goal of this work it is proposed to study collapse mechanisms more systematically by utilizing the modal identification capability and ultimately aid the development of future design specifications.

It is worth noting here that theory developed in this research is applicable to all the thin-walled members, but the focus of all applications herein is cold-formed steel.

## **1.5 Outline of thesis**

This dissertation consists of a total of 7 chapters including two appendices.

Chapter 1 contains the background and motivation of this research. A brief summary of the current design methods are provided. Numerical methods for analyzing the elastic buckling and collapse analysis and their limitations are introduced.

Chapter 2 presents the full derivation of the new finite strip method for general end boundary conditions by utilizing the trigonometric longitudinal shape functions available in the literature. The elastic and geometric stiffness matrices are provided in a general form with only specific integrals remaining boundary condition dependent. Validation against plate and members are illustrated by comparing the solution against FEM solutions obtained through ABAQUS with shell finite elements. Other considerations such as springs, longitudinal terms, and the possibility of an element-wise finite strip method are discussed.

Based on the work of Chapter 2, the existing constrained Finite Strip method (*cFSM*) for pin-pin boundary conditions is extended into the new generalized notation for general end boundary conditions in Chapter 3. Orthogonalization and normalization that forms the different bases are discussed in detail. Recommendations are provided regarding the choice of basis and normalization.

In Chapter 4, an automatic mode identification method for shell FEM elastic buckling analysis is proposed. Construction of the base functions from *cFSM* is discussed. Modal identification results of FEM solutions are validated and the applicability of any arbitrary boundary conditions and members with perforations are explored.

Following the same idea in Chapter 4, the modal identification method is extended to nonlinear FEM collapse analysis in Chapter 5. Applicability of modal identification to collapse analysis with geometric and material nonlinearities is illustrated through numerical studies.

Chapter 6 shows the application of the finite strip method and modal identification with the Direct Strength Method of design, specifically addressing how to utilize participation result of the modal identification solution.

Chapter 7 provides a summary of this research and lists recommendations for future research on numerical analysis and design of cold-formed steel structures.

Appendix A includes the remaining integrals that depend on the longitudinal shape functions in FSM.

Appendix B provides the flowchart and interfaces for the developed code CUFSM v4.

## Chapter 2 Conventional finite strip method for general end boundary conditions

### 2.1 Introduction

The semi-analytical finite strip method (FSM) provides the most widely used approach for identifying the characteristic stability modes of a thin-walled member. In particular, the “signature curve” of the stability of a member in terms of buckling half-wavelength vs. buckling load provides an efficient solution. A limitation of commonly available FSM solutions, such as the open source program CUFSM [25], is that they are only applicable to simply supported ends.

This chapter provides the derivation and validation studies for the extension of CUFSM to general boundary conditions, namely: clamped-clamped ( $C-C$ ), simple-clamped ( $S-C$ ), clamped-free ( $C-F$ ), clamped-guided ( $C-G$ ), and simple-simple ( $S-S$ ). Specially selected longitudinal shape functions are employed to represent the various general end boundary conditions. The resulting elastic and geometric stiffness matrices are presented in closed-form with only specific presolved integrals remaining boundary condition dependent. Verification problems are provided against eigenbuckling shell finite element analysis solutions implemented in ABAQUS [45].

Particular attention is paid to the number of longitudinal terms required to provide converged solutions in the analysis of typical thin-walled members with the full suite of

boundary conditions, and loading. Supplemental restraint/bracing is common in thin-walled members and typically modelled in FSM as an additional spring foundation. The implementation of a spring model in FSM with general boundary conditions is demonstrated and verified with analytical solution. Comparison of spring modelling between FSM and shell finite element method (FEM) is provided to highlight the difference between the two methods in linear perturbation analysis. Moreover, an FSM approach where the boundary conditions are specified strip-by-strip is explored and shown to be inappropriate.

## 2.2 Finite strip method

### 2.2.1 Degree of freedoms and shape functions

A typical strip for a thin-walled member is depicted in Figure 2-1, along with the degrees of freedom ( $u_1, v_1, w_1, \theta_1$ , etc.) applied end tractions ( $T_1, T_2$ ) and the global/member ( $X, Y, Z$ ) and local/strip ( $x, y, z$ ) coordinate systems.

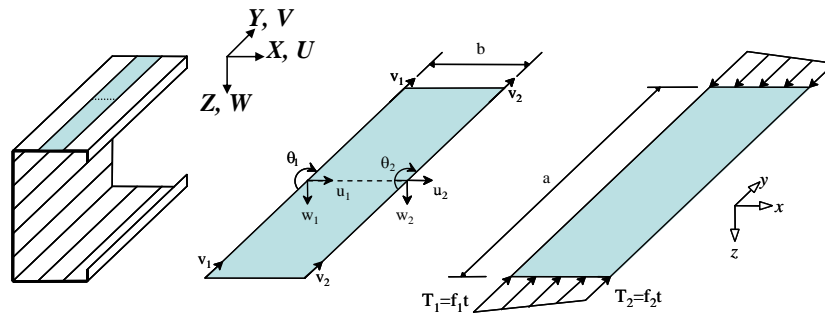


Figure 2-1 Coordinates, Degree of Freedom, and loads of a typical strip [46]

The  $u, v$  and  $w$  displacement fields are approximated with shape functions,  $N$ , and nodal displacements  $d$  as:

$$\begin{Bmatrix} u \\ v \end{Bmatrix} = \sum_{m=1}^q [N_{uv[m]}] d_{uv[m]} \quad \text{and} \quad w = \sum_{m=1}^q [N_{w[m]}] d_{w[m]} \quad (2-1)$$

where  $d_{uv[m]} = [u_{1[m]} \quad v_{1[m]} \quad u_{2[m]} \quad v_{2[m]}]^T$ ,  $d_{w[m]} = [w_{1[m]} \quad \theta_{1[m]} \quad w_{2[m]} \quad \theta_{2[m]}]^T$ ,

$N_{uv[m]}$  and  $N_{w[m]}$  are summed for each  $[m]$  (longitudinal) term, up to  $q$ , specifically:

$$u = \sum_{m=1}^q \left[ \left(1 - \frac{x}{b}\right) \frac{x}{b} \right] \begin{Bmatrix} u_{1[m]} \\ u_{2[m]} \end{Bmatrix} Y_{[m]} \quad \text{and} \quad v = \sum_{m=1}^q \left[ \left(1 - \frac{x}{b}\right) \frac{x}{b} \right] \begin{Bmatrix} v_{1[m]} \\ v_{2[m]} \end{Bmatrix} Y'_{[m]} \frac{a}{\mu_{[m]}} \quad (2-2)$$

$$w = \sum_{m=1}^q \left[ 1 - \frac{3x^2}{b^2} + \frac{2x^3}{b^3} \quad x \left(1 - \frac{2x}{b} + \frac{x^2}{b^2}\right) \quad \frac{3x^2}{b^2} - \frac{2x^3}{b^3} \quad x \left(\frac{x^2}{b^2} - \frac{x}{b}\right) \right] Y_{[m]} d_{w[m]} \quad (2-3)$$

and  $\mu_{[m]} = m\pi$ . Note, the use of the bracketed  $m$ , i.e.,  $[m]$  is to help distinguish the role of the longitudinal terms in later derivations, particularly the cFSM derivations that follow.

The shape function of the strip in the transverse direction is the same as a classical beam finite element, while in the longitudinal direction,  $Y_{[m]}$ , is employed and trigonometric functions [12] are utilized, namely:

$$S-S: \quad \text{simple-simple} \quad Y_{[m]} = \sin(m\pi y / a) \quad (2-4)$$

$$C-C: \quad \text{clamped-clamped} \quad Y_{[m]} = \sin(m\pi y / a) \sin(\pi y / a) \quad (2-5)$$

$$S-C: \quad \text{simple-clamped} \quad Y_{[m]} = \sin[(m+1)\pi y / a] + [(m+1)/m] \sin(m\pi y / a) \quad (2-6)$$

$$C-F: \quad \text{clamped-free} \quad Y_{[m]} = 1 - \cos[(m-1/2)\pi y / a] \quad (2-7)$$

$$C-G: \quad \text{clamped-guided} \quad Y_{[m]} = \sin[(m-1/2)\pi y / a] \sin(\pi y / 2 / a) \quad (2-8)$$

### 2.2.2 Elastic stiffness matrix

The strain in the strip consists of two portions: membrane and bending. The membrane strains,  $\varepsilon_M$ , are at the mid-plane of the strip and are governed by plane stress

assumptions. The bending strains,  $\varepsilon_B$ , follow Kirchoff thin plate theory and are zero at the mid-plane, and a function of  $w$  alone [11, 25]:

$$\varepsilon = \varepsilon_M + \varepsilon_B \quad (2-9)$$

$$\{\varepsilon_M\} = \begin{Bmatrix} \varepsilon_x \\ \varepsilon_y \\ \gamma_{xy} \end{Bmatrix}_M = \begin{Bmatrix} \partial u / \partial x \\ \partial v / \partial y \\ \partial u / \partial y + \partial v / \partial x \end{Bmatrix}_M = \sum_{m=1}^q [N'_{uv[m]}] d_{uv[m]} = \sum_{m=1}^q [B_{M[m]}] d_{uv[m]} \quad (2-10)$$

$$\{\varepsilon_B\} = \begin{Bmatrix} \varepsilon_x \\ \varepsilon_y \\ \gamma_{xy} \end{Bmatrix}_B = \begin{Bmatrix} -z\partial^2 w / \partial x^2 \\ -z\partial^2 w / \partial y^2 \\ 2z\partial^2 w / \partial x \partial y \end{Bmatrix}_B = \sum_{m=1}^q z [N'_{w[m]}] d_{w[m]} = \sum_{m=1}^q z [B_{B[m]}] d_{w[m]} \quad (2-11)$$

Based on the generalized “strain”-displacement relation [47, 48], the internal strain energy for a strip of constant thickness  $t$  is:

$$U = \frac{1}{2} \int_V \{\varepsilon\}^T \{\sigma\} dV = \sum_{m=1}^q \sum_{n=1}^q \frac{1}{2} d_{[m]}^T \left( t \int_0^a \int_0^b B_{[m]}^T [D] B_{[n]} dx dy \right) d_{[n]} = \sum_{m=1}^q \sum_{n=1}^q \frac{1}{2} d_{[m]}^T k_e^{[mn]} d_{[n]} \quad (2-12)$$

where the stress is connected to the strain by an orthotropic plane stress constitutive relation:  $\sigma = D\varepsilon$ . Note,  $D = D^T$  and also,  $d_{[m]} = [d_{uv[m]}^T \quad d_{w[m]}^T]^T$  (See [48]). Matrix  $k_e^{[mn]}$  is the elastic stiffness matrix corresponding to half-wave numbers  $m$  and  $n$  which can be separated for membrane ( $M$ ) and bending ( $B$ ),

$$k_e^{[mn]} = \begin{bmatrix} k_{eM}^{[mn]} & \cdot \\ \cdot & k_{eB}^{[mn]} \end{bmatrix} \quad (2-13)$$

$$k_{eM}^{[mn]} = t \int_0^a \int_0^b B_{M[m]}^T [D_M] B_{M[n]} dx dy \quad \text{and} \quad k_{eB}^{[mn]} = \int_0^a \int_0^b B_{B[m]}^T [D_B] B_{B[n]} dx dy \quad (2-14)$$

Substitution and integration yield the following closed-form expressions for the membrane,  $k_{eM}^{[mn]}$ , and the bending,  $k_{eB}^{[mn]}$ , elastic stiffness matrices:

$$k_{eM}^{[mn]} = t \begin{bmatrix} \left( \frac{E_1 I_1}{b} + \frac{G b I_5}{3} \right) & \left( -\frac{E_2 v_x I_3}{2c_2} - \frac{G I_5}{2c_2} \right) & \left( -\frac{E_1 I_1}{b} + \frac{G b I_5}{6} \right) & \left( -\frac{E_2 v_x I_3}{2c_2} + \frac{G I_5}{2c_2} \right) \\ \left( -\frac{E_2 v_x I_2}{2c_1} - \frac{G I_5}{2c_1} \right) & \left( \frac{E_2 b I_4}{3c_1 c_2} + \frac{G I_5}{b c_1 c_2} \right) & \left( \frac{E_2 v_x I_2}{2c_1} - \frac{G I_5}{2c_1} \right) & \left( \frac{E_2 b I_4}{6c_1 c_2} - \frac{G I_5}{b c_1 c_2} \right) \\ \left( -\frac{E_1 I_1}{b} + \frac{G b I_5}{6} \right) & \left( \frac{E_2 v_x I_3}{2c_2} - \frac{G I_5}{2c_2} \right) & \left( \frac{E_1 I_1}{b} + \frac{G b I_5}{3} \right) & \left( \frac{E_2 v_x I_3}{2c_2} + \frac{G I_5}{2c_2} \right) \\ \left( -\frac{E_2 v_x I_2}{2c_1} + \frac{G I_5}{2c_1} \right) & \left( \frac{E_2 b I_4}{6c_1 c_2} - \frac{G I_5}{b c_1 c_2} \right) & \left( \frac{E_2 v_x I_2}{2c_1} + \frac{G I_5}{2c_1} \right) & \left( \frac{E_2 b I_4}{3c_1 c_2} + \frac{G I_5}{b c_1 c_2} \right) \end{bmatrix} \quad (2-15)$$

$$k_{eB}^{[mn]} = \frac{1}{420b^3} \begin{bmatrix} \left( 5040D_x I_1 - 504b^2 D_y I_2 \right) & \left( 2520b D_x I_1 - 462b^3 D_y I_2 \right) & \left( -5040D_x I_1 + 504b^2 D_y I_2 \right) & \left( 2520b D_x I_1 - 42b^3 D_y I_2 \right) \\ \left( -504b^2 D_x I_3 + 156b^4 D_y I_4 \right) & \left( -42b^3 D_x I_3 + 22b^5 D_y I_4 \right) & \left( +504b^2 D_x I_3 + 54b^4 D_y I_4 \right) & \left( -42b^3 D_x I_3 - 13b^5 D_y I_4 \right) \\ \left( +2016b^2 D_{xy} I_5 \right) & \left( +168b^3 D_{xy} I_5 \right) & \left( -2016b^2 D_{xy} I_5 \right) & \left( +168b^3 D_{xy} I_5 \right) \\ \left( 2520b D_x I_1 - 462b^3 D_y I_2 \right) & \left( 1680b^2 D_x I_1 - 56b^4 D_y I_2 \right) & \left( -2520b D_x I_1 + 42b^3 D_y I_2 \right) & \left( 840b^2 D_x I_1 + 14b^4 D_y I_2 \right) \\ \left( -42b^3 D_x I_3 + 22b^5 D_y I_4 \right) & \left( -56b^4 D_x I_3 + 4b^6 D_y I_4 \right) & \left( +42b^3 D_x I_3 + 13b^5 D_y I_4 \right) & \left( +14b^4 D_x I_3 - 3b^6 D_y I_4 \right) \\ \left( +168b^3 D_{xy} I_5 \right) & \left( +224b^4 D_{xy} I_5 \right) & \left( -168b^3 D_{xy} I_5 \right) & \left( -56b^4 D_{xy} I_5 \right) \\ \left( -5040D_x I_1 + 504b^2 D_y I_2 \right) & \left( -2520b D_x I_1 + 42b^3 D_y I_2 \right) & \left( 5040D_x I_1 - 504b^2 D_y I_2 \right) & \left( -2520b D_x I_1 + 462b^3 D_y I_2 \right) \\ \left( +504b^2 D_x I_3 + 54b^4 D_y I_4 \right) & \left( +42b^3 D_x I_3 + 13b^5 D_y I_4 \right) & \left( -504b^2 D_x I_3 + 156b^4 D_y I_4 \right) & \left( +42b^3 D_x I_3 - 22b^5 D_y I_4 \right) \\ \left( -2016b^2 D_{xy} I_5 \right) & \left( -168b^3 D_{xy} I_5 \right) & \left( +2016b^2 D_{xy} I_5 \right) & \left( -168b^3 D_{xy} I_5 \right) \\ \left( 2520b D_x I_1 - 42b^3 D_y I_2 \right) & \left( 840b^2 D_x I_1 + 14b^4 D_y I_2 \right) & \left( -2520b D_x I_1 + 462b^3 D_y I_2 \right) & \left( 1680b^2 D_x I_1 - 56b^4 D_y I_2 \right) \\ \left( -42b^3 D_x I_3 - 13b^5 D_y I_4 \right) & \left( +14b^4 D_x I_3 - 3b^6 D_y I_4 \right) & \left( +42b^3 D_x I_3 - 22b^5 D_y I_4 \right) & \left( -56b^4 D_x I_3 + 4b^6 D_y I_4 \right) \\ \left( +168b^3 D_{xy} I_5 \right) & \left( -56b^4 D_{xy} I_5 \right) & \left( -168b^3 D_{xy} I_5 \right) & \left( +224b^4 D_{xy} I_5 \right) \end{bmatrix} \quad (2-16)$$

where  $c_1 = \frac{m\pi}{a}$ ,  $c_2 = \frac{n\pi}{a}$ ,  $I_1 = \int_0^a Y_{[m]} Y_{[n]} dy$ ,  $I_2 = \int_0^a Y_{[m]}'' Y_{[n]}'' dy$ ,  $I_3 = \int_0^a Y_{[m]} Y_{[n]}'' dy$ ,

$$I_4 = \int_0^a Y_{[m]}'' Y_{[n]}'' dy, I_5 = \int_0^a Y_{[m]}' Y_{[n]}' dy, E_1 = \frac{E_x}{1 - \nu_x \nu_y}, E_2 = \frac{E_y}{1 - \nu_x \nu_y}, D_x = \frac{E_x t^3}{12(1 - \nu_x \nu_y)}$$

$$D_y = \frac{E_y t^3}{12(1 - \nu_x \nu_y)}, D_1 = \frac{\nu_y E_x t^3}{12(1 - \nu_x \nu_y)} = \frac{\nu_x E_y t^3}{12(1 - \nu_x \nu_y)}, [D_M] = \begin{bmatrix} E_1 & \nu_x E_2 & 0 \\ \nu_y E_1 & E_2 & 0 \\ 0 & 0 & G \end{bmatrix},$$

$$[D_B] = \begin{bmatrix} D_x & D_1 & 0 \\ D_1 & D_y & 0 \\ 0 & 0 & D_{xy} \end{bmatrix}, D_{xy} = \frac{G t^3}{12}$$

See Appendix A for the explicit integration results of  $I_1$  to  $I_5$ . The preceding has been derived independent of [12] and [11] and terms corrected, including the (2, 1) term in  $k_{eB}$  [11]. The full elastic stiffness matrix  $k_e$  can be expressed as:

$$k_e = \left[ k_e^{[mn]} \right]_{q \times q} \quad (2-17)$$

where each  $k_e^{[mn]}$  submatrix is 8x8 and  $q^2$  such submatrices exist.

For the simple-simple (S-S) boundary conditions  $I_1$  through  $I_5$  are zero when  $m \neq n$  leaving only a diagonal set of submatrices in  $k$ . It is this efficiency for the S-S boundary condition that leads to the attractive nature of that solution and the universality of the buckling load vs. buckling half-wavelength curve for S-S boundary conditions.

For all other boundary conditions  $k$  has non-zero submatrices off the main diagonal and interaction of buckling modes of different half-wavelengths occur and the half-wavelength vs. buckling load curve loses its special significance. In essence, for all boundary conditions other than S-S, FSM has the same identification problems as FE analysis, unless other tools such as the constrained FSM are implemented.

### 2.2.3 Geometric stiffness matrix

For axially applied edge tractions  $T_1$ ,  $T_2$  (see Figure 2-1) a basis for the geometric stiffness is the additional work ( $V_P$ ) created as the plate shortens due, e.g., to out-of-plane bending, specifically, per [12, 25]:

$$V_P = \frac{1}{2} \int_0^a \int_0^b (T_1 - (T_1 - T_2) \frac{x}{b}) \left[ \left( \frac{\partial u}{\partial y} \right)^2 + \left( \frac{\partial v}{\partial y} \right)^2 + \left( \frac{\partial w}{\partial y} \right)^2 \right] dx dy \quad (2-18)$$

The derivatives of the displacements can be written in terms of appropriate derivatives of the shape functions. For example, the partial derivative of  $w$  can be expressed as:

$$(\partial w / \partial y)^2 = \left( \sum_{m=1}^q [N'_{w[m]}] d_{w[m]} \right)^2 = \left( \sum_{m=1}^q G_{B[m]} d_{w[m]} \right)^2 = \sum_{m=1}^q \sum_{n=1}^q d_{w[m]}^T G_{B[m]}^T G_{B[n]} d_{w[n]} \quad (2-19)$$

Similar derivations are employed for the membrane deformations  $u$  and  $v$  of the strip.

$$\left\{ \begin{array}{l} (\partial u / \partial y)^2 \\ (\partial v / \partial y)^2 \end{array} \right\} = \left( \sum_{m=1}^q [N'_{uv[m]}] d_{uv[m]} \right)^2 = \left( \sum_{m=1}^q G_{M[m]} d_{uv[m]} \right)^2 = \sum_{m=1}^q \sum_{n=1}^q d_{uv[m]}^T G_{M[m]}^T G_{M[n]} d_{uv[n]} \quad (2-20)$$

The potential energy  $V_p$  can then be written as

$$V_p = \frac{1}{2} \int_0^a \int_0^b (T_1 - (T_1 - T_2) \frac{x}{b}) \left( \sum_{m=1}^q \sum_{n=1}^q d_{[m]}^T G_{[m]}^T G_{[n]} d_{[n]} \right) dx dy = \sum_{m=1}^q \sum_{n=1}^q \frac{1}{2} d_{[m]}^T k_g^{[mn]} d_{[n]} \quad (2-21)$$

Similar to the elastic stiffness matrix, the geometric stiffness matrix  $k_g^{[mn]}$  corresponding to half-wave numbers  $m$  and  $n$  is broken into membrane,  $k_{gM}^{[mn]}$  and bending,  $k_{gB}^{[mn]}$ :

$$k_g^{[mn]} = \begin{bmatrix} k_{gM}^{[mn]} & \cdot \\ \cdot & k_{gB}^{[mn]} \end{bmatrix} \quad (2-22)$$

$$k_{gM}^{[mn]} = \int_0^a \int_0^b (T_1 - (T_1 - T_2) \frac{x}{b}) G_{M[m]}^T G_{M[n]} dx dy \quad \text{and} \quad k_{gB}^{[mn]} = \int_0^a \int_0^b (T_1 - (T_1 - T_2) \frac{x}{b}) G_{B[m]}^T G_{B[n]} dx dy \quad (2-23)$$

The explicit expressions can be obtained via substitution and integration:

$$k_{gM}^{[mm]} = \begin{bmatrix} \frac{(3T_1 + T_2)bI_5}{12} & 0 & \frac{(T_1 + T_2)bI_5}{12} & 0 \\ & \frac{(3T_1 + T_2)ba^2I_4}{12\mu_m\mu_n} & 0 & \frac{(T_1 + T_2)ba^2I_4}{12\mu_m\mu_n} \\ & & \frac{(T_1 + 3T_2)bI_5}{12} & 0 \\ \text{symmetric} & & & \frac{(T_1 + 3T_2)ba^2I_4}{12\mu_m\mu_n} \end{bmatrix} \quad (2-24)$$

$$k_{gB}^{[mm]} = \begin{bmatrix} \frac{(10T_1 + 3T_2)bI_5}{35} & \frac{(15T_1 + 7T_2)b^2I_5}{420} & \frac{9(T_1 + T_2)bI_5}{140} & -\frac{(7T_1 + 6T_2)b^2I_5}{420} \\ & \frac{(5T_1 + 3T_2)b^3I_5}{840} & \frac{(6T_1 + 7T_2)b^2I_5}{420} & -\frac{(T_1 + T_2)b^3I_5}{280} \\ & & \frac{(3T_1 + 10T_2)bI_5}{35} & -\frac{(7T_1 + 15T_2)b^2I_5}{420} \\ \text{symmetric} & & & \frac{(3T_1 + 5T_2)b^3I_5}{840} \end{bmatrix} \quad (2-25)$$

where  $\mu_m = m\pi$ ;  $\mu_n = n\pi$ ;  $I_4 = \int_0^a Y_{[m]}'' Y_{[n]}'' dy$ ;  $I_5 = \int_0^a Y_{[m]}' Y_{[n]}' dy$

See appendix A for the explicit integration results of  $I_4$  and  $I_5$ . Several terms in  $k_{gM}$  and  $k_{gB}$  in [12] have been corrected by independent derivation by the authors. Finally, the geometric stiffness can be expressed in its full form as:

$$k_g = \left[ k_g^{[mm]} \right]_{q \times q} \quad (2-26)$$

#### 2.2.4 Assembly

Assembly of the local stiffness matrices ( $k_e$  and  $k_g$ ) into the global stiffness matrices ( $K_e$  and  $K_g$ ) proceeds in a manner similar to conventional finite element analysis or the classical finite strip method [25]. First, the coordinates must be transformed from local to global based on the strip orientation (angle  $\alpha$ ). For strip  $j$  at strip line (node)  $i$  and for the  $m^{\text{th}}$  term in the longitudinal series, this transformation follows from the coordinate systems established in Figure 2-1 as:

$$\begin{bmatrix} u_{i[m]} \\ w_{i[m]} \end{bmatrix} = \begin{bmatrix} \cos \alpha^{(j)} & \sin \alpha^{(j)} \\ -\sin \alpha^{(j)} & \cos \alpha^{(j)} \end{bmatrix} \begin{bmatrix} U_{i[m]} \\ W_{i[m]} \end{bmatrix} \text{ and } \begin{bmatrix} v_{i[m]} \\ \theta_{i[m]} \end{bmatrix} = \begin{bmatrix} 1 & 0 \\ 0 & 1 \end{bmatrix} \begin{bmatrix} V_{i[m]} \\ \Theta_{i[m]} \end{bmatrix} \quad (2-27)$$

These may be collected into a matrix form for all DOF (note, total DOF = 4 DOF  $\times$  2 nodes  $\times$   $q$  longitudinal terms) in strip  $j$  as

$$d^{(j)} = \Gamma^{(j)} D^{(j)} \quad (2-28)$$

where,  $\Gamma^{(j)}$  is defined as following based on Eq. (2-27):

$$\Gamma^{(j)} = \left[ \Gamma_{[m]}^{(j)} \right]_{4p \times q} \quad (2-29)$$

$$\Gamma_{[m]}^{(j)} = \begin{bmatrix} \cos a^{(j)} & 0 & \sin a^{(j)} & 0 \\ 0 & 1 & 0 & 0 \\ -\sin a^{(j)} & 0 & \cos a^{(j)} & 0 \\ 0 & 0 & 0 & 1 \end{bmatrix} \quad (2-30)$$

Thus, strip  $j$ 's global stiffness matrices are formed from the transformation matrix as:

$$K_e^{(j)} = \Gamma^{(j)T} k_e^{(j)} \Gamma^{(j)} \text{ and } K_g^{(j)} = \Gamma^{(j)T} k_g^{(j)} \Gamma^{(j)} \quad (2-31)$$

With all DOF in global coordinates the global stiffness matrices may be assembled as an appropriate summation of the strip stiffness matrices:

$$K_e = \bigcup_j K_e^{(j)} \text{ and } K_g = \bigcup_j K_g^{(j)} \quad (2-32)$$

where the assembly occurs over  $n_{\text{strips}}$ . Note,  $K_e$  is a square matrix of dimension 4 DOF  $\times$  2 nodes/strip  $\times$   $q$  terms  $\times$   $n_{\text{strips}}$ .

## 2.2.5 Stability solution

For a given distribution of edge tractions on a member the geometric stiffness matrix scales linearly, resulting in the elastic buckling problem:

$$K_e \Phi = \Lambda K_g \Phi \quad (2-33)$$

where,  $\Lambda$  is a diagonal matrix containing the eigenvalues (buckling loads) and  $\Phi$  is a fully populated matrix corresponding to the eigenmodes (buckling modes) in its columns.

For simply supported boundary conditions, due to the resulting orthogonality in  $K_e$  and  $K_g$  the solutions for any  $m$  are independent – and further the buckling load for any  $m$  may be found by performing the solution for  $m=1$  at a length equal to  $a/m$ . As a result, it has become conventional to express FSM solutions in terms of the first buckling load over a series of lengths ( $a$ ) as opposed to FEM solutions where typically a model is solved for many buckling loads at a single length.

For FSM with non simply-supported boundary conditions the orthogonality is lost, and thus the special meaning of an  $m=1$  solution with varying length  $a$  is lost as well. Nonetheless, in the material that follows the classical FSM presentation is employed; however, given that many longitudinal ( $m$ ) terms are used the solution should be interpreted as a function of physical length, as opposed to half-wavelength. In fact, it would be equally valid to use the FEM approach and examine higher mode solutions at a given length, instead of varying  $a$ .

## 2.3 Validation studies for finite strip solution

To provide validation studies for the selected FSM displacement fields, namely the  $Y_{[m]}$  of Eq.'s (2-4) - (2-8) comparisons are made to classical plate buckling solutions and shell finite element models of plates and full members.

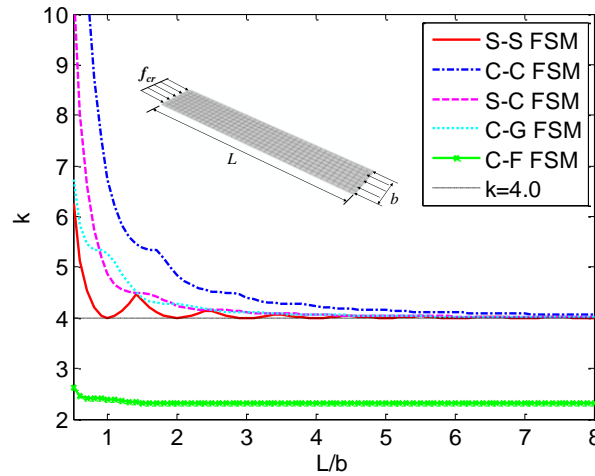
### 2.3.1 Plate studies: comparison to classical solution

The local buckling stress ( $\sigma_{cr}$ ) of a plate may be characterized as

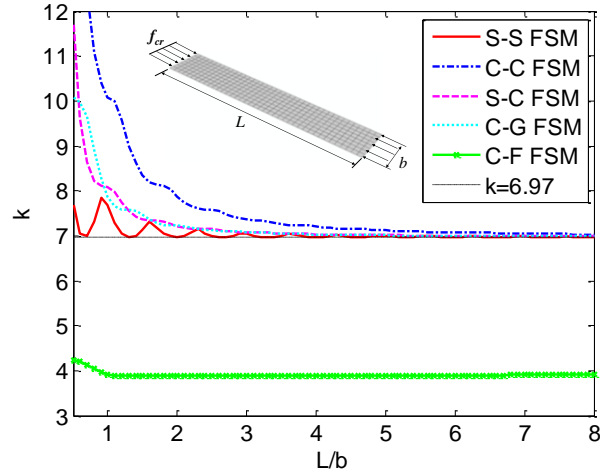
$$\sigma_{cr} = k \frac{\pi^2 E}{12(1-\nu^2)} \left(\frac{t}{b}\right)^2 \quad (2-34)$$

where  $k$  is the plate buckling coefficient and is dependent on loading and boundary conditions,  $E$  and  $\nu$  are material properties,  $t$  is the plate thickness, and  $b$  the plate width. For a 63.5 mm wide, 1.27 mm thick plate, and with the material linear elastic, isotropic, with  $E=203,000$  MPa and  $\nu=0.3$ , the plate buckling coefficient is determined for all five considered end boundary conditions: simple-simple ( $S-S$ ), clamped-clamped ( $C-C$ ), simple-clamped ( $S-C$ ), clamped-guided ( $C-G$ ), and clamped-free ( $C-F$ ) and for two longitudinal edge boundary conditions: simple-simple ( $s-s$ ) and clamped-clamped ( $c-c$ ) and reported and compared to classical solutions in Figure 2-2.

The results are in excellent agreement with theory and show the important length dependent behaviour in the stability solution which is introduced by the use of non-simply-supported boundary conditions.



(a)  $s-s$  longitudinal edges



(b) *c-c* longitudinal edges

Figure 2-2 Buckling coefficients of plates in compression with varying end conditions

### 2.3.2 Plate studies: comparison to finite element solution

To study the accuracy of the solutions for shorter plates, where the end boundary conditions have the greatest influence, shell finite element models are developed in ABAQUS [45]. The models employ the S9R5 thin shell finite element, and the Lanczos method is employed for eigenvalue extraction. The material is assumed to be linear elastic, isotropic, with  $E=203,000$  MPa and  $\nu=0.3$ .

Stability results for FSM and FEM are provided for a uniformly compressed plate with clamped-clamped (C-C) boundary conditions at the loaded ends and simple supports (s-s) along the longitudinal plate edges (Figure 2-3) and C-C at the loaded ends and clamped-clamped (c-c) supports along the longitudinal plate edges (Figure 2-5). The FSM solutions are nearly coincident with the FEM solutions, both in terms of plate buckling coefficient (i.e., buckling stress) and buckled shape, see Figure 2-4 and Figure 2-6. The errors (differences) are relatively uniform over the lengths studied: the FEM

method is 0.5% lower for the C-C, s-s condition and 0.67% lower for the C-C, c-c condition.

Stability solutions for uniformly compressed plates as a function of plate length were completed in FSM and FEM for all 5 of the considered end boundary conditions, and for both simple supports on the unloaded edges and clamped boundary conditions on the unloaded edges, as summarized in Figure 2-7 and Figure 2-8. The figures demonstrate that the assumed longitudinal displacement functions ( $Y_{[m]}$ ) provide accurate solutions for plates.

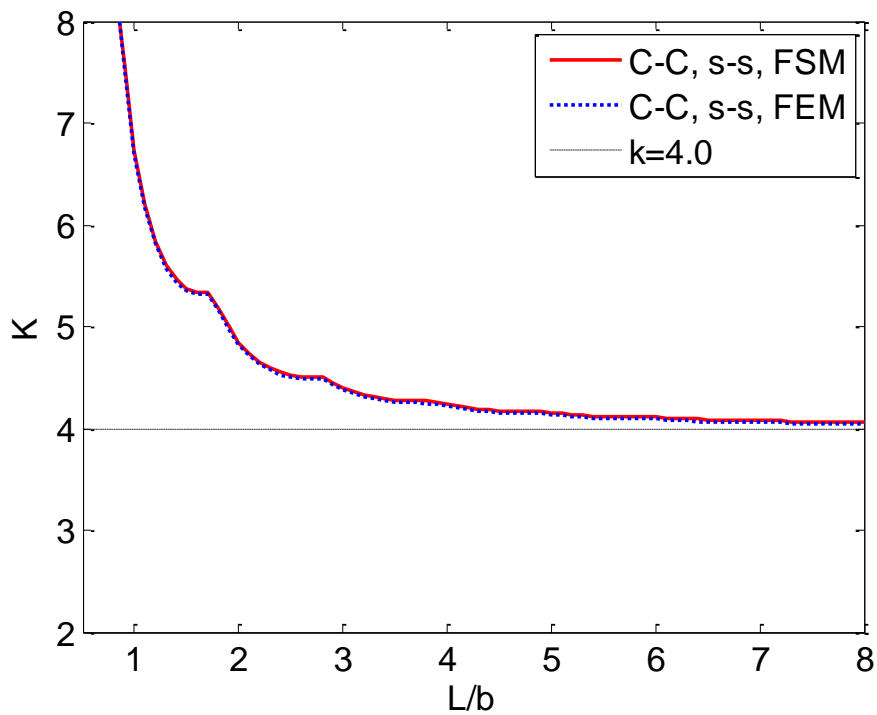
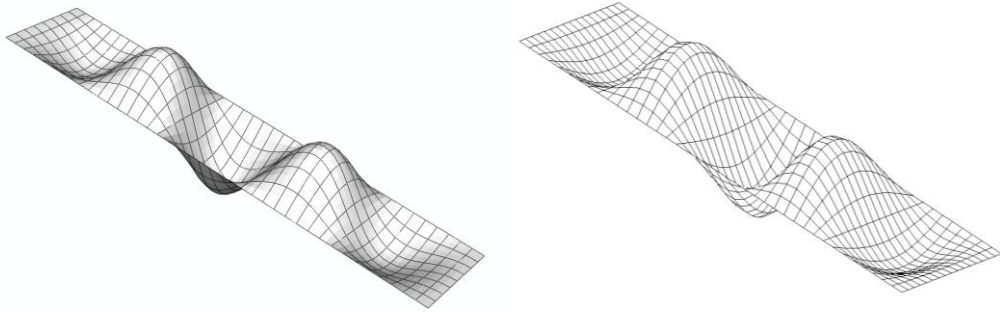


Figure 2-3 Buckling coefficients FEM and FSM results, C-C, s-s



Step: Step-1  
 Mode 1: EigenValue = 44.095

(a) Mode shape of FEM result at  $L/b=5$  (b) Mode shape of FSM result at  $L/b=5$

Figure 2-4 Buckling mode shapes of FEM and FSM at  $L/b=5$ , C-C, s-s

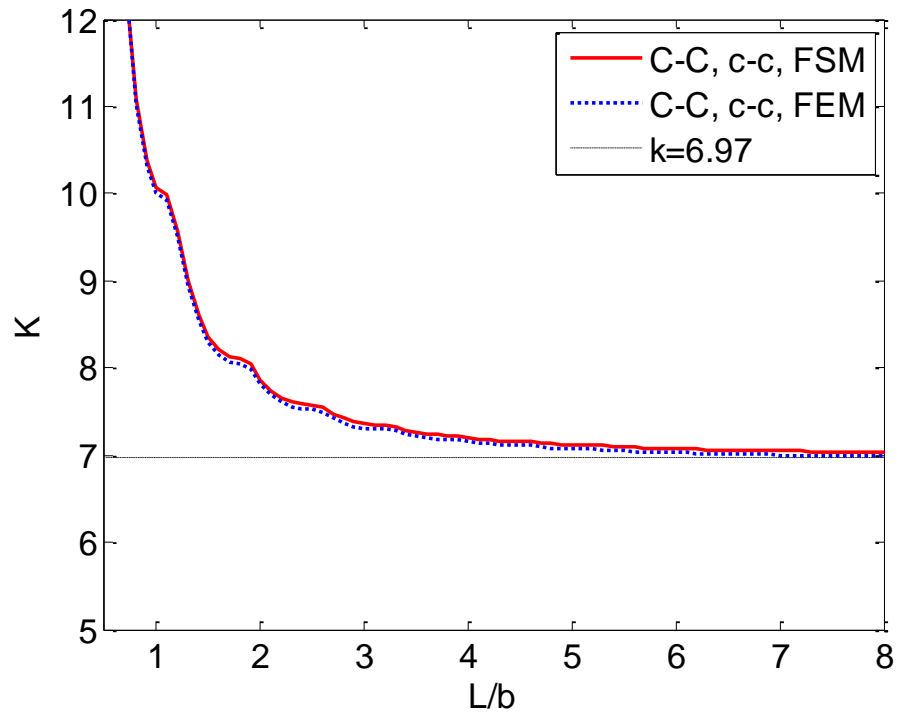
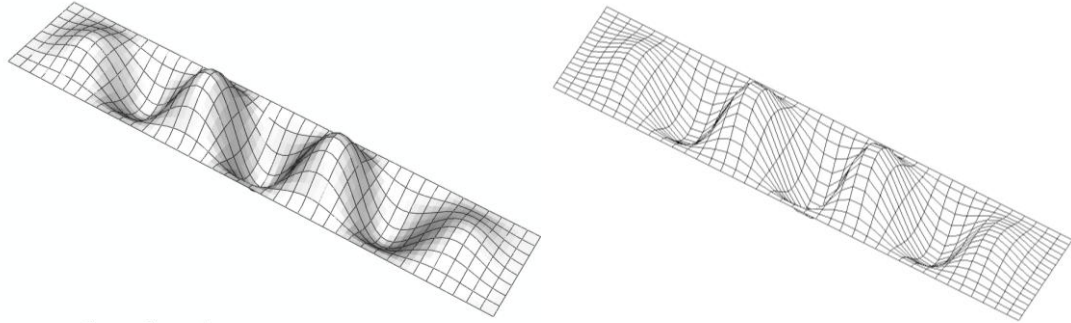


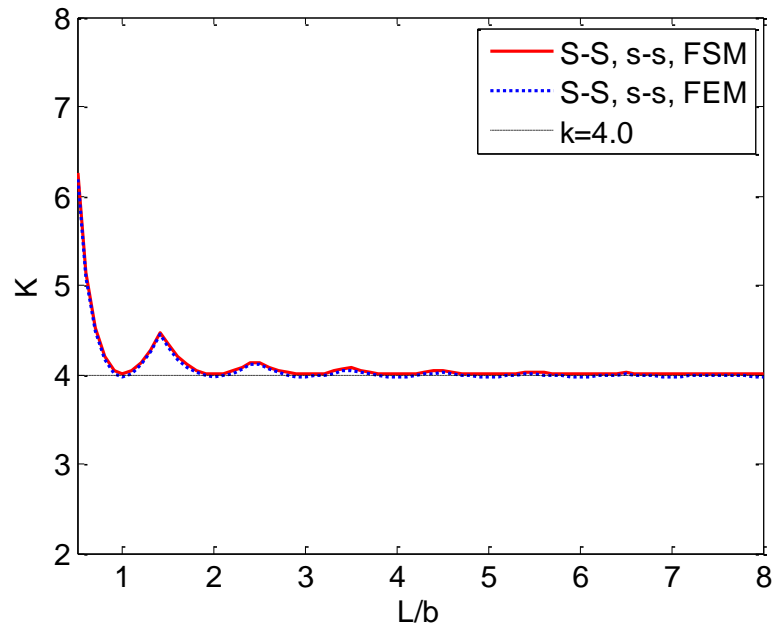
Figure 2-5 Buckling coefficients FEM and FSM results, C-C, c-c



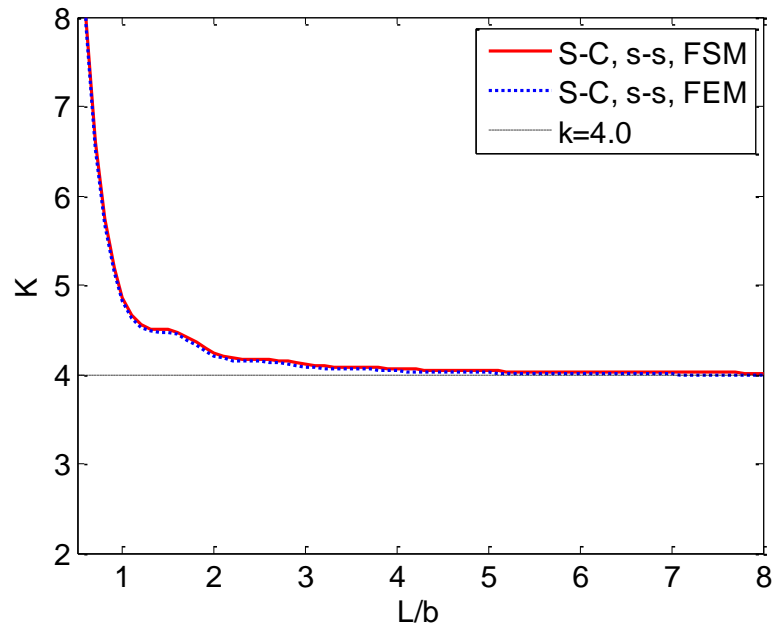
Step: Step-1  
 Mode 1: EigenValue = 75.419

(a) Mode shape of FEM result at  $L/b=5$  (b) Mode shape of FSM result at  $L/b=5$

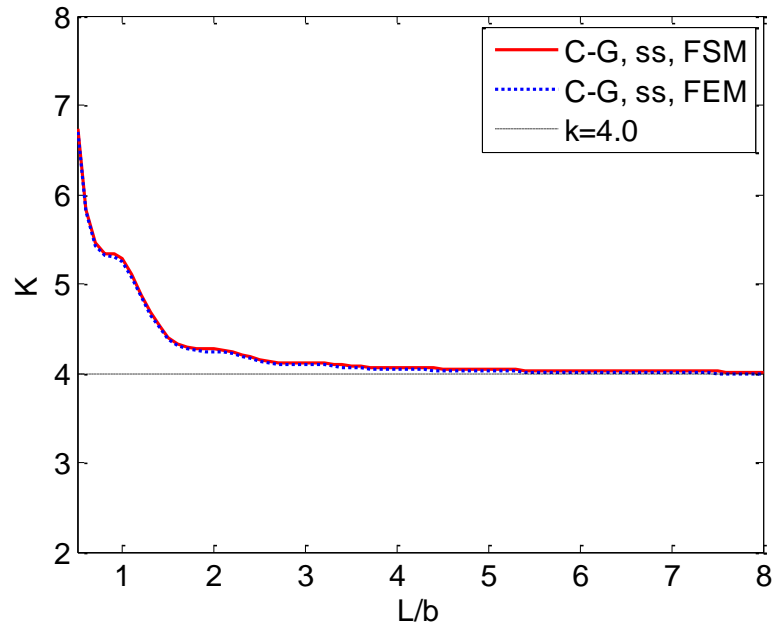
Figure 2-6 Buckling mode shapes of FEM and FSM at  $L/b=5$ , C-C, c-c



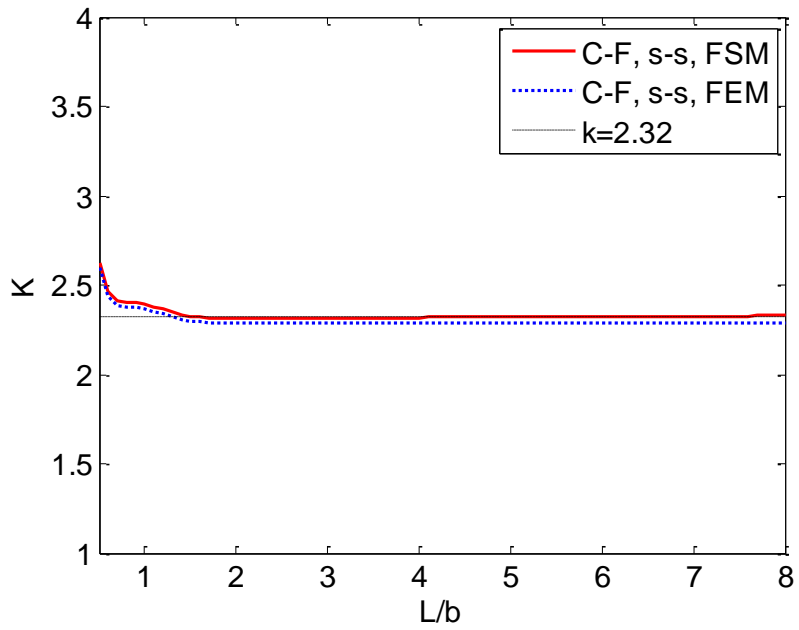
(a) simply supported on unloaded edges, S-S



(b) simply supported on unloaded edges, S-C

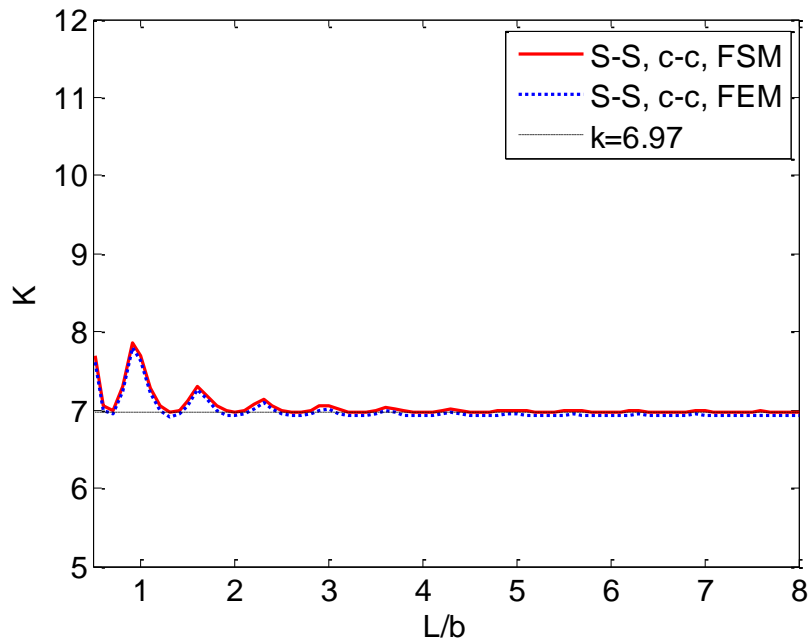


(c) simply supported on unloaded edges, C-G

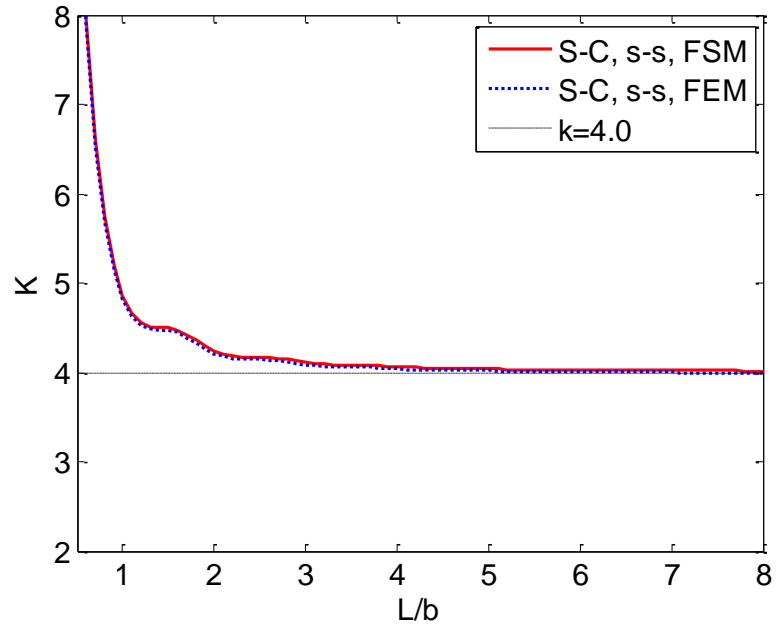


(d) simply supported on unloaded edges, C-F

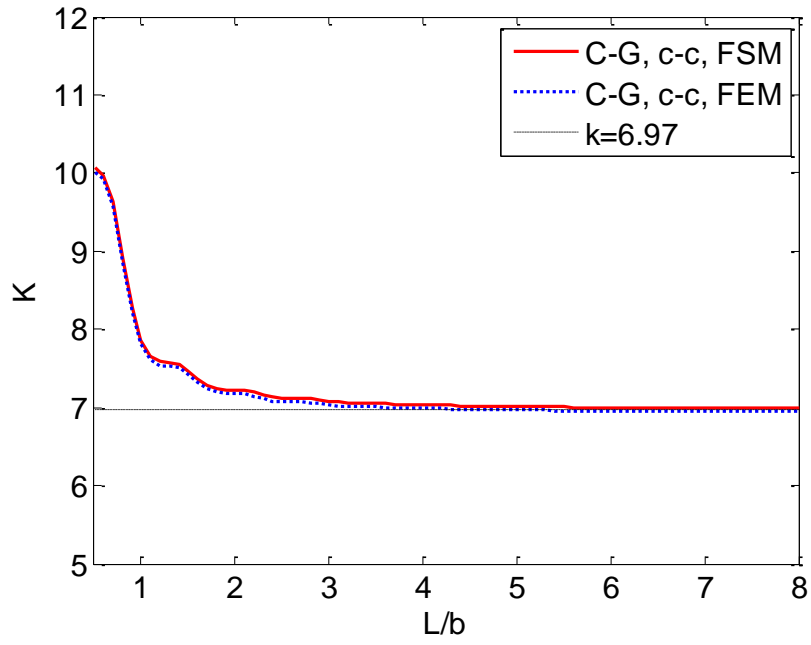
Figure 2-7 simply supported on unloaded edges (s-s), various boundary conditions on loaded edges



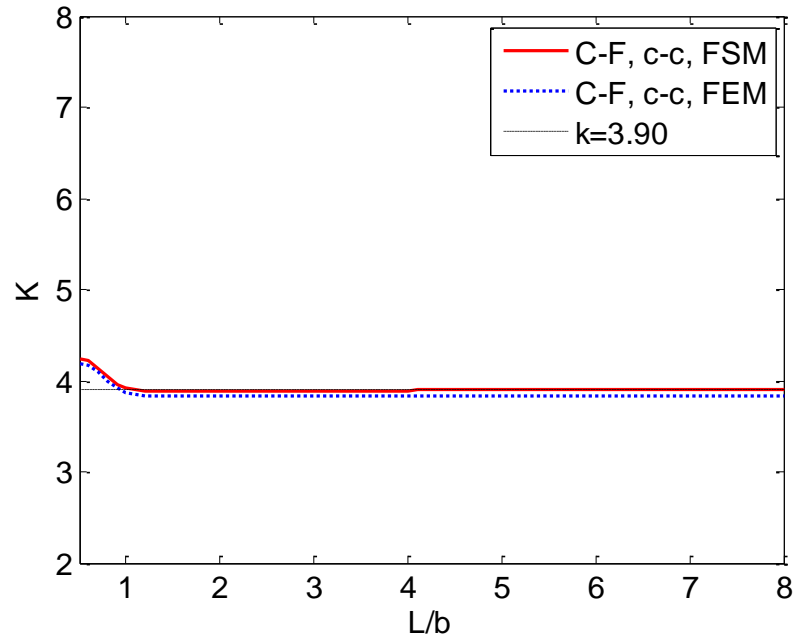
(a) clamped on unloaded edges, C-C



(b) clamped on unloaded edges, S-C



(c) clamped on unloaded edges, C-G



(d) clamped on unloaded edges, C-F

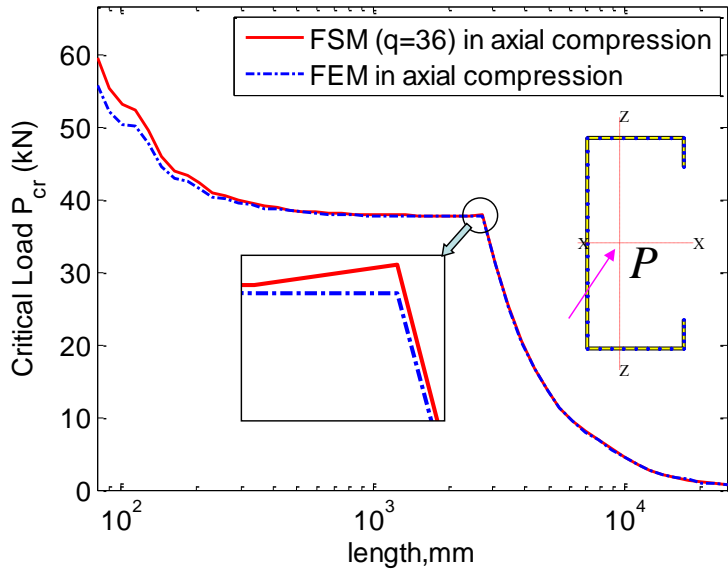
Figure 2-8 clamped on unloaded edges (c-c), various boundary conditions on loaded edges

### 2.3.3 Member studies

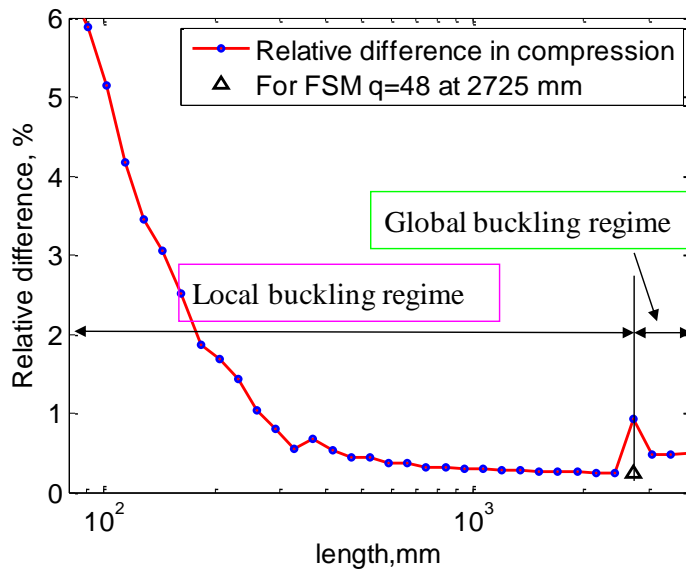
The previous studies demonstrate that the  $Y_{[m]}$  of Eq.'s (2-4) – (2-8) provide excellent approximation of isolated plates. In this section the validation studies are extended to a common thin-walled member: a lipped channel. Specifically, an SSMA 350S162-43 stud [49] with out-to-out web depth of 89 mm, out-to-out flange width of 41.3 mm, out-to-out lip length of 12.7 mm, and a design thickness of 1.146 mm. The material is assumed to be linear elastic, isotropic, with  $E=203,000$  MPa and  $\nu=0.3$ . In both FSM and FEM the member is modelled as a straight-line model (no corners). Three loading cases are considered: axial compression, major-axis bending, and minor-axis bending with flange lips in compression. Clamped-clamped end boundary conditions are employed.

The stability solution under axial compression, as a function of member length, for both the FSM and FEM models are provided in Figure 2-9(a). The FSM solution (with 36  $m$  terms employed) is an excellent approximation of the FEM solution; however at short lengths and at the transition point between local and global buckling ( $L=2725$  mm) the FSM solution is modestly stiffer than the FEM solution. Figure 2-9(b) provides the error between the FSM and FEM solutions. Increasing the number of longitudinal terms (from 36 to 48  $m$  terms at  $L=2725$  mm) in the FSM solution is demonstrated to decrease the error between the two solutions.

Note, in this solution the distortional buckling mode is at a higher critical stress than the local mode, so the first (elastic) buckling mode is always local buckling even at intermediate lengths – see Figure 2-10. Also, note in Figure 2-10 that the magnitude of the buckling wave varies along the length, which does not happen with simply supported ends. To determine the distortional buckling mode using conventional FSM higher buckling modes would need to be examined, this further supports the need for modal decomposition, only possible with constrained FSM solutions.

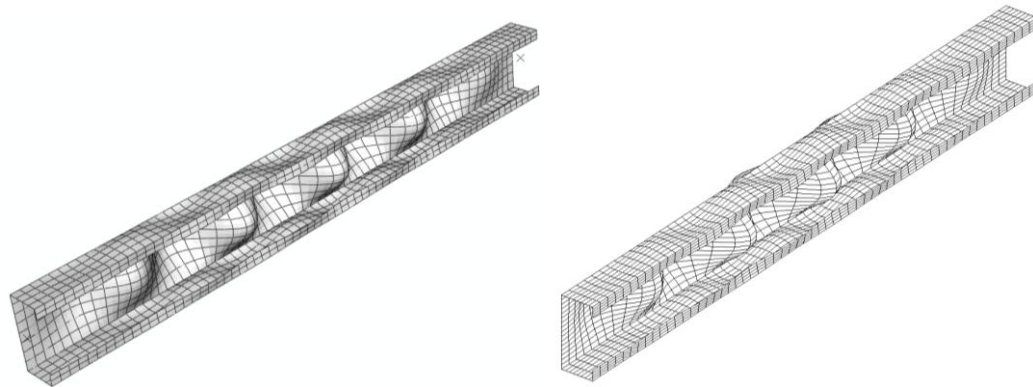


(a) Critical loads



(b) Relative difference

Figure 2-9 Stability under compression for a 350S162-43 with clamped ends



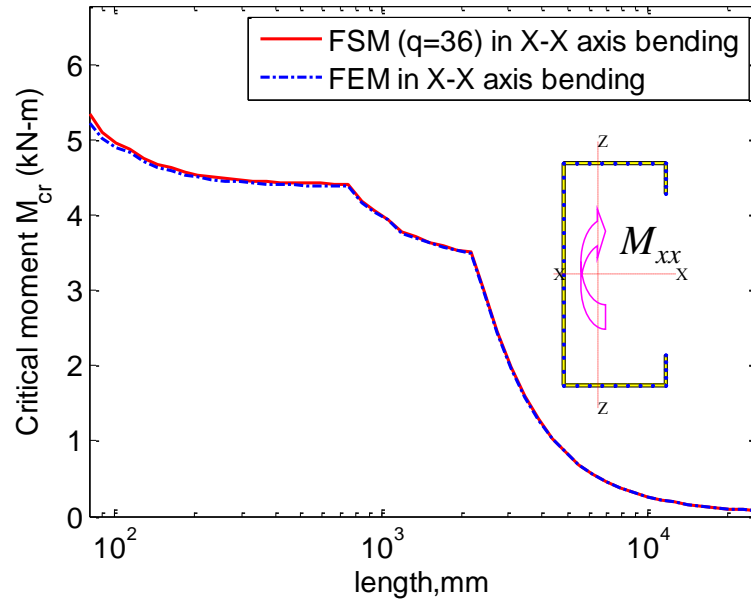
(a) FEM, L=750 mm

(b) FSM, L=750 mm

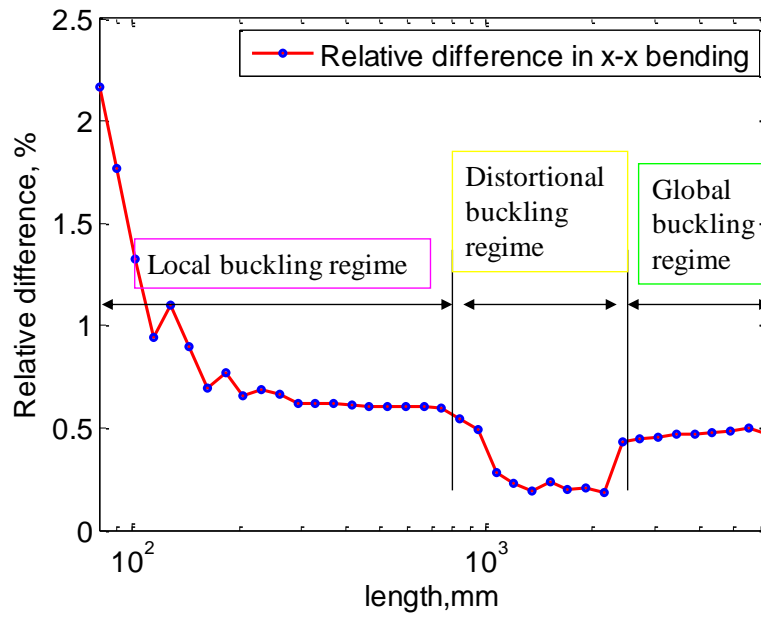
Figure 2-10 Mode shapes for a 350S162-43 in compression with clamped ends

The stability results for FSM and FEM in major-axis bending are provided in Figure 2-11 and Figure 2-12. Differences between the FSM and FEM solution are essentially negligible in Figure 2-11(b) although at very short lengths (members with shorter length than the depth of the section) the FSM solution is on the order of 1 to 2% stiffer. In major-axis bending, at intermediate lengths, distortional buckling is lower than local buckling and thus appears in the results; further, the FSM and FEM solutions are essentially coincident in the predicted mode shape, see Figure 2-12.

In minor-axis bending (with the flange tips in compression) the stability results (Figure 2-13) are again in good agreement as are the predicted mode shapes (Figure 2-14). The difference between the FSM and FEM models remains less than 1% for distortional and global buckling and approximately 1% for local buckling, see Figure 2-13(b). Overall, it may be concluded that the selected shape functions are working with the desired accuracy and that the method has been implemented successfully.



(a) Critical moments



(b) Relative difference

Figure 2-11 Stability in major-axis bending for a 350S162-43 with clamped ends

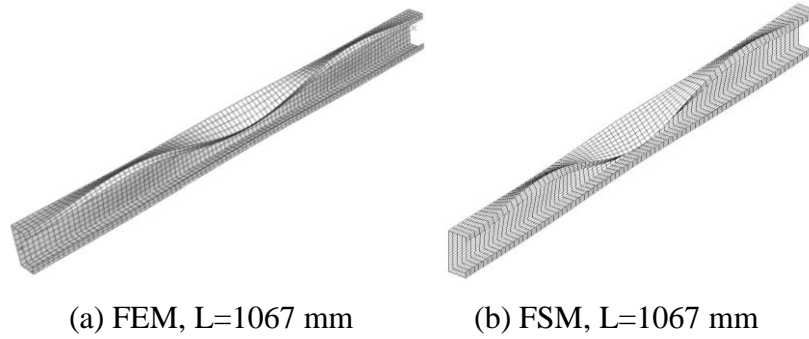


Figure 2-12 Mode shapes for a 350S162-43 in major-axis bending with clamped ends

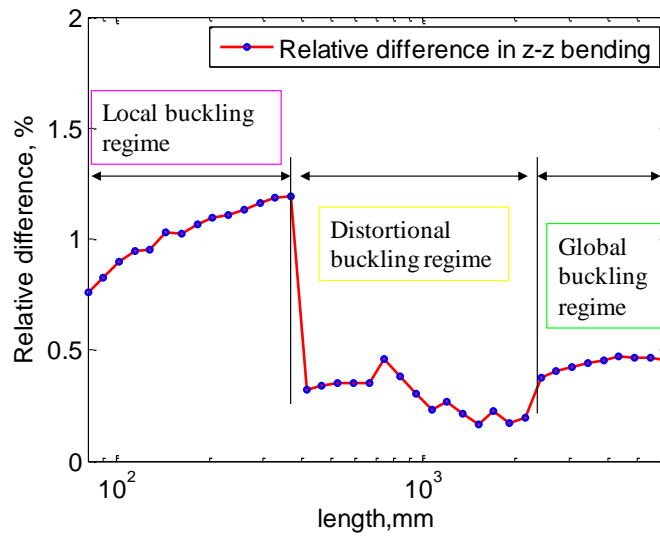
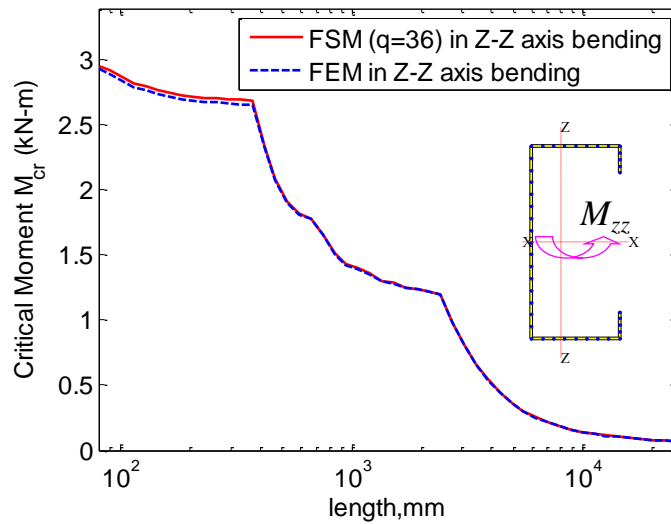
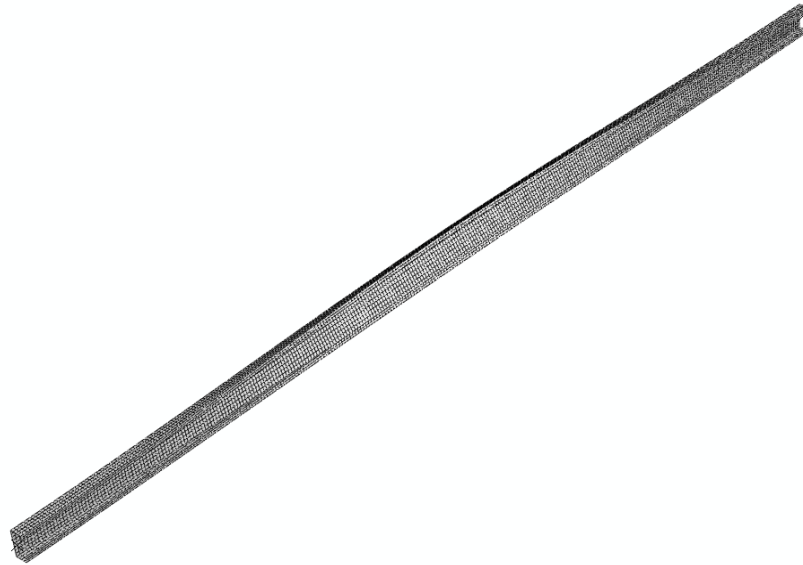
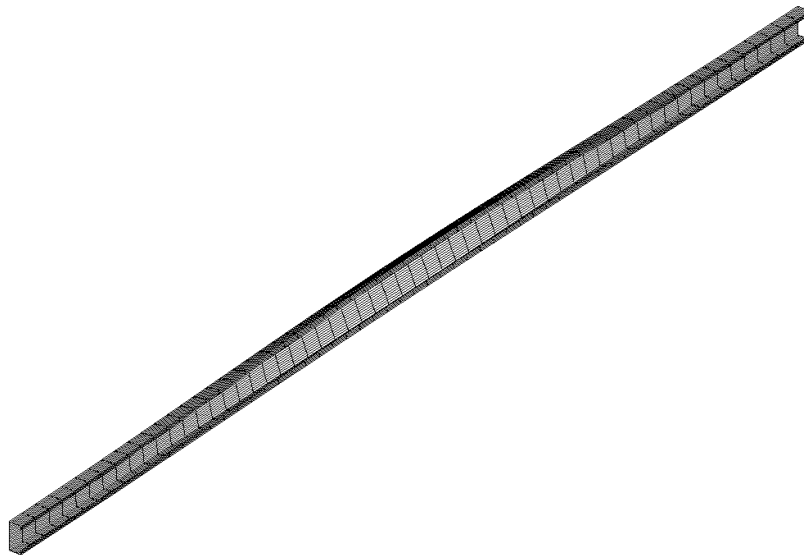


Figure 2-13 Stability in minor-axis bending for a 350S162-43 with clamped ends



(a) FEM,  $L=3445$  mm



(b) FSM,  $L=3445$  mm

Figure 2-14 Mode shapes for a 350S162-43 in minor-axis bending with clamped ends

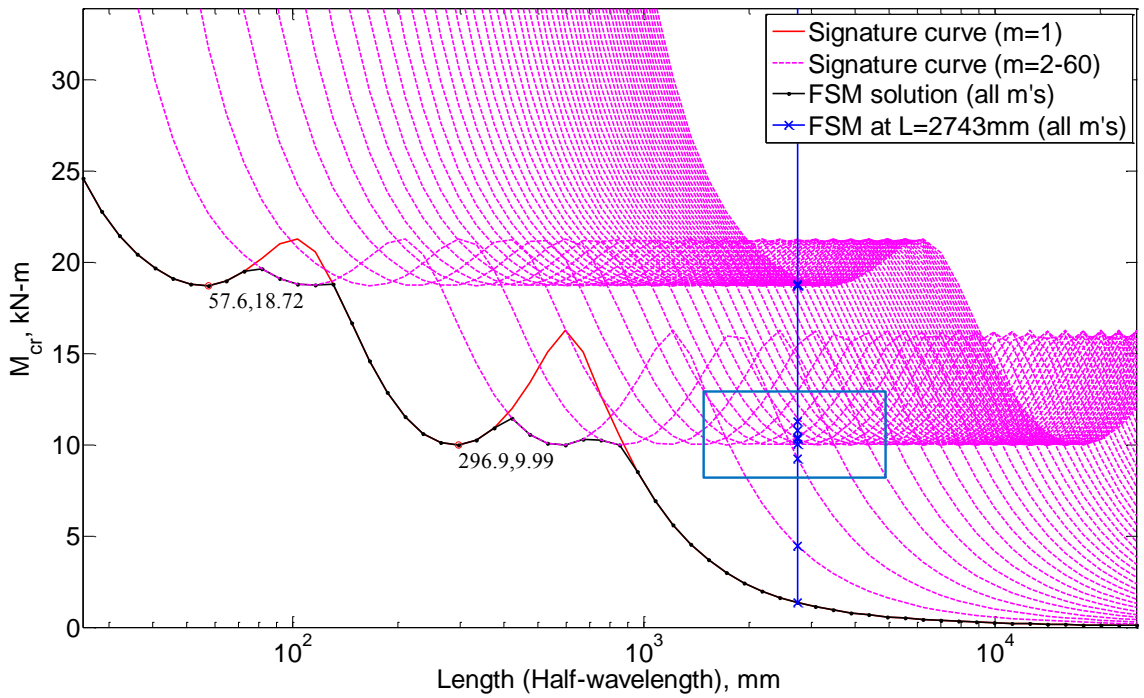
## 2.4 Signature curve and general finite strip method solution

The signature curve of the stability solution in terms of buckling half-wavelength vs. buckling load, as popularized by Hancock [24], provides an efficient means for identifying the characteristic buckling modes. The signature curve and its efficiency result from the fact that the specially selected longitudinal shape function, which is the sine functions as shown in Eq. (2-4), is orthogonal. However, the longitudinal displacement field represented by this shape function is limited to simply-supported (S-S) boundary conditions. When the longitudinal shape functions are expanded to accommodate more general boundary conditions as given in Eq. (2-5) to (2-8), the loss of orthogonality of the longitudinal shape functions for non-simply supported boundary conditions makes the stability solutions potentially coupled between longitudinal terms (in other words, the mode shape is mixed by different half-wavelengths). Hence, the signature curve based on a single longitudinal term, loses its meaning in identifying the characteristic buckling modes for such boundary conditions.

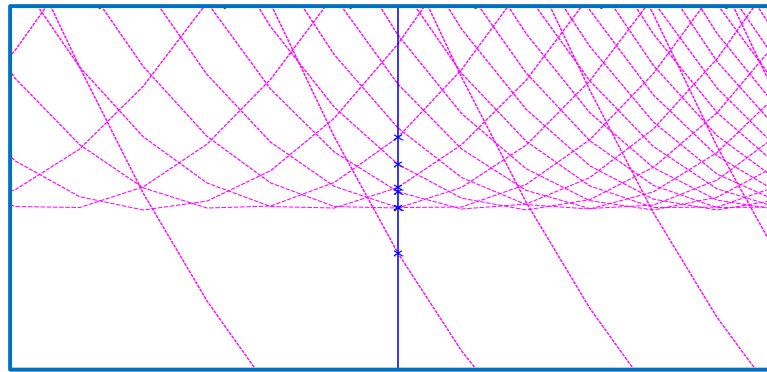
To better understand this orthogonality in the stability solution of S-S boundary conditions, the stability solutions including 60 signature curves (for longitudinal term from 1 to 60) for a 400S162-68 SSMA stud section under major-axis bending are provided in Figure 2-15. In addition, the general solution as a function of physical length instead of the half-wavelength (all the longitudinal term  $m$  are included in one analysis) is also shown in Figure 2-15 to reveal the relationship with the signature curves for S-S boundary conditions. From Figure 2-15, signature curves of all the higher  $m$  longitudinal term are simply horizontal translation of the  $m=1$  signature curve. The  $m=1$  signature curve establishes a lower bound curve for global buckling with long half-wavelengths.

While all the signature curves together form two plateaus: the distortional buckling plateau (the lower one in Figure 2-15) and local buckling plateau (the upper one in Figure 2-15). Meanwhile, the general stability solutions of varying lengths take the lower path of all the signature curves combined. Now, consider a member of length  $L = 2743$  mm, the traditional way to find the essential buckling modes (local, distortional, global) is to examine all the higher modes at  $L = 2743$  mm, which have been organized in increasing order similar to FEM solution, as shown by the vertical line in Figure 2-15 (a). All the higher modes are intersecting with the signature curves at different half-wavelength as shown in Figure 2-15 (b). The 1<sup>st</sup> global buckling mode can be found in the  $m=1$  signature curve at the physical length, the 1<sup>st</sup> distortional and local buckling modes can be found in the distortional and local plateaus, respectively, at the physical length. All of these indirectly confirm the orthogonality of stability solutions of different longitudinal terms for simply-simply supported boundary conditions.

Therefore, FSM solutions for  $S-S$  boundary conditions for any  $m$  are independent due to the resulting orthogonality in  $K_e$  and  $K_g$ . As a result, it has become conventional to express FSM solutions of  $S-S$  boundary conditions in terms of the first buckling load over a series of lengths (signature curve) as opposed to FEM solutions where typically a model is solved for many buckling loads at a single length by examining higher mode solutions.



(a) Stability solutions of signature curves and general FSM solution



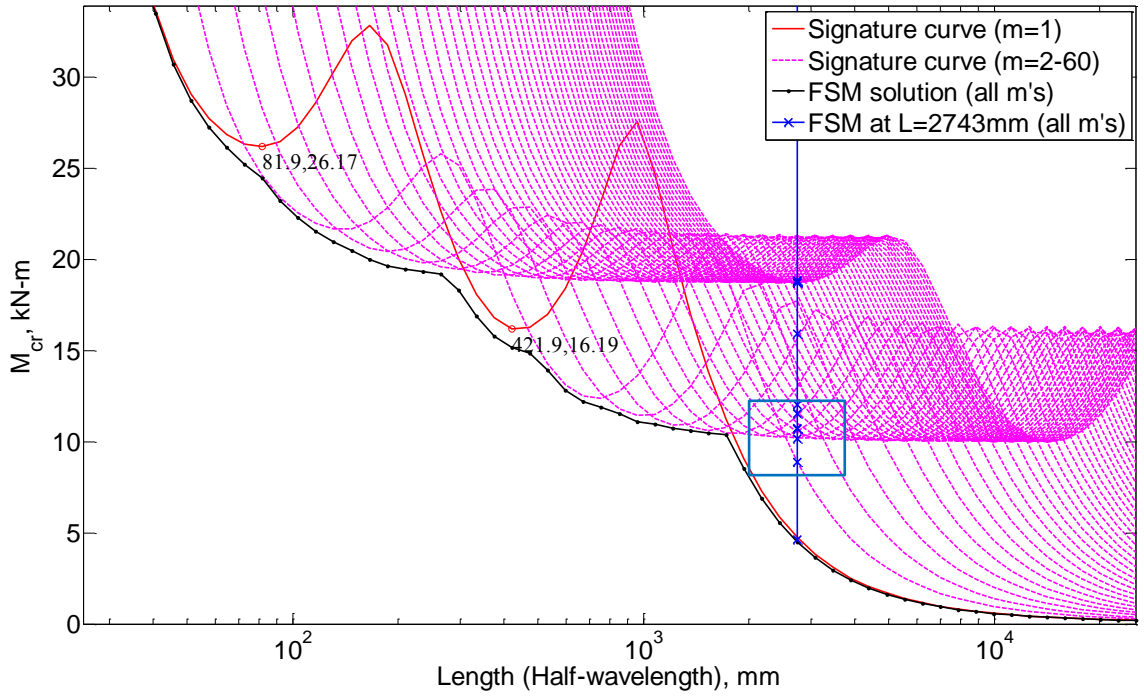
(b) Zoom in where higher modes intersecting with signature curves

Figure 2-15 Stability solutions of SSMA 400S162-68 under major-axis bending for S-S

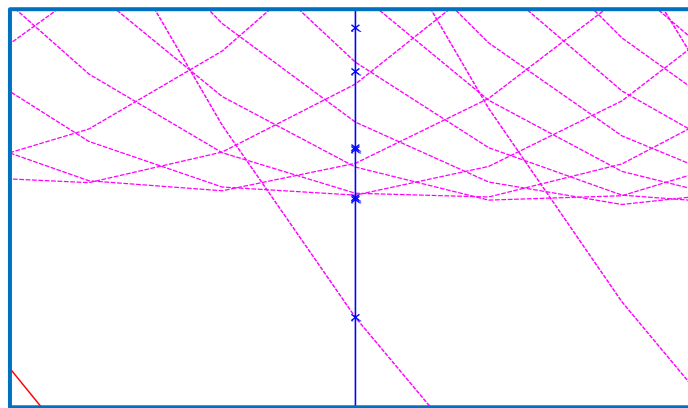
Performing the similar signature curve solution for the same member for non-simply supported boundary conditions, for instances, C-C boundary conditions, Figure 2-16 illustrates the relationship of stability solution of signature curves with those of general boundary conditions. For FSM with non simply-supported boundary conditions the

orthogonality is lost, and thus the special meaning of the signature curve (an  $m=1$  solution with varying length  $a$ ) is lost, as shown in Figure 2-16 (a). Given that many longitudinal ( $m$ ) terms are used the solution should be interpreted as a function of physical length, as opposed to half-wavelength. Different from S-S, the higher modes at a physical length do not intersect with the signature curves anymore as shown in Figure 2-16 (b). In fact, the FSM solution captures the potential interaction of longitudinal terms. Hence, for all the non-simply supported boundary conditions, it would be equally valid to use the FEM approach and examine higher mode solutions at a given length (e.g., at  $L=2743$  mm as shown), instead of varying half-wavelength as shown in Figure 2-16.

Even though the signature curves for non-simply supported boundary conditions are not valid to examine the buckling behavior, some insights provided are still useful. As shown in Figure 2-16, these signature curves still form two plateaus (though slightly descending) that associate with distortional and local buckling, respectively. Comparing these plateaus with those in S-S as shown in Figure 2-17, they are almost identical. This tells us that for relatively long members, even boundary conditions have little impacts on critical loads for local and distortional buckling.



(a) Stability solutions of signature curves and general FSM solution



(b) Zoom in where higher modes NOT intersecting with signature curves

Figure 2-16 Stability solutions of SSMA 400S162-68 under major-axis bending for C-C

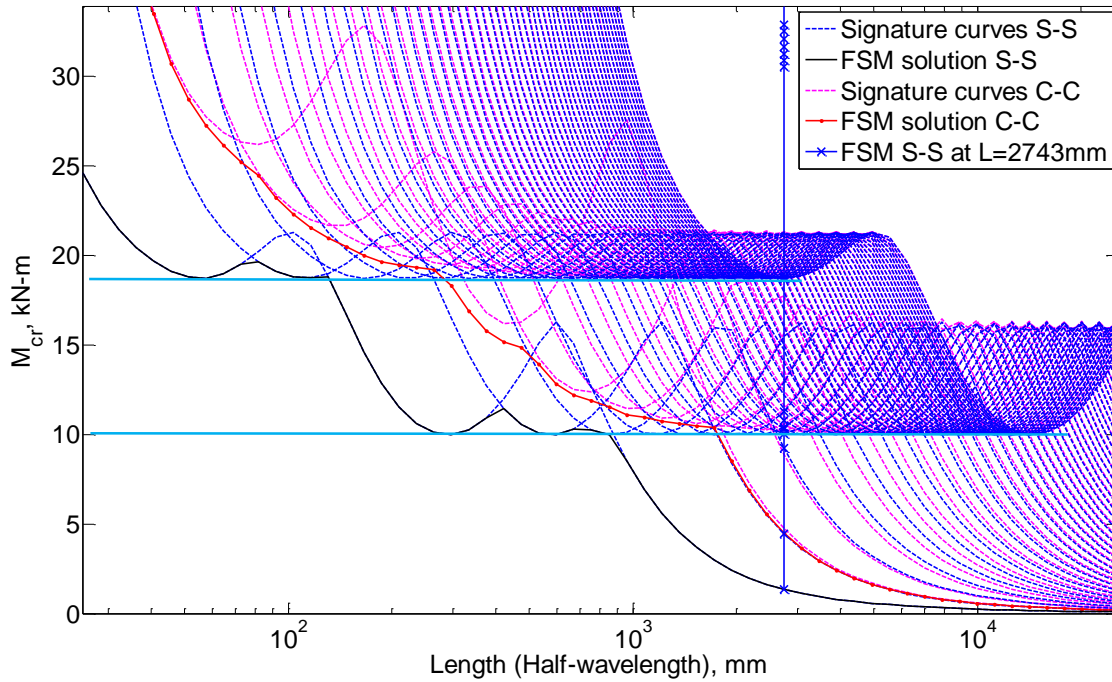
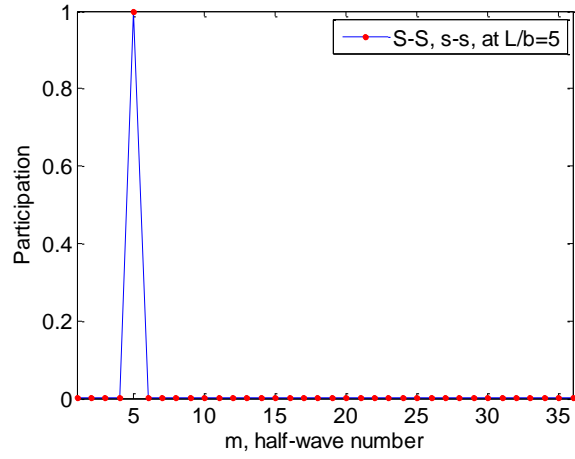


Figure 2-17 Stability solutions of SSMA 400S162-68 under major-axis bending for both S-S and C-C combined

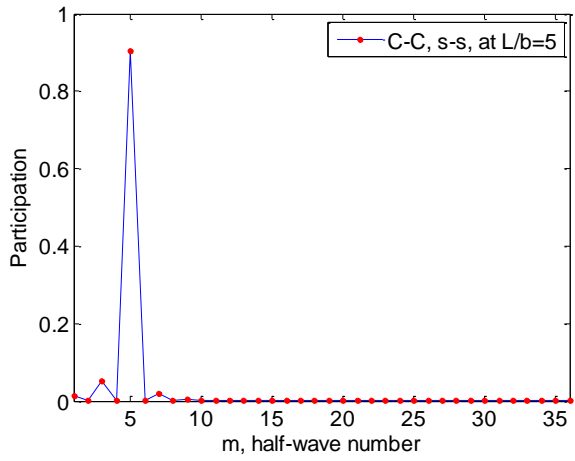
## 2.5 Longitudinal terms

A key feature of the FSM method presented here is the necessity to use a longitudinal series ( $Y_{[m]}$ ) to properly capture the buckling mode in a given length when end conditions other than simply supported are employed. Specific examination of the longitudinal terms which are necessary for capturing the buckling modes provides a great deal of information about the importance of this longitudinal series.

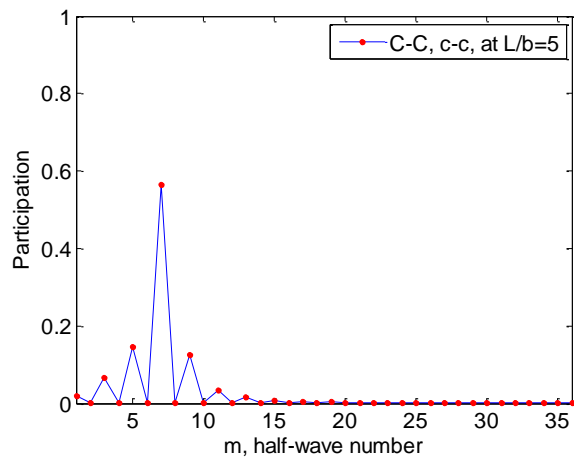
Consider the uniformly loaded plate in Section 2.3.1, the participation of the various  $m$  terms for three sets of boundary conditions at  $L/b=5$  is provided in Figure 2-18. For simply supported boundary conditions the plate buckles into 5 half-waves and only  $m=5$  participates in the solution (Figure 2-18(a)). This solution demonstrates the orthogonality present in the simply supported solution.



(a) S-S, s-s



(b) C-C, s-s



(c) C-C, c-c

Figure 2-18 Participation of longitudinal terms at L/b=5

If the member ends are clamped, but the unloaded sides still remain simply supported, the buckling mode still appears to be in the form of 5 half-waves (Figure 2-4(c)) but the half-waves are not of constant magnitude and Figure 2-18(b) reveals that  $m=3$  and 7 provide a small participation to the solution in addition to the dominant  $m=5$ . Finally, if the plate is clamped on all sides the mode shape is dominated by 7 half-waves (Figure 2-6(c)), but significant contributions exist for  $m=3, 5, 9, 11$  and even higher odd modes. In fact, 42% of the participation occurs from modes other than  $m=7$ . The coupling that occurs is real and necessary for accurate prediction of the buckling mode, and although the mode shape has a dominant visual half-wavelength quantitative examination of the participations demonstrate that the behaviour is more complicated than a single half-wavelength description.

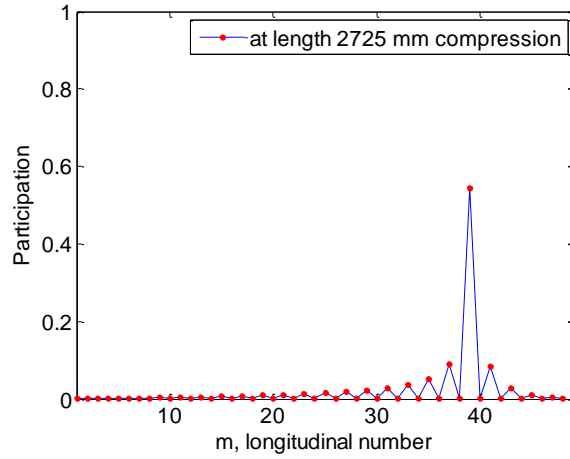
As the participation plots of Figure 2-18 indicate, 36 longitudinal ( $m$ ) terms were included in the analysis, but only a few terms are practically relevant at a given length. In fact, knowing the simply-supported half-wavelength in local buckling ( $L_{cr\ell}$ ) we can conclude that the  $m$  near  $L/L_{cr\ell}$  (5 in the example of Figure 2-18) are of greatest importance. The dimension of the eigenvalue problem that must be solved is directly tied to the number of included longitudinal terms (see DOF discussion in Section 2.2.1), thus computational efficiency is compromised by using a large number of terms in all situations.

For members, local buckling is not the only mode of interest. If the simply supported half-wavelengths are known for local ( $L_{cr\ell}$ ), distortional ( $L_{crd}$ ), and global buckling ( $L_{cre}$ ) these represent the three regimes for  $m$  of greatest interest, i.e.  $m$  near  $L/L_{cr\ell}$ ,  $L/L_{crd}$ , and

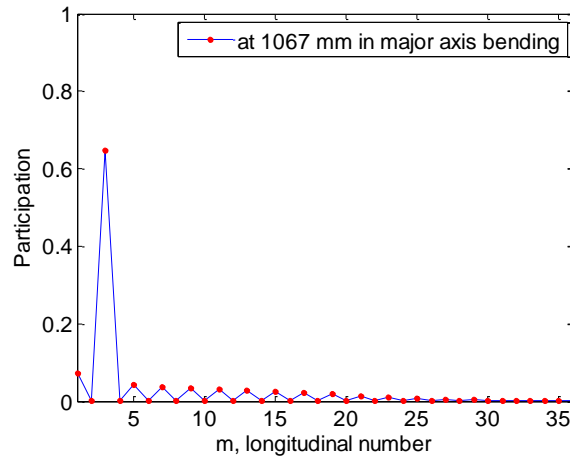
$L/L_{cre}$ . In Section 2.4, we analyzed the relationship of signature curves and general FSM solutions. The local and distortional buckling regimes for  $m$  of greatest interest are immediately illustrated by two plateaus in Figure 2-17, where the longitudinal terms  $m$  of the plateaus at a physical length are near  $L/L_{cr\ell}$  and  $L/L_{crd}$  for local and distortional buckling, respectively. Different with the concept of effective length in Euler buckling, in FSM context the longitudinal term for Euler buckling is always  $m=1$  for all boundary cases. Note, this,  $m=1$ , global is only rigorously true for bare member.

To illustrate these three regimes, consider the 350S162-43 of Section 3.3 as a clamped-clamped column at  $L=2725$  mm, i.e. the location in Figure 2-9 where FSM (with  $m=36$  terms) and FEM had the greatest difference. Classical FSM with simply supported boundary conditions is completed and  $L_{cr\ell}=68.6$  mm. The difference in Figure 2-9 at  $L=2725$  mm may be attributed to not providing high enough  $m$  terms to cover local buckling, namely,  $L/L_{cr\ell} \sim 39$ , but only 36 terms are employed. Figure 2-19(a) indicates that  $m=37$ , 39, and 41 are the dominant terms.

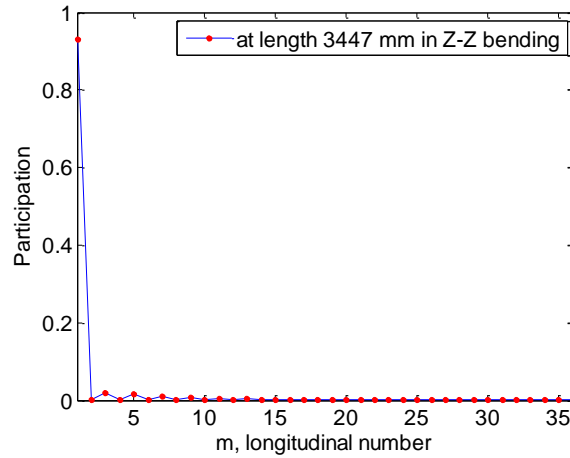
Now, consider the 350S162-43 as a beam in major-axis bending at  $L= 1067$  mm, where distortional buckling is the controlling mode. Classical FSM with simply supported boundary conditions is completed and  $L_{crd}=371$  mm and  $L/L_{crd} \sim 3$ . Figure 2-19(b) indicates that  $m=3$  is by far the dominant term. For global buckling, for instance for the beam bent about the  $z$ - $z$  axis, the dominant term is  $m=1$  (Figure 2-19(c)), as expected.



(a) local region (m=48)



(b) distortional region



(c) global region

Figure 2-19 Participation of the longitudinal terms

Thus, an approximate method which may be utilized to greatly increase computational efficiency is to only include those  $m$  terms near:  $L/L_{cr\ell}$ ,  $L/L_{crd}$ , and  $L/L_{cre}$ . The proposed approximation numbers that shall be included in the analysis are selected as following: 7 longitudinal terms around  $L/L_{cr\ell}$  and  $L/L_{crd}$ , and 3 longitudinal terms around  $L/L_{cre}$  (essentially  $m=1, 2,$  and  $3$ ). The advantages of this are that: 1) increase of the computational efficiency; 2) almost no reduction of the accuracy of the solution; 3) the three essential buckling modes are all included in the solution.

## **2.6 Spring modeling**

Restraint of a thin-walled member such as in a purlin-sheeting system or wall system with bracing and sheathing are common. These kinds of restraints can be modeled as a set of springs or spring foundations along the member, the influence of which can be considered in the stability behavior of the member.

### **2.6.1 Spring stiffness in FSM**

For continuous springs/spring foundations, the stiffness of the springs must be added into the FSM analysis. An equivalent stiffness must be determined from the spring foundation stiffness and this spring stiffness added to the elastic stiffness matrix  $K_e$  in Eq.'s (2-15) and (2-16).

In finite strip and finite element models, the springs are generally defined at certain nodes. Therefore, the transverse shape functions (linear or cubic polynomial function in Eq.'s (2-2) and (2-3)) are unit vectors depending on the direction of the foundation springs. Consequently, the strain energy in the spring can be calculated similar to equivalent nodal loads as following:

$$U_{spring} = \frac{1}{2} \int_0^a \{d\}^T \{F\} dy \quad (2-35)$$

where, in the spring model,  $\{F\} = k \{d\}$ ,  $\{d\} = [U \ V \ W \ \Theta]^T$  is the nodal displacement vector,  $k$  is a matrix consisting of the corresponding spring foundation stiffness with specified direction (e.g., in the units of  $F/L/L$  for translational spring, and of  $F \ L/rad/L$  for rotational spring) in diagonal, which is  $diag(K_X, K_Y, K_Z, K_\Theta)$ , and  $a$  is the strip length.

Since the nodal displacement in the strip is a summation over several longitudinal terms as shown in Eq. (2-4) and (2-8), the strain energy in the spring for the strip can be rewritten as:

$$U_{spring} = \sum_m^q \sum_n^q \frac{1}{2} \{d\}_{[m]}^T K_{spring}^{[mm]} \{d\}_n \quad (2-36)$$

where

$$K_{spring}^{[mm]} = \begin{bmatrix} K_X I_1 & & & \\ & K_Y I_5 & & \\ & & K_Z I_1 & \\ & & & K_\Theta I_1 \end{bmatrix} \text{ and } I_1 = \int_0^a Y_{[m]} Y_{[n]} dy, \quad I_5 = \int_0^a Y'_{[m]} Y'_{[n]} dy$$

For the simply supported boundary case, for instance,  $I_1$  is zero when  $m \neq n$  while it is  $a/2$  when  $m=n$ . See Appendix A for the explicit integration results of  $I_1$  and  $I_5$ .

## 2.6.2 Analytical solution for global buckling

### 2.6.2.1 Flexural buckling

For a simple column with elastic spring foundation, the flexural buckling solution can be found in Theory of Elastic Stability by Timoshenko and Gere [50]. Now, let us extend the analytical solution of flexural buckling to more general boundary conditions.

In the general boundary case, assume the buckling curve in the longitudinal direction is represented by the equation:

$$w = \sum_m^q A_{[m]} Y_{[m]} \quad (2-37)$$

where, similar to the definition in FSM,  $m$  is longitudinal term, up to  $q$ , and  $Y_{[m]}$  is the assumed buckling curve in the longitudinal direction that satisfies the boundary conditions. For the general boundary conditions studied here,  $Y_{[m]}$  is given in Eqs. (2-4) - (2-8).

By neglecting the strain energy due to axial stress, the strain energy of bending and the spring foundation are expressed by assuming the cross section and spring stiffness are constant along the length as

$$U = \frac{1}{2} EI \int_0^a (w'')^2 dy + \frac{1}{2} k \int_0^a (w)^2 dy \quad (2-38)$$

At the same time, the work done by the external compression force  $P$  can be expressed as:

$$W_{ext} = \frac{1}{2} P \int_0^a (w')^2 dy \quad (2-39)$$

Then, the potential energy in the system is:

$$\Pi = U - W_{ext} = \frac{1}{2} EI \int_0^a (w'')^2 dy + \frac{1}{2} k \int_0^a (w)^2 dy - \frac{1}{2} P \int_0^a (w')^2 dy \quad (2-40)$$

Substituting  $w$  into Eq. (2-40), the potential energy can be rewritten as:

$$\Pi = \frac{1}{2} EI \sum_m^q \sum_n^q A_{[m]} \int_0^a Y_{[m]}'' Y_{[n]}'' dy A_{[n]} + \frac{1}{2} k \sum_m^q \sum_n^q A_{[m]} \int_0^a Y_{[m]} Y_{[n]} dy A_{[n]} - \frac{1}{2} P \sum_m^q \sum_n^q A_{[m]} \int_0^a Y_{[m]}' Y_{[n]}' dy A_{[n]} \quad (2-41)$$

The principle of minimum potential energy thus leads to the following eigenvalue problem in matrix form:

$$(EI[I_4] + k[I_1])A = P[I_5]A \quad (2-42)$$

where,  $A$  is the vector consisting of  $[A_{[1]} A_{[2]} A_{[3]} \dots A_{[45]}]$ , and

$$I_1 = \int_0^a Y_{[m]} Y_{[n]} dy, \quad I_4 = \int_0^a Y_{[m]}'' Y_{[n]}'' dy, \quad I_5 = \int_0^a Y_{[m]}' Y_{[n]}' dy \quad (2-43)$$

For a simply supported column,  $I_1$ ,  $I_4$  and  $I_5$  are zero when  $m \neq n$ , which leads to a set of diagonal matrices. Therefore, the buckling curve is uncoupled between different  $m$  longitudinal terms. Substitute  $I_1$ ,  $I_4$  and  $I_5$  into Eq. (2-42), the critical load can be obtained:

$$P_{cr} = \frac{\pi^2 EI}{a^2} \left( m^2 + k \frac{a^4}{m^2 \pi^4 EI} \right) \quad (2-44)$$

which is the same as that in [50] and is known as Euler buckling.

For other than simply supported boundary conditions, matrices  $[I_1]$ ,  $[I_4]$ , and  $[I_5]$  have nonzero off-diagonal terms which means different  $m$  longitudinal terms are coupled. The eigenvalue problem of Eq. (2-42) must be solved for several longitudinal terms in full matrix form to take account of their potential coupling.

An I-beam section has been selected here to compare the FSM solution and analytical solutions. The section has a height of 100mm, width of 60mm, and thickness of 2mm. The material is assumed to be linear elastic, isotropic, with  $E=210,000$  MPa and  $\nu=0.3$ . The spring is in the weak-axis direction with a foundation stiffness of  $k=0.001$  N/mm/mm.

For simply supported boundary conditions, both FSM and Euler solutions with and without springs are shown in Figure 2-20. Figure 2-20 demonstrates the excellent agreement between the two solutions. In fact, when there is no spring, the member

selected always buckles in minor-axis bending; while with the spring, both solutions show the transition of the buckling mode from  $m=1$  to  $m=2$ . However, when the column length is long, the FSM solution is able to capture the lower buckling mode – major-axis bending. That is where these two solutions (analytical/Euler and FSM) separate.

For all the other boundary conditions, both FSM and Euler solutions should take into account the coupling effect between longitudinal terms. Comparisons are shown in Figure 2-21 - Figure 2-24 for C-C, S-C, C-F, and C-G, respectively. Similar to the S-S case, excellent agreement can be found for all the cases. In addition, for longer columns, the FSM solution departs to a lower critical mode (major-axis bending) when the spring is present.

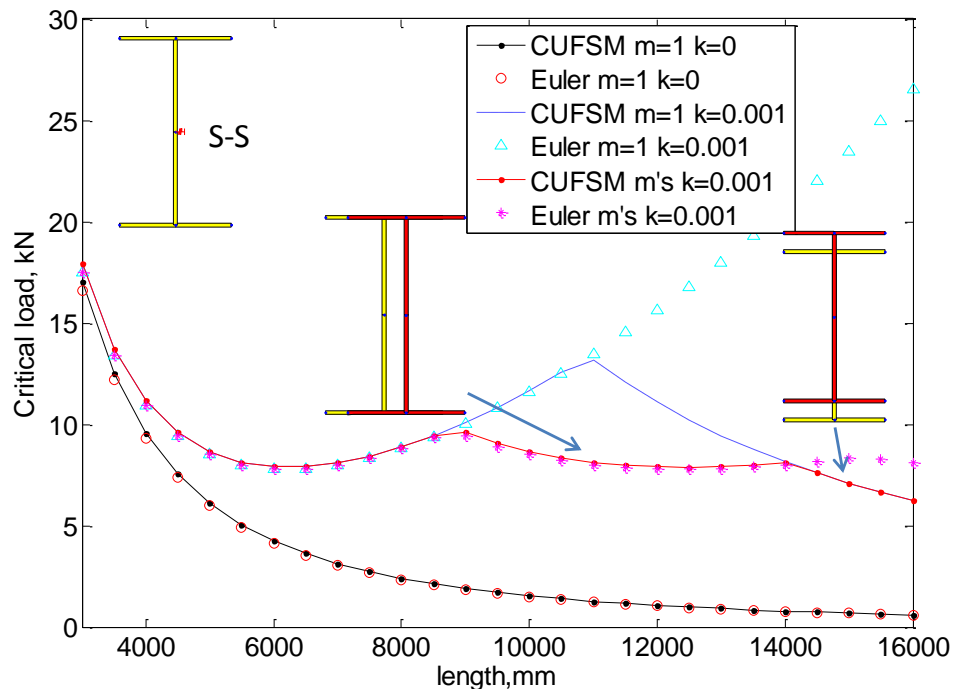


Figure 2-20 FSM and analytical solutions of the column with/without springs for S-S

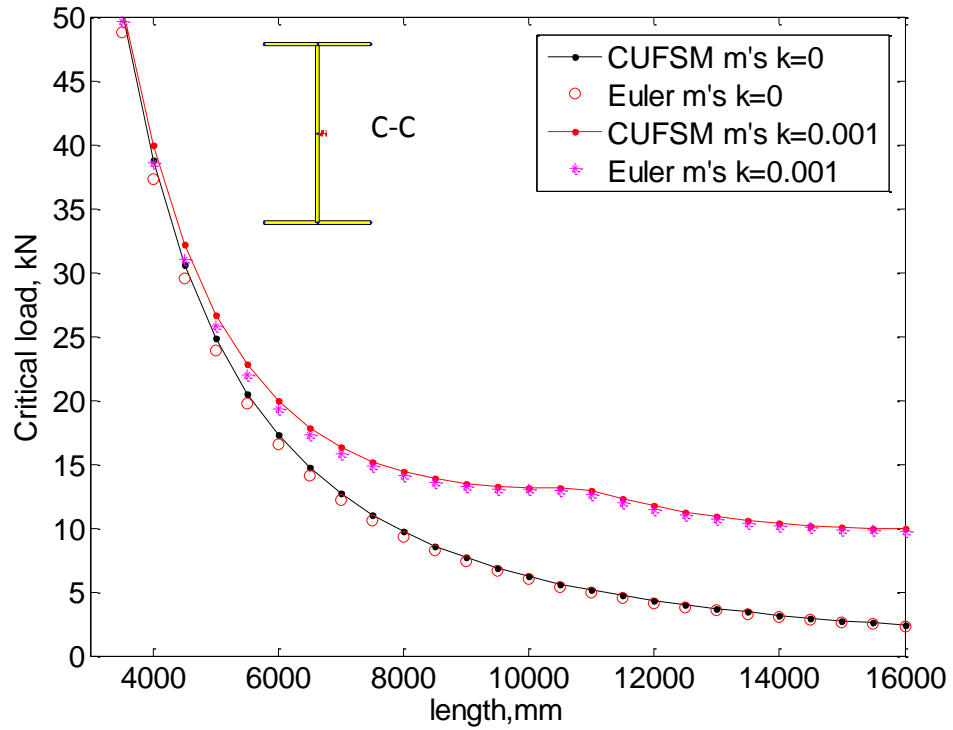


Figure 2-21 FSM and analytical solutions of the column with/without springs for C-C

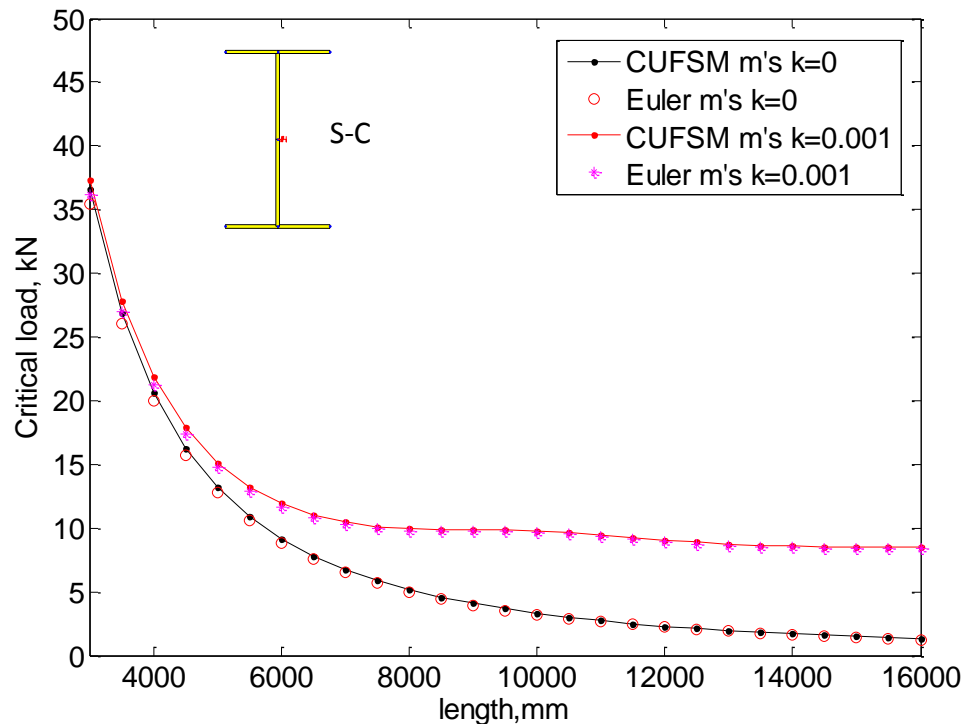


Figure 2-22 FSM and analytical solutions of the column with/without springs for S-C

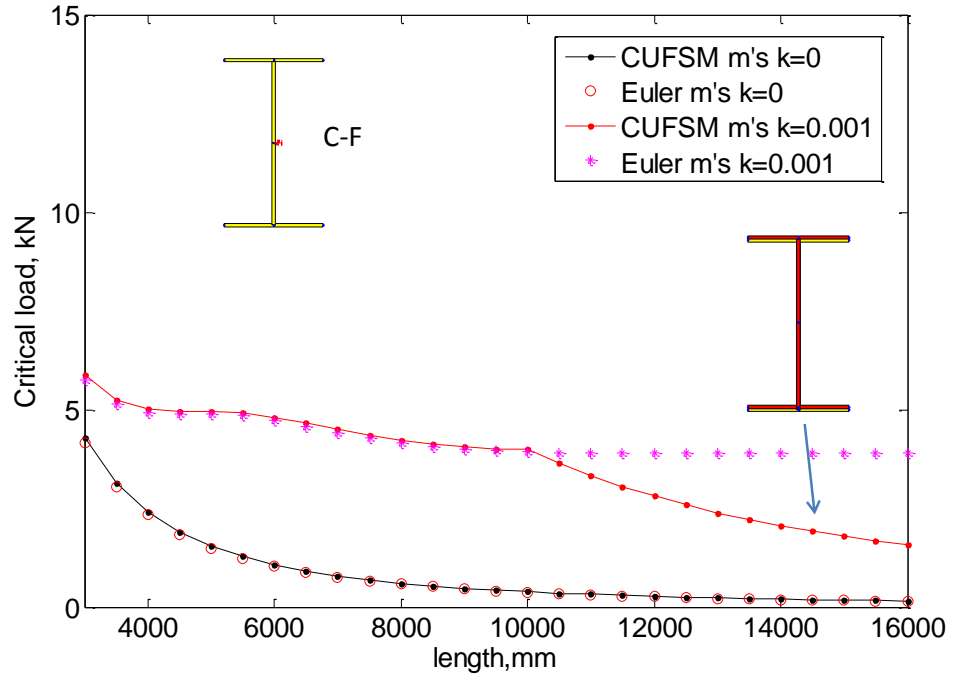


Figure 2-23 FSM and analytical solutions of the column with/without springs for C-F

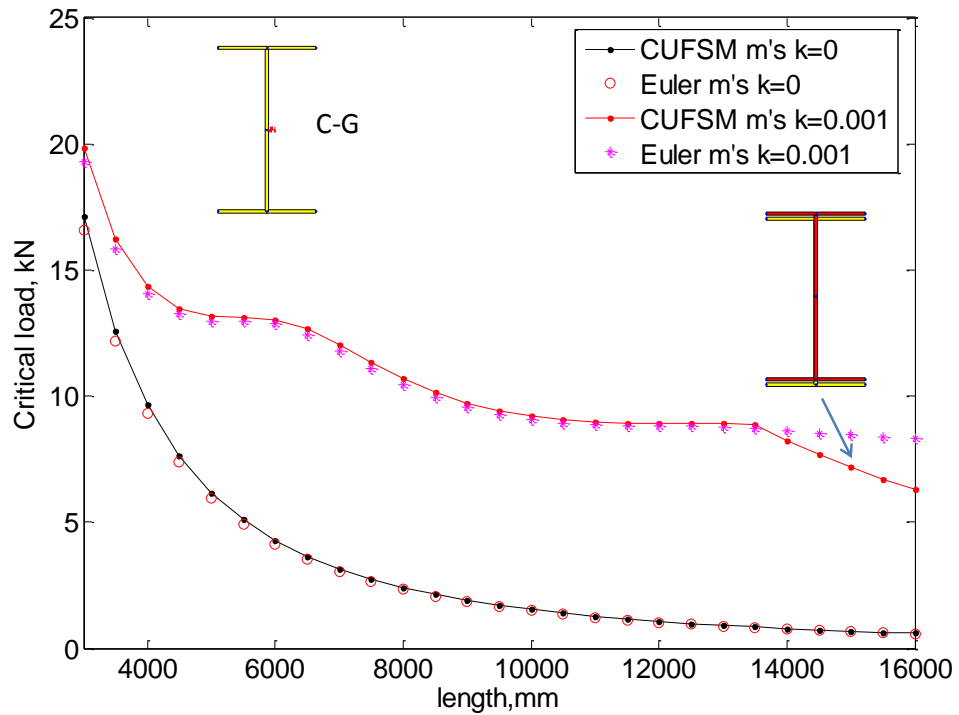


Figure 2-24 FSM and analytical solutions of the column with/without springs for C-G

### 2.6.2.2 Flexural-torsional buckling

In the previous study, the analytical solution is restricted to flexural buckling in one direction. For general column buckling, flexural buckling in both directions and torsional buckling should be considered simultaneously, especially when the cross-section is not symmetric. For common singly symmetric section the coupling results in flexural-torsional buckling.

For general boundary conditions, assume the buckling curve in the longitudinal direction is represented by the equation:

$$u = \sum_m^q A_{[m]} Y_{[m]} = \sum_m^q [1 \ 0 \ 0] Y_{[m]} d_{[m]} \quad (2-45)$$

$$w = \sum_m^q B_{[m]} Y_{[m]} = \sum_m^q [0 \ 1 \ 0] Y_{[m]} d_{[m]} \quad (2-46)$$

$$\theta = \sum_m^q C_{[m]} Y_{[m]} = \sum_m^q [0 \ 0 \ 1] Y_{[m]} d_{[m]} \quad (2-47)$$

where, similar to the definition in FSM,  $m$  is the longitudinal term, up to  $q$ ,  $Y_{[m]}$  is the assumed buckling curve in the longitudinal direction that satisfies the boundary conditions, and  $d_{[m]} = [A_{[m]} \ B_{[m]} \ C_{[m]}]^T$ . For the general boundary conditions studied here,  $Y_{[m]}$  is given in Eqs. (2-4) - (2-8).

The modeling of the springs is illustrated in Figure 2-25 with a channel section as an example. Displacement  $u$  is in  $x$  direction,  $w$  in  $z$  direction and rotation  $\theta$  in  $x$ - $z$  plane. All the displacements are with respect to the shear center.

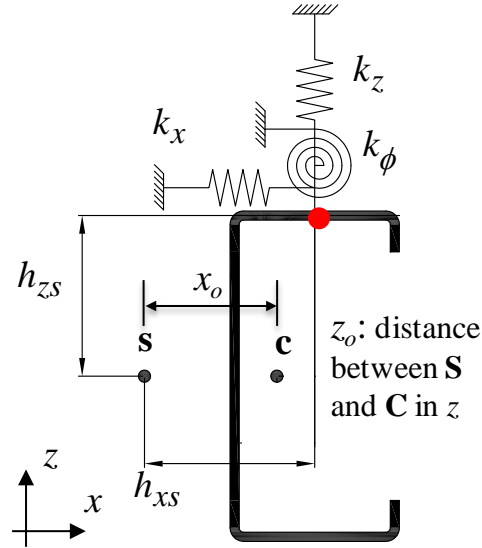


Figure 2-25 Illustration of cross section and springs

By neglecting the strain energy due to axial stress, the strain energy by bending and the spring foundation are expressed as the following (assuming the cross section and spring stiffness are constant along the length):

$$U_{strain} = \frac{1}{2} EI_{zz} \int_0^a (u'')^2 dy + \frac{1}{2} EI_{xx} \int_0^a (w'')^2 dy + \frac{1}{2} EI_{xz} \int_0^a (u'' w'') dy + \frac{1}{2} GJ \int_0^a (\theta'')^2 dy + \frac{1}{2} EC_w \int_0^a (\theta'')^2 dy \quad (2-48)$$

$$U_{spring} = \frac{1}{2} k_x \int_0^a (u - h_{zs} \theta)^2 dy + \frac{1}{2} k_z \int_0^a (w + h_{xs} \theta)^2 dy + \frac{1}{2} k_\theta \int_0^a (\theta)^2 dy \quad (2-49)$$

where,  $I_{xx}$ ,  $I_{zz}$  are the second moment of inertia,  $I_{xz}$  is the product moment of inertia,  $J$  is Saint-Venant torsional constant,  $C_w$  is the warping constant,  $k_x$ ,  $k_z$ ,  $k_\theta$  are the foundation spring stiffness,  $h_x$  is the distance in  $x$  direction of spring  $k_x$  relative to shear center,  $h_{zs}$  is the distance in  $z$  direction of spring  $k_x$  relative to shear center. See Timoshenko and Gere's book [50] for a similar solution through equilibrium equations. At the same time, the work done by the external compression force  $P$  can be expressed as:

$$W_{ext} = \frac{1}{2} P \int_0^a [(u')^2 + (w')^2 + r_o^2 (w')^2 - 2z_o u' \theta' + -2x_o u' \theta'] dy \quad (2-50)$$

where  $x_o$  is the distance between shear and shape center in  $x$ ,  $z_o$  is the distance between shear and shape center in  $z$ ,  $r_o$  is the radius of gyration, given by  $r_o^2 = x_o^2 + y_o^2 + (I_x + I_y) / A$ .

Substituting  $u$ ,  $w$ , and  $\theta$  into Eq.'s (2-48) - (2-50), the strain energy and external work can be rewritten as:

$$U = U_{strain} + U_{spring} = \frac{1}{2} \sum_m^q \sum_n^q d_{[m]}^T K_{str}^{[mn]} d_{[m]} \quad (2-51)$$

$$W_{ext} = \frac{1}{2} P \sum_m^q \sum_n^q d_{[m]}^T K_{ext}^{[mn]} d_{[m]} \quad (2-52)$$

where,

$$K_{str}^{[mn]} = \begin{bmatrix} EI_{zz} I_4 + k_x I_1 & EI_{xz} I_4 & -k_x I_1 h_z \\ EI_{xz} I_4 & EI_{xx} I_4 + k_z I_1 & k_z I_1 h_x \\ -k_x I_1 h_z & k_z I_1 h_x & GJ I_5 + EC_w I_4 + k_x I_1 h_z^2 + k_z I_1 h_x^2 + k_\theta I_1 \end{bmatrix}$$

$$K_{ext}^{[mn]} = \begin{bmatrix} I_5 & 0 & -z_o I_5 \\ 0 & I_5 & x_o I_5 \\ -z_o I_5 & x_o I_5 & r_o^2 I_5 \end{bmatrix}$$

The explicit integration results of  $I_1$  and  $I_5$  can be found in the appendix A. Then, the potential energy in the system is:

$$\Pi = U_{strain} + U_{spring} - W_{ext} \quad (2-53)$$

The principle of minimum potential energy thus leads to the following eigenvalue problem in matrix form:

$$[K_{str}^{[mn]}]_{q \times q} d = P [K_{ext}^{[mn]}]_{q \times q} d \quad (2-54)$$

where,  $d$  is a vector  $\left[ d_{[1]}^T \quad d_{[2]}^T \quad \cdots \quad d_{[q]}^T \right]^T$ ,

Solving the above eigen problem yields the critical load for the global buckling mode. This solution captures all possible global buckling modes, namely: major-axis bending, minor-axis bending, torsional, including coupling of any mode for any of the boundary conditions (S-S, C-C, S-C, C-G, and C-F) studied here.

For a channel section, with and without springs, the stability solutions of long members by FSM and the analytical method are provided in the following figures for each boundary condition case. The section has a web height of 100mm, flange width of 60mm, lip length of 10mm and thickness of 2mm. Young's modulus of the material is 210 GPa, and the Poisson ratio is 0.3. The springs are foundation stiffness in the weak-axis direction with  $K_x=0.1$  N/mm/mm and in the rotational direction with  $K_\theta=10$  N/rad/mm (see Figure 2-25).

Either with or without springs, FSM solutions show excellent agreement with the developed "analytical" solutions for all the boundary conditions. Also, as an illustration, the buckling mode transfers from weak-axis bending to major-axis bending due to the springs in Figure 2-26 for S-S boundary conditions.

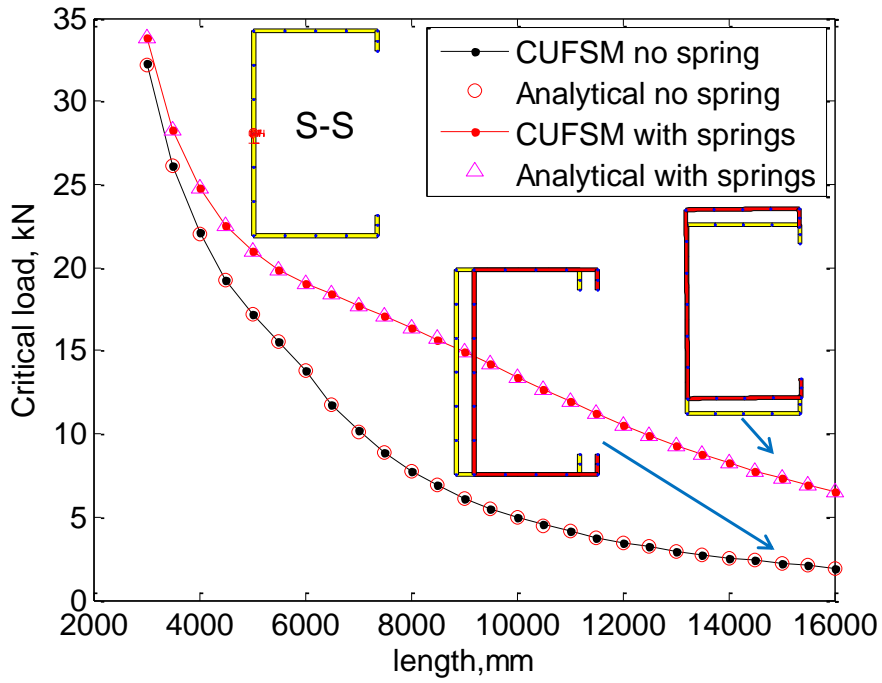


Figure 2-26 FSM and analytical solution of column for S-S with/without springs

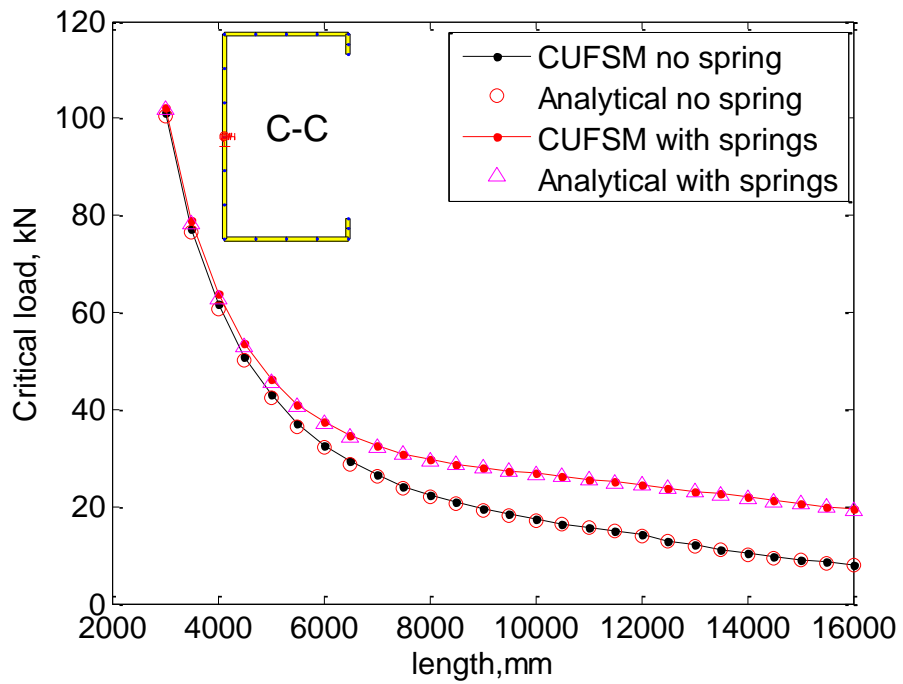


Figure 2-27 FSM and analytical solution of column for C-C with/without springs

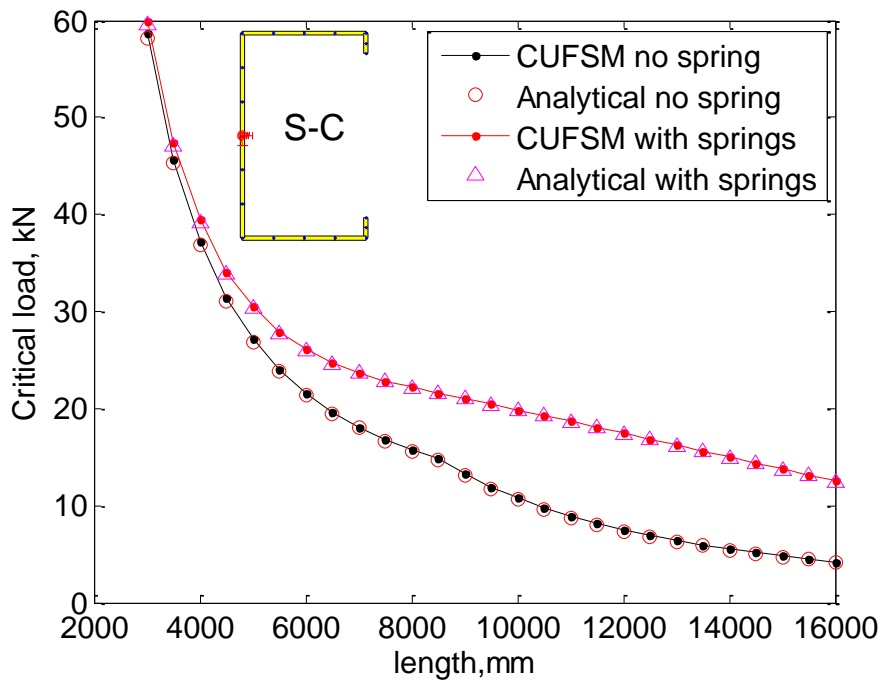


Figure 2-28 FSM and analytical solution of column for S-C with/without springs

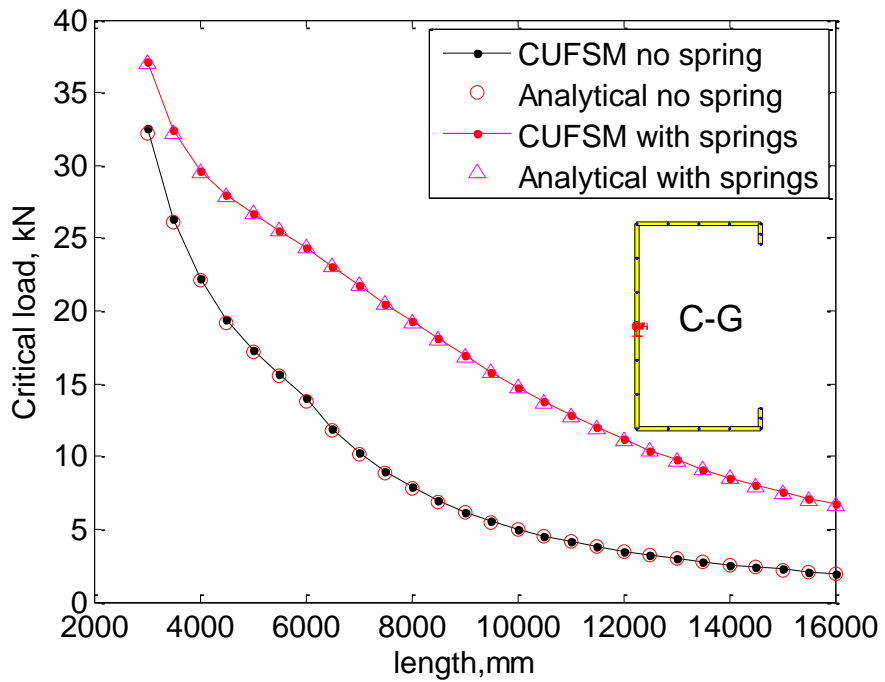


Figure 2-29 FSM and analytical solution of column for C-G with/without springs

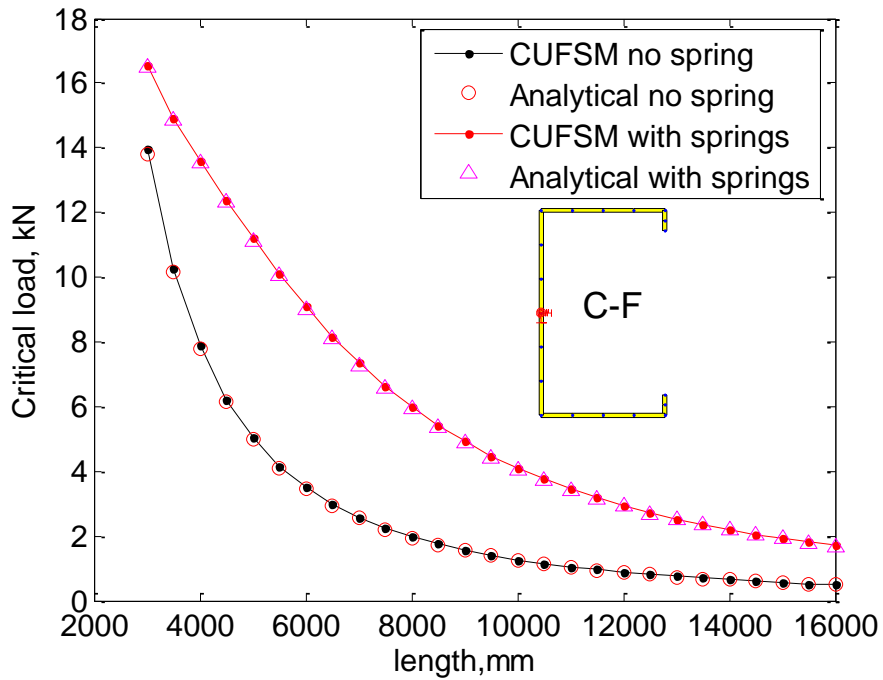


Figure 2-30 FSM and analytical solution of column for C-F with/without springs

### 2.6.3 Comparison with shell FEM

Elastic buckling analysis (also known as eigenvalue buckling analysis), which is a linear perturbation procedure, predicts the theoretical buckling strength of a member usually based on the perfect geometry. Imperfections and nonlinearities are not included in the analysis. However, eigenvalue buckling analysis is preceded by a static analysis to obtain the stress distribution in the member. The geometric stiffness matrix is formulated based upon this stress distribution. With the elastic and geometric stiffness matrices, the results solved by the eigenvalue buckling analysis give the load factors (eigenvalues) that scale the load applied in the static analysis and also the corresponding buckling mode shapes (eigenvectors).

The FSM stability solution for general boundary conditions with springs shows excellent agreement with the “analytical” Euler solution as presented in the previous section. In this section, a more extensive verification has been performed against a shell FEM solution. For the same cross section used to verify the flexural-torsional buckling with springs (as shown in Figure 2-31), the stability solutions under axial compression, as a function of member length, for both the FSM and FEM models are provided in Figure 2-32 for this member with/without springs. Different from the verification work in Section 2.3, the S4 shell element in ABAQUS library is used here. In terms of the critical loads as shown in Figure 2-32, the FSM solutions show excellent agreement with FEM solutions in both cases. The predicted mode shapes are also the same for both FSM and FEM as illustrated in Figure 2-33 (at  $L=2.42$  m). The spring scenario considered in this study has almost no impact on local buckling load for short columns. For intermediate columns (in the range: 760 ~ 2500 mm), the critical mode ( $1^{\text{st}}$  eigenmode) is distortional buckling without springs, while distortional buckling has been restrained by the springs and the critical mode is local buckling – see Figure 2-33. Moreover, the global buckling loads have been enhanced by the springs as well.

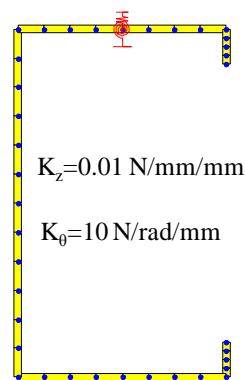


Figure 2-31 Continuous springs in the member length

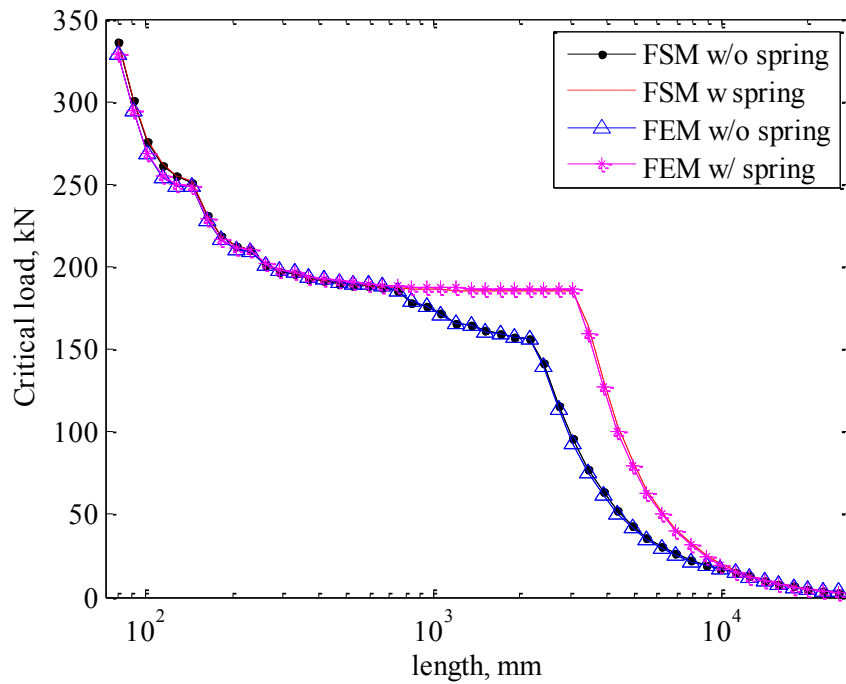
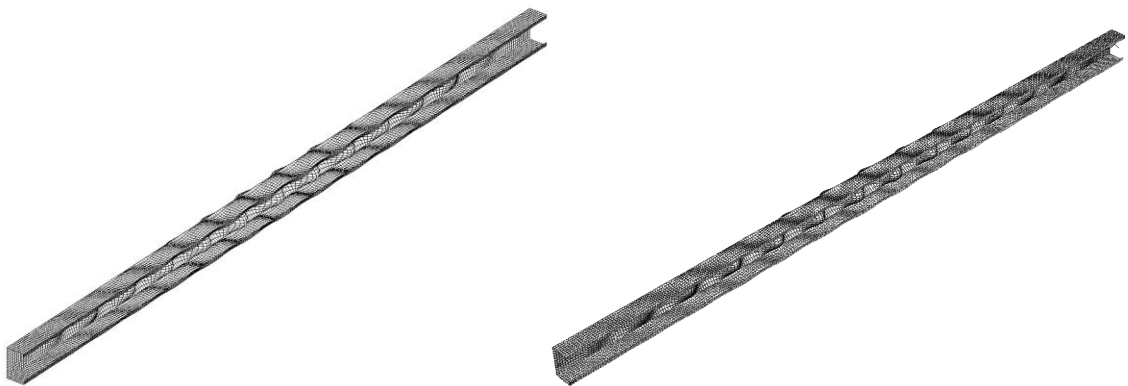


Figure 2-32 FSM and FEM solutions of column for C-C with/without springs



(a) FSM (b) FEM

Figure 2-33 Buckling mode shapes of FEM and FSM at L=2.42m

Now, for the same member with springs shown in Figure 2-31, the stability solutions of FSM under major-axis bending (top flange in compression) are compared with FEM solutions. The critical loads as a function of member length are shown in Figure 2-34.

Tremendous differences are observed especially for long members, for which FSM predicts either local buckling (in Figure 2-35a) or global buckling while FEM always predicts localized local/distortional interacted mode at two ends (in Figure 2-35b).

However, for FSM (as implemented), the stress distribution is pre-assumed as longitudinal nodal stresses at the ends and no gradient is present along the length. Therefore, when the springs are considered in the model, while FSM remains the pre-assumed stress distribution (as shown in Figure 2-36(a)), a static analysis performed in FEM may result in a different stress distribution, especially at the ends of the beam (as shown in Figure 2-36(b)). While, stress distribution in FSM is uniform along the length, gradient of the stress distribution is observed in FEM model.

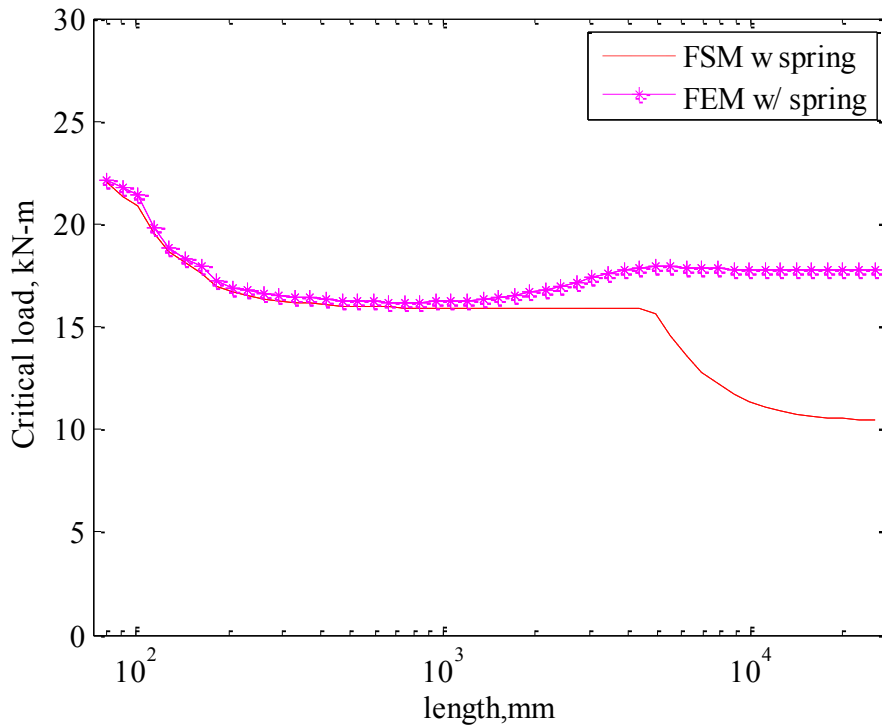
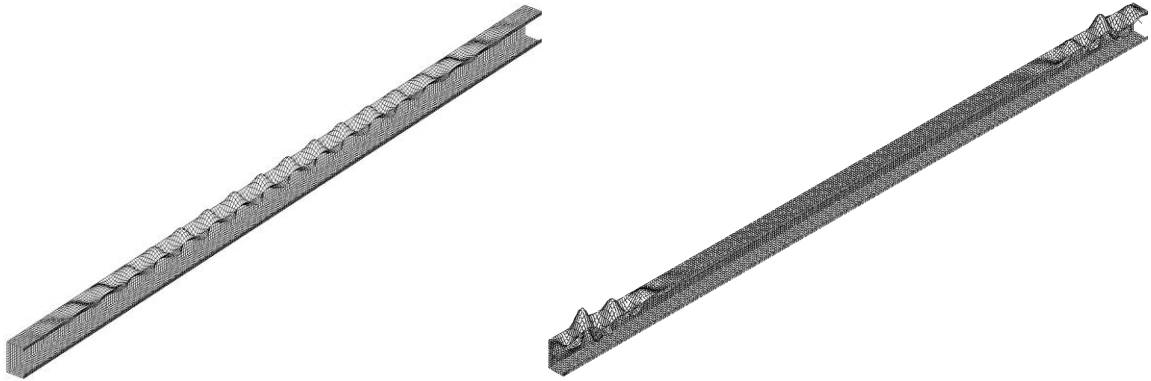
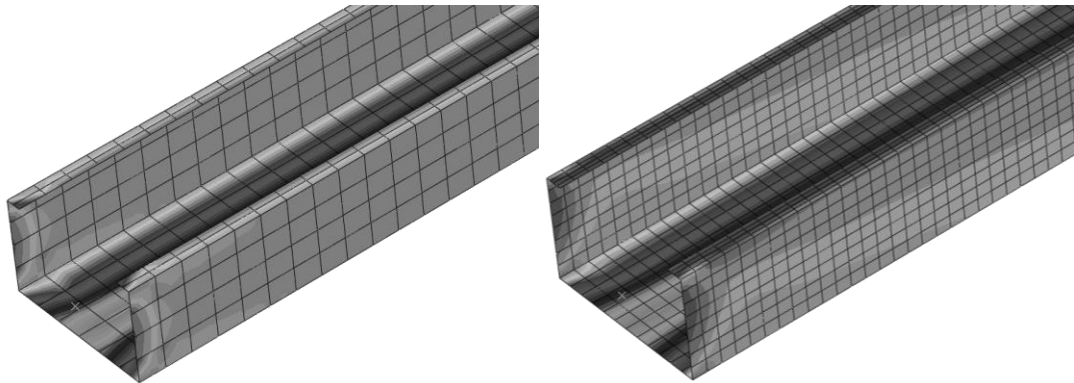


Figure 2-34 FSM and FEM solutions of beam member with springs for C-C



(a) FSM buckling mode (b) FEM buckling mode

Figure 2-35 FSM and FEM buckling mode shapes at  $L=2.42\text{m}$



(a) FSM

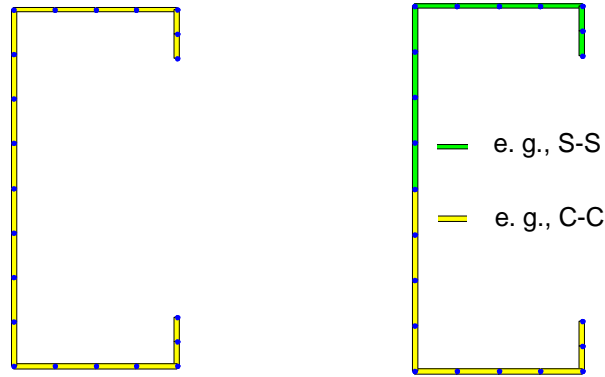
(b) FEM

Figure 2-36 Pre-buckling stress distribution in FSM and FEM for spring modeling

## 2.7 Element-wise finite strip method

The general boundary condition conditions in FSM include S-S, S-C, C-C, C-G, and C-F represented by the specially selected longitudinal shape functions of Eq.'s (2-4) – (2-8). However, the longitudinal shape is applied in a strip-by-strip sense, as illustrated in Figure 2-1, the default application in FSM is that the boundary condition at the end is the same for all the strips (Figure 2-37(a)), as opposed to the possibility that the member may

be restrained differently in parts at the ends. For instance, as shown in Figure 2-37(b), the upper part of section is simply supported and the lower part is clamped.



(a) uniform boundary conditions (b) element-wise boundary conditions

Figure 2-37 uniform boundary conditions and element-wise boundary conditions at the ends

In the latter case (Figure 2-37(b)), the boundary condition can be specified strip-by-strip (element-wise) in FSM. The stability solutions of the boundary case in Figure 2-37(b) are provided as a function of member length in Figure 2-38. In FEM, complication arises on how to appropriately handle the warping fixity of C-C boundary conditions implied in FSM. In our models, for convenience, the term “locally fixed” is used to represent that the cross section of C-C boundary condition part is assumed to be warping free; while the term “globally fixed” represents that the cross section of C-C boundary condition part is assumed to be warping fix by direct fixity (or realized through rigid body definition). The FEM solutions in Figure 2-38 demonstrate significant differences from the FSM solutions. FSM uses longitudinal shape function to represent the longitudinal field, thus the discontinuity at the boundary between S-S and C-C still preserves in the longitudinal direction. This clearly violates the concept of Saint-Venant’s

principle that the discontinuity should only affect a small region at the end. Consider the stress distribution of a plate under compression with mixed boundary conditions at ends, where half of the nodes are clamped and the rest are simply supported. The stress discontinuity, as shown in Figure 2-39 is only observed at the ends (Though, from a strict point of view, the stress contour shown here from FEM (ABAQUS, von Mises stress) is the smoothed stresses found by averaging the discontinuous stresses element by element.).

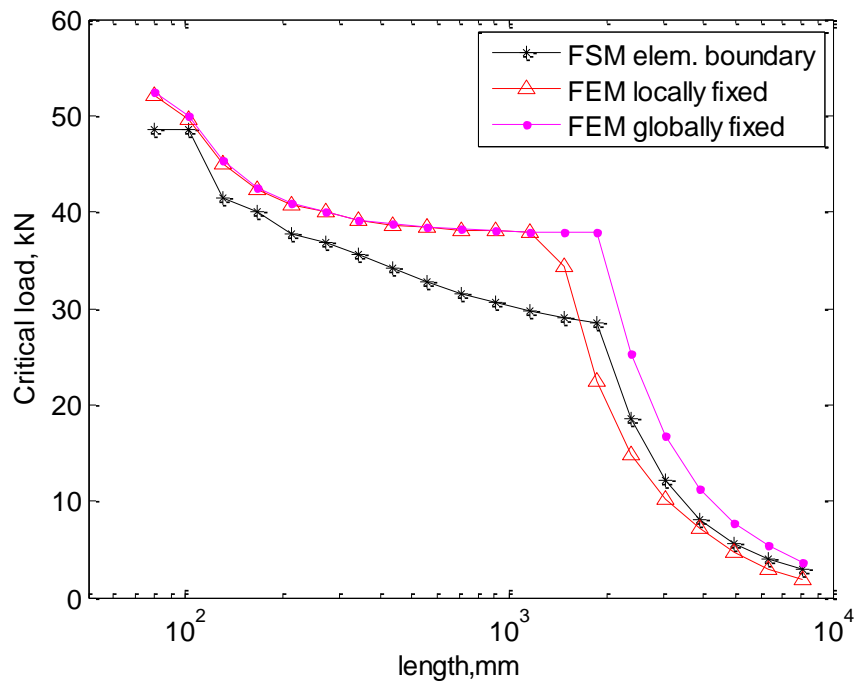


Figure 2-38 Stability solution of FSM and FEM for mixed end boundary conditions

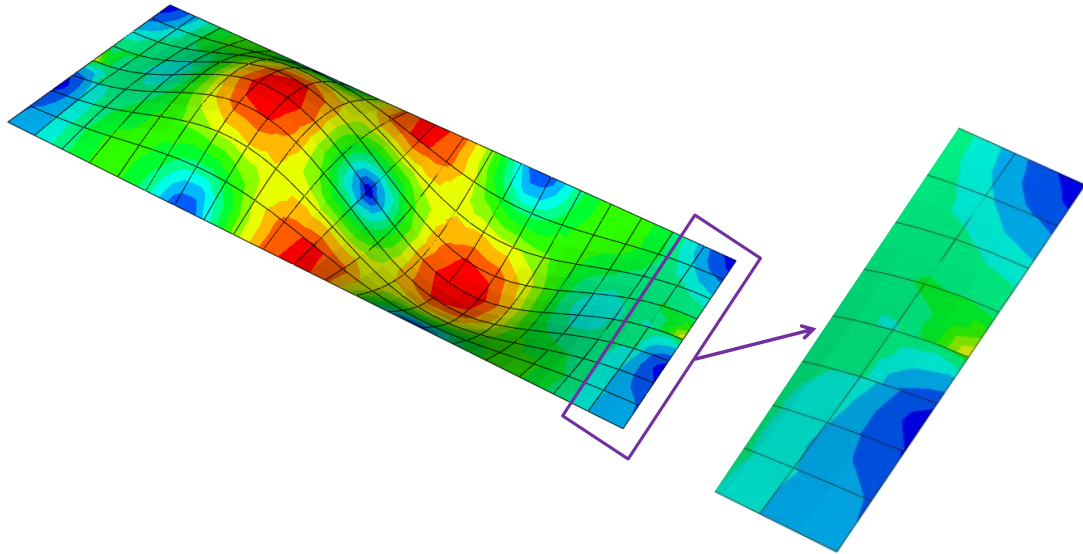


Figure 2-39 Stress distribution of plates with mixed end boundary conditions

## 2.8 Summary

The application of the semi-analytical finite strip method to general end boundary conditions (simple-simple, clamped-clamped, simple-clamped, clamped-guided, and clamped-free) is explicitly derived, implemented, and validated. The validation studies show excellent agreement between eigenbuckling solutions by FSM and shell FEM with general end boundary conditions.

However, one must take care to insure enough (or the proper) longitudinal terms are included in the series to capture all buckling modes of interest. For any end boundary condition other than simple supports, multiple longitudinal half-waves participate in the solution, even when simple buckling patterns may be visually identified. The relationship between signature curves and general FSM solutions reveals the buckling characteristics of local, distortional, and global modes. Longitudinal terms of greatest interests included in the buckling analysis are then recommended as an approximation to increase the computational efficiency.

Springs are appropriately accounted in the FSM modeling. Verification studies show excellent agreement with an analytical solution for global buckling. However, pre-buckling stress in FSM is different from that in an FEM model with springs, especially for beam members, resulting in different buckling prediction. Analyst should be aware of this difference.

As demonstrated herein the boundary conditions should not be mixed in the same FSM model.

## Chapter 3 Constrained finite strip method for general end boundary conditions

### 3.1 Introduction

In recent years two new approaches have provided a formal means to identify the stability of thin-walled members: Generalized Beam Theory (GBT) and the constrained Finite Strip Method (*c*FSM) see [38] for a full comparison. GBT and *c*FSM employ a series of mechanical assumptions that separate the modes. In the case of GBT the implementation is in the form of an enriched beam element transformed from nodal, to modal, degrees of freedom. In the case of *c*FSM the implementation is in the form of constraint matrices that separate the degrees of freedom into those consistent with local, distortional, and global buckling. Further, while GBT has been implemented for general boundary conditions [31, 32] *c*FSM has not. The attraction of formal identification of the buckling modes is not just a theoretical one, as design methods such as the Direct Strength Method [4] directly utilize this information to predict ultimate strength.

The existing *c*FSM implementation [26-28] is limited in its applicability to simply supported end boundary conditions. Given the successful validation of the finite strip method for general boundary conditions, namely simply-simply (*S-S*), clamped-clamped (*C-C*), simply-clamped (*S-C*), clamped-guided (*C-G*), and clamped-free (*C-F*), this chapter explores the fundamental derivations required to extend the constrained Finite

Strip Method, or *cFSM* to any boundary condition. First, the focus of the discussion is on the derivation of the constraint matrices ( $R_M$ ) appropriate for constraining the general deformation fields to global ( $G$ ), distortional ( $D$ ), local ( $L$ ), or other ( $ST/O$ ) deformations. Then, possible transformation of the constraint matrices inside each separated subspace ( $G, D, L, ST/O$ ) is discussed. These different constraint matrices are called different bases. For modal identification purposes, different normalization schemes on the basis are available and how to categorize the identification coefficients also has impacts on the participation result. Hence, recommendations on the choices for basis and normalization are discussed for automated strength prediction by establishing agreed upon methods for modal decomposition and identification.

### **3.2 Buckling mode definition**

The essential feature of *cFSM* is the separation of general deformations into those deformations consistent with Global ( $G$ ), distortional ( $D$ ), local ( $L$ ), and other ( $ST/O$ ) deformation modes. The deformation modes are defined by the mechanical assumptions inherent within each mode. These mechanical assumptions are motivated from the pioneering work of Generalized Beam Theory [31, 32] and have been successfully implemented in *FSM* for S-S boundary conditions [25-28]. The mode definitions center on the following 3 mechanical criteria:

- Criterion #1 - Vlasov's hypothesis: (a)  $(\gamma_{xy})_M = 0$ , i.e. there is no in-plane shear, (b)  $(\epsilon_x)_M = 0$ , i.e. there is no in-plane transverse strain, and (c)  $v$  is linear in  $x$  direction within a flat part (i.e. between any two fold locations).

Criterion #2 - Longitudinal warping: (a)  $v \neq 0$ , i.e. the warping displacement is not constantly equal to zero along the whole cross-section, and (b) the cross-section is in transverse equilibrium.

Criterion #3 - Undistorted section:  $\kappa_{xx} = 0$ , i.e. there is no transverse flexure.

In general, Criterion 1 may be tied to classical beam theory, or, as named - Vlasov's hypothesis. While warping is allowed, certain membrane deformations are restrained through no in-plane shear and transverse strain. In addition, even warping should be linearly distributed within a flat plate. Criterion 2 indicates that non-zero warping (longitudinal, or  $v$  deformation) should exist in the cross section. Since local plate deformations have no deformation at the center plane of the plate in longitudinal direction (only bending plate deformation), this provides a separation between local plate deformations and other deformation modes. Criterion 3 essentially relates to distortion of the cross-section. Theoretically, this provides a means to separate global from distortional buckling modes, though the separation is realized through a practical understanding about global buckling modes (of course, still satisfying this criterion) instead of checking the transverse flexure as shown later in deriving the  $R_G$  constraint matrix.

The separation of the  $G$ ,  $D$ ,  $L$ ,  $ST/O$  deformation modes are completed by implementing the above three criteria as detailed in Table 3-1. The modes implied by these criteria are in good agreement with current practice for a wide range of practical problems. However, cases exist where the applied definition leads to results not in line with current engineering practice [51].

Table 3-1 Mode classification

	<i>G</i> modes	<i>D</i> modes	<i>L</i> modes	<i>ST/O</i> modes
Criterion #1--Vlasov's hypothesis	YES	YES	YES	NO
Criterion #2--Longitudinal warping	YES	YES	NO	N/A
Criterion #3--Undistorted section	YES	NO	N/A	N/A

### 3.3 Notations and framework of constrained finite strip method

The basic notation, coordinate systems, etc. established in Chapter 2 (Figure 2-1) for conventional FSM apply here as well. Longitudinal displacements ( $V$ ) play a special role in  $c$ FSM, and owing to a shared terminology with Generalized Beam Theory are generically termed warping displacements. This may be distinguished from the transverse displacements ( $U, W, \Theta$ ) which occur in a given strip.

An additional classification for the nodes is also introduced: main nodes (at fold-lines, indicated with a subscript  $m$  without brackets) and sub-nodes (within the flats, indicated with a subscript  $s$ ) as illustrated in Figure 3-1. Therefore, the total number of nodes (or nodal lines) is  $n$ , consisting of  $nm$  main nodes and  $ns$  sub-nodes ( $nm + ns = n$ ). Also, the total number of plate elements (or strips) is  $(n-1)$  and the total number of main plate elements (or strips) is  $(nm-1)$ . For the derivations presented here the sequential node and element numbering systems depicted in Figure 3-1 is assumed. Thus, only open singly branched cross-sections are considered at this point.

Once  $X$  and  $Z$  (global) coordinates of all the  $n$  nodes, thickness ( $t$ ) of all the strips, member length ( $a$ ), and material properties are known, a member can be defined. The width and angle ( $b$  and  $\alpha$ , respectively) of the strips is calculated from the nodal

coordinates. In the following derivations individual nodes are referenced by subscripts, e.g., the  $X$  coordinate of the first nodal line is:  $X_1$ , while strips are referenced by superscripts in parentheses, e.g., the width of the last strip is:  $b^{(n-1)}$ , or the width of the last main strip is:  $b^{(nm-1)}$ .

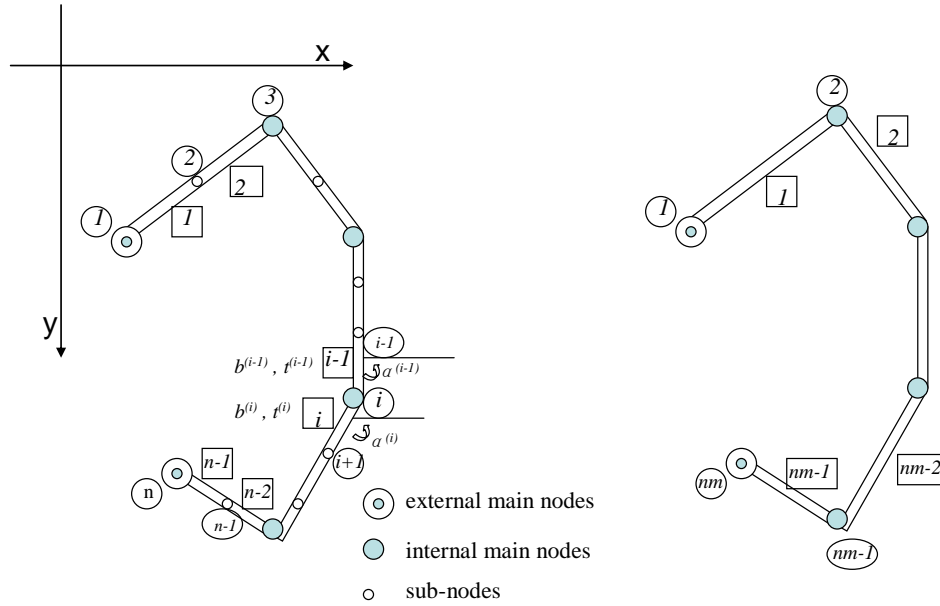


Figure 3-1 Node classification and numbering scheme

The key feature of  $cFSM$ , and similar to the work established in [26], is that the general displacement field  $d$  may be constrained to any modal space ( $G, D, L, ST/O$  or any combination) via:

$$d = R_M d_M \quad (3-1)$$

where  $R_M$  is the constraint matrix for the selected modal space(s) and  $d_M$  is the resulting deformations within that space. Note, here subscript  $M$  refers to the modal space ( $G, D, L, ST/O$  or any combination thereof) and not membrane deformations as in the stiffness matrix derivations. Also note, in the case of general boundary conditions where the longitudinal displacement fields are a series the total DOF:  $TND=4n \times q$ , instead of  $4n$

where  $q$  is the total number of  $m$  longitudinal terms included. This is obviously a significant expansion over the  $4n$  problem size of [26]. Thus  $R_M$  which in [26] is  $4n \times$ dimension of the given  $M$  space, is now  $4n \times$ dimension of the given  $M$  space  $\times q$ .  $R_M$  is the key towards applications of cFSM in terms of modal decomposition and identification.

Modal decomposition is illustrated through constraining the eigenvalue problem of Eq. (2-31). Introducing Eq. (3-1) into Eq. (2-31) and pre-multiplying by  $R_M^T$ , the constrained eigenvalue problem for mode or modes  $M$  results:

$$K_{e,M} \Phi_M = K_{g,M} \Phi_M \Lambda_M \quad (3-2)$$

where,  $K_{e,M}$  and  $K_{g,M}$  are the elastic and geometric stiffness matrix of the constrained FSM problem, respectively, and defined as  $K_{e,M} = R_M^T K_e R_M$  and  $K_{g,M} = R_M^T K_g R_M$ ;  $\Lambda_M$  is a diagonal matrix containing the eigenvalues for the given mode or modes, and  $\Phi_M$  is the matrix corresponding eigenmodes (or buckling modes) in its columns.

Combined defined constraint matrices of each subspace ( $G, D, L, ST/O$ ) span the original FSM DOF space, and provide an alternative basis organized in  $G, D, L, ST/O$ . Using this basis, any nodal displacement vector,  $d$ , (deformed shape or buckling mode) may be transformed into the basis spanned by the buckling classes, via

$$c = R^{-1}d \quad (3-3)$$

where the coefficients in  $c$  represent the contribution to a given column of basis  $R$ . The participation of each mode class is calculated based on these coefficients. However, the participation is not unique and largely depends on the choices of basis, normalization scheme of the basis, and also how to calculate the participation for each subspace given the contribution coefficients.

Systematic explanation and study of these choices influence on both modal decomposition and modal identification results has been provided in [52] for S-S stability solution represented by signature curve. Additional discussions will be expanded to general FSM solutions in this chapter.

### 3.4 Derivations of constraint matrix $R$

As discussed above, the constraint matrix plays a central role in  $c$ FSM. The constraint matrix for each buckling class ( $G$ ,  $D$ ,  $L$ , and  $ST/O$ ) is constructed by exercising the standard FSM space based on the criteria provided in Table 3-1. The same strategy as in [28] is followed. The constraint matrix  $R_{GD}$  of  $GD$  space is defined by enforcing criteria #1 and #2, and then separation of  $GD$  space into  $G$  and  $D$  is conducted by following criterion #3. Indeed, defining the constraint matrices  $R_G$  and  $R_D$  is the most challenging. The constraint matrices for  $L$  and  $ST/O$  are formed sequentially and relatively easier by employing their related criteria.

#### 3.4.1 Derivation of $R_{GD}$

##### 3.4.1.1 Implementation of Criteria #1 – Vlasov’s hypothesis

When considering Vlasov’s hypothesis, sub-nodes are disregarded and only main nodes are considered, which are assumed to be numbered from  $1$  to  $nm$ . The width of the flat plate between main nodes is denoted as  $b$ . The displacement fields are defined in terms of Eq.’s (2-1)-(2-8). Conditions (a) and (b) of Vlasov’s hypothesis implies:

$$\varepsilon_x = \frac{\partial u}{\partial x} = 0 \quad \text{and} \quad \gamma_{xy} = \frac{\partial u}{\partial y} + \frac{\partial v}{\partial x} = 0 \quad (3-4)$$

Considering  $\varepsilon_x=0$  implies:

$$\varepsilon_x = \frac{\partial u}{\partial x} = \sum_{m=1}^q \left[ -\frac{1}{b} \quad \frac{1}{b} \right] \begin{Bmatrix} u_{1[m]} \\ u_{2[m]} \end{Bmatrix} Y_{[m]} = 0 \quad (3-5)$$

where subscript 1 and 2 refer to the main node numbers, similar expressions may be derived for 2,3 etc. Noting that all  $Y_{[m]}$  are a function of  $y$  alone, and that  $y$  is arbitrarily chosen in the longitudinal direction, the coefficients of  $Y_{[m]}$  must be zero, thus:

$$u_{1[m]} = u_{2[m]} = u_{[m]} \text{ for } m=1, 2, \dots, q \quad (3-6)$$

Considering  $\gamma_{xy}=0$  implies:

$$\gamma_{xy} = \frac{\partial u}{\partial y} + \frac{\partial v}{\partial x} = \sum_{m=1}^q \left[ u_{[m]} + \left( -\frac{v_{1[m]}}{b} + \frac{v_{2[m]}}{b} \right) \frac{a}{\mu_m} \right] Y'_{[m]} = 0 \quad (3-7)$$

Again  $Y_{[m]}$ , or  $Y'_{[m]}$  in this case, must be zero for this condition to be met, resulting in:

$$u_{1[m]} = u_{2[m]} = u_{[m]} = (v_{1[m]} - v_{2[m]}) \frac{1}{bk_{[m]}} \text{ for } m=1, 2, \dots, q \quad (3-8)$$

where  $k_{[m]} = \mu_{[m]}/a = m\pi/a$ . Thus, the derivation is identical to [26] with the exception that the notation now incorporates the  $m$  half-waves employed. The local displacements are transferred to global displacements via Eq. (2-27); note local  $v$  is equal to global  $V$  (i.e.  $v=V$ ). Utilizing connectivity of the strips all of the global  $U$  and  $W$  (at the main nodes) may be written in terms of the warping displacement  $V$ . The procedure is identical to [26] and provided explicitly in [48] the result of enforcing (a) and (b) of Vlasov's hypothesis may be expressed as:

$$U_{m[m]} = \frac{1}{k_{[m]}} S_1 V_{m[m]} \text{ and } W_{m[m]} = -\frac{1}{k_{[m]}} C_1 V_{m[m]} \quad (3-9)$$

where  $U_{m[m]}$  and  $W_{m[m]}$  are  $(mn-2)$  element vectors with the  $U$  and  $W$  DOF for internal main nodes from 2 to  $(nm-1)$  corresponding to longitudinal term  $m$ ,  $V_{m[m]}$  is an  $nm$

element vector with the  $V$  warping displacements of the main nodes corresponding to longitudinal term  $m$ , while  $S_I$  and  $C_I$  are  $(nm-2) \times nm$  matrices containing only basic cross-section geometry data. Explicit expressions of  $S_I$  and  $C_I$  are provided in the following:

$$S_I = \begin{bmatrix} \left(\frac{\sin \alpha^{(2)}}{D_2 b^{(1)}}\right) & \left(-\frac{\sin \alpha^{(2)}}{D_2 b^{(1)}} - \frac{\sin \alpha^{(1)}}{D_2 b^{(2)}}\right) & \left(\frac{\sin \alpha^{(1)}}{D_2 b^{(2)}}\right) & 0 & 0 & 0 & 0 & 0 \\ 0 & \left(\frac{\sin \alpha^{(3)}}{D_2 b^{(2)}}\right) & \left(-\frac{\sin \alpha^{(3)}}{D_2 b^{(2)}} - \frac{\sin \alpha^{(2)}}{D_2 b^{(3)}}\right) & \left(\frac{\sin \alpha^{(2)}}{D_2 b^{(3)}}\right) & 0 & 0 & 0 & 0 \\ \vdots & \vdots \\ 0 & 0 & 0 & 0 & \times & \times & \times & 0 \\ 0 & 0 & 0 & 0 & 0 & \times & \times & \times \end{bmatrix} \quad (3-10)$$

$$C_I = \begin{bmatrix} \left(\frac{\cos \alpha^{(2)}}{D_2 b^{(1)}}\right) & \left(-\frac{\cos \alpha^{(2)}}{D_2 b^{(1)}} - \frac{\cos \alpha^{(1)}}{D_2 b^{(2)}}\right) & \left(\frac{\cos \alpha^{(1)}}{D_2 b^{(2)}}\right) & 0 & 0 & 0 & 0 & 0 \\ 0 & \left(\frac{\cos \alpha^{(3)}}{D_2 b^{(2)}}\right) & \left(-\frac{\cos \alpha^{(3)}}{D_2 b^{(2)}} - \frac{\cos \alpha^{(2)}}{D_2 b^{(3)}}\right) & \left(\frac{\cos \alpha^{(2)}}{D_2 b^{(3)}}\right) & 0 & 0 & 0 & 0 \\ \vdots & \vdots \\ 0 & 0 & 0 & 0 & \times & \times & \times & 0 \\ 0 & 0 & 0 & 0 & 0 & \times & \times & \times \end{bmatrix} \quad (3-11)$$

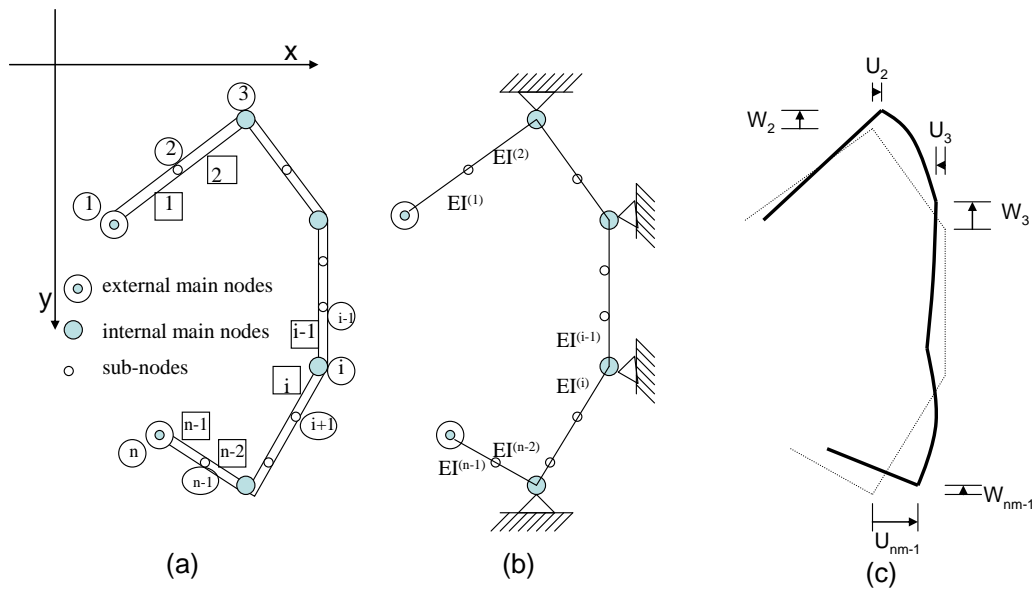
The last feature of Vlasov's hypothesis is that the warping displacements must be linear across the main nodes. The selected shape function implicitly ensures linearity across a strip. Thus the sub-node warping displacements (subscript  $s$ ) are calculated by linear interpolation:

$$V_{s[m]} = B_v V_{m[m]} \quad (3-12)$$

where,  $V_{s[m]}$  is a vector of the warping displacements of the sub-nodes corresponding to the half-wave number  $m$ , and the elements of matrix  $B_v$  are solely calculated from the strip widths, as in [26]. Note, Vlasov's hypothesis does provide certain restriction on the external main nodes, but these are handled subsequently in the derivation.

### 3.4.1.2 Implementation of Criteria #2 – longitudinal warping

The second formal mechanical criterion states: (a) warping must be non-zero, and (b) any transverse displacements must be in equilibrium within a cross-section [28, 48]. Given Vlasov’s hypothesis as embodied in Eq. (3-9), if warping displacements,  $V$ , are non-zero then non-zero transverse displacements,  $U$  and  $W$ , at the main nodes will result. To achieve (b) which requires equilibrium in the transverse cross-section, the  $U_m$  and  $W_m$  at the main nodes are applied as kinematic displacements to an equivalent multi-span beam model of the cross-section, as depicted in Figure 3-2. This must be completed for each  $m$  term, i.e. for  $q$  cross-sections.



(a) cross section (b) equivalent multi-span beam (c) displacements at main nodes

Figure 3-2 Cross-section model for enforcement of Criterion #2

In previous work, i.e. [26, 28], the kinematic displacements at the main nodes  $U_m$  and  $W_m$  were solved for only a single longitudinal term, i.e. for only one cross-section. However, for general boundary conditions as implied in Eq.’s (2-1)-(2-8):



where  $I_1 = \int_0^a Y_{[m]} Y_{[n]} dy$ , see Eq. (16) for other terms.

The local strip is transformed to global coordinates and assembly performed. Thus, equilibrium of the cross-section in the transverse direction is embodied in the matrix stiffness expression:

$$K_{e,t} d_t = q_t \quad (3-15)$$

where  $K_{e,t}$  is the global stiffness matrix,  $d_t$  is the displacement vector of the displacements ( $U$ ,  $W$ ,  $\Theta$ ) of the equivalent beam, and  $q_t$  is the vector of the nodal forces for the same DOFs. The kinematic displacements at the main nodes  $U_m$  and  $W_m$  are shown in Eq. (3-13) for general boundary conditions. Therefore,  $d_t$  should also take the form similar to Eq. (3-13) which is a summation over longitudinal terms:

$$d_t = \sum_{m=1}^q (d_t)_{[m]} Y_{[m]} \quad (3-16)$$

Eq. (3-15) is expanded into known,  $k$ , and unknown,  $u$ , displacements and forces.

$$\begin{bmatrix} K_{e,t,kk} & K_{e,t,ku} \\ K_{e,t,uk} & K_{e,t,uu} \end{bmatrix} \begin{bmatrix} d_{t,k} \\ d_{t,u} \end{bmatrix} = \begin{bmatrix} q_{t,k} \\ q_{t,u} \end{bmatrix} \quad (3-17)$$

where the known displacements  $d_{t,k}$  are at the main nodes:  $U_m$  and  $W_m$ , and the unknown displacements  $d_{t,u}$  are the remaining  $U_s$ ,  $W_s$  at the sub-nodes and all  $\Theta$  DOF. Recognizing that no external forces are applied and expanding the lower portion:

$$K_{e,t,uk} d_{t,k} + K_{e,t,uu} d_{t,u} = 0 \quad (3-18)$$

Substituting the known and unknown displacements of Eq. (3-16) into Eq. (3-18), it can be rewritten as:

$$\sum_{m=1}^q \left( K_{e,t,uk} (d_{t,k})_{[m]} + K_{e,t,uu} (d_{t,u})_{[m]} \right) Y_{[m]} = 0 \quad (3-19)$$

Since the transverse stress resultants should be in equilibrium of any cross section in the longitudinal direction, the coefficient of  $Y_{[m]}$  must be zero, which leads to

$$(d_{t,u})_{[m]} = -K_{e,t,uu}^{-1} K_{e,t,uk} (d_{t,k})_{[m]} \text{ for } m=1, \dots, q \quad (3-20)$$

Or in more explicit form:

$$\begin{bmatrix} U_{s[m]} \\ W_{s[m]} \\ \Theta_{[m]} \end{bmatrix} = -K_{e,t,uu}^{-1} K_{e,t,uk} \begin{bmatrix} U_{m[m]} \\ W_{m[m]} \end{bmatrix} \text{ for } m=1, \dots, q \quad (3-21)$$

Thus, all terms which satisfy Eq. (3-21) meet part (b) of the criterion #2. As a practical matter this may be completed term-by-term as suggested above, or  $K_{e,t}$  may be assembled into a global matrix including all  $q$  terms.

### 3.4.1.3 Assembly of $R_{GD}$

Recall that the constraint matrices represent the means by which the mechanical criteria of Table 1 are enforced on the general FSM displacement fields (vectors). In the case of the  $GD$  space (of particular importance because it reflects the fundamental space for GBT and in essence all deformations consistent with even expanded beam theories) the requirement is that criteria #1 and #2 are enforced. Criterion #3 will be employed to separate  $G$  and  $D$ . The strategy of assembling  $R_{GD}$  is outlined as follows: 1) assemble  $[R_{GD}]_{[m]}$  for each longitudinal term,  $m$ ; 2) assemble each  $[R_{GD}]_{[m]}$  into the larger  $R_{GD}$ . Note, each  $[R_{GD}]_{[m]}$  has sub-matrices as given below:

$$[R_{GD}]_{[m]} = \begin{bmatrix} R_{GD,Vm[m]}^T & R_{GD,Vs[m]}^T & R_{GD,Um[m]}^T & R_{GD,Wm[m]}^T & R_{GD,Us[m]}^T & R_{GD,Ws[m]}^T & R_{GD,\Theta[m]}^T \end{bmatrix} \quad (3-22)$$

Based on the derivations of the preceding two sections, the submatrices in  $[R_{GD}]_{[m]}$  are determined as follows, and follow directly from [26]. For  $R_{GD,Vm[m]}$ , the selection is arbitrary for the construction of  $R_{GD}$ , thus the simplest solution is set  $R_{GD,Vm[m]}$  equal to the  $nm$ -order identity matrix:

$$R_{GD,Vm[m]} = I \quad (3-23)$$

For  $R_{GD,Vs[m]}$  the sub-node warping displacements ( $V_{s[m]}$ ) follow from Eq. (3-12):

$$R_{GD,Vs[m]} = B_v R_{GD,Vm[m]} \quad (3-24)$$

Vlasov's hypothesis provides  $R_{GD,Um[m]}$  and  $R_{GD,Wm[m]}$  in the form of Eq. (3-9):

$$R_{GD,Um[m]} = \frac{1}{k_{[m]}} S_1 R_{GD,Vm[m]} \quad \text{and} \quad R_{GD,Wm[m]} = \frac{1}{k_{[m]}} C_1 R_{GD,Vm[m]} \quad (3-25)$$

Finally enforcing equilibrium at the cross-section level provides the remaining DOF, and thus  $R_{GD,Us[m]}$ ,  $R_{GD,Ws[m]}$ , and  $R_{GD,\Theta[m]}$  are determined from Eq. (3-21):

$$\begin{bmatrix} R_{GD,Us[m]} \\ R_{GD,Ws[m]} \\ R_{GD,\Theta[m]} \end{bmatrix} = K_{e,t,uu}^{-1} K_{e,t,uk} \begin{bmatrix} R_{GD,U[m]} \\ R_{GD,W[m]} \end{bmatrix} \quad (3-26)$$

Therefore,  $[R_{GD}]_{[m]}$  may be obtained from its partitions, and  $R_{GD}$  may be assembled for each longitudinal term as a partitioned diagonal matrix:

$$R_{GD} = \begin{bmatrix} [R_{GD}]_{[1]} & & & \\ & \ddots & & \\ & & [R_{GD}]_{[m]} & \\ & & & \ddots \\ & & & & [R_{GD}]_{[q]} \end{bmatrix} \quad (3-27)$$

#### 3.4.1.4 Separation of $R_{GD}$ into $R_G$ and $R_D$

Criterion #3 of Table 1 states that the only difference between the  $G$  and  $D$  space is whether or not the cross-section distorts. The  $GD$  space is characterized by the fact that

warping displacements at the main nodes ( $V_{m[m]}$ ) fully define the displacement field. Thus, the separation of  $G$  and  $D$  represents the determination of which  $V_{m[m]}$  lead to cross-section distortion, and which do not.

As discussed previous, instead of mathematically exercising criterion  $\kappa_{xx} = 0$ , the  $G$  space is understood to be spanned by 4 warping deformation fields: pure axial, bending about any two non-coincident axes, and torsion. The remaining  $V_{m[m]}$  (size  $nm-4$  DOF) span the  $D$  space, which may be organized arbitrarily, though enforcing orthogonality is convenient as shown in [26-28]. In addition, when  $nm \leq 4$ , cross-section like L, T, and X has no remaining  $D$  space. These cross-sections have their shear center exactly at the only internal main node. Consequentially, the warping function for pure torque is constantly zero over the whole cross section. In this sense, there are only three global buckling modes left for these cross-sections and the pure torsional buckling mode will take place among local buckling modes [51].

To utilize the above information we seek a transformation matrix,  $H_{GD}$ , such that:

$$H_{GD} = [H_G \quad H_D], \text{ and } d_{GD} = [H_G \quad H_D] \begin{bmatrix} d_G \\ d_D \end{bmatrix} \quad (3-28)$$

Introduction of this definition into Eq. (3-1), results in:

$$d = R_{GD} [H_G \quad H_D] \begin{bmatrix} d_G \\ d_D \end{bmatrix} = [R_G \quad R_D] \begin{bmatrix} d_G \\ d_D \end{bmatrix} \quad (3-29)$$

As shown, construction of  $R_{GD}$ ,  $H_G$ , and  $H_D$  lead to the separated  $R_G$  and  $R_D$  constraint matrices, which are desired. Accordingly, construction of  $H$  is performed for each longitudinal term  $m$ . Since warping vectors for each longitudinal term are

proportional to each other and the magnitude can be any value,  $[H_G]_{[m]}$  is assigned the same for all longitudinal terms  $m$ .

Calculations of  $[H_G]_{[m]}$  and  $[H_D]_{[m]}$  are the same as in [28].  $[H_G]_{[m]}$  are the warping vectors defined by the warping distributions of the four global buckling modes (one axial mode, two bending modes, and one torque mode). The warping distributions of these four modes are illustrated in Figure 3-3 for a channel section. Note, the dimensions and properties of the channel section are not provided for the concept of these distributions is the important thing for this illustration. Also note,  $G$  modes may be defined about principle axes or about geometric axes. Also the pure torsion mode does not have to be about the shear center, although CUFSM (and GBT) do choose to do this.

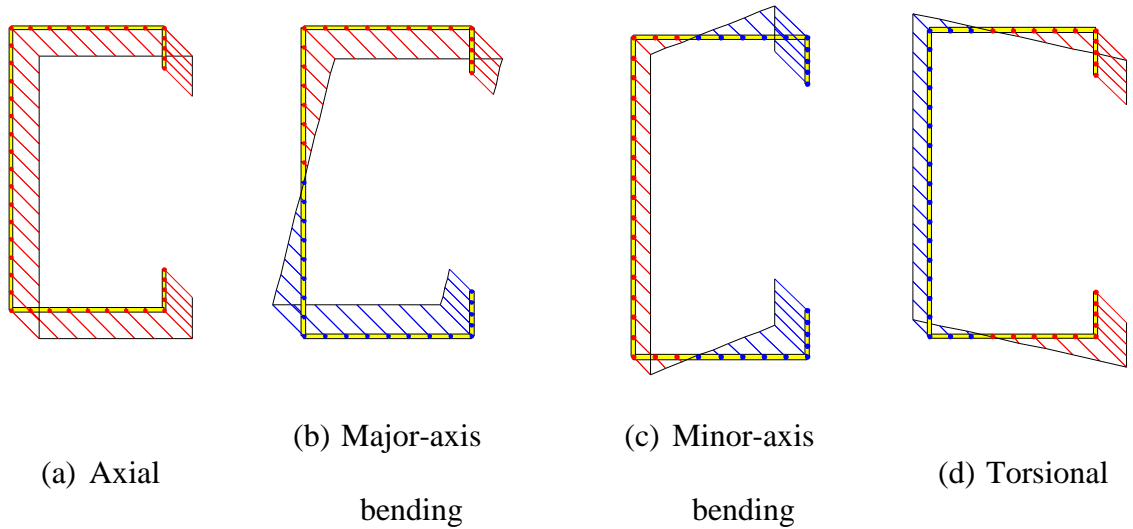


Figure 3-3 Warping vectors of four global modes

$[H_D]_{[m]}$  is found by enforcing orthogonality to the  $G$  space within  $GD$ , the orthogonality condition follows the one used in GBT:

$$\int v_i(x)v_j(x)t(x)dx = 0 \quad (3-30)$$

where the integral is over the whole cross-section,  $t(x)$  is the thickness, while  $v_i(x)$  and  $v_j(x)$  are two arbitrary warping functions of the  $G$  and  $D$  space, respectively. Finally, this leads to the following condition by integrating over the cross-section:

$$[H_D]_{[m]}^T A [H_G]_{[m]} = 0 \quad (3-31)$$

where  $A$  is a matrix containing only cross section information. Hence,  $[H_D]_{[m]}$  is also the same for all the longitudinal terms.

Specifically,  $R_{GD}$  is a partitioned diagonal matrix with  $q$ ,  $n \times nm$  submatrices, where  $q$  is the total number of longitudinal terms, thus the complete dimension is  $(q n) \times (q nm)$ . Similarly,  $H_G$  is a partitioned diagonal matrix populated with  $q$ ,  $nm \times 4$  submatrices, and  $H_D$  with  $q$   $nm \times (nm-4)$  submatrices. Consequentially, the resulting constraint matrices of  $R_G$  and  $R_D$  are also partitioned diagonal matrices with  $q n \times 4$  and  $n \times (nm-4)$  submatrices in the diagonal (similar to Eq. (3-27)), respectively.

### 3.4.2 Derivation of $R_L$

Determination of the  $L$  space (and  $R_L$ ) is based on criteria established in Table 1: Vlasov's hypothesis is enforced, there is no longitudinal warping, and the transverse cross-section does not have to be in equilibrium. Vlasov's hypothesis connects  $U$  and  $W$  of the main nodes to the warping displacement of the main nodes  $V$ . Specifically, since  $V_{m[m]}$  is zero,  $U_{m[m]}$  and  $W_{m[m]}$  must also be zero. The condition of no warping at the main nodes and linear warping distributions also implies no warping for the sub-nodes, therefore  $V_{s[m]}$  is zero. Thus, for the  $L$  space:

$$R_{L[m]} = \left[ R_{L,V_{m[m]}}^T \quad R_{L,V_{s[m]}}^T \quad R_{L,U_{m[m]}}^T \quad R_{L,W_{m[m]}}^T \quad R_{L,U_{s[m]}}^T \quad R_{L,W_{s[m]}}^T \quad R_{L,\Theta_{m[m]}}^T \right]^T \quad (3-32)$$

$$R_{L,V_{m[m]}} = [0], R_{L,V_{s[m]}} = [0], R_{L,U_{m[m]}} = [0] \text{ and } R_{L,W_{m[m]}} = [0] \quad (3-33)$$

The remaining displacements are local  $w$  of the sub-nodes, local  $w$  of the external main nodes, and  $\theta$  at all nodes. Transformation of the local  $w$  implies global displacements of the sub-nodes:  $U_{s[m]}$  and  $W_{s[m]}$ . Thus, for the  $L$  space:

$$R_{L,U_{s[m]}} = [S_3 \quad 0], R_{L,W_{s[m]}} = [C_3 \quad 0], \text{ and } R_{L,\Theta[m]} = [0 \quad I] \quad (3-34)$$

where,  $S_3$  and  $C_3$  are diagonal matrices (both with  $(ns+2) \times (ns+2)$  dimension),  $I$  is the an  $n \times n$  identity matrix, and  $S_3$  is expressed as  $diag(-\sin\alpha_1, -\sin\alpha_2, \dots)$ , and  $C_3$  as  $diag(\cos\alpha_1, \cos\alpha_2, \dots)$ . Note,  $\alpha_i$  is the strip angle at the location of the given  $i$ -th node, and for sub-nodes the strip angle is the same for both nodes in the strip, by definition. Finally, the full  $R_L$  matrix, a partitioned diagonal matrix similar to Eq. (3-27), is constructed for all  $m$  terms from the  $R_{L[m]}$  sub-matrices.

### 3.4.3 Derivation of $R_{ST}/R_O$

The applicable criterion for the  $ST/O$  space is that Vlasov's hypothesis may be violated: transverse strains and/or the in-plane shear are non-zero, and a non-linear warping distribution between main nodes may exist. From a mechanical point of view like in GBT, this space includes the shear and transverse extension modes. In addition, this space is essentially a space exclusive of the  $GDL$  space but within the standard FSM space – a null space of  $GDL$  space mathematically. Therefore, there are two approaches we can use to define this space [28]: 1) define a set of independent vectors with unit transverse extensions (the  $T$  space,  $R_T$ ) and unit shear deformations (the  $S$  space,  $R_S$ ); 2) employing a more mathematically approach, defined directly as the null space of  $GDL$  (the  $O$  space,  $R_O$ ). Null space of matrix  $A$  is a set of all vectors  $x$  for which  $Ax=0$  in linear algebra.

For the  $ST$  space,  $S$  and  $T$  may be formed from strip-wise shear and transverse extension. However, different strategies lead to slightly different  $R_S$  and  $R_T$  spaces, e.g. +1,-1 for  $v$  in a strip, or +1, 0 for  $v$  in a strip. Though  $S$  and  $T$  spaces are defined separately, there is not much practical importance for this separation. Therefore, the  $ST$  space ( $R_{ST}$ ) a union of  $S$  and  $T$  spaces is considered as a whole in most applications.

For the  $O$  space, a more mathematical approach is employed and  $R_O$  is defined as the null space of the  $GDL$  space. Orthogonalization against the  $GDL$  space may be in terms of  $K_e$ ,  $K_g$ , or in a vector sense, via:

$${}^e R'_O \left[ K_e \right]_m \left[ R_{GDL} \right]_m = 0, \quad {}^g R'_O \left[ K_g \right]_m \left[ R_{GDL} \right]_m = 0, \quad {}^v R'_O \left[ R_{GDL} \right]_m = 0 \quad (3-35)$$

$${}^e R_O^T K_e R_{GDL} = 0, \quad {}^g R_O^T K_g R_{GDL} = 0, \quad \text{or} \quad {}^v R_O^T R_{GDL} = 0 \quad (3-36)$$

Since  $K_e$ ,  $K_g$  and  $R_{GDL}$  are known, the constraint matrix  ${}^e R_O$ ,  ${}^g R_O$  and  ${}^v R_O$  are respectively defined (as strain energy orthogonal, work orthogonal, and vector orthogonal) although they are not unique. It is worth mentioning that  $K_e$  is the elastic stiffness matrix, and  $K_g$  is the geometric stiffness matrix when the cross-section is under axial compression. The  $O$  basis obtained through Eq. (3-35) implies the  $O$  modes are defined within each longitudinal term, without consideration of the potential coupling among longitudinal terms, and is referred to as  ${}^e R'_O$ ,  ${}^g R'_O$ , and  ${}^v R'_O$ , which are all partitioned diagonal matrices. However,  $O$  modes defined by Eq. (3-36) include all the longitudinal terms (up to  $q$ ); thus the problem size is significantly enlarged. Since the  $K_e$  and  $K_g$  matrices are not partitioned diagonal matrices for non-simply supported boundary conditions, the  $O$  spaces defined with respect to them are no longer a block diagonal matrix as shown in Eq. (3-27) because of the coupling between the longitudinal terms.

Instead, it is a fully populated matrix,  $(4 \times n \times q) \times (4 \times n \times q)$ , where  $n$  is total nodes and  $q$  is the total longitudinal terms.

The other mode spaces defined above ( $R_{ST}$  and all kinds of  $R_O$ ) are all equivalent. They may lead to slight different results in modal decomposition and identification. Recommendation based on numerical studies will be made later in this chapter.

### 3.5 Bases

Combined, the defined constraint matrices of each buckling mode classes ( $G, D, L, ST/O$ ) span the FSM space and represent a transformation inside the standard FSM space. In fact, they form an alternative basis of the standard FSM space organized in  $G, D, L$ , and  $ST/O$ . While the  $R_G, R_D, R_L, R_{ST}/R_O$  matrices define the  $G, D, L$ , and  $ST/O$  spaces, transformation of the bases inside those spaces is also still possible, and potentially desirable.

#### 3.5.1 Natural basis

In the constrained Finite Strip Method the initial separation of the general deformations into the  $G, D, L, ST/O$  spaces employ what is termed as the natural basis. The full derivation of the natural basis has been illustrated in Section 3.4 by examining the associated mechanical definitions of each subspace  $G, D, L$ , and  $ST/O$ . In a practical manner, the constraint matrix for  $G, D, L$ , and  $ST/O$  can be constructed for each longitudinal term,  $m$ , individually as demonstrated in the derivation. Note,  $O$  space should be defined by Eq. (3-35) excluding the potential coupling between longitudinal terms. Thus, the constraint matrix  $R$  including  $G, D, L$ , and  $ST/O$  is a partitioned diagonal matrix as shown below:

$$R = \begin{bmatrix} [R]_{[11]} & & & \\ & \ddots & & \\ & & [R]_{[mm]} & \\ & & & \ddots & \\ & & & & [R]_{[qq]} \end{bmatrix} \quad (3-37)$$

where submatrix  $[R]_{[m]}$  is the constraint matrix corresponding to longitudinal term  $m$ , and consists of four sub-matrices  $[[R_G]_{[m]} [R_D]_{[m]} [R_L]_{[m]} [R_{ST}]_{[m]} / [R_O]_{[m]}]$ .

However, for constraint matrix of  $O$  space defined by Eq. (3-36) considering the potential coupling between longitudinal terms, the constraint matrix  $R$  including  $G$ ,  $D$ ,  $L$ , and  $ST/O$  is a fully populated matrix.

$$R = \begin{bmatrix} [R]_{[11]} & \cdots & [R]_{[1q]} \\ \vdots & [R]_{[mm]} & \vdots \\ [R]_{[q1]} & \cdots & [R]_{[qq]} \end{bmatrix} \quad (3-38)$$

Each sub-matrix is organized in a similar manner as the sub-matrices in Eq. (3-37), and consist of four sub-matrices. However, in this case, only sub-matrix  $[R_O]_{[mm]}$  of the four sub-matrices is nonzero for the off-diagonal sub-matrices in Eq. (3-38).

The natural basis has its own attractiveness because it is a straightforward enforcement of the mechanical criteria underlying each mode. Further, the natural basis defines the subspaces of  $G$ ,  $D$ ,  $L$  and  $ST/O$ , which are essential to the constrained eigenvalue problem. However, the natural basis is not similar to the modal spirit of GBT and thus an alternative basis is also explored.

### 3.5.2 Modal basis

Suppose the constrained eigenvalue problem is solved within a certain subspace ( $G$ ,  $D$ ,  $L$  or  $ST/O$ ) defined with the natural basis. The resulting eigenvector spans the original natural basis subspace. Thus the new spanned subspace can be seen as another base system for the same subspace. One important characteristic of this new base system is that the base vectors of each subspace ( $G$ ,  $D$ ,  $L$  and  $ST/O$ ) are orthogonal to each other, with respect to the elastic (or geometric) stiffness matrix. Also, it has some physical appeal, similar to GBT, in that only a few basis vectors may be needed within a subspace since the deformations involve the full cross-section.

The modal basis is defined through the constrained eigenvalue solution  $M$  – each subspace. Depending on the loading conditions the eigenvalue solution varies and accordingly the orthogonal base system. Therefore, the modal basis can be defined by using the simplest loading: axial compression (axial modal basis) or the applied loading on the member (applied modal basis). The constrained eigenvalue problem is the same as in Eq. (3-2) except that the load condition is axial compression for the axial modal basis and subscript  $M$  is uniquely within each subspace ( $G$ ,  $D$ ,  $L$ , or  $ST/O$ ). The elastic and geometric stiffness matrices are populated with off-diagonal sub-matrices for non-simply supported boundary conditions, thus the stability solution is coupled with the longitudinal terms even within the pure modes. Consequently, the modal basis can be defined either with consideration of the coupling effect or not.

#### 3.5.2.1 Uncoupled modal basis

Construction of the uncoupled modal basis is basically the same as in [6] except that the constrained eigenvalue problem is solved repeatedly for all the longitudinal terms

included and the column length is the physical length instead of the unit length. Consequently, for each subspace, the orthogonal axial modes can be expressed as follows:

$$\left( [R_M^T]_{[m]} [K_e]_{[m]} [R_M]_{[m]} - \Gamma [R_M^T]_{[m]} [K_g (\sigma = 1)]_{[m]} [R_M]_{[m]} \right) [\Phi_M]_{[m]} = 0 \quad (3-39)$$

and the axial modal basis itself is constructed from

$$[\bar{R}_M]_{[m]} = [R_M]_{[m]} [\Phi_M]_{[m]} \quad (3-40)$$

The physical result of this methodology is that the pure modes ( $G$ ,  $D$ ,  $L$ , or  $O/ST$ ) are only orthogonal within each longitudinal term.

If the constrained eigenvalue problem in Eq. (3-39) is solved for the applied loading instead of the axial uniform loading, the applied modal basis can be constructed with these eigenvectors as given below:

$$[\tilde{R}_M]_{[m]} = [R_M]_{[m]} [\Phi_M]_{[m]} \quad (3-41)$$

### 3.5.2.2 Coupled modal basis

If the longitudinal coupling effect is considered, the orthogonality of the pure modes for each subspace  $M$  is no longer just within each longitudinal term. Thus, the new orthogonal axial modes can be expressed as follows:

$$\left( R_M^T K_e R_M - \Gamma R_M^T K_g (\sigma = 1) R_M \right) \Phi_M = 0 \quad (3-42)$$

The associated axial modal basis for each subspace  $M$  ( $G$ ,  $D$ ,  $L$ , or  $O/ST$ ) with each longitudinal term is expressed as following:

$$\bar{R}_M = R_M \times \Phi_M \quad (3-43)$$

Similar to the definition of  $R_O$  in Eq. (3-36), the axial modal basis  $\bar{R}$  defined here are no longer partitioned diagonal matrices.

For applied modal basis  $\tilde{R}_M$ , it can be constructed by using the eigenvectors of the similar constrained eigenvalue problem with applied loading instead of the axial uniform loading.

### 3.5.3 Summary of the bases

The natural basis is essential to cFSM, though it lacks of physical appeal, while the modal basis requires extra computational effort, but has more attractive physical appeal. The potential basis choices are summarized in Table 2. Details of how to define the subspaces ( $G$  and  $ST$ ) in natural basis are appended, which have negligible impact on the solutions (i.e. modal decomposition and identification) though conceptually different.

Table 3-2 Summary of the bases

Subspaces	Orthogonalization in subspaces				
	Natural basis (not orthogonal)	Modal basis (orthogonal)			
		Uncoupled <sup>(c)</sup>	Axial		Applied
	Uncoupled		Coupled	Uncoupled	Coupled
GD	$R_{GD}$	$[\bar{R}_{GD}]_m$	$\bar{R}_{GD}$	$[\tilde{R}_{GD}]_m$	$\tilde{R}_{GD}$
G	$R_G^{(a)}$	$[\bar{R}_G]_m$	$\bar{R}_G$	$[\tilde{R}_G]_m$	$\tilde{R}_G$
D	$R_D$	$[\bar{R}_D]_m$	$\bar{R}_D$	$[\tilde{R}_D]_m$	$\tilde{R}_D$
L	$R_L$	$[\bar{R}_L]_m$	$\bar{R}_L$	$[\tilde{R}_L]_m$	$\tilde{R}_L$
ST/O	Shear+Trans. ext. <sup>(b)</sup> $R_{ST} = R_S \cup R_T$	$[\bar{R}_S]_m \cup [\bar{R}_T]_m$	$\bar{R}_S \cup \bar{R}_T$	$[\tilde{R}_S]_m \cup [\tilde{R}_T]_m$	$\tilde{R}_S \cup \tilde{R}_T$
	Null of GDL $[{}^e R_O]_m$ or $[{}^g R_O]_m$ or $[{}^v R_O]_m$	$[{}^e \bar{R}_O]_m$ or $[{}^g \bar{R}_O]_m$ or $[{}^v \bar{R}_O]_m$	${}^e \bar{R}_O$ or ${}^g \bar{R}_O$ or ${}^v \bar{R}_O$	$[{}^e \tilde{R}_O]_m$ or $[{}^g \tilde{R}_O]_m$ or $[{}^v \tilde{R}_O]_m$	${}^e \tilde{R}_O$ or ${}^g \tilde{R}_O$ or ${}^v \tilde{R}_O$

- (a) G modes may be defined about principle axes or about geometric axes. Also pure torsion mode does not have to be about shear center, though CUFSM (and GBT) does choose to do this.
- (b) S and T may be formed from strip-wise shear and transverse extension, e.g. +1,-1 for  $v$  in a strip, or +1,0 for  $v$  in a strip leading to different S and T spaces. It is (1,0) in our definition.
- (c) Uncoupled basis means the null space of GDL or the orthogonalization is performed inside each longitudinal term  $m$ . The resulted basis is a block diagonal matrix. Coupled natural basis refers to  $R_o = {}^e R_o$  or  ${}^g R_o$  or  ${}^v R_o$  while GDL spaces are the same.

For natural and modal bases (whether coupled or uncoupled), there are several choices of other space definitions ( $ST/O$ ). In the current literature, and as provided in the previous implementation of CUFSM (version 3.12), the solution space is within one longitudinal term so no distinction between uncoupled and coupled bases is necessary. Note, with the preceding notation all currently existing  $c$ FSM basis definitions (only involving a single longitudinal term  $m$ ) may now be defined for general end boundary conditions, the:

- natural base system ( $R_G, R_D, R_L$ , and  $R_{ST}$ ),
- partially orthogonal axial modal basis ( $\bar{R}'_G, \bar{R}'_D, \bar{R}'_L$ , and  $\bar{R}'_{ST}$ ), and
- fully orthogonal axial modal basis ( $\bar{R}'_G, \bar{R}'_D, \bar{R}'_L$ , and  ${}^e\bar{R}'_O$ ).

Note, the above base systems follow the original notions in previous  $c$ FSM. For general end boundary conditions, partially or fully orthogonal are obsolete. Here the focus is on natural basis, axial modal basis or applied modal basis, coupled or uncoupled versus of said bases.

Obviously, other basis set choices are possible depending mainly on the selection of other space definitions ( $ST/O$ ).

### 3.6 Normalizations

For modal identification purpose, base vectors ought to be appropriately normalized to provide uniform classification results.

The contribution coefficients ( $c$ ) in Eq. (3-3) are dependent on the normalization (i.e. scaling) of the base vectors (columns of  $R$ ,  $\bar{R}$ , or  $\tilde{R}$ ). Normalization may be achieved in a variety of ways. In existing work [25, 28], three options have been consistently pursued:

vector norm; strain energy norm; and work norm. If  $R_i$  is the  $i^{\text{th}}$  column base vector of the natural basis  $R$  (here we only use natural basis  $R$  to illustrate the definitions) the normalizations are mathematically defined as:

- *vector norm*: normalized by setting  $\|R_i\| = 1$ ,
- *strain energy norm*: normalized by setting  $\sqrt{R_i^T K_e R_i} = 1$ , and,
- *work norm*: normalized by setting  $\sqrt{R_i^T \bar{K}_g R_i} = 1$ .

where,  $K_e$  is the elastic stiffness matrix and  $\bar{K}_g$  is the geometric stiffness matrix based axial uniform loading as shown in Eq. (3-39) or (3-42).

Given the rather extensive set of potential possibilities, based on bases and normalization, Table 3-3 provides a full summary. Note, in Table 3-3, the basis could be coupled or uncoupled basis.

### 3.7 Modal decomposition

As briefly mentioned in Section 3.3, with the constraint matrix in place, it is possible to decompose the modes to a specific class or even to a single buckling mode by solving the constrained eigenvalue problem of Eq. (3-3). For general boundary conditions, the procedure is the same as the existing *c*FSM except the  $m$  longitudinal terms should be included, which consequently enlarges the problem size.

To illustrate the capability of *c*FSM for general boundary conditions, the  $G$ ,  $D$ , and  $L$  modes are decomposed from the general FSM solution using the natural basis described before and the critical loads are plotted in Figure 3-4 against the general FSM solution for SSMA stud section 250S137-68 [49] under axial compression with *C-C* boundary

conditions. The total number of  $m$  longitudinal terms included in the FSM or  $c$ FSM solution is 36. Note, although several bases are defined in Section 3.5, the decomposed solution inside a mode class ( $G$ ,  $D$ , and  $L$ ) is independent of the selection of bases and also whether it is normalized or not. Corresponding generalized beam theory (GBT) solutions are also given in Figure 3-4. Though GBT enriches the cross section deformation with modal based degree of freedom finite element discretization is employed to represent the longitudinal field.

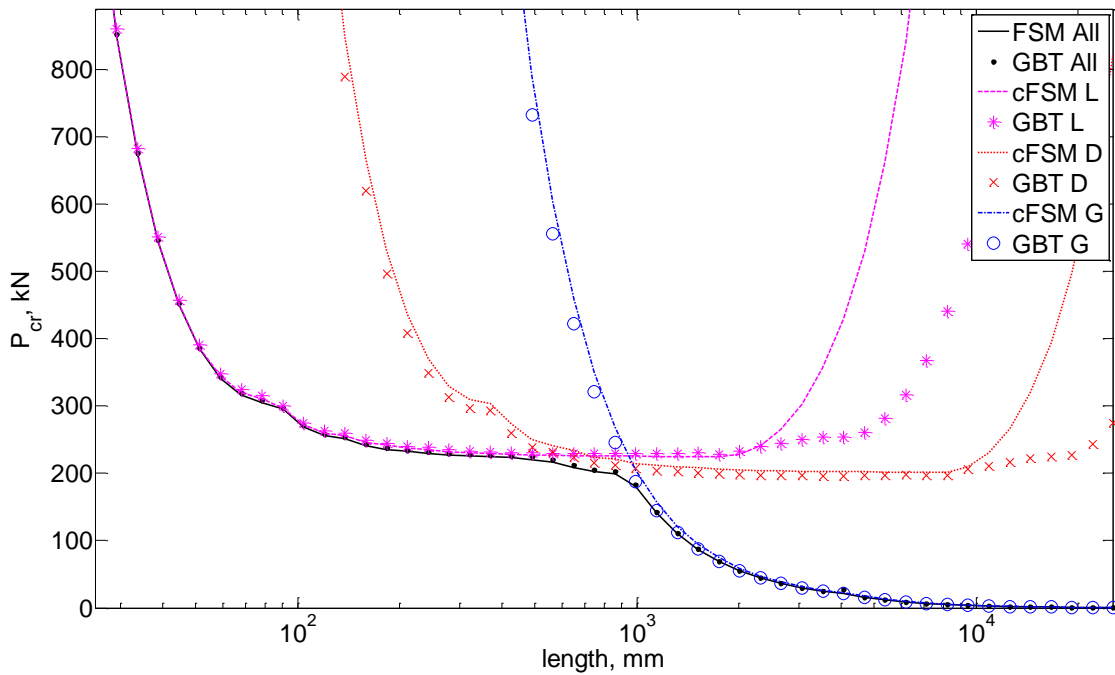


Figure 3-4 FSM and pure  $c$ FSM solutions against GBT solutions

Table 3-3 A summary of normalized subspaces

Space	Orthogonalization	Normalization		
		Strain Energy	Work	Vector
M=G,D,L or combinations	No (Natural)	$R_M^{ e }$	$R_M^{ g }$	$R_M^{ v }$
	Axial Modal	$\bar{R}_M^{ e }$	$\bar{R}_M^{ g }$	$\bar{R}_M^{ v }$
	Applied Modal	$\tilde{R}_M^{ e }$	$\tilde{R}_M^{ g }$	$\tilde{R}_M^{ v }$
ST	No (S+T)	$R_{ST}^{ e }$	$R_{ST}^{ g }$	$R_{ST}^{ v }$
	Axial Modal (S+T)	$\bar{R}_{ST}^{ e }$ or $\bar{R}_S^{ e } \cup \bar{R}_T^{ e }$	$\bar{R}_{ST}^{ g }$ or $\bar{R}_S^{ g } \cup \bar{R}_T^{ g }$	$\bar{R}_{ST}^{ v }$ or $\bar{R}_S^{ v } \cup \bar{R}_T^{ v }$
	Applied Modal (S+T)	$\tilde{R}_{ST}^{ e }$ or $\tilde{R}_S^{ e } \cup \tilde{R}_T^{ e }$	$\tilde{R}_{ST}^{ g }$ or $\tilde{R}_S^{ g } \cup \tilde{R}_T^{ g }$	$\tilde{R}_{ST}^{ v }$ or $\tilde{R}_S^{ v } \cup \tilde{R}_T^{ v }$
O	No (null of GDL)	${}^e R_O^{ e }$	${}^e R_O^{ g }$	${}^e R_O^{ v }$
		${}^g R_O^{ e }$	${}^g R_O^{ g }$	${}^g R_O^{ v }$
		${}^v R_O^{ e }$	${}^v R_O^{ g }$	${}^v R_O^{ v }$
	Axial Modal (null of GDL)	${}^e \bar{R}_O^{ e }$	${}^e \bar{R}_O^{ g }$	${}^e \bar{R}_O^{ v }$
		${}^g \bar{R}_O^{ e }$	${}^g \bar{R}_O^{ g }$	${}^g \bar{R}_O^{ v }$
		${}^v \bar{R}_O^{ e }$	${}^v \bar{R}_O^{ g }$	${}^v \bar{R}_O^{ v }$
	Applied Modal (null of GDL)	${}^e \tilde{R}_O^{ e }$	${}^e \tilde{R}_O^{ g }$	${}^e \tilde{R}_O^{ v }$
		${}^g \tilde{R}_O^{ e }$	${}^g \tilde{R}_O^{ g }$	${}^g \tilde{R}_O^{ v }$
		${}^v \tilde{R}_O^{ e }$	${}^v \tilde{R}_O^{ g }$	${}^v \tilde{R}_O^{ v }$

The conventional FSM solution has three buckling regimes: local, distortional, and global buckling. These may be ascertained along the length by examining the first mode at each length. In the local buckling regime, the *c*FSM solution for pure local buckling shows excellent agreement with the conventional FSM solution. The solution for pure distortional buckling modes by *c*FSM suggests a stiffer response than conventional FSM, as shown in Figure 3-4. For long members, the *c*FSM curve for pure global buckling modes shows the same tendency as conventional FSM but modestly higher critical loads. These observations are consistent with previous *c*FSM results on simply supported boundary conditions.

Comparing the FSM and GBT, the general solutions from the conventional FSM and GBT report almost the same results with the relative differences within 1%. For longer members, the pure local and distortional buckling modes show a significant difference in critical loads between *c*FSM and GBT. This is because both *c*FSM and GBT need finer mesh (increase the longitudinal terms in the analysis for *c*FSM) to capture the multi-wave local and distortional modes. As studied in Section 2.5, the most important longitudinal terms are near  $L/L_{cr\ell}$  and  $L/L_{crd}$  for pure local and distortional buckling modes, respectively, where  $L_{cr\ell}$  and  $L_{crd}$  are the separate local and distortional buckling half-wave lengths of the associated signature curve. In the GBT analysis, mesh sensitivity must be taken into consideration when using finite element discretization for longitudinal field. To capture the relative short half-wavelength local or distortional buckling behavior of a long member, the maximum element size should be less than the half-wavelength of the local or distortional buckling mode. Thus, the GBT results shown in Figure 3-4 require a finer mesh to obtain a better accuracy.

To illustrate this, pure local and distortional solutions are re-analyzed and provided in Figure 3-5 by using the longitudinal terms recommended previously for *c*FSM (see section 2.5). For longer members, the local and distortional plateaus are obtained similar to what is implied in Figure 2-17.

Additional fundamental differences also exist between *c*FSM and GBT, owing primarily to the different mechanical backgrounds of the two methods. For example, in GBT the global buckling modes are handled by a beam model with a constitutive law that follows the 1D form of Hooke's law; while *c*FSM solutions are calculated on a plate model that obeys the 2D form of Hooke's law, this results in a systematic difference in the reported *G* solutions. Further discussion can be found in [27].

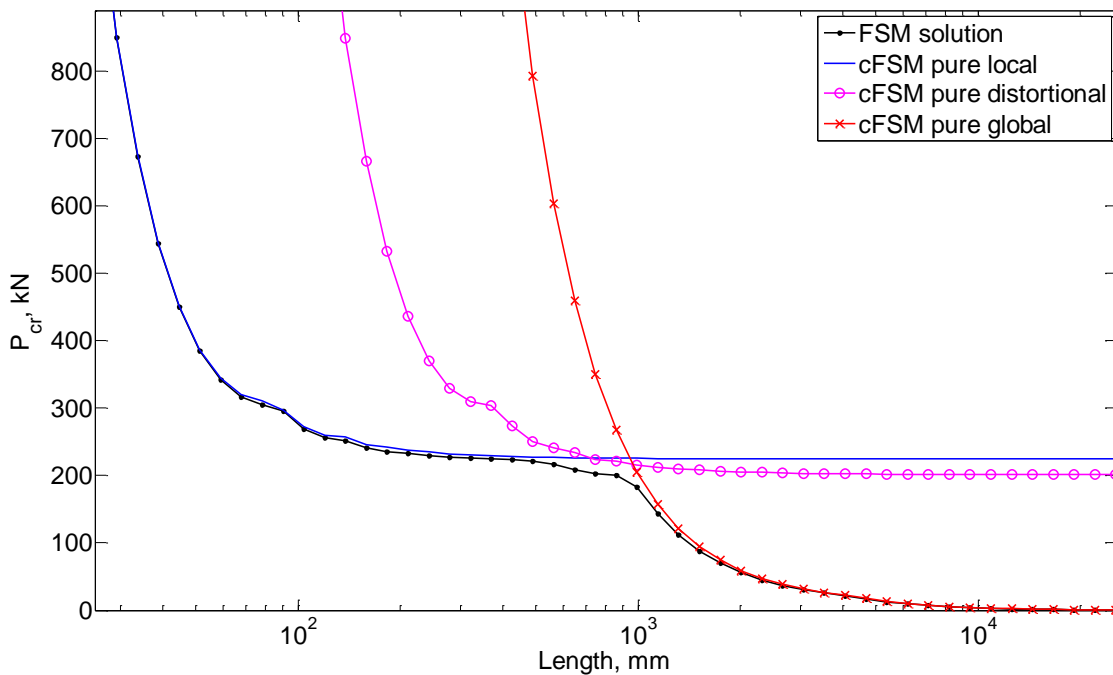
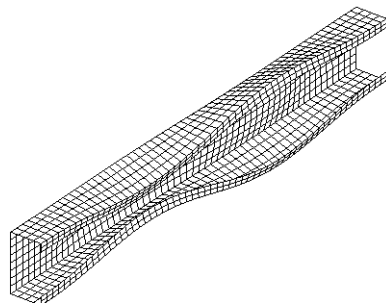


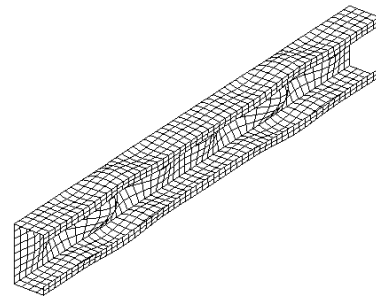
Figure 3-5 Modal decomposition of *c*FSM

A comparison of the identified mode shapes for FSM and pure mode *c*FSM is provided in Figure 3-6. At  $L^* = 490$  mm in Figure 3-4, the 1<sup>st</sup> buckling mode is shown in

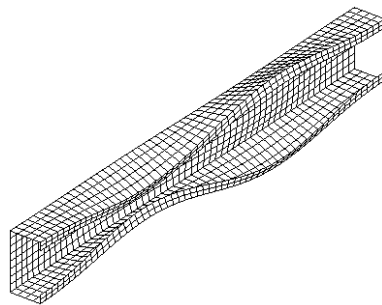
Figure 3-6(a), this mode may be visually identified as distortional buckling (though other modes are present as shown later in the modal classification) with a critical load of 220.6  $kN$ , and the 5<sup>th</sup> mode, as shown in Figure 3-6(b), is identified as local buckling with a critical load of 227.3  $kN$ . The *c*FSM pure distortional and pure local buckling modes are also provided in Figure 3-6(c) and (d) with critical loads of 250  $kN$  and 230.4  $kN$ , respectively. Consistent with the constraining nature of the pure modal solutions, the buckling loads are slightly higher than the general FSM, especially for distortional buckling.



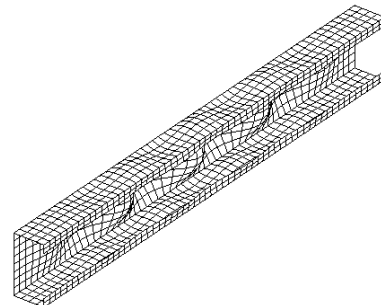
(a) 1<sup>st</sup> mode of FSM



(b) 5<sup>th</sup> mode of FSM



(c) Distortional mode of *c*FSM



(d) Local mode of *c*FSM

Figure 3-6 Buckling modes of the conventional FSM and *c*FSM

Modal decomposition may also be used to search the participation of longitudinal terms for pure local and distortional buckling, and then these longitudinal terms used to

force the member to buckle in local or distortional buckling mode as described in the application with DSM section in Chapter 6.

### 3.8 Modal Identification

The  $G$ ,  $D$ ,  $L$ , and  $ST/O$  subspaces, as defined by the constraint matrices  $R$ , provide a complete alternative basis to the standard FSM basis and represent a transformation of the solution from the original nodal degrees of freedom to a basis that separates  $G$ ,  $D$ ,  $L$ , and  $ST/O$  modes. After appropriate normalization (i.e., scaling), this basis may be used to evaluate the contribution of the different deformation modes ( $G$ ,  $D$ ,  $L$ , and  $ST/O$ ) on any general deformed shape. This procedure is known as modal identification. Modal identification provides a means to determine the contribution of the different buckling classes ( $G$ ,  $D$ ,  $L$  and  $ST/O$ ) in a given FSM stability solution. For the case of FSM with general boundary conditions, the essential idea of modal classification is the same as in existing  $c$ FSM except the summation over  $m$  longitudinal terms increases the problem size. In addition, coupled and uncoupled bases increase the complication as well. Using the defined  $c$ FSM bases, natural ( $R$ ) or modal basis ( $\bar{R}$ , or  $\tilde{R}$ ), any nodal displacement vector  $d$ , which can be any deformed shape or buckling mode, may be transformed into the basis spanned by the buckling classes, via

$$c = R^{-1}d, c = \bar{R}^{-1}d \text{ or } c = \tilde{R}^{-1}d \quad (3-44)$$

where the coefficients in  $c$  represent the contribution to a given column of  $R$  ( $\bar{R}$ , or  $\tilde{R}$ ). Modal classification can be achieved by summing the coefficients corresponding to the columns of a given class ( $G$ ,  $D$ ,  $L$  or  $ST/O$ ). Hence, for the categorized buckling classes,

$G$ ,  $D$ ,  $L$ , and  $ST$  (or  $O$ ), with organized constraint matrix  $R$ , the contribution relation in Eq. (3-44) may be rewritten as:

$$d = [R_G \quad R_D \quad R_L \quad R_{ST/O}] \begin{bmatrix} C_G \\ C_D \\ C_L \\ C_{ST/O} \end{bmatrix} \quad (3-45)$$

where  $C_G$ ,  $C_D$ ,  $C_L$ , and  $C_{ST/O}$  are column vectors that include the contribution coefficients for each vector inside each deformation class. Note, the coefficients are dependent both on the selected basis (e.g.  $ST$  vs.  $O$ ) and on the normalization of the base vectors (i.e. the columns of  $R$ ).

Two options are considered for calculating the participation ( $p_M$ ) of space  $M$  in a general deformation ( $d$ ) given the contribution coefficients ( $c$ ):

- $L^1$  norm: which also may be regarded as the absolute sum (Manhattan distance), and is the method employed in CUFSM 3 [25]:

$$p_M = \|C_M\|_1 / \sum_{M=G,D,L,ST/O}^4 \|C_M\|_1 \quad (3-46)$$

- $L^2$  norm: also known as Euclidean norm:

$$p_M = \|C_M\|_2 / \sum_{M=G,D,L,ST/O}^4 \|C_M\|_2 \quad (3-47)$$

where  $\| \cdot \|_1$  and  $\| \cdot \|_2$  are defined as:

$$\|x\|_1 := \sum_i |x_i| \quad \text{and} \quad \|x\|_2 := \sqrt{\sum_i x_i^2} \quad (3-48)$$

For block diagonal bases (e.g., natural basis, uncoupled modal basis), solely for computational efficiency, the modal classification can be performed for each longitudinal term, instead of solving Eq. (3-44) for all the longitudinal terms as a whole. The

computational effort is significantly reduced, especially when many longitudinal terms are included in the analysis. Also, the classification can be performed within each longitudinal term based on  $L^1$  or  $L^2$  norm and then added together with weighting factors that are the contribution of each longitudinal term  $m$ , as shown in [53]. This is referred to as the “*weighted factor*” approach to modal classification. Though this approach is obsolete, some results can be found in [53].

To illustrate modal classification for general boundary conditions, the conventional FSM stability solution provided in Section 3.7 for modal decomposition has been examined for the participation of the  $G$ ,  $D$ ,  $L$ , and  $ST/O$ . The classification results at three separate lengths (local, distortional and global buckling regimes) are provided for the 3 different  $c$ FSM bases with the corresponding GBT results in Table 3-4. Note, the natural basis  $R$  refers to the basis that consists of  $[R_G R_D R_L R_{ST}]$  with vector normalization; while the axial modal bases consist of  $ST$  space with vector normalization in Section 3.5. The uncoupled axial modal basis are defined without consideration of the coupling of longitudinal terms as in Eq. (3-39) while the coupled axial modal basis considers the coupling of longitudinal terms as in Eq. (3-42). Note, for natural basis and the uncoupled axial mode basis, the constraint matrices are block diagonal.

Table 3-4 Participation of G, D, L and ST for C-C boundary conditions, vector norm

Basis	Sum Option	Local Regime at 137 mm				Dist. Regime at 490 mm				Global Regime at 2009 mm			
		G	D	L	ST	G	D	L	ST	G	D	L	ST
Natural	$L^1$	0.5	1.4	92.7	5.5	0.9	31.8	63.6	3.6	96.0	1.2	1.4	1.5
	$L^2$	1.3	6.9	88.9	2.9	2.2	79.6	17.4	0.7	99.3	0.5	0.1	0.1
Axial modal (uncoupled)	$L^1$	1.8	5.4	90.1	2.7	1.8	62.0	34.7	1.5	96.6	1.2	1.8	0.4
	$L^2$	1.3	7.1	90.8	0.7	2.2	80.6	16.9	0.2	99.3	0.5	0.2	0.0
Axial modal (coupled)	$L^1$	1.7	6.4	87.8	4.1	2.0	62.2	34.7	1.1	98.2	0.8	0.9	0.2
	$L^2$	1.3	7.0	91.1	0.6	2.5	83.9	13.4	0.2	99.5	0.4	0.1	0.0
GBT		0.2	1.5	98.3	n/a	3.6	52.9	43.6	n/a	99.8	0.1	0.0	n/a

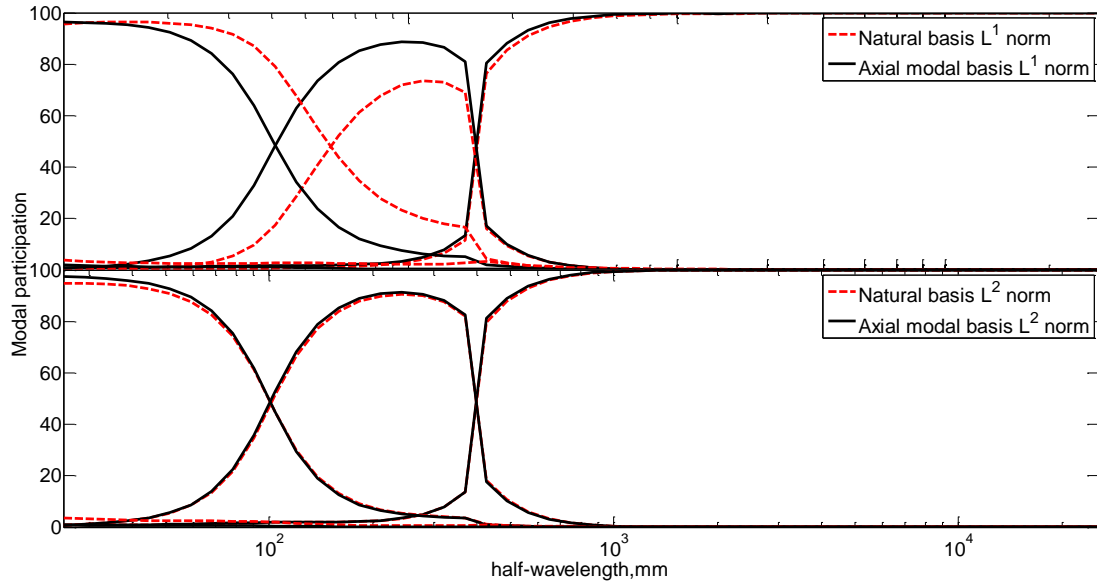
In general, Table 3-4 shows that even at physical lengths where one buckling class dominates, the different buckling classes nearly always participate in the solution. For example, the distortional buckling mode at 490 mm shows this interaction. Even though, for certain cases, the mode is nearly pure mode by one dominated buckling mode class, for instance, the global regime in Table 3-4.

Obviously, modal identification is sensitive to basis as reported in Table 3-4, where slightly different participation results are found between different bases. More significantly, summation options for the contribution coefficients  $C$  have a big impact on the participation results. The distortional buckling mode at 490 mm demonstrates the sensitivity to solution methods. Paradoxically, the  $L^1$  norm option results for the natural basis suggest that local buckling dominates for what appears to be a distortional buckling mode (see Figure 3-6). When the  $L^2$  norm option is employed, all the bases report consistent participation results with a distortional buckling contribution around 80%. The sensitivity of modal identification to norm ( $L^1$  or  $L^2$ ) on contribution coefficients has been studied by the author in [52] for the signature curve. The key findings are reconstructed for the member studied here. The modal identification results with vector normalization are shown in Figure 3-7. In Figure 3-7(a), modal identifications of natural and axial modal bases show significant differences in the local/distortional transition regime when using  $L^1$  norm; while negligible differences are found when using the  $L^2$  norm. This trend can also be found from Table 3-4, that natural, uncoupled and coupled axial modal bases provide consistent and relatively close participation when  $L^2$  norm is used. The fact that the  $L^2$  norm is able to provide participation predictions that are nearly independent of basis, as shown in Figure 3-7 (a) and Table 3-4, suggests that the  $L^2$  norm for

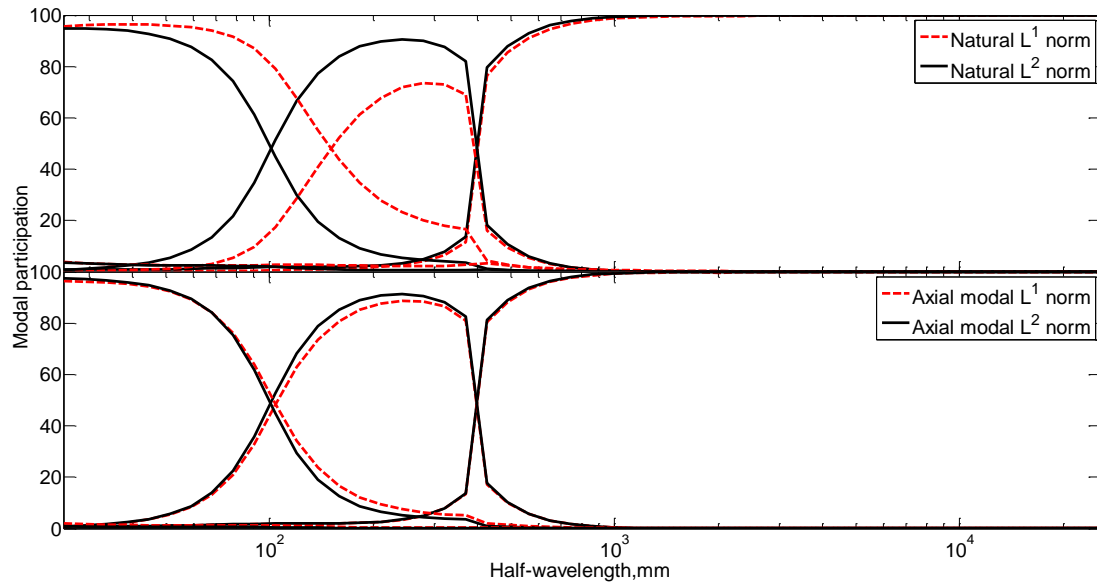
classification holds distinct advantages. Figure 3-7(b) further illustrates the difference of  $L^1$  and  $L^2$  norm in terms of participations for the same basis. The consistent result given by axial modal basis of both  $L^1$  and  $L^2$  norm suggests that when selecting the basis, axial modal basis should be preferred.

Basically, *cFSM* and *GBT* report similar classification results although with obvious differences in the details. The *GBT* basis definition is more similar to the axial modal basis in *cFSM*, and the sum option on the contribution coefficients with  $L^1$  norm. Close results can be found between *GBT* and *cFSM* with  $L^1$  norm, especially in the distortional regime at 490 mm as given in Table 3-4.

Similarly, participation of *G*, *D*, *L*, and *ST/O* using work normalization can be solved and is provided in Table 3-5. The classification results are similar to those in Table 3-4 though slightly higher *ST* participation is observed especially for the natural basis. The inconsistent participation in the distortional regime predicted by the  $L^1$  norm still exists. Although not as close as those in the vector normalization case, the  $L^2$  norm still provide consistent classification independent of bases.



(a) Comparison between different bases of same summation norm



(b) Comparison between two summation norms of same basis

Figure 3-7 Sensitivity of modal identification to  $L^1$  and  $L^2$  norm in signature curve

Table 3-5 Participation of G, D, L and ST for C-C boundary conditions, work norm

Basis	Sum Option	Local Regime at 137 mm				Dist. Regime at 490 mm				Global Regime at 2009 mm			
		G	D	L	ST	G	D	L	ST	G	D	L	ST
Natural	$L^1$	2.5	1.8	66.8	28.9	1.5	24.6	61.8	12.1	84.7	3.5	2.6	9.2
	$L^2$	3.7	6.7	78.3	11.3	3.1	65.8	28.8	2.2	97.5	1.5	0.3	0.7
Axial modal (uncoupled)	$L^1$	7.1	4.9	75.8	12.2	2.8	46.4	45.1	5.8	90.9	3.9	2.1	3.1
	$L^2$	3.6	6.4	86.9	3.2	3.0	63.8	32.3	0.8	98.0	1.4	0.3	0.3
Axial modal (coupled)	$L^1$	3.8	5.3	81.6	9.3	2.9	51.3	43.5	2.3	98.1	1.0	0.4	0.6
	$L^2$	1.9	5.6	91.3	1.2	3.5	74.7	21.4	0.4	99.5	0.4	0.0	0.1
GBT		0.2	1.5	98.3	n/a	3.6	52.9	43.6	n/a	99.8	0.1	0.0	n/a

### 3.9 Recommendation of basis, normalization, and summation of participation options

Different bases, orthogonalization, and normalization options are available when employing *cFSM*, as presented previously. Though all the bases are mechanically correct and equivalent, they do perform differently with respect to modal decomposition and modal identification. Systematic explanation and study of the selection of basis and normalization has been provided in [52] by the author based on a study for signature curve (S-S results). Combined with modal decomposition and identification in the previous section, recommendations are provided in this section for users of *cFSM*.

Although the *natural basis* is necessary, the *modal basis* is far more powerful. The one exception to this is in the *G* space where separation of the deformations into orthogonal directions has certain conveniences. For general use the *modal basis* with an axial reference load is logical, while the extension to other reference loads (e.g., pure bending) is advantageous for certain problem specific studies. In addition, although the coupled modal basis is more realistic, the uncoupled modal basis holds the advantages in computational efficiency and simplicity. *Uncoupled modal basis* is recommended.

Normalization of the base vectors is required, but strain energy norm is not recommended. Both vector norm and work norm are viable options. Mesh sensitivity of the vector norm in modal identification solutions makes the work norm preferred when possible. Work norm is recommended. However, for simplicity, vector norm is also recommended.

Normalization of the participation results is required, and the simplicity of the  $L^1$  norm leads to its adoption in the literature [26-28] and previous versions of CUFSM [25]. However, the  $L^2$  norm is demonstrated herein to significantly reduce dependence on the choice of basis when coupled with either the vector norm or work norm. The  $L^2$  norm is recommended and has been implemented in the latest version of CUFSM [54].

As far as the definition of the modes that violate Vlasov's hypothesis is concerned: the  $O$  space, being the null space of  $GDL$ , is mathematically convenient, but the resulting modes have little physical sense, and provide no advantage over the more mechanically oriented definition of the  $ST$  space. Although the  $ST$  space is not fully orthogonal to  $GDL$  (and hence termed partially orthogonal previously) it is much more readily conceptualized and leads to more consistent modal identification results in studied examples. The use of  $ST$  definition is recommended.

### **3.10 Summary**

In this chapter, the theoretical derivation and implementation of the constrained finite strip method ( $c$ FSM) for the stability solution of thin-walled members is presented for general boundary conditions. The proposed method provides a means of decomposing the general deformation field into global ( $G$ ), distortional ( $D$ ), local ( $L$ ) and other ( $O$  or

*ST*) modes for general boundary conditions, i.e. simple-simple, clamped-clamped, simple-clamped, clamped-free, and clamped-guided.

The theoretical background of the method for general boundary conditions is shown, and the procedure for defining the pure buckling modes (in the natural basis,  $R$ ) is explicitly presented. Alternatives for defining the other ( $O$ ) modes either as Shear ( $S$ ) and transverse extension ( $T$ ) modes, or the more mathematical notion of the null of the  $GDL$  space, are presented and related options discussed. Utilizing the natural basis to define the mode basis (axial or applied) by solving the constrained eigenvalue problem within each space is presented. Summary of the available bases and normalization is discussed.

Numerical examples of modal decomposition of the stability results are presented using the developed  $cFSM$  methodology and compared with Generalized Beam Theory (GBT). Further, modal identification (providing the participation in the  $G$ ,  $D$ ,  $L$ , and  $O$  or  $ST$  classes) is studied for FSM stability modes. Recommendations for basis, normalization of the base vectors, normalization of the participation results, and selection of the  $ST$  or  $O$  space are made for users of  $cFSM$ .

## Chapter 4 Modal Identification for elastic buckling FE analysis

### 4.1 Introduction

With all the advances in computational power, the finite element method (FEM), utilizing shell elements, has become more common in analyzing the stability of thin-walled structures. FEM's unique applicability to model complex geometric and boundary conditions make it especially popular. However, for the elastic buckling problem, FEM requires a laborious and subjective mode identification using visual investigation of the mode shapes. A successful quantitative mode identification method, using the constrained finite strip method (*cFSM*), has been proposed for FEM buckling analysis by Ádány, et al. [38]. The method uses the original *cFSM* base functions, which correspond to simple-simple (S-S) supported end boundary conditions. Earlier studies [38] show that the S-S *cFSM* base functions are applicable only to end conditions without (local or global) translational movement.

Recently, *cFSM* has been extended and implemented by the author and colleagues [46, 53, 54]. New base functions are proposed for more general end boundary conditions, namely: clamped-clamped (C-C), simple-clamped (S-C), clamped-guided (C-G), and clamped-free (C-F). In this chapter, these new base functions are applied for the modal identification of buckling analyses with general boundary conditions in FEM. More

importantly, a fundamental set of base vectors are proposed, which can potentially handle arbitrary end boundary conditions.

## 4.2 Extrapolation of *c*FSM base function to FEM context

To complete modal identification of an FEM solution, base vectors or functions including the separation of fundamental global (*G*), distortional (*D*), local (*L*) and shear and transverse extension (*ST/O*) are generated from the constrained finite strip method (*c*FSM). Since shell finite element solutions have in general 6 degrees of freedom (DOF) (3 translational and 3 rotational displacements) while in FSM there are 4 DOF displacements (i.e., 3 translational displacements (*U*, *V*, *W*) and 1 rotational displacement about longitudinal direction ( $\Theta$ )) appropriate extrapolation of the base function to the FEM context is necessary. Based on the local FSM coordinates (Figure 2-1), the other two rotational displacements can be interpolated from the FSM displacement shape functions.

Therefore, rotation displacement about x-axis is obtained via:

$$\theta_x = \frac{\partial w}{\partial y} \quad (4-1)$$

Rotation about z-axis, which may be referred to as the drilling degree of freedom, can be handled in two ways: 1) ignore the normal rotation by set the drilling DOF zero (This does not imply there are no  $\Theta_z$  rotation in global coordinates because of the transformation from local to global coordinates); 2) interpret the drilling DOF as a true rotation of the vertex node:

$$\theta_z = \frac{1}{2} \left( \frac{\partial v}{\partial x} - \frac{\partial u}{\partial y} \right) \quad (4-2)$$

In the studies, the drilling DOF is handled by following the first method. If the analysis has significant geometric and/or material nonlinearity, using the latter may be beneficial. It is worth noting here that in ABAQUS shell element library, there are some elements excluding the drilling DOFs such as S9R5, S8R4, and S4R5, etc. ABAQUS usually doesn't report the rotational displacements for these elements, this poses a problem for our modal identification in which the rotational displacements are necessary to correctly identify buckling modes.

In case the nodes do not coincide between FSM and FEM. Interpolation can be used based on the transverse and longitudinal shape functions in FSM.

It is worth noting here that special attention must be paid to the coordinate systems used in FSM and FEM. FSM's use of a left-handed coordinate system means FEM and FSM coordinate systems are nearly always different, therefore transformation of the displacements to the FEM solution is required.

## **4.3 Identification Method**

### **4.3.1 Minimization problem**

Once the base functions in the FE context are derived from the  $c$ FSM base functions, any FEM eigenvector can be approximated by a linear combination of these base functions. In other words, the underlying idea is that given the base functions  $R_{FE}$  including a set of base vectors in column, a linear combination coefficients  $c$  of these base vectors is sought to fit the FE displacement vector  $d$ . However, the system of linear equations to be solved is normally an overdetermined system. Such a system usually has no solution, so the goal is instead to find the coefficients  $c$  which fit the equations best.

The problem can be mathematically expressed as:

$$d_{err} = d_{FE} - R_{FE}c \quad (4-3)$$

where,  $d_{err}$  is the residual error of the approximation,  $R_{FE}$  is base functions in the FE context, and  $c$  is the contribution coefficients. This is a linear least square problem where the best approximation is defined as that which minimizes the sum of the squared residual error. Therefore, a minimization problem given below is solved to find the best approximation:

$$\min d_{err}^T d_{err} \quad (4-4)$$

Substituting Eq. (4-3) into Eq. (4-4), the least square problem can be rewritten as

$$\min (d_{FE} - R_{FE}c)^T (d_{FE} - R_{FE}c) \quad (4-5)$$

Provided that the base vectors in  $R_{FE}$  are linearly independent, the least square problem has a unique solution based on the minimum condition:

$$\frac{d[(d_{FE} - R_{FE}c)^T (d_{FE} - R_{FE}c)]}{dc} = 0 \quad (4-6)$$

which leads to the normal equation for the optimal solution  $c^*$  that provides the minimal sum of the squared residual error:

$$R_{FE}^T R_{FE} c^* = R_{FE}^T d_{FE} \quad (4-7)$$

### 4.3.2 Participation evaluation

Similar to modal identification in cFSM, two options are available as to how the participation of each mode class M (G, D, L, and ST/O) is summed:

- $L^1$  norm (used in [25]):

$$p_M = \|c_M^*\|_1 / \sum_{M=G,D,L,ST/O}^4 \|c_M^*\|_1 \quad (4-8)$$

- $L^2$  norm:

$$p_M = \|c_M^*\|_2 / \sum_{M=G,D,L,ST/O}^4 \|c_M^*\|_2 \quad (4-9)$$

where  $\| \cdot \|_1$  and  $\| \cdot \|_2$  are defined as:

$$\|x\|_1 := \sum_i |x_i| \quad \text{and} \quad \|x\|_2 := \sqrt{\sum_i x_i^2}$$

The modal identification has shown near independence of choices of bases when using the  $L^2$  norm in  $c$ FSM. Since the FEM base functions are derived from  $c$ FSM base functions through interpolation based on the shape functions; logically,  $L^2$  norm is also preferred in the FE modal identification. Therefore, the FE modal identification in this study is based on the  $L^2$  norm, unless otherwise specified.

Since the modal identification is sensitive to bases the recommended basis uncoupled axial modal basis with ST definition, is employed to provide a consistent solution. In addition, vector norm is used, but on the base vectors in FE context ( $R_{FE}$ ).

### 4.3.3 Error estimation

The most convenient and simple way to measure the error is to evaluate the  $L^2$  norm of the residual error  $d_{err}$  relative to the  $L^2$  norm of the displacement vector  $d_{FE}$ :

$$ERROR = \sqrt{d_{err}^T d_{err}} / \sqrt{d_{FE}^T d_{FE}} \quad (4-10)$$

## 4.4 Numerical studies: FSM-like boundary conditions

The semi-analytical finite strip method (e.g., CUFSM) is based on specially selected longitudinal shape functions to represent the longitudinal displacement field. These

longitudinal shape functions are intended to simulate the actual boundary conditions, i.e., S-S, C-C, S-C, C-F, and C-G, while certain restrictions may apply based on these shape functions, especially involving the warping displacement, which has great impact on the buckling behaviors for a thin-walled member. In terms of the FSM-like boundary conditions in this study, the boundary conditions of the FE model are set by the implied boundary cases of the longitudinal shape functions in *c*FSM. FSM-like boundary conditions in the FE model can be summarized as given:

- S-S: warping free at both ends while translational displacements are restrained. Warping fixity is added to the nodes in the middle length of the member.
- C-C: warping fixed at both end while all the translational and rotational displacements are restrained also.
- S-C: warping free at simply support end while translational displacements are restrained; warping fixed at clamped end while all the translational and rotational displacements are restrained also.
- C-F: warping fixed at clamped end while all the translational and rotational displacements are restrained also; the other end is free.
- C-G: warping fixed at clamped end while all the translational and rotational displacements are restrained also; warping fixed at guided end while rotational displacements are restrained.

#### **4.4.1 Finite element modeling**

The shell finite element solution of the eigenvalue buckling analysis is performed in the commercial code ABAQUS. The member used to illustrate the application and

capabilities of the proposed modal identification method is a symmetric lipped channel section. The dimensions of the cross section are shown in Figure 4-1 and a straight-line model is employed (no round corners). The labeled dimensions are for the center-line model. The material is assumed to be elastic, isotropic, and homogenous with a Young's modulus of 210000 MPa and Poisson's ratio of 0.3. The member's length is 2000 mm with the boundary conditions stated previously under axial compression loading.

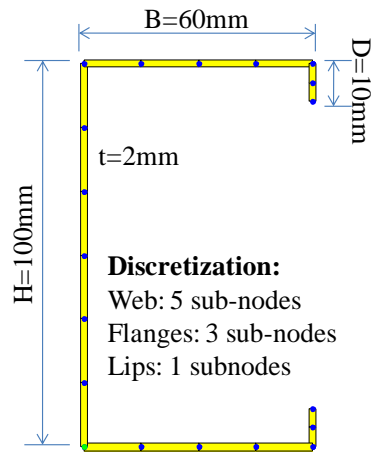


Figure 4-1 Dimension of the cross section and discretization

The element type for the study is a 4-node, 24 DOF shell element (S4, a general purpose shell element in the ABAQUS library). Parametric studies regarding the mesh density have been completed by Ádány et al. using ANSYS [55, 56]. The “relatively fine” mesh is used here with 3, 5 and 1 sub-nodes in flanges, web and lips, respectively. In addition, the mesh density in the longitudinal direction is specially chosen to ensure the aspect ratio of any element is between  $\frac{1}{2}$  and 2 except of the lips where the aspect ratio is allowed to be as high as 3. The solver to extract the eigenvalues and eigenvectors is the Lanczos method. Selected buckling mode shapes from the FE eigen buckling solution (ABAQUS) are illustrated in Figure 4-2.

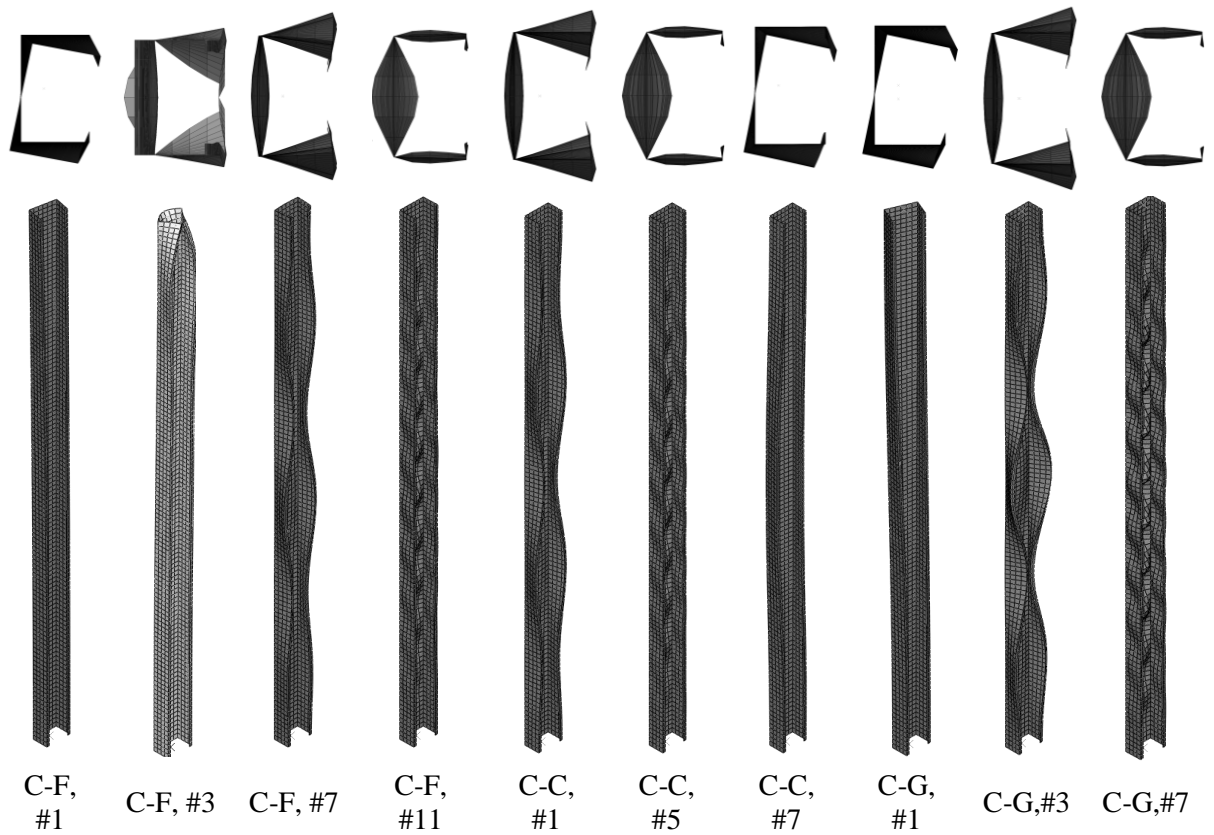


Figure 4-2 FE buckling modes for selected cases

#### 4.4.2 Associated base function

Based on the geometry and material properties of the member in the FE models, base functions can be built up following the procedure in Chapter 3. It is logical that the boundary conditions in *cFSM* employed to build up the base functions should match the boundary conditions in the FE model. More specifically, base functions  $R$  from *cFSM* are based on the boundary conditions corresponding to the FE model's, and to interpolate the base function  $R_{FE}$  in FE context the associated longitudinal shape functions are employed. The base functions built up through this definition are called the *associated* base

functions. It is worth noting here that only for special ideal boundary conditions, as defined above, are the *associated* base functions available, otherwise no matching base functions in *cFSM* for FE model's boundary conditions exist. Such a situation requires ad-hoc base functions as proposed later – and termed the *generalized* base functions. Sample base functions for different boundary conditions are illustrated in Figure 4-3. Notice that the base function is characterized by the cross-section deformation and the longitudinal half-wavelength (reflected by the longitudinal term  $m$ ). In addition, the differences of base functions for different boundary conditions are observed, as illustrated for S-S and C-F. As stated before, the basis in *cFSM* is uncoupled, thus, the base functions of other than S-S ignore the coupling effect between longitudinal terms as illustrated for C-F.

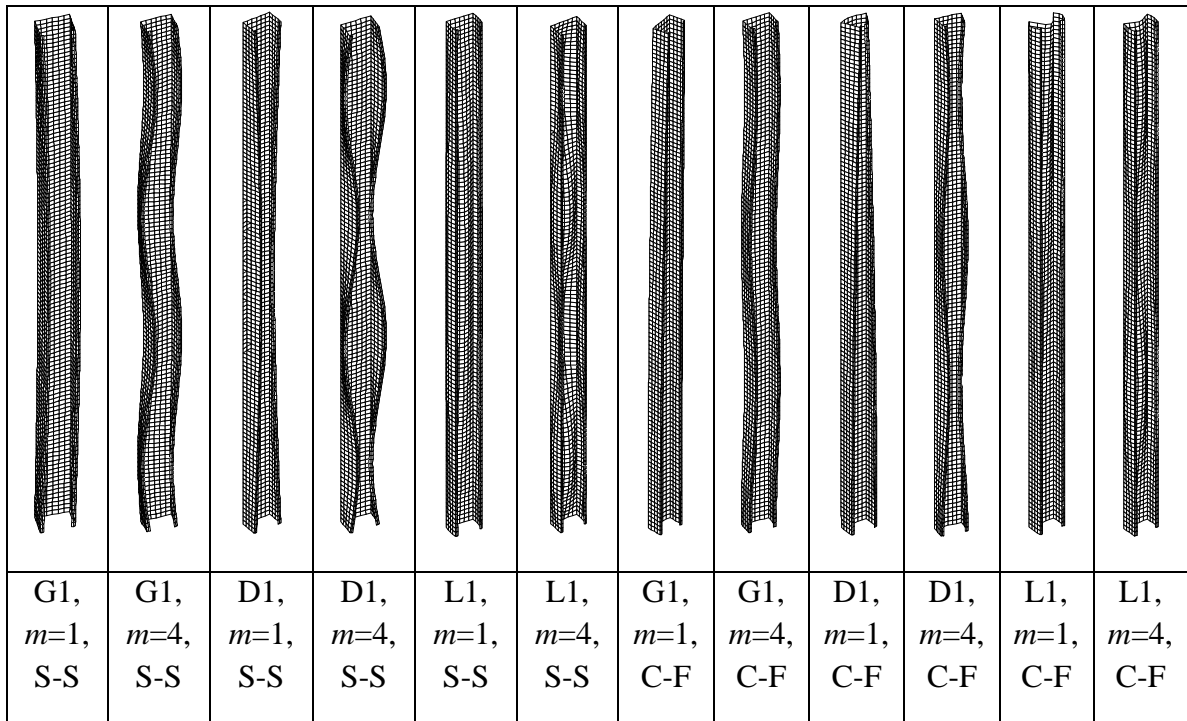


Figure 4-3 FEM base functions for different boundary conditions

#### 4.4.2.1 Modal identification

To fully capture modal information in the deformation modes of the FE model, sufficient longitudinal terms (associated with the smallest half-wavelength mode needed) should be included in the base functions. For the member studied here, the longitudinal terms in the *cFSM* base functions are 40 in total (from 1 to 40 by default unless otherwise specified) for all the boundary conditions. The modal identifications are performed on the first 50 buckling modes of each case by using the *associated* base function with 40 longitudinal terms. This covers those modes that the buckling loads are less than  $N$  times the first buckling loads ( $N$  is usually less than 10). Participations of the  $G$ ,  $D$ ,  $L$ , and  $ST$  along with the calculated errors for each mode in each boundary case, specifically S-S, C-C, S-C, C-G, and C-F, are provided in the following figures along with the critical loads.

The modal identification for the S-S FSM-like boundary conditions has been studied in [55] though different other mode definitions ( $ST/O$ ) are used. In [56], the other modes  $O$  are the null space of  $GDL$  space with respect to elastic stiffness matrix  $K_e$  while the other modes  $ST$  here are defined more directly from the shear and transverse extensions of all the strips (See further in Section 3.4.3). As shown, other modes contributions are negligible by  $ST$  definition. This is consistent with the conclusion drawn by the authors in [52].

The results, in terms of participation of modes and their errors, are consistent with those in [56]. The *cFSM* approximations are excellent and with small errors for most modes. The the participation results are also in accordance with engineering expectations. Dominant  $G$ ,  $D$ , and  $L$  modes can be easily found for the case studied here. The higher modes with significant errors (e.g., modes #45, #47, #49 and #50 in S-S in Figure 4-9)

are due to the lack of larger longitudinal terms in the base functions to account for local buckling with short half-wavelengths. Including larger longitudinal terms will remove (or significantly reduce) this error as illustrated for the case of FSM-like S-S boundary conditions in Table 4-1. The errors are reduced to negligibly small if the *c*FSM base functions include several higher longitudinal terms, and the participations are now more in accordance with engineering expectations. In particular, for the 47<sup>th</sup> mode, this is a local buckling dominant mode with some contributions of distortional buckling as correctly predicted when including higher longitudinal terms in the base functions as given in Table 4-1.

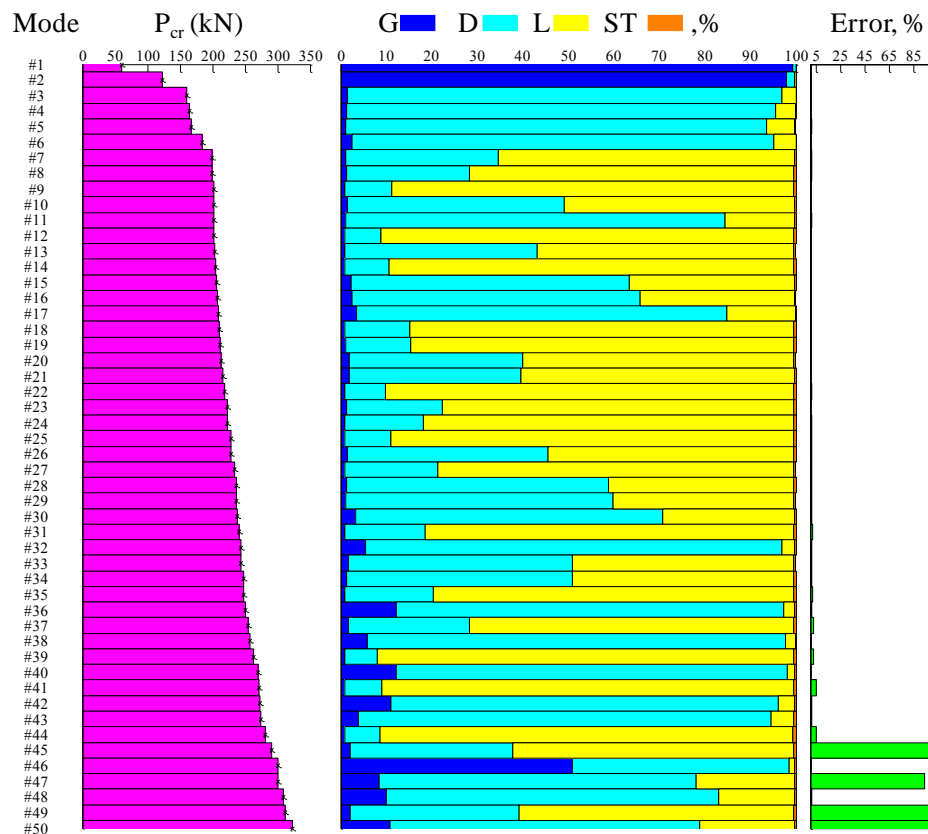


Figure 4-4 Critical loads, participations, and identification error of FE solution of FSM-like S-S boundary conditions

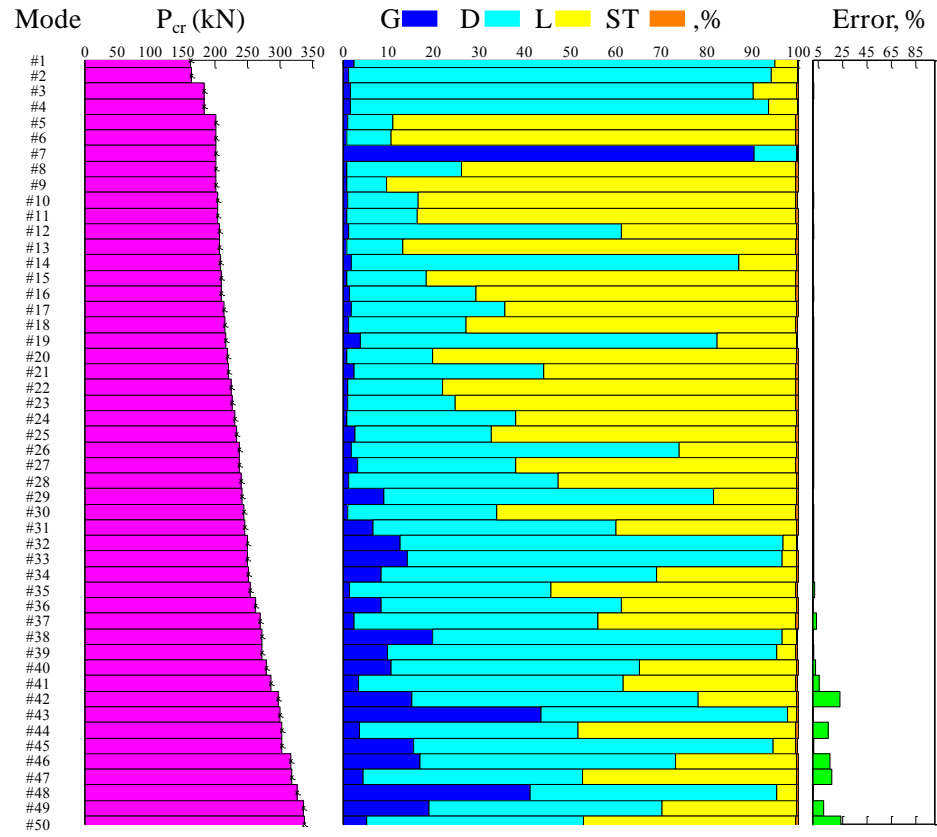


Figure 4-5 Critical loads, participations, and identification error of FE solution of FSM-like C-C boundary conditions

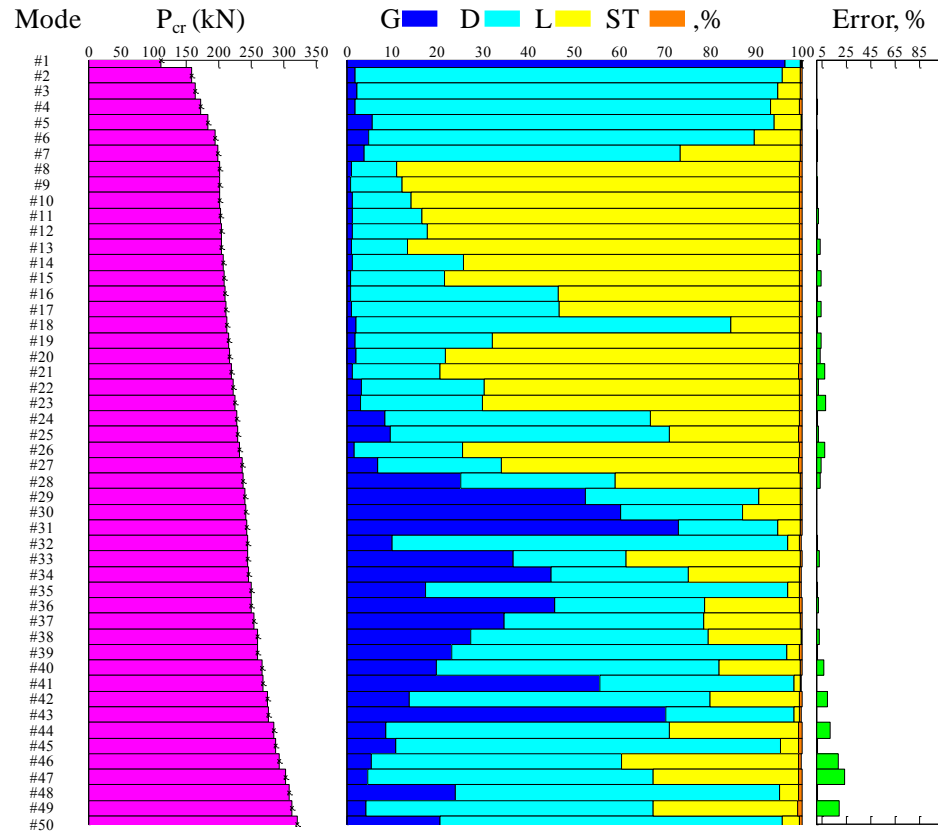


Figure 4-6 Critical loads, participations, and identification error of FE solution of FSM-like S-C boundary conditions

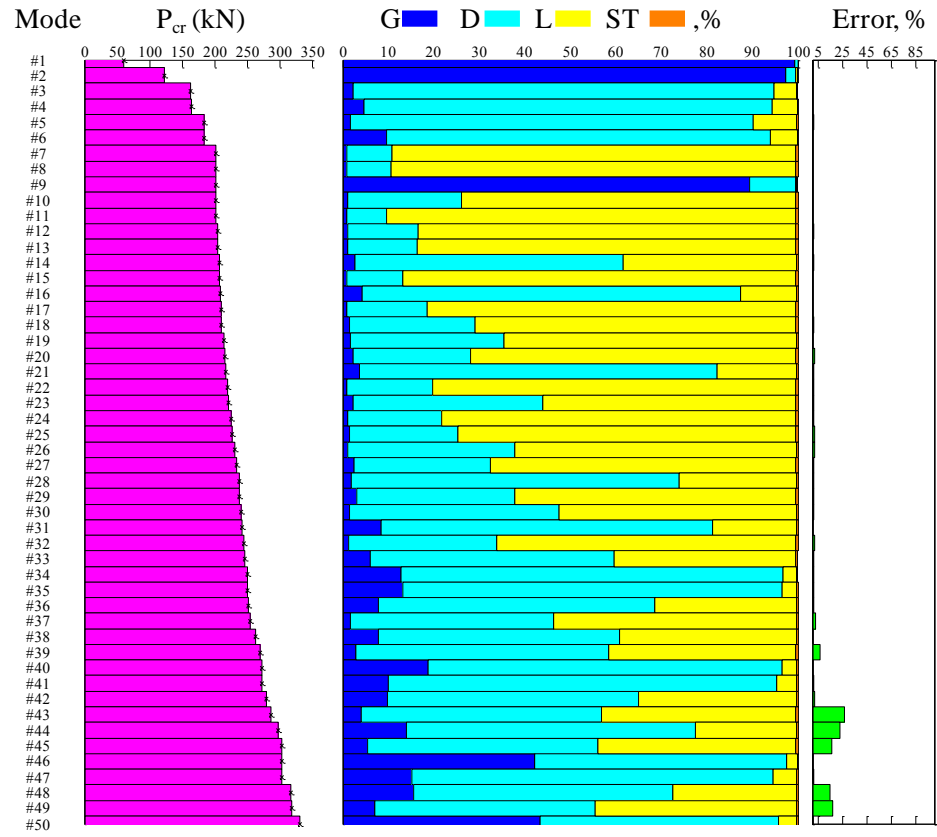


Figure 4-7 Critical loads, participations, and identification error of FE solution of FSM-like C-G boundary conditions

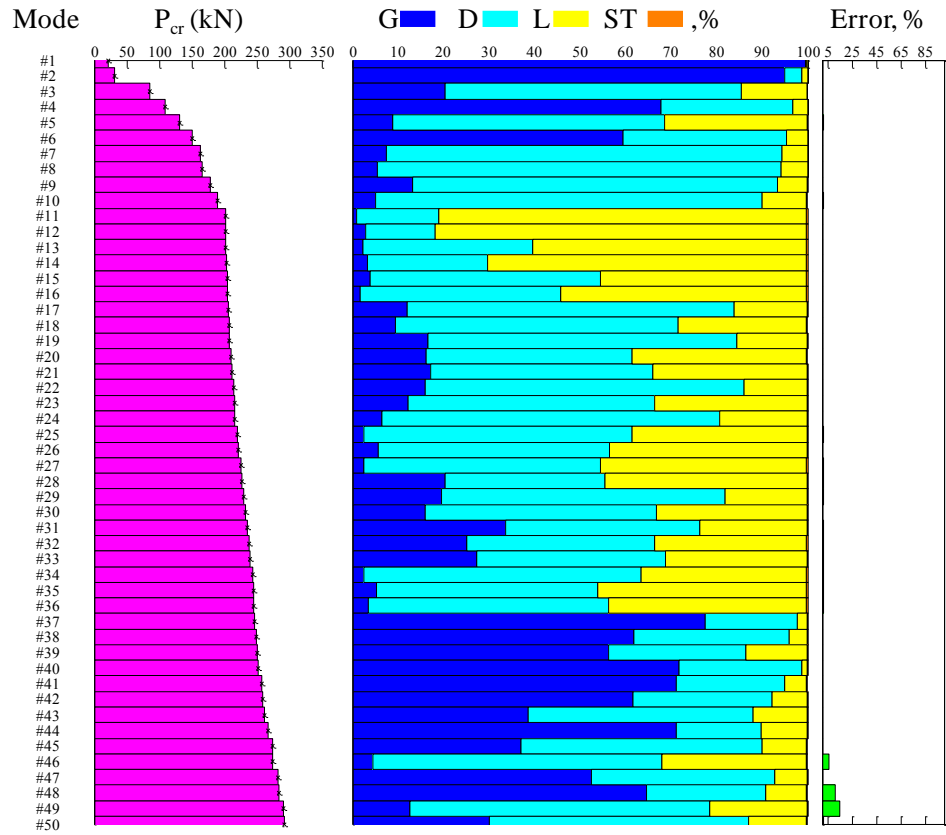


Figure 4-8 Critical loads, participations, and identification error of FE solution of FSM-like C-F boundary conditions

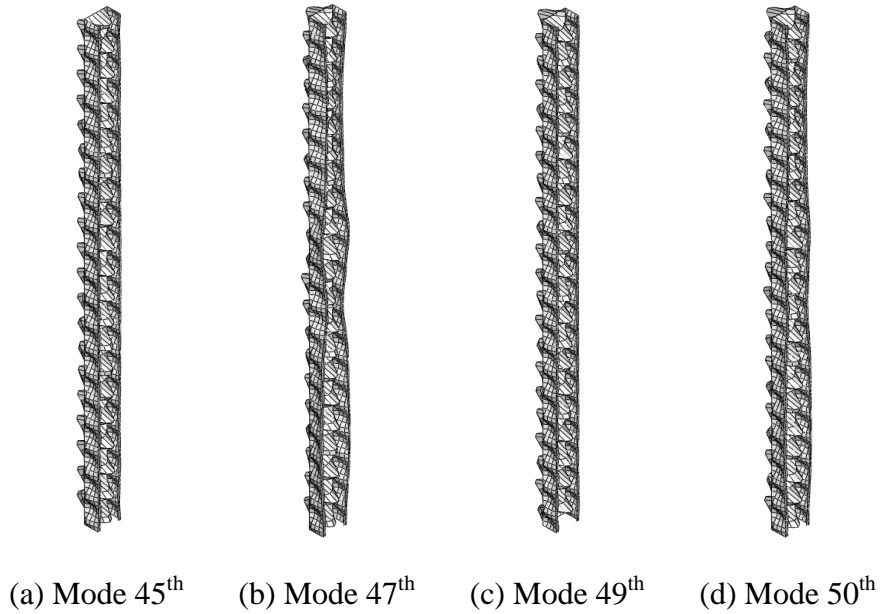


Figure 4-9 Higher mode shapes of FE solution of FSM-like S-S boundary

Table 4-1 Participations and errors of FE solution of FSM-like S-S boundary conditions by base functions with different longitudinal terms

Mode #	40 longitudinal terms in base functions					46 longitudinal terms in base functions				
	G (%)	D (%)	L (%)	ST (%)	Error (%)	G (%)	D (%)	L (%)	ST (%)	Error (%)
44	0.9	7.8	90.7	0.6	4.7	0.9	7.7	89.2	2.2	1.1
45	2.1	35.6	61.8	0.5	99.6	0.8	4.1	92.8	2.4	1.6
46	50.9	47.7	1.2	0.2	0.5	48.8	49.1	1.3	0.8	0.5
47	8.5	69.5	21.8	0.2	93.7	3.0	24.1	71.0	1.8	1.5
48	10.0	73.1	16.7	0.2	0.8	9.9	72.8	16.7	0.5	0.6
49	2.1	37.1	60.3	0.5	99.9	0.8	2.8	94.0	2.5	2.4
50	10.8	68.1	20.9	0.2	97.9	2.5	15.1	80.2	2.1	2.3

In general, adding more longitudinal terms in the base functions will reduce the errors. However, matrix singularity may be introduced if too many longitudinal terms are included and artificially high *ST* mode participation is then observed. To avoid this, one can either exclude *ST* base vectors, since *ST* contribution is negligible; or restrain the longitudinal terms so that smallest half-wavelength is at least 2 times the element size in the longitudinal direction.

For selected boundary condition cases, C-C and C-F, the FE deformed shapes and *c*FSM approximated shapes are presented in Figure 4-10 for selected local, distortional, and global buckling modes as determined from identification results. As can be seen, the *c*FSM approximated shapes are almost identical to the FE deformed shapes.

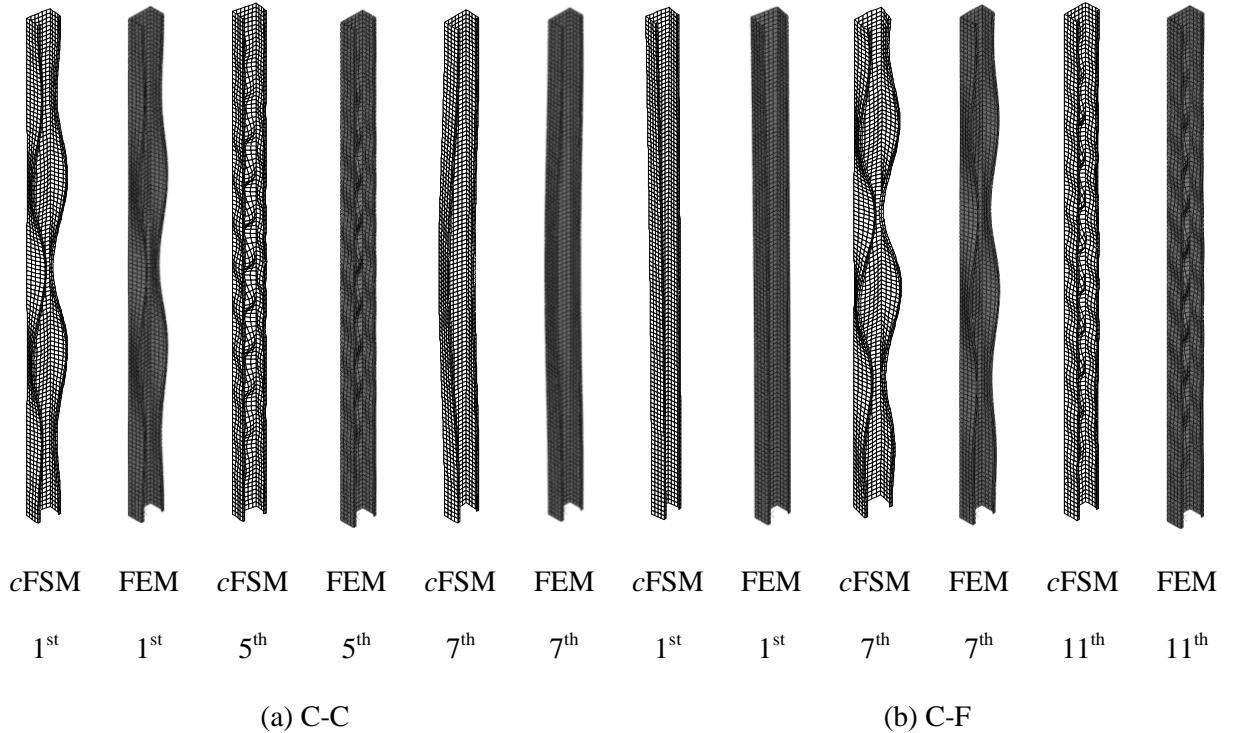


Figure 4-10 FEM deformed shapes compared with identified mode shapes from *cFSM* for some selected modes (add C-F #3)

#### 4.4.2.2 Comparison to *FSM*

Since the boundary conditions of the FE models are equivalent to those implied by the *FSM* longitudinal shape functions (note, the boundary conditions can be only matched to certain extent and not exactly identical), the buckling solutions can potentially be compared with the same loading. However, exact match in the order of higher buckling modes is not possible due to inherent difference between the *FSM* and *FEM* models and the different eigen-mode extraction methods. Thus, the comparisons are limited to those modes that are distinct local, distortional, and global buckling (characteristic modes), and these modes are usually the 1<sup>st</sup>/lowest modes in their kind. The selection of the modes is based on observation, selection of reasonably high modal participation and also mode

shape. Automating this process is an important topic of future research. The comparisons between the FEM solution and the FSM solution, in terms of the participations and critical loads for the characteristic buckling modes, are shown in Table 4-2. First, modal identification of FEM and FSM solutions provides close participation prediction for all the boundary cases. Second, for the long member studied here, critical loads of local and distortional buckling modes are almost the same. The differences in terms of critical loads between FEM and FSM are small. For critical loads of global and distortional buckling, the differences are negligible. However, FEM models predict critical loads 5% higher than FSM for the local buckling mode.

Table 4-2 Participations and critical loads of FEM and FSM solutions

Boundary case	Dominant mode	Mode number	FEM solution					FSM solution				
			G (%)	D (%)	L (%)	ST (%)	P <sub>cr</sub> (kN)	G (%)	D (%)	L (%)	ST (%)	P <sub>cr</sub> (kN)
S-S	G	#1	99.4	0.6	0.0	0.0	60.4	99.4	0.6	0.0	0.0	60.6
	D	#3	1.4	95.5	3.1	0.1	160.3	1.3	95.3	3.3	0.1	159.5
	L	#9	0.9	10.3	88.4	0.5	201.5	0.9	6.9	91.8	0.5	191.0
C-C	G	#7	90.3	9.4	0.2	0.1	201.6	88.0	11.5	0.3	0.1	201.7
	D	#1	2.5	92.4	5.0	0.1	163.7	2.2	92.3	5.4	0.1	162.3
	L	#5	1.0	10.0	88.5	0.5	201.5	0.9	7.7	91.0	0.5	191.3
S-C	G	#1	96.4	3.4	0.1	0.2	112.2	95.3	4.4	0.2	0.1	113.7
	D	#2	1.8	94.0	4.0	0.2	159.1	1.6	93.9	4.4	0.1	157.9
	L	#8	1.1	9.9	88.5	0.5	201.5	0.9	12.4	86.3	0.5	191.1
C-F	G	#1	99.6	0.1	0.3	0.0	22.0	99.7	0.1	0.2	0.0	22.1
	D	#7	7.4	87.0	5.6	0.1	163.2	6.0	86.2	7.7	0.1	164.1
	L	#11	0.8	18.2	80.8	0.3	201.5	3.9	12.7	82.9	0.5	191.3
C-G	G	#1	99.3	0.7	0.0	0.0	60.6	99.1	0.8	0.0	0.0	60.7
	D	#3	2.3	92.5	5.0	0.1	163.7	3.2	91.3	5.4	0.1	163.2
	L	#7	0.9	10.0	88.6	0.5	201.5	0.9	9.4	89.3	0.5	191.1

#### 4.4.3 Generalized base function

The *associated* base functions have been demonstrated in the previous section to be capable of identifying the buckling modes of FEM solutions with so-called FSM-like boundary conditions. However, in reality, for instance in a frame, the boundary conditions of a member may hardly be idealized as any of those defined in FSM. In most circumstances, the member's end boundary conditions should be treated as partially rigid instead of assuming free to move (no rigidity), simply-supported (only free to rotate) or

fixed (no translational and rotational move). In some complex systems, the influences of the sheathing or cladding can result in very different boundary condition scenarios than those idealized in FSM. Depending on connection details, the boundary conditions at the ends can even be mixed inside the cross section. Obviously, it is impossible to have *associated* base functions for each practical situation. Thus, it is advisable to find a set (or a group) of base functions that handle not only the idealized FSM-like boundary conditions but also the more general boundary conditions aforementioned, i.e., *generalized* base functions.

#### ***4.4.3.1 Incapability of associated base function***

Before the generalized base function is proposed, let us examine a single set of the *associated* base function. The *associated* base function for S-S provides a fundamental set because of the orthogonality property of the longitudinal shape functions. The *associated* base function for S-S has been used to perform modal identification for FSM-like boundary conditions in the above section. The modal identification results are shown in Figure 4-11 - Figure 4-14 for FSM-like boundary conditions other than S-S by using S-S base functions in cFSM. The critical loads associated with each mode are not shown. For FSM-like C-C and S-C boundary conditions, S-S base function is able to provide excellent identification results as demonstrated in Figure 4-11 and Figure 4-12 with negligible errors for most of the modes. Similar to identification results by the *associated* base functions, some of the higher modes need larger longitudinal terms to capture the smaller half-wavelength local buckling.

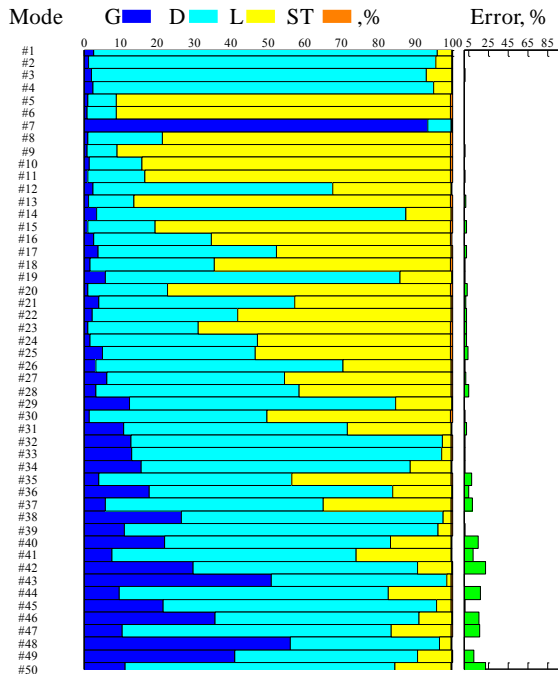


Figure 4-11 Participations and identification error of FE solution of FSM-like C-C by S-S *cFSM* base function

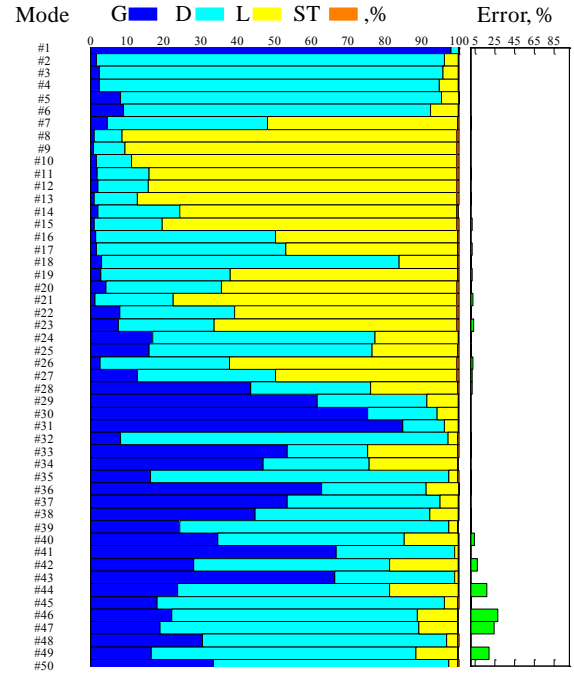


Figure 4-12 Participations and identification error of FE solution of FSM-like S-C by S-S *cFSM* base function

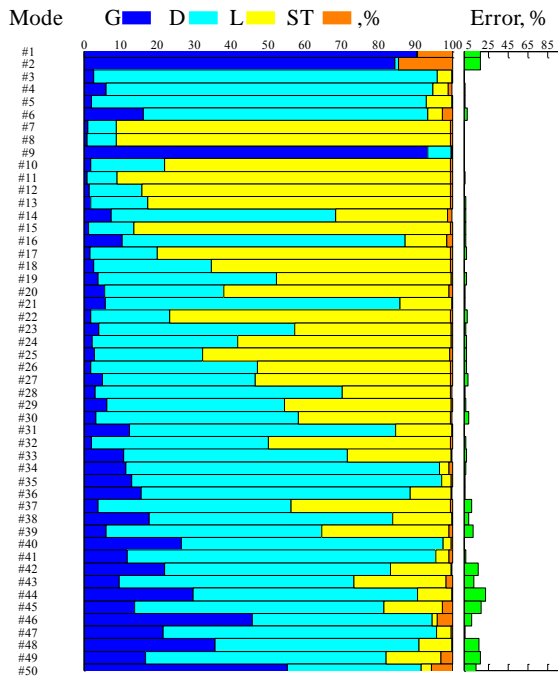


Figure 4-13 Participations, and identification error of FE solution of FSM-like C-G by S-S *cFSM* base function

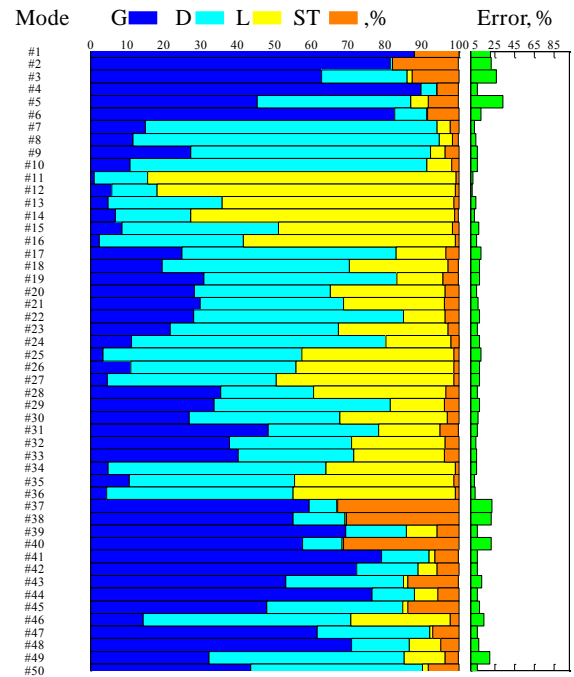


Figure 4-14 Participations and identification error of FE solution of FSM-like C-F by S-S *cFSM* base function

However, the S-S *c*FSM base function fails to correctly identify many of the buckling modes for C-G and C-F boundary conditions. Many of the modes give relatively large errors, though several of them can be attributed to lack of higher longitudinal terms to account for the smaller half-wavelength local buckling. Excepting those, the rest with large errors have a common feature: the end of the buckling mode has translational displacements (guided or free), which the S-S base function, having no translation displacements at both ends, cannot capture. For instances, 1<sup>st</sup> mode in C-G and C-F as shown in Figure 4-2.

In addition, similar modal identification can be performed by using C-F base function for all the other FSM-like boundary conditions. Although the results are not shown here, it is found that C-F base function is capable of appropriately identifying the buckling modes for C-G, and even C-S and C-C but not for S-S.

It is worth noting that the discussion above is based on the predicted errors. The approximated participations are also consistent if the S-S or C-F base function is capable of modal identification for other boundary conditions (e.g., S-S for C-C and C-S, C-F for C-G, C-S, and C-C) although slight differences are observed. More detailed comparison will be discussed, in the context of the proposed generalized base function, in the following sections.

#### ***4.4.3.2 Proposed generalized base function***

A *generalized* set of base functions can be defined in various ways. Since the S-S base function has been proven to effectively capture modal participations of buckling modes without translational movements at the ends, adding base vectors to this base function which are capable of identifying end translational movements could potentially

resolve this issue. Hence, a useful set is proposed as follows: augment the full set of S-S base functions with the fundamental C-F&F-C base functions added, where *fundamental* means the  $G$ ,  $D$  and  $L$  base functions with one single longitudinal term  $m=1$ . The longitudinal shape functions for S-S and C-F boundary conditions are expressed as follows:

$$\text{S-S: } Y_{[m]} = \sin(m\pi y/a) \quad \text{C-F: } Y_{[m]} = 1 - \cos[(m-1/2)\pi y/a] \quad (4-11)$$

C-F and F-C are symmetric pairs that enable translational movements at either end of the member. The proposed *generalized* base functions are the combination of S-S functions with several longitudinal terms and the fundamental C-F and F-C base functions with one ( $m=1$ ) longitudinal term. A direct illustration of this combination for the longitudinal field is shown in Figure 4-15.

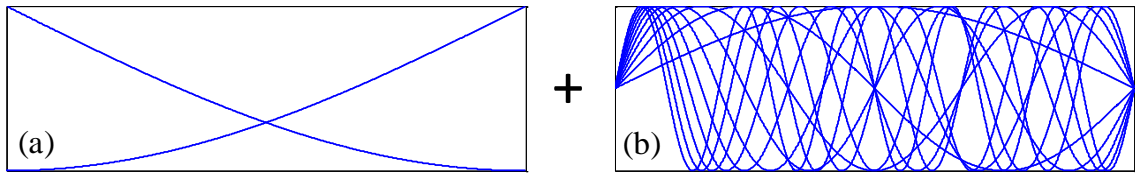


Figure 4-15 Longitudinal field diagram: (a) C-F&F-C  $m=1$ ; (b) S-S  $m=1,2,\dots,10$

Note, the  $ST/O$  base functions in the fundamental C-F&F-C base functions are not included in the *generalized* base functions. Numerical studies show if  $ST/O$  base functions in C-F and F-C for the  $m=1$  longitudinal term are included, participations are predicted with large (artificial)  $ST$  contributions compared to participations of the *associated* base function. If only one (either from C-F or from F-C) set is included, the  $ST$  participation is in the expected range. It seems the similarities of the base vectors of a pair (C-F&F-C), especially the  $ST$  base vectors, are too great even with only  $m=1$  longitudinal term, which may numerically result in higher  $ST$  participation. Therefore,  $ST$  base vectors are not included in the base functions, at least for one of them. In fact, if

both of the  $ST$  base vector in C-F and F-C for  $m=1$  longitudinal term are ignored the solution provides almost the same  $ST$  participation compared to ignoring only one of them. Thus, for computational efficiency, both  $ST/O$  of C-F&F-C  $m=1$  terms are not included into the generalized base functions. As will be discussed later, since the  $ST$  participation is negligible for most cases, all the  $ST$  base vectors in the *generalized* base function can be excluded to save computational time. (Note,  $ST$  contributions are generally small in cold-formed steel since shear deformations are negligible. For other materials, thicker member, etc.,  $ST$  participation can increase.)

Figure 4-16 illustrates selected S-S, C-F and F-C base functions with one longitudinal term. The first global, distortional, and local modes are presented for the member defined in the previous Section (however, the length has been scaled down). Differences are apparent, especially at the ends.

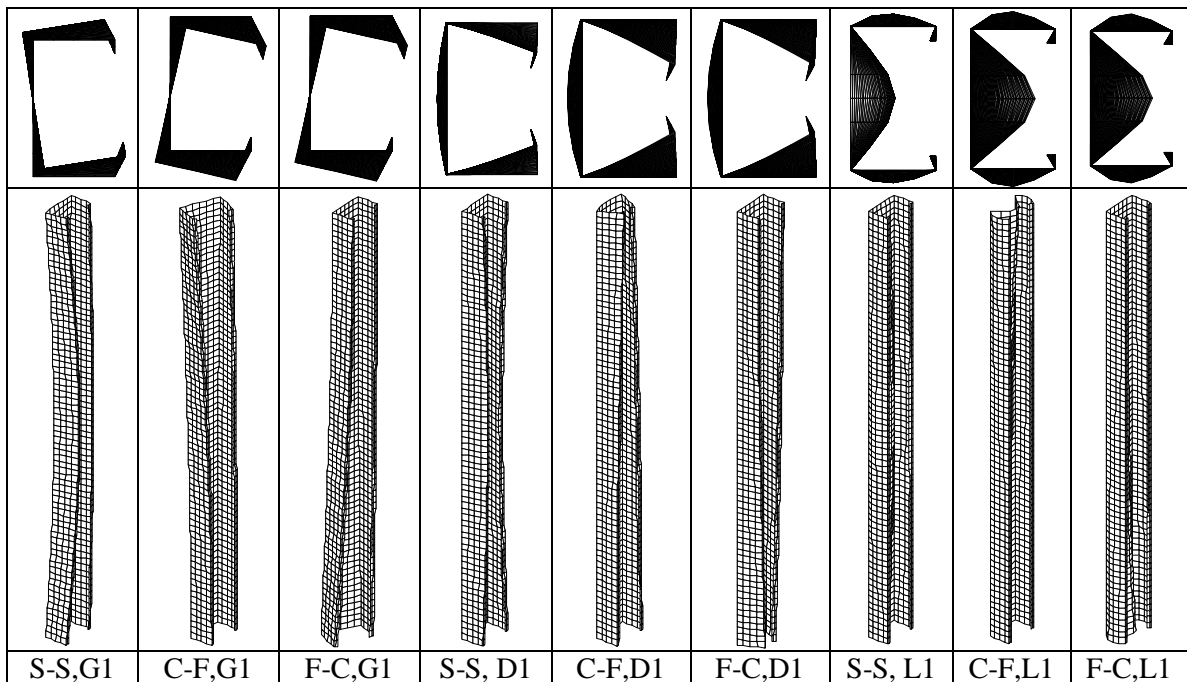


Figure 4-16 S-S, C-F, and F-C of  $m=1$ , G1, D1, L1

#### 4.4.3.3 Modal identification

Modal identification is performed for the FSM-like boundary conditions listed in Section 4.4 by using the proposed *generalized* base functions. The longitudinal terms in *c*FSM base functions of S-S are 40 (from 1 to 40) in total with the fundamental base functions of C-F&F-C pair with the  $m=1$  longitudinal term only. The participations for FSM-like S-S are the same as those identified with the *associated* base functions. For boundary conditions other than FSM-like S-S, the modal identifications are provided in Figure 4-17 through Figure 4-20. The only difference is that the critical loads are not provided.

As far as the identification error is concerned, the errors for *generalized* base functions are in the same level as those using the *associated* base functions. This indicates the applicability of the *generalized* base functions to modal identification of general boundary conditions, at least from one aspect. Moreover, the indication of the participation results is also in accordance with engineering expectations. This can be confirmed by comparing the modal identification participations with the selected buckling modes of the FEM solutions as shown in Figure 4-2.

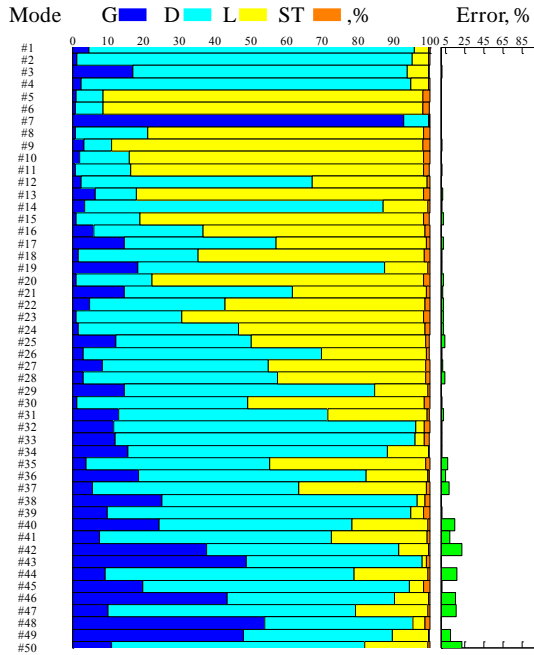


Figure 4-17 Participations and identification error of FE solution of FSM-like C-C by generalized base function

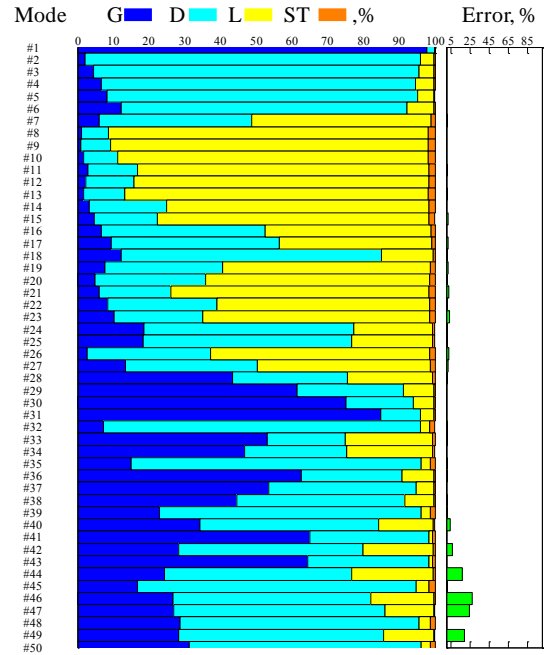


Figure 4-18 Participations and identification error of FE solution of FSM-like S-C by generalized base function

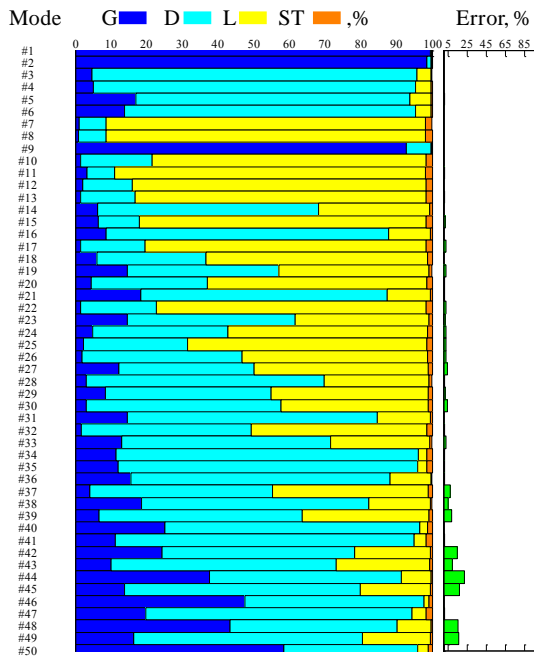


Figure 4-19 Participations, and identification error of FE solution of FSM-like C-G by generalized base function

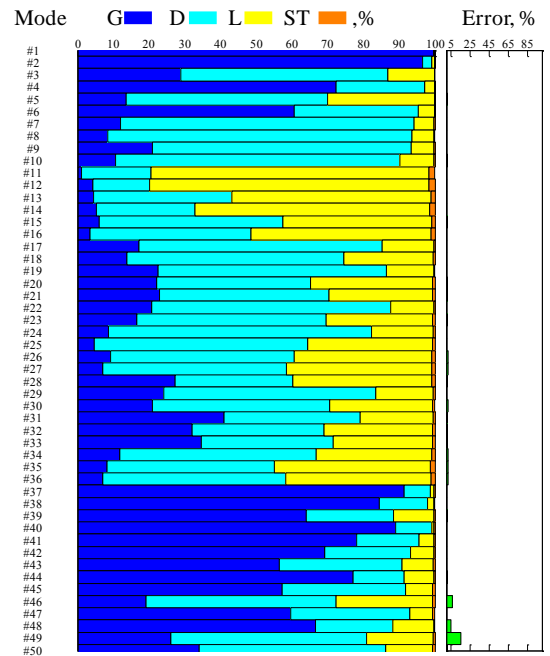


Figure 4-20 Participations and identification error of FE solution of FSM-like C-F by generalized base function

#### 4.4.4 Comparison of participations between associated and generalized base functions

Similar to modal identification in the FSM solution, participations of buckling modes are sensitive to the choice of basis and normalization of the base vectors. For FEM modal identification, all the sensitivities formed in FSM modal identification still exist in FEM modal identification. In addition, the *generalized* base functions that are built up from the base functions of *cFSM* of two boundary conditions (S-S, C-F&F-C) add one more complexity to the sensitivity.

For the member studied with the FSM-like boundary conditions, the participations given by the *associated* base functions are deemed to provide the most reliable results. The *generalized* base functions provide an approximated participation. Though modal identification seems reasonable, as shown in section 4.4.3.3, direct comparisons with those by *associated* base functions are needed to provide the verification of this approximation. The full comparisons of participations for FEM solutions of C-C and C-F boundary conditions are given in Table 4-3. The relative difference of participations and errors predicted by *generalized* base functions to those by *associated* base functions are provided for the first 40 modes. Note, the first 40 modes usually provide enough information to find the characteristic (*G*, *D*, and *L*) buckling modes. At the same time, this can exclude the higher modes with large identification errors, e.g., 46<sup>th</sup> mode.

Table 4-3 Modal identification differences by generalized base functions relative to those  
by associated base functions for C-C

Mode #	$\Delta G$ (%)	$\Delta D$ (%)	$\Delta L$ (%)	$\Delta ST$ (%)	$\Delta Error$ (%)	Mode #	$\Delta G$ (%)	$\Delta D$ (%)	$\Delta L$ (%)	$\Delta ST$ (%)	$\Delta Error$ (%)
1	2.2	-1.3	-1.0	0.2	0.0	21	12.1	5.3	-17.9	0.5	0.4
2	0.1	1.0	-1.2	0.2	0.0	22	3.8	17.1	-21.9	0.9	1.2
3	15.2	-11.6	-3.8	0.2	0.0	23	0.0	5.8	-7.0	1.1	1.2
4	0.8	0.5	-1.5	0.2	0.0	24	0.8	7.8	-9.5	1.0	0.9
5	0.1	-2.3	0.9	1.4	0.0	25	9.6	7.7	-18.1	0.8	2.6
6	0.0	-2.0	0.6	1.4	0.2	26	1.3	-5.6	3.6	0.7	0.0
7	2.6	-2.6	-0.1	0.1	0.0	27	5.1	11.8	-17.7	0.8	0.3
8	0.2	-5.1	3.7	1.3	-0.1	28	1.8	8.4	-11.0	0.8	3.3
9	2.4	-1.0	-2.7	1.4	0.7	29	5.6	-2.4	-3.4	0.3	-0.1
10	0.9	-1.4	-0.8	1.3	-0.4	30	0.2	15.0	-16.2	1.0	0.1
11	0.1	-0.1	-1.4	1.3	1.0	31	6.3	5.2	-11.9	0.5	1.5
12	1.3	4.6	-6.5	0.5	-0.1	32	-1.0	0.3	-0.4	1.2	0.0
13	5.6	-0.9	-6.0	1.3	1.7	33	-2.1	1.3	-0.4	1.2	0.0
14	1.6	-1.6	-0.3	0.3	0.0	34	7.1	12.1	-19.3	0.1	0.1
15	0.2	0.4	-1.9	1.3	1.9	35	2.4	7.1	-10.3	0.8	5.6
16	4.5	2.8	-8.4	1.0	-0.7	36	10.0	11.0	-21.3	0.2	4.3
17	12.7	8.7	-22.0	0.6	1.7	37	3.3	4.0	-7.9	0.6	5.0
18	0.5	7.5	-9.0	1.0	-0.3	38	5.3	-5.3	-1.0	1.0	0.0
19	14.4	-9.4	-5.3	0.2	0.0	39	0.1	-0.6	-0.8	1.4	0.0
20	0.2	2.4	-4.0	1.3	2.0	40	13.8	-0.6	-13.4	0.2	11.8
<b>Statistical summary:</b>											
				$\Delta G$ (%)	$\Delta D$ (%)	$\Delta L$ (%)	$\Delta ST$ (%)	$\Delta Error$ (%)			
				Mean:	3.6	1.4	-5.8	0.8	1.1		
				Min:	-2.1	-11.6	-22.0	0.1	-0.7		
				Max:	15.2	15.0	3.7	1.4	11.8		

Table 4-4 Modal identification differences by generalized base functions relative to those  
by associated base functions for C-F

Mode #	$\Delta G$ (%)	$\Delta D$ (%)	$\Delta L$ (%)	$\Delta ST$ (%)	$\Delta Error$ (%)	Mode #	$\Delta G$ (%)	$\Delta D$ (%)	$\Delta L$ (%)	$\Delta ST$ (%)	$\Delta Error$ (%)
1	0.0	0.0	0.0	0.0	0.0	21	5.8	-1.5	-4.9	0.5	0.3
2	1.5	-1.1	-0.4	0.0	0.0	22	4.8	-3.1	-1.9	0.2	0.0
3	8.4	-7.1	-1.4	0.0	0.0	23	4.5	-1.4	-3.6	0.6	0.4
4	4.5	-4.3	-0.3	0.1	0.0	24	2.2	-0.6	-2.0	0.3	0.0
5	4.8	-3.3	-1.6	0.1	-0.1	25	2.3	0.7	-3.6	0.6	-0.5
6	1.3	-1.4	-0.1	0.2	0.0	26	3.7	0.5	-4.8	0.7	1.3
7	4.6	-4.7	-0.1	0.2	0.0	27	4.5	-0.6	-4.6	0.7	0.9
8	3.1	-3.6	0.3	0.2	0.0	28	6.9	-2.0	-5.6	0.7	0.2
9	7.8	-7.8	-0.2	0.2	0.0	29	4.6	-2.9	-2.0	0.3	-0.1
10	5.5	-5.3	-0.4	0.2	0.0	30	4.9	-1.1	-4.3	0.6	1.5
11	0.3	1.4	-3.0	1.4	0.1	31	7.3	-4.4	-3.3	0.4	-0.1
12	1.6	0.5	-3.5	1.4	-0.1	32	6.9	-4.3	-3.1	0.6	0.5
13	2.2	1.5	-4.6	1.0	0.3	33	7.5	-4.5	-3.6	0.6	0.5
14	1.9	1.3	-4.4	1.2	-0.1	34	9.4	-5.8	-4.3	0.7	0.8
15	2.1	0.8	-3.7	0.7	0.2	35	3.0	-1.7	-2.2	1.0	1.0
16	1.9	0.8	-3.5	0.9	-0.1	36	3.7	-1.7	-2.9	0.9	0.3
17	5.0	-3.5	-1.8	0.3	0.1	37	14.0	-13.1	-1.2	0.3	0.0
18	4.2	-1.3	-3.3	0.4	-0.1	38	22.6	-20.7	-2.2	0.3	0.0
19	6.0	-4.0	-2.2	0.3	0.0	39	7.8	-5.9	-2.2	0.3	0.6
20	6.1	-2.3	-4.4	0.6	0.0	40	17.2	-16.8	-0.7	0.3	0.0
<b>Statistical summary:</b>											
				$\Delta G$ (%)	$\Delta D$ (%)	$\Delta L$ (%)	$\Delta ST$ (%)	$\Delta Error$ (%)			
				Mean:	5.6	-3.7	-2.5	0.5	0.2		
				Min:	0.0	-20.7	-5.6	0.0	-0.1		
				Max:	22.6	1.5	0.3	1.4	1.5		

To begin with, both base functions are capable of resolving identification error to a practically negligible level (see Figure 4-5, Figure 4-8, Figure 4-17 and Figure 4-20). Next, the differences in terms of the participations are practically small for most modes, especially the first 30 modes. This is especially true for distinct modes (e.g., mode #1 distortional, #5 local, #7 global in Figure 4-17 for C-C). Further, from an average point of view, the differences are practically small for the first 40 modes, as summarized in Table 4-3 and Table 4-4. Hence, it can be safely concluded that the participation results are in good agreement.

However, differences do exist, even significant differences for some modes are observed in Table 4-3 and Table 4-4. Two observations can be drawn from the comparison tables:

First, the *generalized* base functions in general tend to predict more *G* contributions than the *associated* base functions and rarely much higher (10 to 20%) than expected. This might be due to the difference of the warping distributions at the ends in *generalized* base functions and the *associated* base functions (see Chapter 3 for definition of warping distributions related to *GD* space). Fundamental base functions with warping free end(s) are forced to adjust to more *G* contributions (sometimes also *D*) for the warping fixed end(s) (e.g., C-C in Table 4-3) in the participations. However, this usually does not affect the modal identification for suitably predicting the dominance of the buckling mode, e.g., modal identification by *generalized* base functions of the 3<sup>rd</sup> mode of C-C still correctly captures the distortional buckling dominance of the mode (with 77% *D* contribution) which is the same as that by *associated* base functions (with 88% *D* contribution)

although larger differences are observed between the two base functions as shown in Table 4-3.

Second, large differences usually exist in modes that are indistinct, or in other words, highly coupled modes; though some exceptions exist. For these highly coupled modes, since the differences of the predicted participations could be big, different base functions may indicate a change in predicted dominance for certain buckling modes, such as the 21<sup>st</sup> mode of C-C; however, this is rare. In addition, coupled modes may have complicated post-buckling reserve and reduced ultimate capacity, that should be treated more carefully.

It is worth noting that neither the *associated* or *generalized* base functions are “correct”. Even though FEM solutions of the FSM-like boundary conditions identified by their *associated* base functions in *cFSM* are thought to be conceptually correct at least in the sense of handling the boundary conditions. However, the FEM solution in general can capture more localized modes than FSM even with the same boundary conditions. In addition, most of the shell elements employed are based on Mindlin plate theory accounting for transverse shear (the FSM solutions do not) that could make a difference in buckling analysis for thicker members. Therefore, as in FSM, there are sensitivities to basis and normalization, the base function itself can be possibly treated as an additional sensitivity for FE modal identification.

Moreover, in elastic buckling analysis, we are greatly interested in characteristic buckling modes (i.e., global, distortional, and local). A comparison of the participations by the *generalized* base functions with the *associated* base functions are given in Table 4-5 for all the FSM-like boundary conditions. The differences are small for these

important modes, which further validates the applicability of the *generalized* base functions.

Table 4-5 Participations of FEM solution by associated and generalized base functions

Boundary case	Dominant mode	Mode number	FEM solution (Associated)				FEM solution (Generalized)			
			G (%)	D (%)	L (%)	ST (%)	G (%)	D (%)	L (%)	ST (%)
<b>S-S</b>	<b>G</b>	#1	99.4	0.6	0.0	0.0	99.4	0.6	0.0	0.0
	<b>D</b>	#3	1.4	95.5	3.1	0.1	1.4	95.5	3.1	0.1
	<b>L</b>	#9	0.9	10.3	88.4	0.5	0.9	10.3	88.4	0.5
<b>C-C</b>	<b>G</b>	#7	90.3	9.4	0.2	0.1	93.4	6.4	0.1	0.1
	<b>D</b>	#1	2.5	92.4	5.0	0.1	4.7	91.3	3.9	0.1
	<b>L</b>	#5	1.0	10.0	88.5	0.5	1.0	7.8	90.7	0.5
<b>S-C</b>	<b>G</b>	#1	96.4	3.4	0.1	0.2	97.9	2.1	0.0	0.0
	<b>D</b>	#2	1.8	94.0	4.0	0.2	2.0	94.1	3.8	0.1
	<b>L</b>	#8	1.1	9.9	88.5	0.5	1.2	7.6	90.7	0.5
<b>C-F</b>	<b>G</b>	#1	99.6	0.1	0.3	0.0	99.7	0.1	0.2	0.0
	<b>D</b>	#7	7.4	87.0	5.6	0.1	11.9	82.3	5.6	0.1
	<b>L</b>	#11	0.8	18.2	80.8	0.3	1.1	19.8	78.7	0.4
<b>C-G</b>	<b>G</b>	#1	99.3	0.7	0.0	0.0	99.6	0.4	0.0	0.0
	<b>D</b>	#3	2.3	92.5	5.0	0.1	4.7	91.3	3.9	0.1
	<b>L</b>	#7	0.9	10.0	88.6	0.5	1.0	7.8	90.7	0.5

In summary, the *generalized* base functions are a suitable substitute for the *associated* base function for FSM-like boundary conditions. In fact, it is the only choice for more complex boundary conditions where no *associated* base functions are available.

#### 4.5 Numerical studies: arbitrary boundary conditions

The proposed *generalized* base functions are capable of performing modal identification for FEM models with arbitrary boundary conditions. To demonstrate the capability of the *generalized* base functions, two sets of boundary conditions are considered for numerical illustration: 1) semi-rigid end boundary conditions; and 2) mixed end boundary conditions.

### 4.5.1 Semi-rigid end boundary conditions

In a real frame, the boundary conditions of a column or beam are in general not actually simply-supported or clamped but highly dependent on the connection detailing and bracing. Therefore, both translational and rotational deformations at the ends are influenced by the stiffness of the connections and the overall frame system. For individual members in a frame, the boundary conditions are treated as semi-rigid boundary conditions. Practically, appropriate rotational/translational springs are employed to simulate the semi-rigid conditions. Three simplified cases are illustrated in Figure 7 to represent the possible scenarios of semi-rigid boundary conditions.

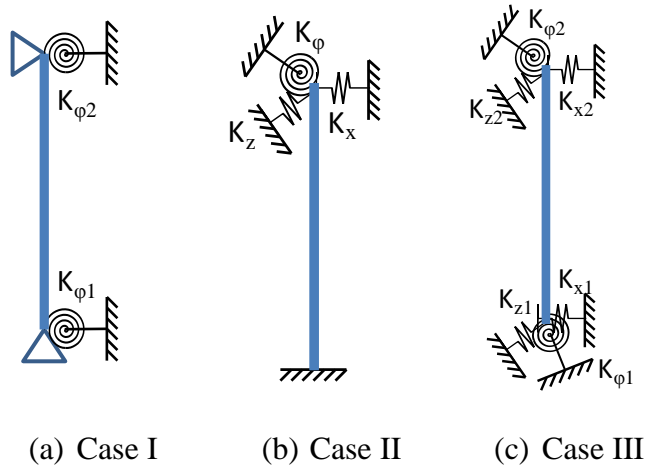


Figure 4-21 Semi-rigid boundary condition cases

Figure 7(a) shows the semi-rigid boundary conditions between S-S and C-C with rotational springs at ends, Figure 7(b) shows the case between C-F and C-C with both translational and rotational springs at one end, and Figure 7(c) shows a more generalized semi-rigid boundary condition case where both ends are capable of deforming translation and rotation.

#### 4.5.1.1 Case I

To investigate the applicability of the *generalized* base functions for semi-rigid case I, a numerical example is studied for a semi-rigid column that is warping free at one end and fixed at other end. The section is the same cross section as used previously (Figure 4-1) with a column length of 2000 mm. The stiffness of the rotational springs are all 300 N-m/rad on each node at both ends (locally restrained rotational springs). The modal identification results by *generalized* base functions (40 longitudinal terms in S-S) are presented in Figure 4-22.

Small errors are found for most of the modes except several higher modes that need larger longitudinal terms to alleviate the error due to local buckling at small half-wavelength as explained in Section 4.4.2.1. The participation results are also in accordance with engineering expectations, found by examining the buckling modes.

In this semi-rigid boundary case, the warping is fixed at one end and free at the other end, which is similar to S-C boundary conditions. For thin-walled members, warping plays a central role in the member's behavior. The effect of rotational springs is less important, at least for columns. Therefore, although the local restrained rotational springs (at each node) have been studied, conclusions can be drawn for globally restrained rotational springs (at the end as a whole). The proposed modal identification method has no problems handling both cases.

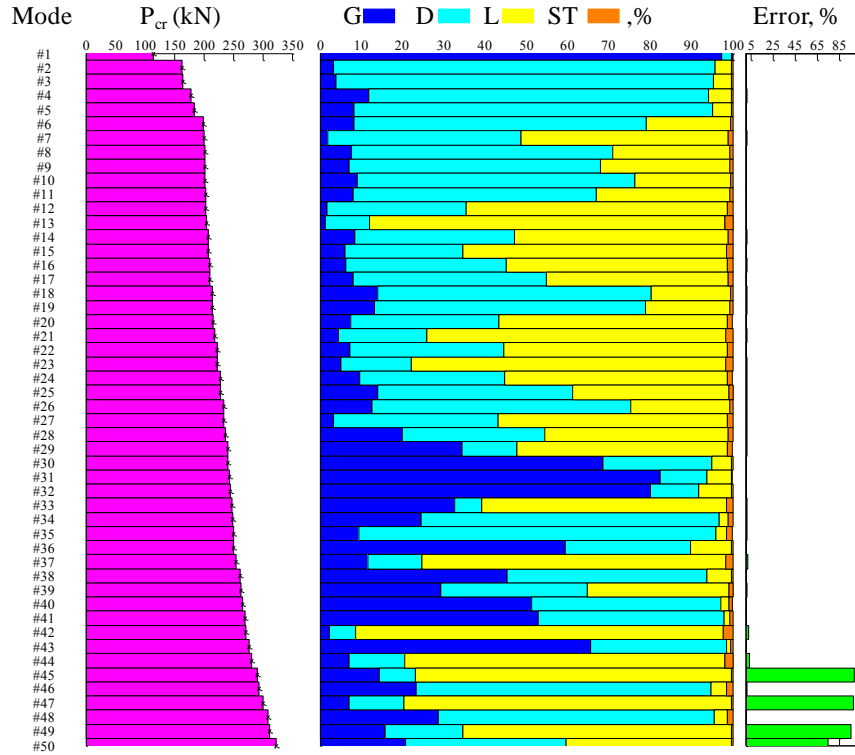


Figure 4-22 Modal identification of semi-rigid case I

#### 4.5.1.2 Case II

For this case, two options are studied to illustrate the proposed modal identification method. The two options depend on where the springs are located at the end of the cross section.

##### (a) Partially restrained at the end as a whole

The boundary conditions and springs are shown in Figure 4-23. The cross section is again that of Figure 4-1 with a length of 2000 mm. The stiffnesses of the springs are:  $K_x=20$  N/mm,  $K_z=10$  N/mm,  $K_{\phi_x}=100$  N-m/rad,  $K_{\phi_z}=100$  N-m/rad, and  $K_{\phi_y}=100$  N-m/rad. The *generalized* base functions (40 longitudinal terms in S-S) are used in identifying the modal participations. Participations are shown in Figure 4-24 with critical loads. Errors are small and participations match engineering expectations, as shown in Figure 4-25.

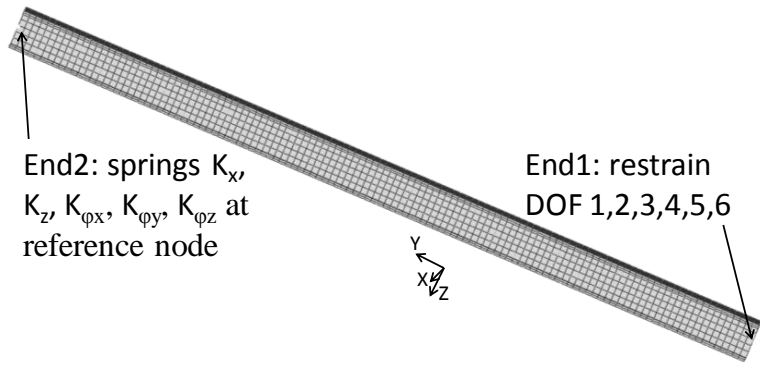


Figure 4-23 Boundary conditions and springs in FEM model

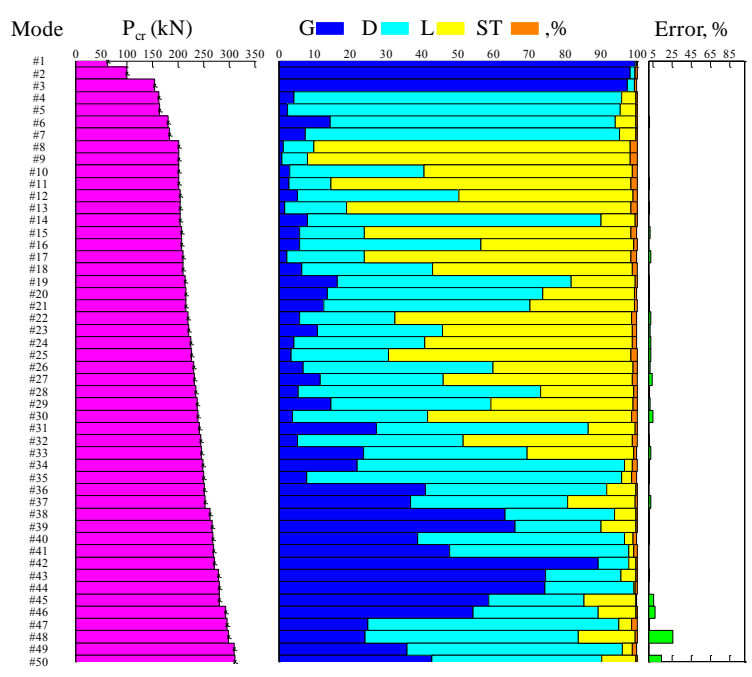


Figure 4-24 Modal identification of semi-rigid case II - partially restrained at the end as a whole

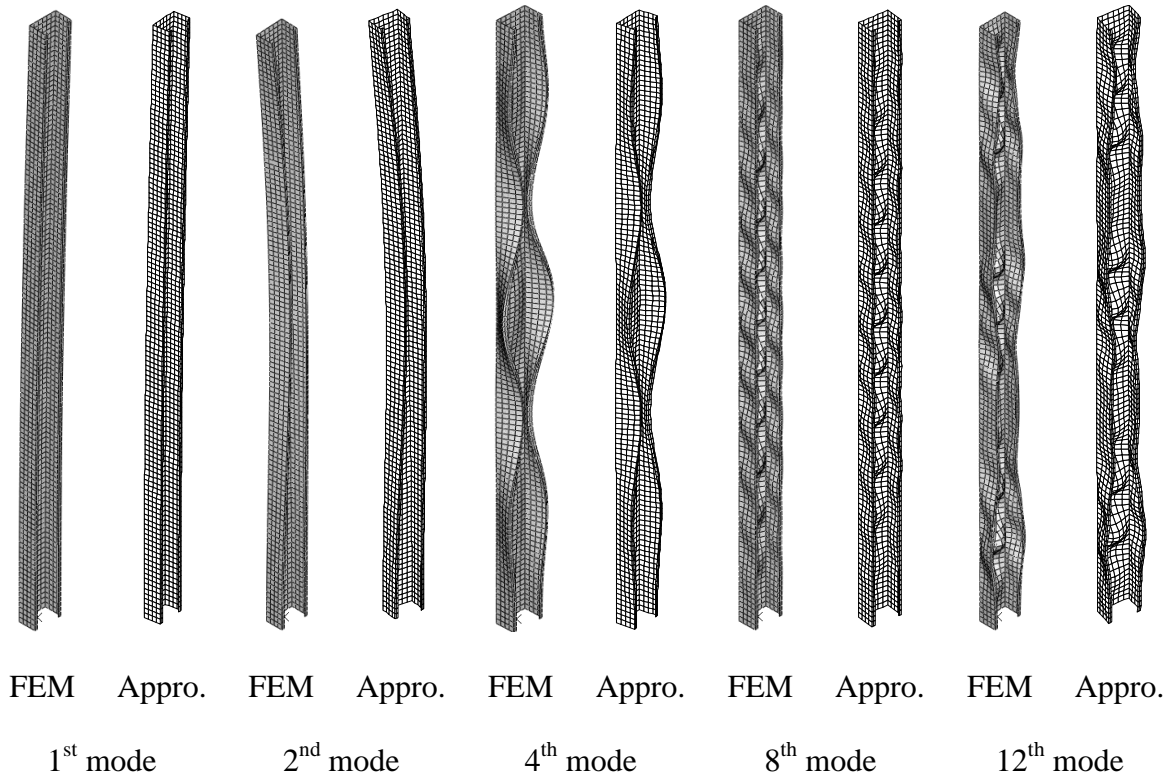


Figure 4-25 FEM and approximated mode shapes for selected modes

(b) Partially restrained ONLY at corners (more general)

The boundary conditions and springs are shown in Figure 4-26. The cross section is again that of Figure 4-1 with a length of 2000 mm. The rotational springs are assumed to be zero in this case, and the translation spring stiffnesses at each node of the four corners are  $\frac{1}{4}$  of the translational spring stiffnesses in the preceding (case a). Modal identification is performed by using the *generalized* base functions (with 40 longitudinal terms in S-S) and participations and errors are provided in Figure 4-27, along with the critical loads. Again, the *generalized* base functions work well even for this more complicated semi-rigid boundary conditions. Localized mode shapes are found because of the discrete spring constraints at the end, as shown in Figure 4-29, along with the *cFSM* approximated shapes.

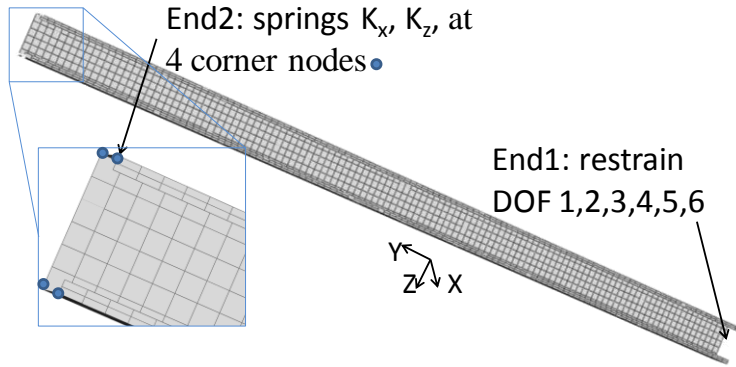


Figure 4-26 Boundary conditions and springs in FEM model

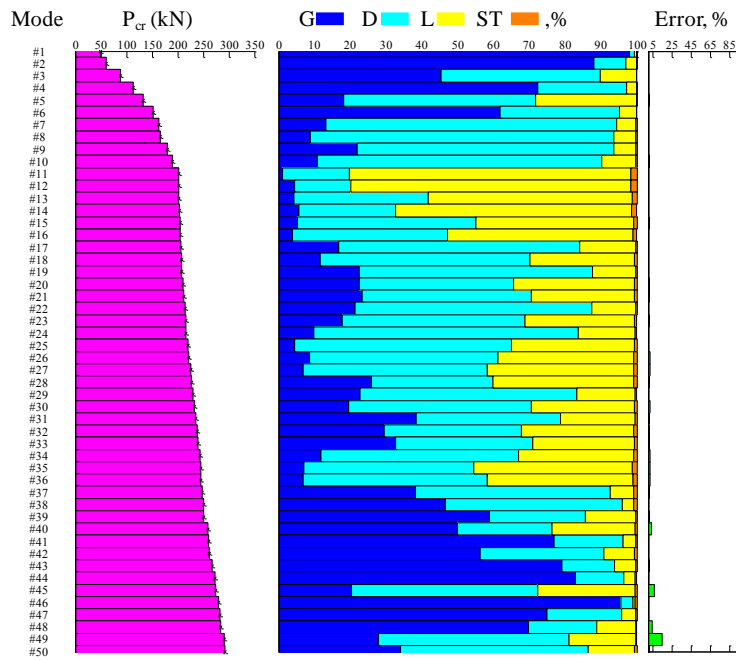


Figure 4-27 Modal identification of semi-rigid case II - partially restrained at four corners

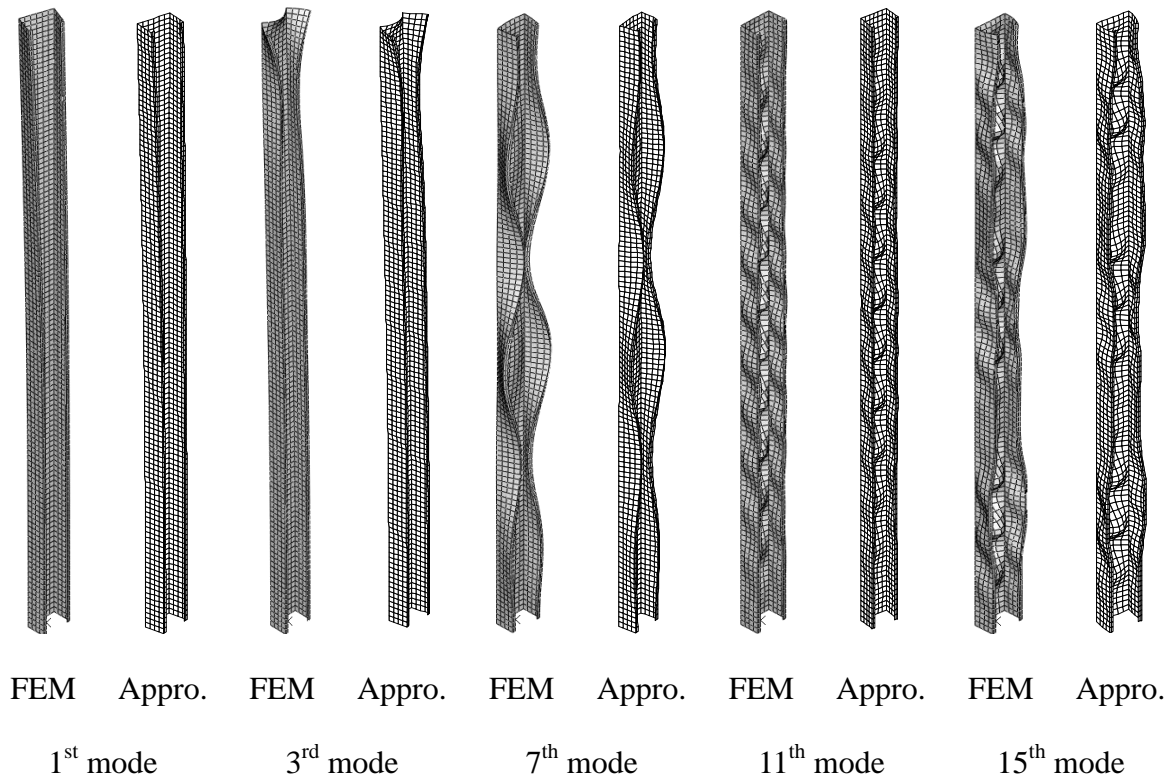


Figure 4-28 FEM and approximated mode shapes for selected modes

#### ***4.5.1.3 Semi-rigid Case III***

For this case, the boundary conditions and springs are shown in Figure 4-29. Note, the system may be kinematically unstable if there are not enough springs or the stiffnesses of the springs are too small. The column length is 2000 mm and again the cross section is that of Figure 4-1. Uniform compression loading is applied as nodal forces at End1. Modal identification is performed using *generalized* base functions (with 40 longitudinal terms in S-S). Participations and errors are provided in Figure 4-27 along with the critical loads. Buckling mode shapes that have translational movements at both ends (1<sup>st</sup> mode) are found, as shown in Figure 4-29 along with the *cFSM* approximated shapes. Again, the *generalized* base functions work well for this semi-rigid boundary conditions.

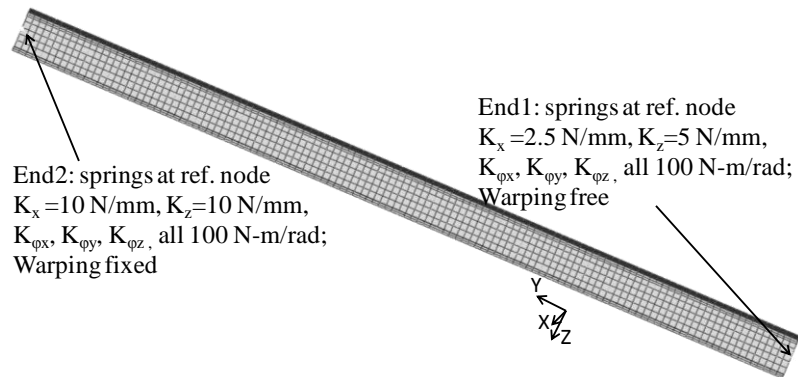


Figure 4-29 Boundary conditions and springs information in FEM model

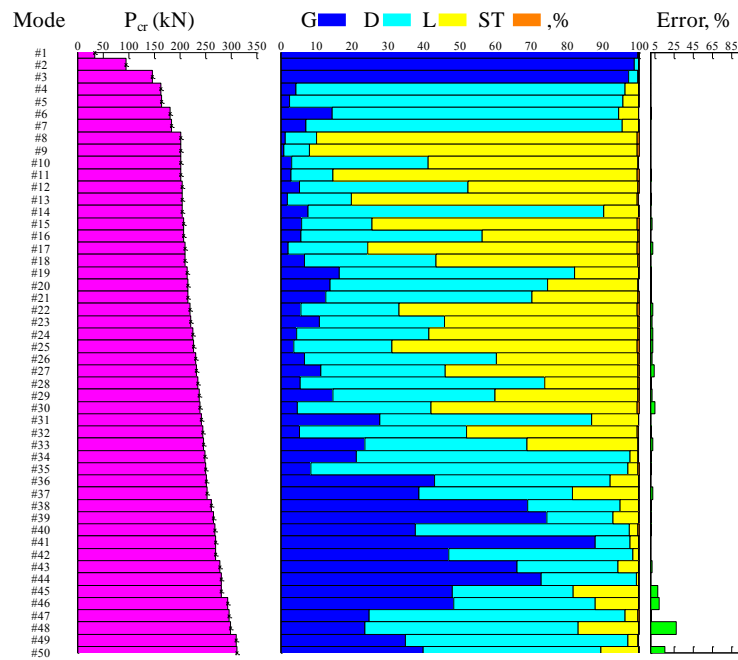


Figure 4-30 Modal identification of semi-rigid case III

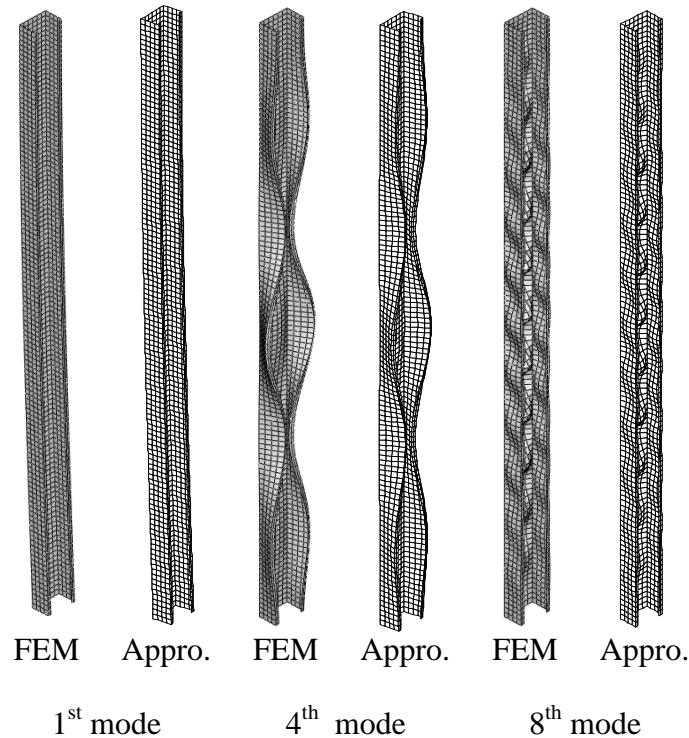


Figure 4-31 FEM and approximated mode shapes for selected modes

#### 4.5.2 Mixed end boundary conditions

Thin-walled cross sections may be restrained differently on each flat plate at the ends, thus resulting in so-called mixed boundary conditions. The discontinuity of the boundary conditions at the junctions generates different stress distributions, which in return change the buckling behavior of the member. FSM is not readily able to correctly capture the buckling behavior as explained in Section 2.7. On the other hand, for such boundary conditions FEM is effective, of course if FEM is employed modal identification is still needed for design (at least for the characteristic modes).

The first thing one should realize when performing the FEM modal identification for mixed boundary conditions is that the applied based vectors from “pure” ends (such as, S-S, C-F) violate all of the mixed boundary conditions in both the cross section and longitudinal direction, thus reducing the numerous errors especially at the ends may not

be possible by using these “pure” base vectors (associated). Hence, the *generalized* base functions are the only choice for modal identification of such boundary conditions.

As illustrated in Figure 4-32, this type of mixed boundary conditions usually has certain nodes at the ends laterally unrestrained. Now, consider the mixed boundary cases in Figure 4-32 for a column ( $L=1200$  mm) with the same cross section as before (Figure 4-1, Section 4.4). Uniform compression loading is applied at both ends.

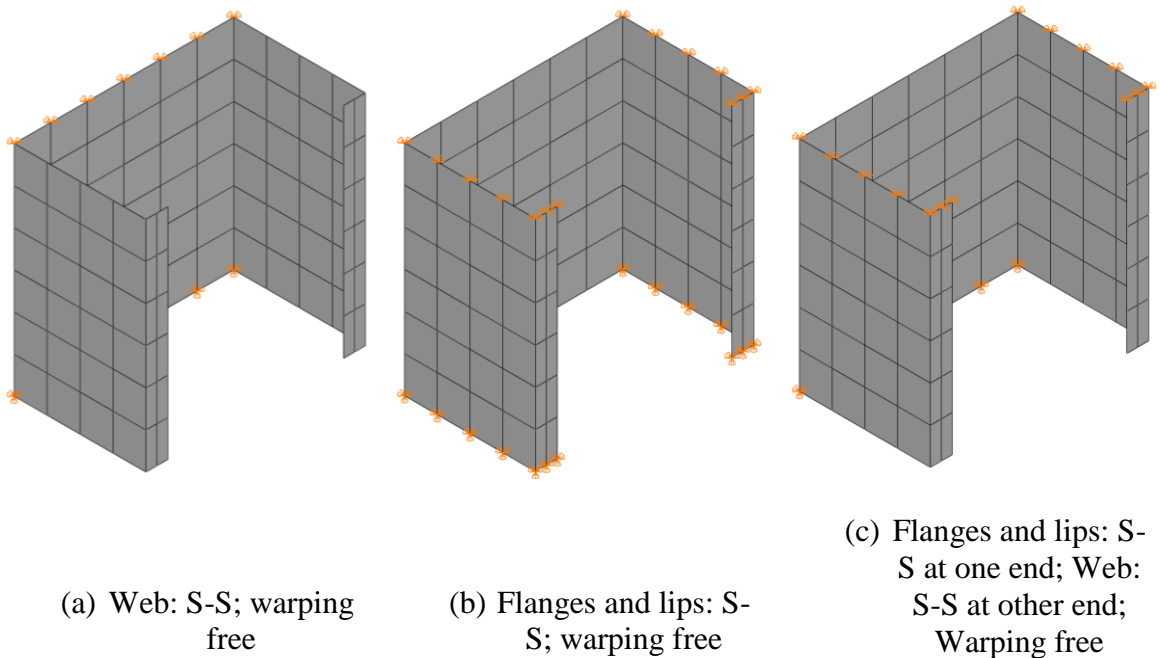


Figure 4-32 Mixed boundary cases

Participations and errors along with the critical loads are provided in Figure 4-33 - Figure 4-35. Buckling mode shapes are shown in Figure 4-29 for selected modes. The identification errors for all the buckling modes are negligible. Moreover, the participation percentage agrees well with those engineering observation. For example, the 1<sup>st</sup> mode of case b shows localized local buckling at the end with some distortional buckling features near the end as well. This is correctly captured by the modal identification, as shown in Figure 4-34. Thus, to sum up, the *generalized* base functions are even able to predict the buckling mode with negligible identification errors for mixed boundary conditions.

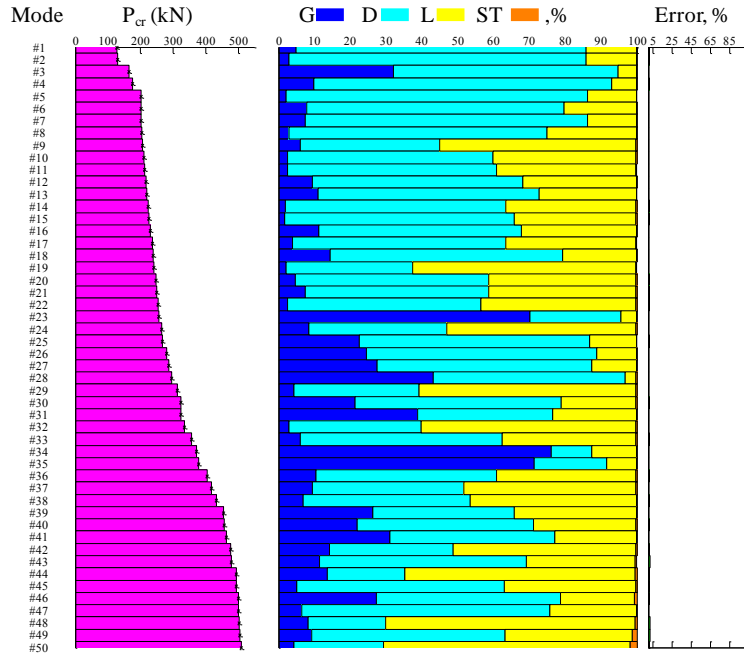


Figure 4-33 Modal identification of mixed boundary case a

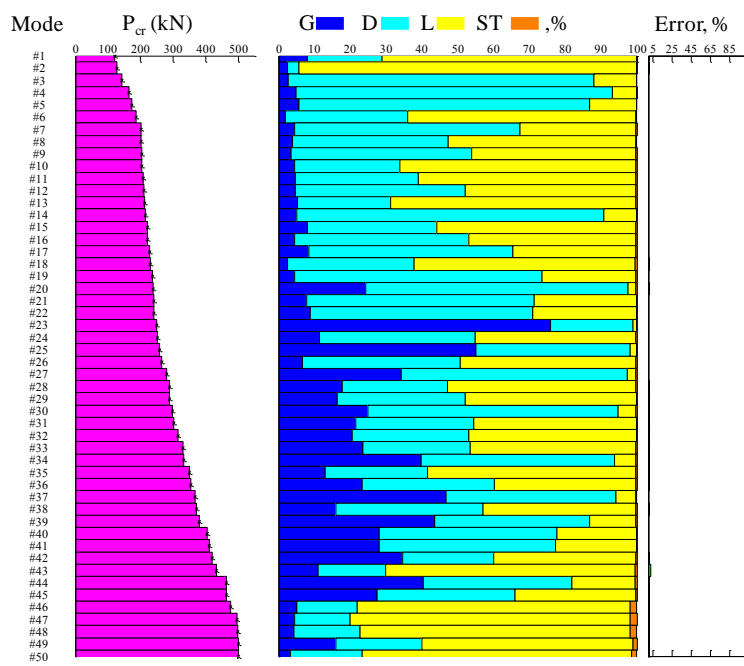


Figure 4-34 Modal identification of mixed boundary case b

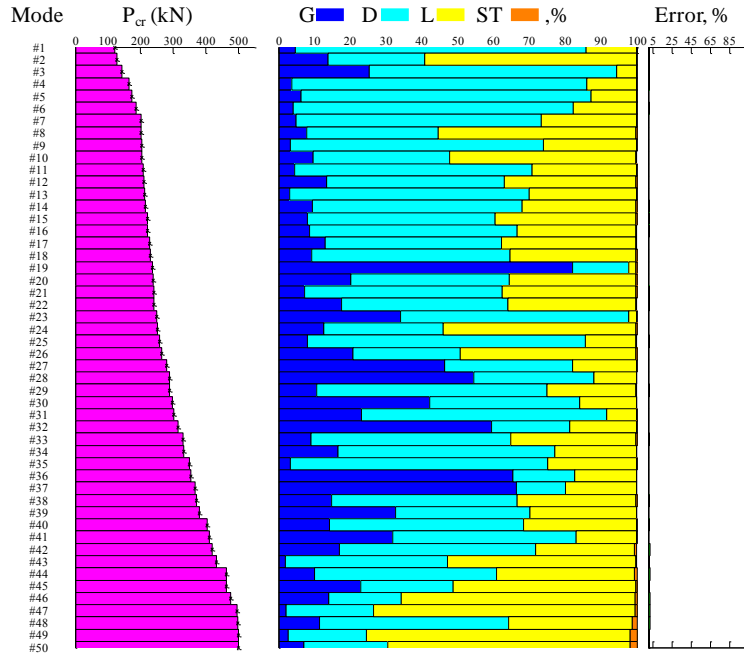


Figure 4-35 Modal identification of mixed boundary case c

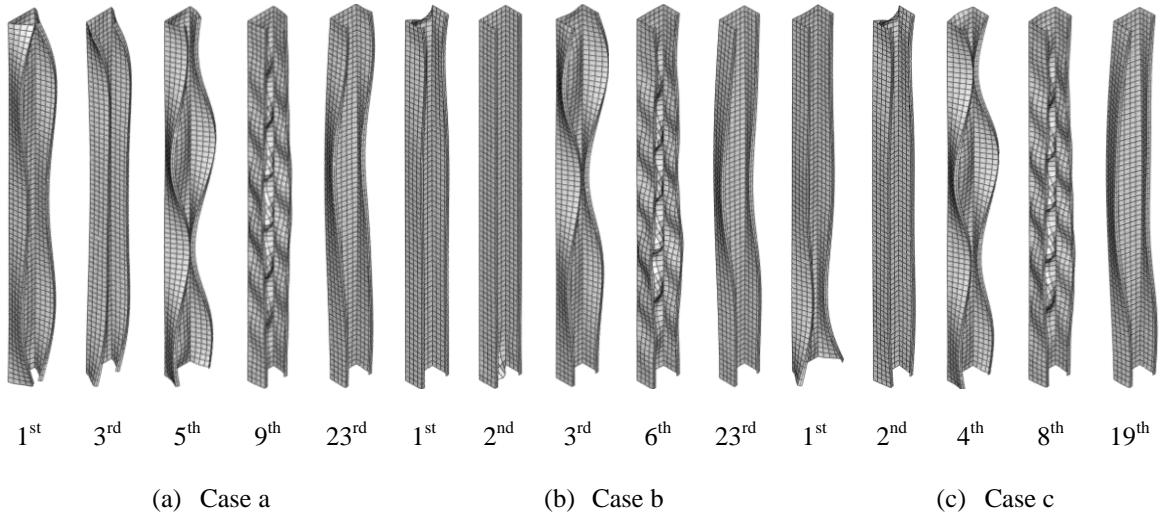


Figure 4-36 FEM mode shapes for selected modes

#### 4.6 Numerical studies: partially restrained members

In a purlin-beam system or a column with sheathing, the contribution of the purlin or wall to the member behavior can be simplified by springs, i.e., mainly one rotational spring and two translational springs. Usually global buckling is greatly restrained by the

spring stiffnesses while distortional buckling is significantly influenced by the springs as well. The proposed modal identification method can handle these kinds of partially restrained systems. Here a simply-supported beam is modeled with rotational and translational springs along the center of the upper flange as shown in Figure 4-37 along with the boundary conditions and loading. The length of the beam is 2000 mm under major-axis bending and springs are distributed every 200 mm along the length. As shown in Figure 4-37, there are three springs at each constrained node, one rotational spring ( $K_\theta$ ) and two translational springs ( $K_x$ ,  $K_z$ ).

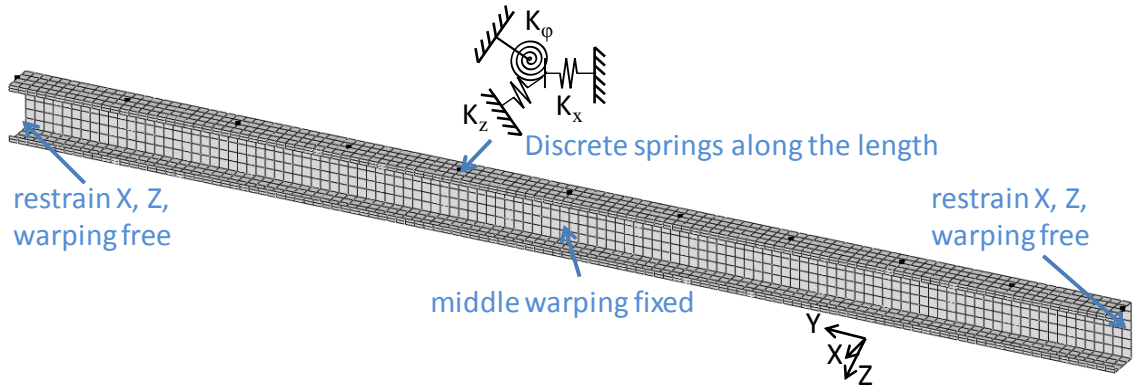


Figure 4-37 Partially restrained simply supported beam

Sheathing or walls interpreted as spring stiffnesses have been studied in terms of their influence on the member's buckling behaviors in the literature [57-61]. Experimental tests determining the spring stiffness of the walls were conducted by Vieira et al [60]. In this section, the elastic buckling behavior is studied again in terms of the modal identification for different spring cases. Of course, the first goal is to demonstrate that the proposed modal identification method can handle the partially restrained member; then interesting mode transitions by changing the stiffness of the restraints (springs) can be observed from the participations. Three cases are considered: 1) Case 1: no springs, in

other words, no restraints on the beam; 2) Case 2: weak springs where  $K_\theta$  is equal to 5.45 N\*mm/rad and  $K_x$  and  $K_z$  are equal to 18.2 N/mm at each node; 3) Case 3: practical level springs where  $K_\theta$  is equal to 54500 N\*mm/rad and  $K_x$  and  $K_z$  are equal to 90.9 N/mm at each node. (See [59] for more information on spring stiffness.)

Modal identification has been performed for the three beam cases by using the *generalized* base functions (with 50 longitudinal terms in S-S). Note, for these cases, where no translational movements exist at the ends, and even with discrete springs along the length, modal identification can be performed by using S-S base functions only as well. As demonstrated previously (Section 4.4.4), *generalized* base functions predict consistent participation results as *associated* base functions, particularly for S-S there is no difference. Since a unified set of base functions that applies to any arbitrary boundary conditions is the ultimate goal, only the results from generalized base functions are discussed here. Participations and errors for the first 50 modes are given in Figure 4-38 - Figure 4-40 along with the critical moments.

As far as the performance of the modal identification is concerned, the selected examples illustrate the applicability of the method for a restrained member. The errors are small, except for several higher modes that include local buckling with smaller half-wavelengths (see Section 4.4.2). It is noticeable that with the restraints of the springs, these local buckling modes with smaller half-wavelengths are more present in the higher modes, e.g., as shown in Figure 4-40. Detailed examination of the participations shows excellent agreement with engineering expectations (as provided in Figure 4-41 for selected buckling modes).

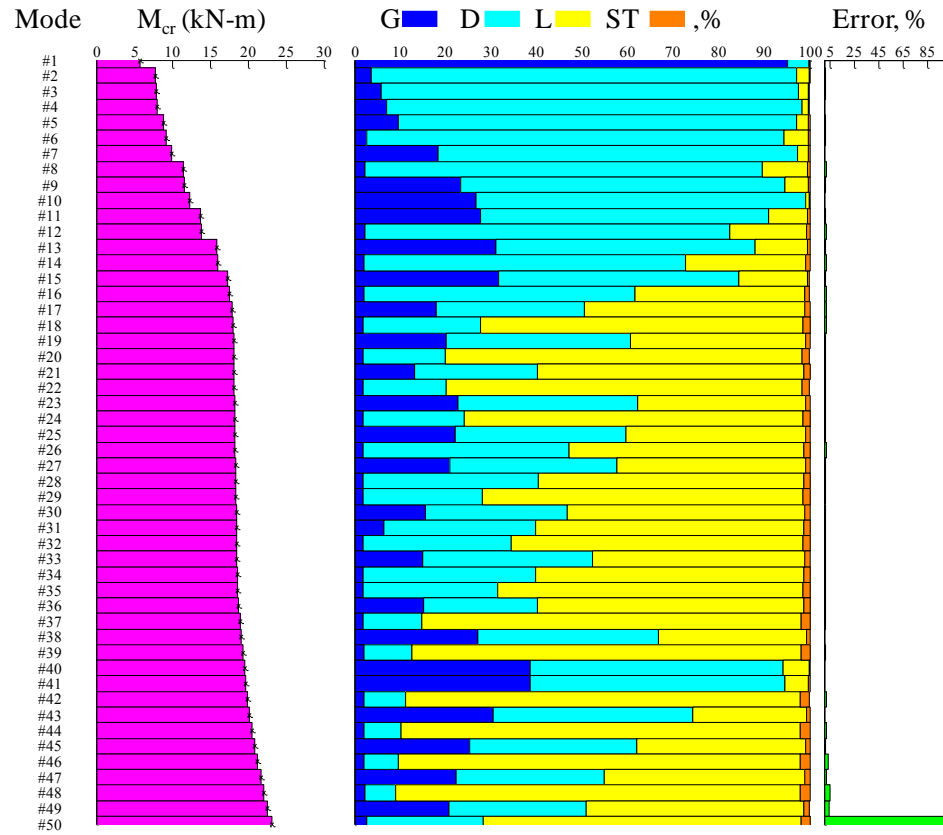


Figure 4-38 Modal identification of beam without springs

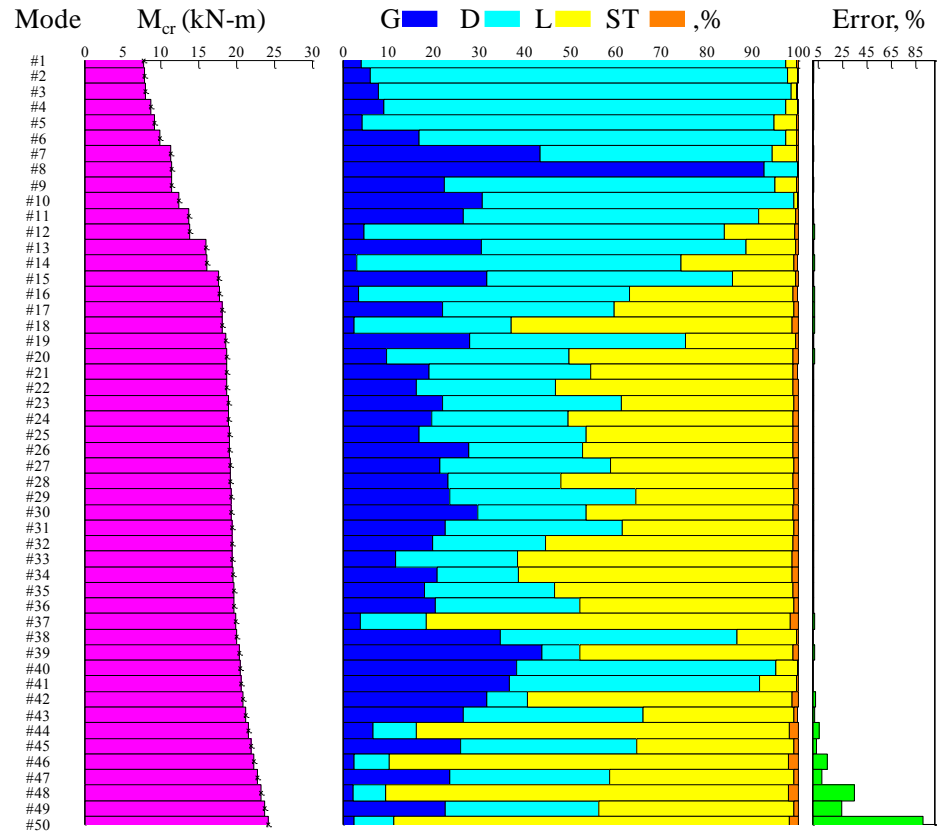


Figure 4-39 Modal identification of beam with weak springs

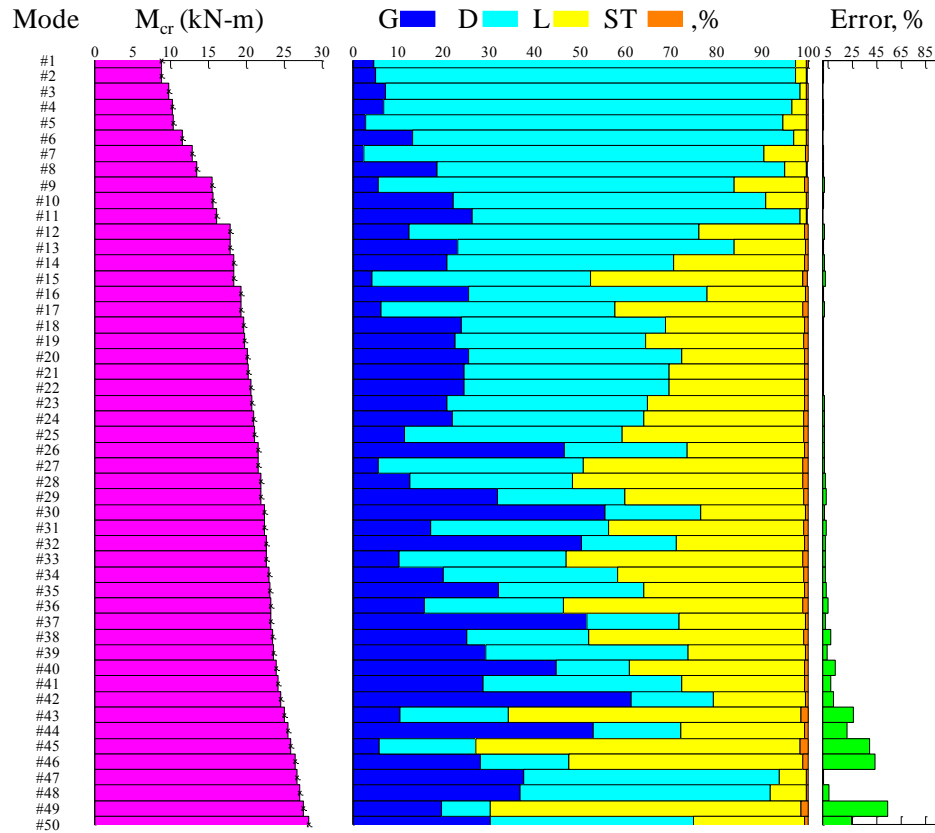


Figure 4-40 Modal identification of beam with practical springs

The characteristic buckling modes can be identified based on the participations, as discussed further in Chapter 7, though quantification is still needed. However, based on the modal identification results and critical loads, the influence of the springs on the buckling behaviors of the beam can still be investigated. Clearly, global buckling is greatly restrained by the springs. Depending on how global buckling is identified, the beam may be interpreted as fully restrained against global buckling with the practical springs (case 3).

The distortional buckling mode dominates as the lowest buckling mode in the presence of weak springs, which is approximately the 2<sup>nd</sup> mode for beam without springs.

For a beam with practical springs, the 1<sup>st</sup> mode is still distortional buckling mode, but at a higher critical moment.

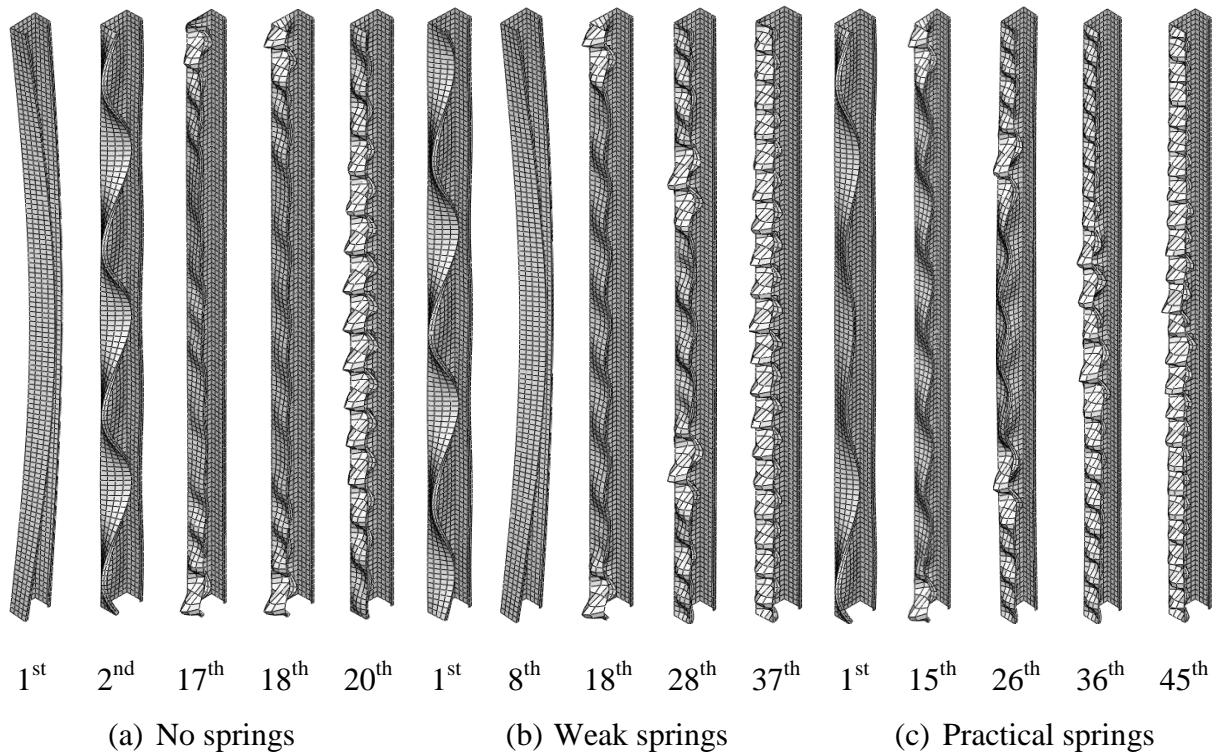


Figure 4-41 Selected buckling modes

For local buckling, it is commonly thought that because the half-wavelength of local buckling is small, springs have less impact on it, as shown in the signature curves by FSM in Figure 4-42. However, since this member has lower distortional buckling, large D contributions to local buckling (mode #18, #20 in Figure 4-41) exist even in the unrestrained beam. With the presence of springs, more DL/GDL interactions are observed. Especially in the beam with practical springs, a distinct local buckling mode may be hard to observe or identify except at relatively high modes with correspondingly high critical moment.

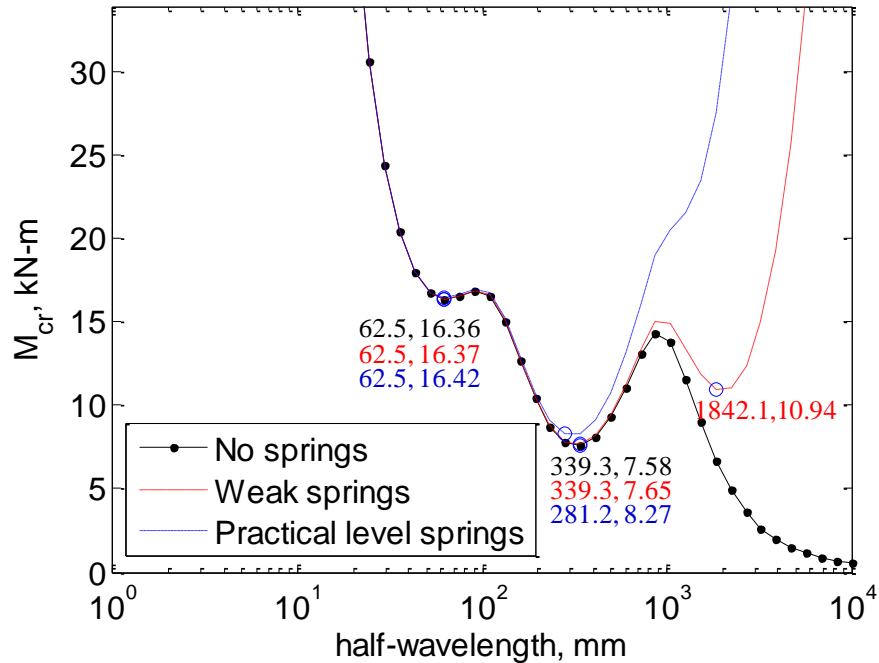


Figure 4-42 springs effects on buckling behavior by FSM

#### 4.7 Numerical studies: unidentical mesh

In the previous numerical studies, the meshes for FEM and cFSM are identical around the cross section. However, in general they do not need to be the same since using the FSM shape functions enables the extrapolation of displacements of additional nodes in forming the base vectors for the FEM nodes. This is extremely useful in the case where the FEM mesh is irregular along the length, e.g., a member with holes. For the same member with FSM-like S-S boundary conditions with highly irregular mesh (generated from an auto-meshing routine) along the length, the modal identification results are provided in Figure 4-43 accordingly. Note, for this specific study, the element (S8R, quadratic shell element with reduced integration in ABAQUS) is also different from that previously used (S4). The irregularity of the mesh can be observed from the selected buckling mode shapes provided in Figure 4-44.

The modal identification (Figure 4-43) shows results consistent with those in Section 4.4, with small errors for most modes. Further, when investigating the buckling mode shapes as shown in Figure 4-44 the indication of the participation demonstrates agreement with engineering expectation. Therefore, extrapolation of the *c*FSM base function through FSM shape functions is validated to approximate the FEM model with an irregular mesh. Essentially, this paves the way towards the application of modal identification on more irregular geometry.

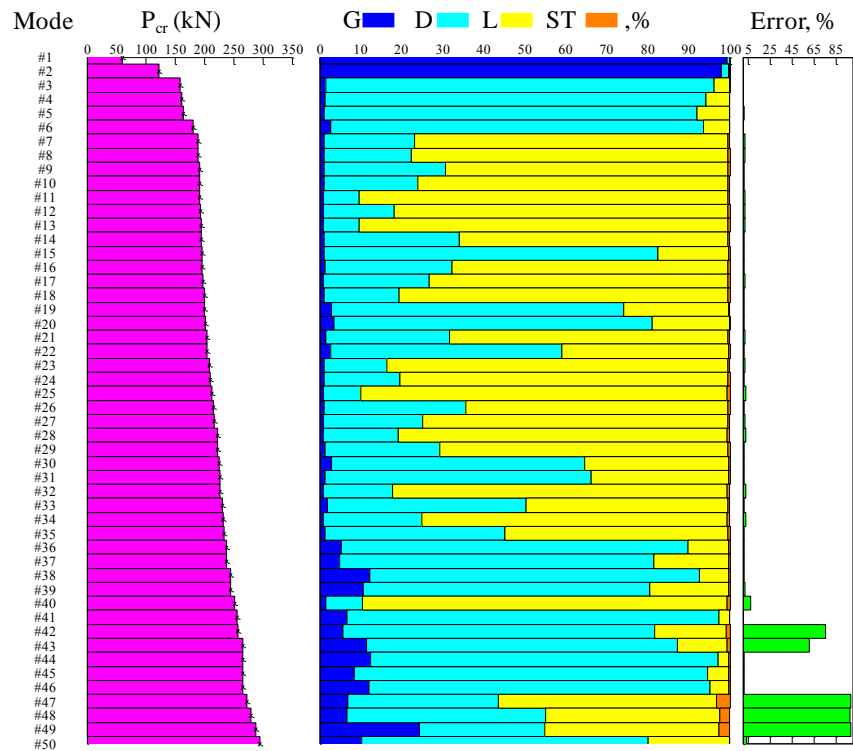


Figure 4-43 Modal identification of unidentical mesh

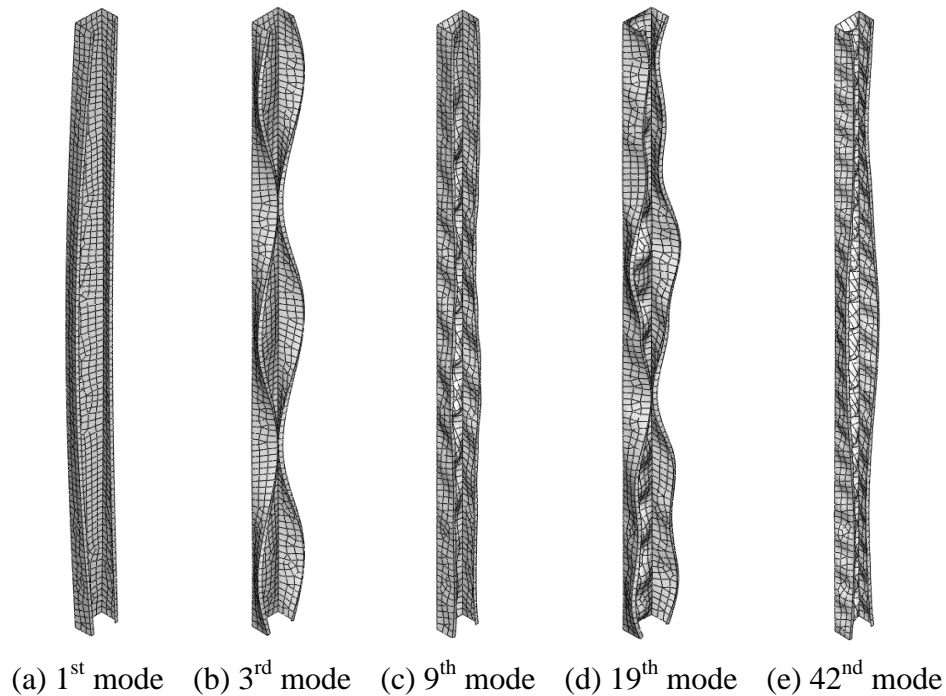


Figure 4-44 Selected buckling mode shapes of irregular mesh model

#### 4.8 Numerical studies: member with holes

Perforations are commonly used in nearly all cold-formed steel applications for services and/or bridging, e.g., isolated holes in studs. The presence of perforations complicates the buckling behavior of the member. In finite element modeling laborious visual investigations of the characteristic buckling modes are much more demanding than in member without holes. One apparent barrier is that for members with changes in geometry exact match between the *c*FSM base functions and the developed finite element models is impossible. Consequently, extrapolation of the *c*FSM base functions for modal identification is needed, as illustrated in Section 4.7 for an unidentical mesh. Moreover, *c*FSM itself is not capable of capturing the changes of section along the length; thus, modal identification using extrapolated base functions from *c*FSM are an approximation for an FE model with perforations. For the same cross section (Figure 4-1), used with

rectangular holes in the web, as shown in Figure 4-45, the modal identification of the stability solution is presented in Figure 4-46. Note, nodal forces to simulate a column member are applied at the ends.

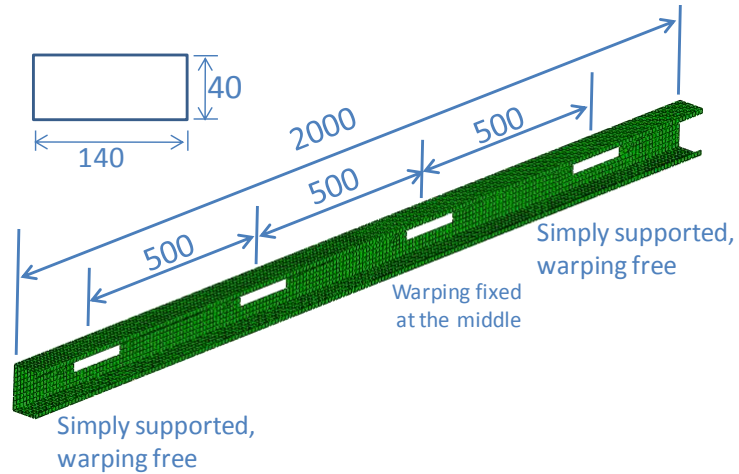


Figure 4-45 Hole location and size and column boundary conditions (mm)

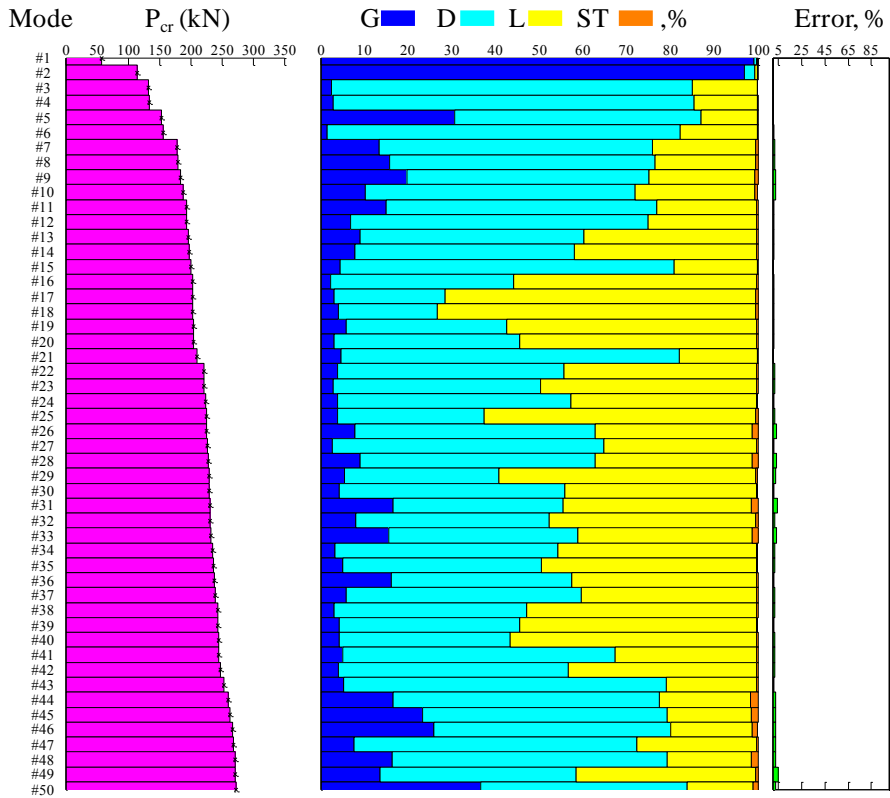


Figure 4-46 Modal identification of column with rectangular holes

The modal identification in Figure 4-46 shows small errors for most modes. Further, the indication of the participation demonstrates good agreement with engineering expectations, when investigating the buckling mode shapes, as shown in Figure 4-47. In particular, even with localized deformation shapes around the holes as shown in Figure 4-47, the proposed modal identification method can capture this deformation with small errors. Moreover, for modes with large global buckling contributions, e.g., the 5<sup>th</sup> mode as shown in Figure 4-47, modal identification also correctly captures this.

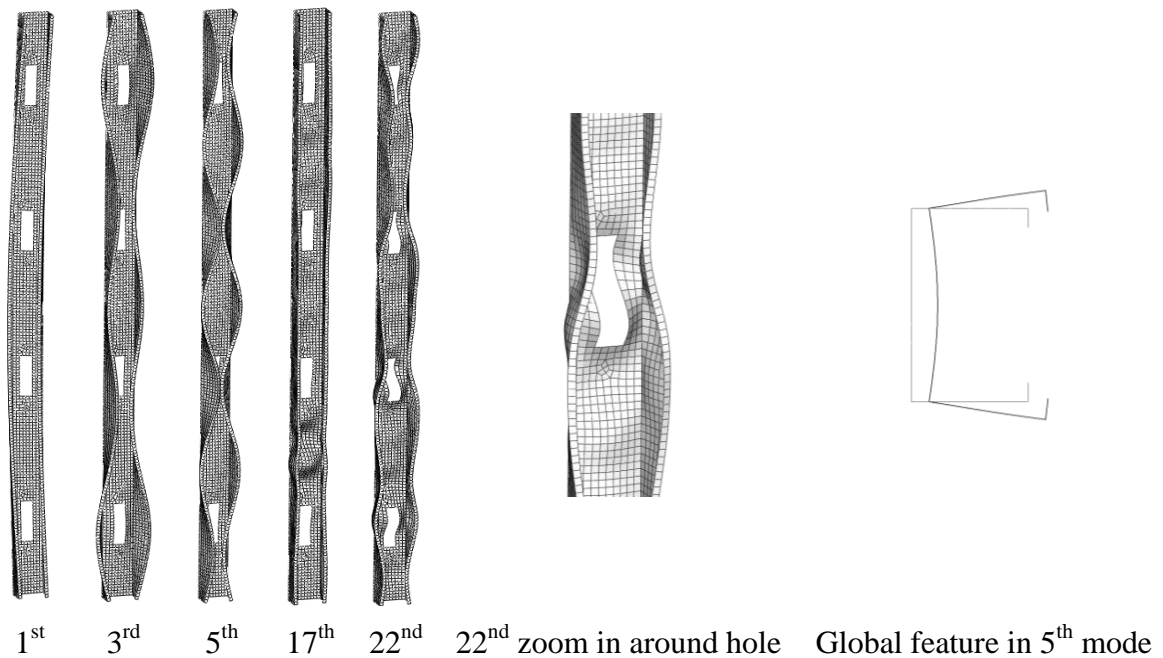


Figure 4-47 Selected buckling mode shapes for column with holes

#### 4.9 Summary

In this chapter, the base vectors from the newly developed constrained finite strip method (*cFSM*) for general end boundary conditions have been utilized for the purposes of modal identification of the buckling modes of shell finite element method (FEM) eigenbuckling analyses. *Associated* base vectors, where the *cFSM* and FEM end

boundary conditions correspond, are shown to provide modal identification in agreement with existing *c*FSM implementations, and with traditional visual observation for modal identification.

*Generalized* base vectors, generated from a subset of the new *c*FSM base vectors, are proposed. The *generalized* base vectors are intended for arbitrary end boundary conditions. Modal identification utilizing *generalized* base vectors is shown to be in good agreement with those utilizing the *associated* base vectors. Further, numerical examples of semi-rigid and mixed end boundary conditions are also provided, and demonstrate the applicability of the *generalized* base vectors to modal identification with arbitrary end boundary conditions. In addition, numerical studies on partially restrained beams indicate the applicability of modal identification for members with intermediate restraints.

Exact match of the finite element and finite strip models in terms of meshing is illustrated to not be necessary by numerical example. Extrapolation of the *c*FSM base functions is able to provide a close modal identification solution even with irregular FEM meshes. This enables the possibility of modal identification on members with geometric change along their length such as holes, for which extrapolation is needed and modal identification is performed in an approximate way because the geometries in *c*FSM and FEM do not exactly match due to the existence of perforation(s). Numerical examples on modal identification with holes demonstrate the applicability of the method towards quantitative classification of buckling modes that are far too laborious to identify by traditional visual observation in FE model.

## Chapter 5 Modal identification for nonlinear FE collapse analysis

### 5.1 Introduction

The strength of thin-walled members is often governed by its buckling behavior, due to its high cross-sectional slenderness. As commonly acknowledged, thin-walled member instabilities can be generally categorized as: local (local-plate), distortional, and global (Euler) buckling. As currently reflected in design specifications, such as AISI-S100 [4], appropriate separation and identification of the buckling modes are necessary, because of the different post-buckling strength and interactions between the modes.

Given the many advances in computation, the Finite Element Method (FEM) employing shell finite elements has become more popular in analyzing thin-walled structures both for elastic (eigenmode) buckling and nonlinear collapse analyses. FEM's unique applicability to handle complex geometry and boundary conditions makes it a natural choice in many situations. However, FEM itself provides no means of modal identification, and instead requires a laborious and completely subjective procedure employing visual investigation.

For elastic buckling analysis, the newly developed constrained finite strip method (cFSM) [2-7] provides the ability to decompose buckling modes as well as categorize (identify) arbitrary buckling modes (or displacements) into the fundamental deformation classes of global ( $G$ ), distortional ( $D$ ), local ( $L$ ), shear and transverse extension ( $ST$ ) as

presented in previous chapter. However, to date, for shell element based nonlinear FEM collapse analysis, failure mode identification is still investigated based on subjective, and largely visual, engineering observations. (A similar observation is true for experimental member testing.) In this chapter, the *c*FSM based modal identification procedure is applied to the nonlinear collapse analysis of shell finite element models with both geometric and material nonlinearity. Note, Generalized Beam Theory has been utilized in nonlinear elastic analysis for a similar purpose [62].

## 5.2 Differences compared to elastic buckling analysis

### 5.2.1 Eigenbuckling identification

In standard FEM notation, the eigenbuckling problem may be stated as:

$$(K_e - \lambda K_g) \varphi = 0 \quad (5-1)$$

where,  $K_e$  is the elastic stiffness,  $K_g$  is the geometric stiffness which depends on the applied loading,  $\lambda$  is the eigenvalue (load factors), and  $\varphi$  is the eigenmode (buckling mode) vector.

In Chapter 4, efforts towards FEM eigenbuckling identification focused on categorizing the buckling mode  $\varphi$  into the four buckling mode classes, *G*, *D*, *L* and *ST*, in terms of participation percentages. This is completed, first by taking the base vectors in *R* of *c*FSM and interpolating them to all the nodal locations in the FEM displacement field, as explained in Section 4.2. The new *c*FSM base functions written in the FEM degrees of freedom are referred to as  $R_{FE}$ . Then, a sizeable minimization problem is solved by approximating the eigenmode vector  $\varphi$  as a linear combination of the base function in  $R_{FE}$ . More details can be found in Section 4.3.

The base functions are formed based upon assumed boundary conditions in *c*FSM. The analytically attractive simply supported boundary conditions (S-S) may not be used without modification as these base functions cannot handle buckling problems where translational movements are allowed at the ends. *Generalized* base functions are proposed in Section 4.4.3 which include the base vector of clamped-free (C-F) and free-clamped (F-C) boundary conditions. More specifically, the proposed *generalized* base functions are the combination of S-S functions with several longitudinal terms and the C-F and F-C base functions with one ( $m=1$ ) longitudinal term as shown in Section 4.4.3. These base functions are applied in the examples shown subsequently for nonlinear analysis.

### 5.2.2 Nonlinear collapse analysis

The nonlinear collapse analysis problem, in an FEM context, can be expressed as:

$$(K_e + K_g + K_p) d = F \quad (5-2)$$

where,  $K_e$  is the conventional elastic stiffness matrix,  $K_g$  is the geometric stiffness matrix and depends upon the current forces applied on the structure,  $K_p$  is the plastic reduction matrix to account for yielding,  $d$  is the displacement vector, and  $F$  is the consistent nodal forces applied on the structure. Note, different from the eigenbuckling problem,  $K_e$  and  $K_g$  here are formulated upon the deformed shape in each increment step (or iteration) when analyzing the nonlinear problem by iterative methods, such as the Newton-Raphson or arc-length method.

For modal identification in the nonlinear collapse analysis the vector to be identified is  $d$ , the displacement vector, as opposed to  $\varphi$ , although, the same identification procedure can be performed on  $d$  to categorize the buckling modes of each step during the collapse analysis by using the *generalized* base functions.

One note, the base functions from *c*FSM used to identify the deformation in the nonlinear collapse analysis are based on the perfect geometry. However, the deformation vectors are normally based on a model of the member with initial geometric imperfections. Based on the author's studies, adding the imperfection field to the deformation vector provides a means to approximately address this geometric discrepancy. Consequently, the deformation vector to be identified is actually:

$$d_{id} = d + d_{imp} \quad (5-3)$$

where,  $d_{id}$  is the deformation vector to be identified in terms of G, D, L, and ST,  $d$  is the deformation vector from Eq. (5-2), and  $d_{imp}$  is the imperfection deviating from the perfect model. This is consistent with defining the *c*FSM base functions on the perfect structure. As deformation ( $d$ ) increase the necessity and relevancy of the imperfection ( $d_{imp}$ ) diminishes

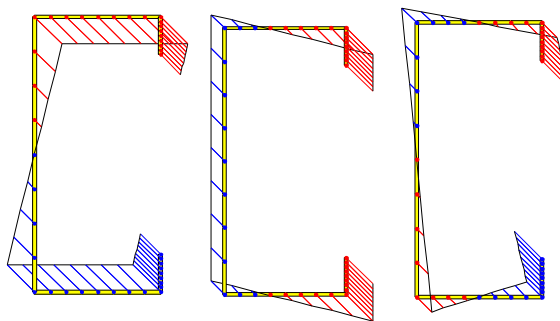
### 5.3 Linear elastic static analysis

Before we get into the details of modal identification for nonlinear FE collapse analysis, a more simple case – linear static analysis is considered. The only difference from what has been described in Section 5.2.2 is that there is no geometric ( $K_g$ ) and plasticity reduction ( $K_p$ ) matrices, and no updating of the elastic stiffness matrix ( $K_e$ ) is necessary for linear elastic static analysis. Modal identification is performed on the displacement vector  $d$ . In this particular study, a special set of linear elastic static analysis is performed.

According to *c*FSM, the global and distortional buckling modes can be uniquely defined by a corresponding warping distribution. In other words, if the warping distribution  $V$  is known for a particular buckling mode in  $GD$  space, the whole

deformation shape of the mode is known by deriving other displacements (i.e.,  $U$ ,  $W$ ,  $\Theta$ , see Section 2.2) from the mechanical assumption in Table 3-1. This poses an interesting question: will the member deform into the corresponding  $GD$  mode in equilibrium if a warping distribution in  $GD$  space is enforced?

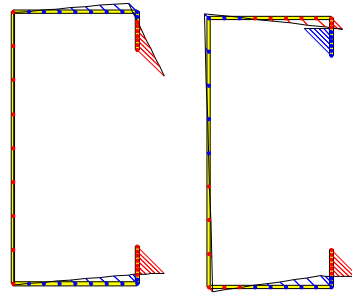
To verify this, a linear elastic static analysis is studied with prescribed warping distribution on a lipped channel section (note, dimension and material properties do not matter as long as used consistently in the whole analysis, nonetheless, the cross section of Figure 4-1 is employed.). Recall, the global buckling modes do not include any cross-section distortion, as specified by the mechanical criteria of  $cFSM$ . Regarding this, the global buckling modes correspond to the traditional definition of the global buckling modes with rigid-body cross-section displacements, which can be seen as major-axis bending, minor-axis bending, and torsion. These three global buckling modes in  $cFSM$  can be described by three special warping functions corresponding to the longitudinal displacements (warping displacement in  $cFSM$  definition) resulting from special loads as shown in Figure 5-1. Thus, each of the warping distributions in Figure 5-1 represents a corresponding global buckling mode.



(a) major-axis bending (b) minor-axis bending (c) pure torsion

Figure 5-1 Warping functions of  $G$  space

According to *cFSM*, the separation of the distortional buckling space (*D* space) from *GD* space is conducted mathematically, since there is no direct definition of the distortional buckling modes. The physical meaning of individual distortional buckling modes is not clear. Currently, a *D* space is sought by finding a null space of the *G* space within the *GD* space from the warping functions. Using the same method in *cFSM* to find the null space *D*, which is the singular value decomposition, there are two buckling modes in *D* space as shown in Figure 5-2. More details of the *GD* space can be referred to in Section 3.4.



(a) Symmetric distortional      (b) Anti-symmetric distortional

Figure 5-2 Warping functions of *D* space

Note, the absolute magnitude of the warping is not important unless combination of warping functions is involved. To see what the deformation will be by enforcing the previously illustrated warping functions, linear elastic static analyses are performed on the lipped channel section as shown. The warping distribution along the length can be extrapolated as following:

$$v = \sum_{m=1}^q v_{[m]} Y'_{[m]} \frac{a}{\mu_{[m]}} \quad (5-4)$$

where,  $Y_{[m]}$  represents the longitudinal shape function,  $m$  is the longitudinal term,  $a$  is the length of the member and  $\mu_{[m]}=m\pi$ .  $v_{[m]}$  is the warping function given in Figure 5-1 and Figure 5-2 associated with longitudinal term  $m$ . For different longitudinal terms, the distribution is the same while the absolute magnitude may be varying.

For  $G$  space, only deformed shapes of the major-axis bending from static analysis are shown for S-S and C-C boundary conditions. The longitudinal term  $m$  used to extrapolate the warping distribution along the length is 1 in Eq. (5-4) for both S-S and C-C. The deformed shapes with displacement magnitude contour are shown in Figure 5-3. They are the major-axis bending we commonly see.

Modal identifications are performed on these two deformed shapes. The participation indicates 99.9% percentage of global buckling mode.

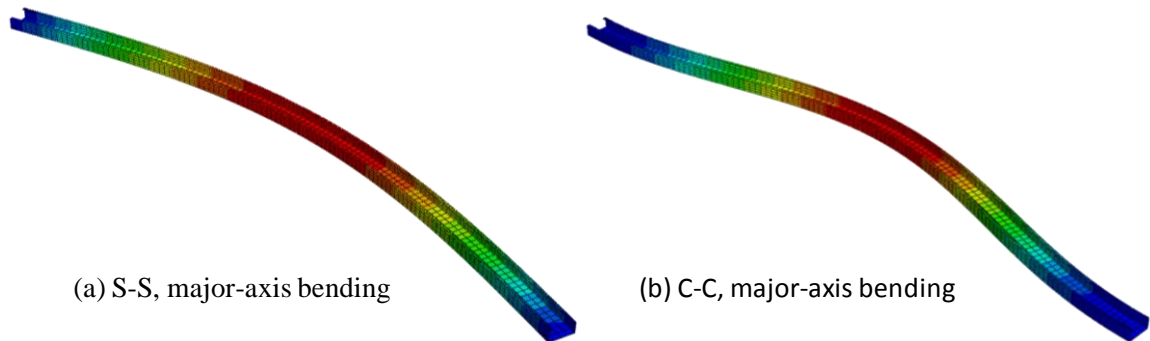
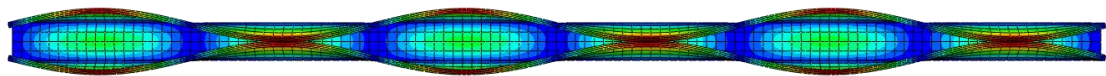


Figure 5-3 Deformed shapes of major-axis bending warping functions for S-S and C-C

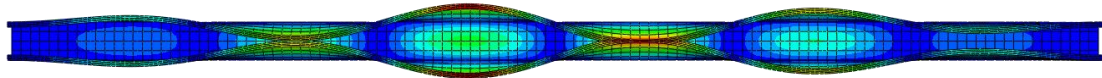
Similarly, deformed shapes for the symmetric distortional warping function of Figure 5-2(a) are illustrated for S-S and C-C boundary conditions. For S-S, the longitudinal terms employed to extrapolate the warping distribution along the length in Eq. (5-4) is 6. For C-C, a combined warping function is employed with majority warping distribution from longitudinal term  $m=6$  and small contribution from 2, 4, 8, and 10 as well, in an attempt to simulate the longitudinal term participation as in Section 2.5. The

deformed shapes with displacement magnitude contour are shown in Figure 5-4. With the multiple longitudinal terms in warping functions of C-C, the deformed shape develops into a coupled distortional buckling mode by multiple half-wave lengths (Note, majority of the deformation is still attributed to longitudinal term  $m=6$  as observed.)

If modal identifications are performed on these two deformed shapes, the participations for both indicate 98% percentage of distortional buckling mode contribution with local buckling as the rest 2%. Though small noise existed as predicted by modal identification, these are still nearly pure distortional buckling modes as expected.



(a) S-S, symmetric distortional with longitudinal term  $m=6$



(b) C-C, symmetric distortional with multiple longitudinal terms

Figure 5-4 Deformed shapes of symmetric distortional warping functions for S-S and C-C

To sum up, there are two conclusions from modal identification of the linear elastic static analysis in this section. First, it can be seen as a verification of the mechanical assumption in Table 3-1 about global and distortional buckling. Second, it demonstrates the applicability of FE modal identification on general displacement vector  $d$ .

#### 5.4 Modeling parameters for nonlinear collapse analysis

Shell finite element modeling of thin-walled structures for ultimate strength prediction and investigation of collapse behavior necessitates the inclusion of both

geometric and material nonlinearity. The solutions of these models are highly sensitive to model inputs, such as geometric imperfections, residual stresses, plastic strain, yield criteria, material model, boundary conditions, and also the fundamental mechanics, particularly with regard to element selection and solution schemes [63]. All the analyses performed herein utilize the commercial finite element package ABAQUS [45]. In this study, residual stresses and plastic strains are not included in this model. Additional model assumptions are discussed in detail as follows.

#### **5.4.1 Element and Mesh**

Prediction of the peak strength and failure behavior of thin-walled structural members requires a fine mesh in nonlinear FEM models to provide reliable results. The shell element used here is the S4 shell element from the ABAQUS library of elements [45], the S4 is a 4-node linear element (fully integrated). In addition, the element aspect ratio is controlled between  $\frac{1}{2}$  to 2 to avoid element distortion under large deformations. Specifically, for all the channel sections studied in this paper, the mesh of the cross section is provided in Section 5.5.1.

#### **5.4.2 Boundary conditions**

The end boundary conditions simulate local-plate simply supported conditions, which imply warping fixity at the member ends. Specifically, all translational degrees of freedom are fixed at one end of the model, at the opposite end the transverse translational degrees of freedom are fixed, while the longitudinal translational degrees of freedom are tied to a single reference node, where the end shortening (loading) is performed.

### **5.4.3 Material model**

The material is assumed to be homogeneous and isotropic and modeled as elastic-perfectly plastic (von Mises yield criteria with isotropic hardening) with Young's modulus  $E=210,000$  MPa, Poisson's ratio  $\nu=0.3$ , and a yield stress of 345 MPa.

### **5.4.4 Imperfections**

Careful treatment of geometric imperfections is of significant importance in modeling cold-formed steel members, because the ultimate strength and post-buckling mechanisms are both imperfection sensitive. Both the imperfection distribution and magnitude are important. In this study, for modeling convenience, the distribution of the imperfection are seeded from the local and/or distortional buckling mode shapes generated from a CUFSM analysis [54], and the magnitude is a function of the plate thickness. It is worth noting here that if one wants to simulate tests or provide strength predictions of cold-formed steel member in a more reliable and accurate manner, the distribution and magnitude of imperfections should be more closely tied to measured data [63, 64].

### **5.4.5 Solution control**

Nonlinear collapse analysis is sensitive to the solution scheme. Thin-walled structures may become unstable when a load reaches its buckling value or when nonlinear material accumulates large plastic strain. The instability could be global (such as a snap-through of a plate) or local (such as failure of a stiffener). Instability problems usually pose convergence difficulties and therefore require the application of special nonlinear techniques. Methods, such as displacement control, arc-length method, and

artificial damping, are typically potentially appropriate for collapse modeling of cold-formed steel members. The method employed in this study is the arc-length method (modified Riks method [65] in ABAQUS).

## **5.5 Modal identification of FEM nonlinear collapse analysis**

### **5.5.1 Cross-sections under study**

Three cold-formed steel members, as shown in Figure 5-5, are selected to study the proposed modal identification method for nonlinear collapse analysis. In Figure 5-5, the nodes illustrate the mesh density within the cross-section. All the members are modeled as columns under the boundary conditions specified in Section 3.1.1. Member (a) with a length of 600 mm in Figure 5-5 is a local dominant model (first buckling mode is the local buckling mode in the eigenbuckling analysis). Member (b) with a length of 1200 mm in Figure 5-5 is a distortional dominant model. Member (c) with a length of 700 mm in Figure 5-5 is a local-distortional interacted model, which means the first FEM eigenbuckling mode is a mixed local and distortional buckling mode. The relatively short length for each section is intended to exclude global buckling from dominating.

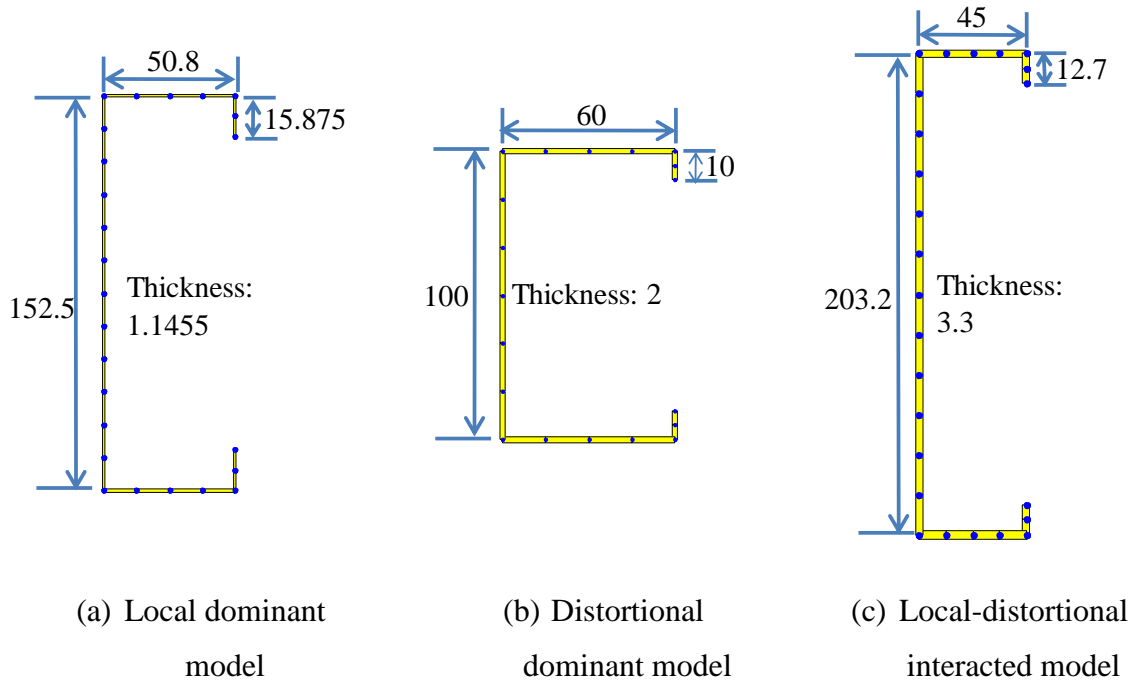


Figure 5-5 Dimensions of cross sections (mm) and mesh

### 5.5.2 Modal identification: perfectly initial geometry (no initial imperfection)

Cold-formed steel members have geometric imperfections during manufacturing. Thus, perfect geometry (no imperfections) does not exist in reality. However, studying the perfect geometry can still provide useful insights about the behavior of cold-formed steel members, as is shown herein. For the cross-sections in Figure 5-5, the first eigenbuckling mode and full nonlinear collapse models are both analyzed with shell finite element analysis.

While eigenbuckling analysis is based on a linear perturbation, static analysis is based on incremental load-deflection response. For modal identification, determining which displacements to consider in the identification analysis requires some judgment. For example, in this study, the applied load (actually an applied displacement) of column end shortening is highly correlated with the fourth global buckling mode ( $G4$ ) of the

*c*FSM base functions used for modal identification. Similarly, in major-axis bending moment the applied deformations are also highly correlated with a global mode *c*FSM base function. In this study, modal identification results both with and without these correlated global modes are provided. For perfect initial geometry, modal identification results without the end shortening (*G4*) deformation (i.e., the *adjusted* participations) are summarized in Table 5-1 along with the elastic buckling load and peak load.

Table 5-1 Participations of eigenmode and nonlinear collapse models

Model		Participation (%)				Load (kN)	
		G	D	L	ST	P <sub>cr</sub>	P <sub>n</sub>
Local dominant model	1 <sup>st</sup> eigenmode	0.4	4.8	94.6	0.1	20.8	
	at peak	0.7	12.8	85.4	1.1		72.9
	at post	0.4	55.9	41.0	2.8		
Distortional dominant model	1 <sup>st</sup> eigenmode	6.0	89.2	4.7	0.1	173.4	
	at peak	0.1	93.8	4.6	1.6		163.8
	at post	0.1	82.6	14.8	2.5		
Local-distortional interacted model	1 <sup>st</sup> eigenmode	2.9	38.5	58.1	0.4	283.8	
	at peak	0.2	50.5	47.1	2.2		296.4
	at post	18.4	52.0	27.5	2.1		

Note: at peak refers to the peak of the load-displacement response in a nonlinear collapse analysis

at post refers to collapse mechanisms at force levels less than 80% of peak deformation

### 5.5.2.1 Local dominated model

Modal identification results for the local dominant model (without imperfections) are summarized in Table 5-1 and shown throughout the nonlinear collapse analysis in Figure 5-6(b). If *G4* (the end shortening mode) is included in the determination of the participations then *G* modes dominate the response in the pre-buckling regime and have significant percentages in the buckling and post-peak regimes (see upper plot of Figure 5-6(b)). However, if *G4* participations are removed, then the eigenmode and peak modal

identification results are similar (Table 5-1) and only in the collapse/post-peak range does distortional buckling significantly participate.

This model demonstrates that a local dominant model (as determined by eigenanalysis and the fact that elastic local buckling is at 20.8 kN, but ultimate collapse at 72.9 kN), if properly considered, is indeed local dominant up to the peak strength, but even in a local dominant model the final collapse mechanisms may have significant contributions from other modes (e.g., distortional). This is consistent with experimental observations in [44]. Finally, it is also worth noting the role of the shear and transverse extension (*ST*) modes. Since no imperfection exists in this model the initial deformations (primarily associated with localized deformations due to the end boundary conditions) have a noticeable *ST* contribution. However, once the buckling fully initiates the *ST* participations decrease to near zero until the post-peak region.

#### ***5.5.2.2 Distortional dominated model***

Modal identification results for the distortional dominant model (without imperfections) are summarized in Table 5-1 and shown throughout the nonlinear collapse analysis in Figure 5-7(b). For the adjusted participations (i.e., *G4* removed, as shown in lower plot of Figure 5-7(b)) the distortional mode participation at peak strength is similar to the distortional buckling mode participation in eigenbuckling analysis (see Table 5-1). However, while the local dominant model has significant post-buckling, the selected distortional dominant model is in the inelastic buckling regime (i.e., with strength of 163.8 kN and elastic buckling of 173.4 kN). Interestingly, in the collapse regime, local buckling participation grows slightly (presumably due to short wavelength localizations

in the plastic mechanism) although distortional buckling remains dominant with participations near 80%.

### ***5.5.2.3 Local/distortional interacted model***

Modal identification results for the local-distortional interacted model (without imperfections) are summarized in Table 5-1 and shown throughout the nonlinear collapse analysis in Figure 5-8(b). While the elastic buckling analysis suggests greater participation for the local mode, the collapse analysis reveals dominance of the distortional mode (with  $G4$  removed). This is consistent with current understanding that distortional buckling has lower post-buckling reserve than local buckling and will dominate response even when at the same buckling load. The presence of a global mode in the collapse regime is a surprise, and warrants further study.

## **5.5.3 Modal identification: models with initial imperfections**

Imperfections have a significant influence on nonlinear collapse analysis. A series of different imperfection distributions and magnitudes are explored for each of the three models and the results summarized here.

### ***5.5.3.1 Local dominant model***

For the local dominant model, five imperfection schemes are considered. The distributions are based directly on the local or distortional buckling mode shapes from CUFSM analysis [54] and listed along with the magnitude of the geometric imperfections in Table 5-2.

Table 5-2 Imperfection cases and their peak loads

Case	Waves along member	Distribution	Magnitude	Peak load (kN)
I	n/a	n/a	0	72.9
II	5	Local	0.1t	72.1
III	1	Outward distortional	0.1t	73.1
IV	1	Inward distortional	0.1t	72.6
V	1	Outward distortional	0.94t	68.3

Note: (1) t is the thickness of the cross-section.

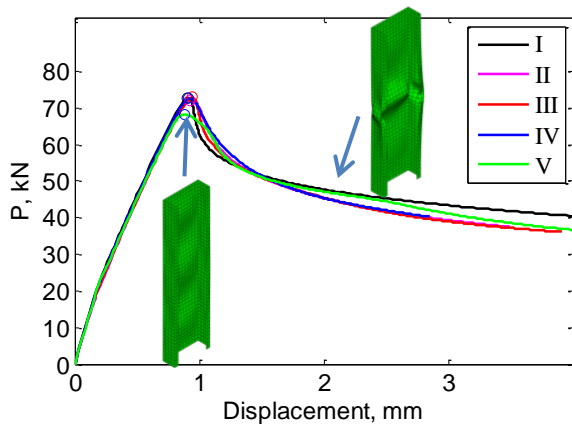
(2) Wave numbers are determined from the characteristic half-wavelengths of local and distortional buckling from CUFSM analysis.

Load-displacement responses for the local dominant models are provided in Figure 5-6(a), and indicate generally mild imperfections sensitivity in the studied cases. The (modal) participations are provided in Figure 5-6(c)-(f) for the cases with imperfections II-V, respectively. When the local imperfection is presented (case II), slightly lower peak load is observed compared to the perfect geometry (case I), and participations (e.g., between local and distortional) remain essentially the same. For this local dominant model, the strength of the member is not greatly influenced by a small amount of distortional imperfection (case II and IV, 0.1t), but is significantly reduced when the magnitude is bigger (case V, 0.94t). Illustrating the point that not all imperfections are detrimental, at small magnitudes the outward distortional imperfection (case III) actually increases the strength above the no imperfection results (case I).

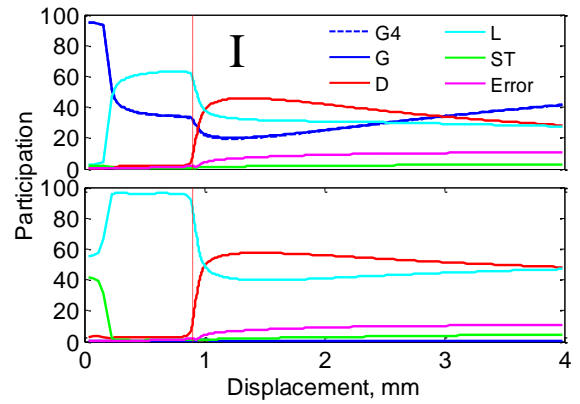
The participation results of Figure 5-6(c)-(f) provide further insights. For a local dominant model with a local imperfection (case II) the results are similar to the no imperfection results (case I) and local participations dominate except in the post-peak range where distortional participation increases significantly.

In the local dominant model with small distortional imperfections (cases III and IV) the initial participations are largely distortional, consistent with the imperfection, but under increasing load to its elastic buckling limit (around 21 kN indicated by the eigenvalue analysis as listed in Table 5-1) local buckling is triggered. The deformations move towards local modes and local participations increase and dominate prior to reaching the peak strength. Again, in the collapse regime, distortional buckling deformations start to grow rapidly and finally take over again.

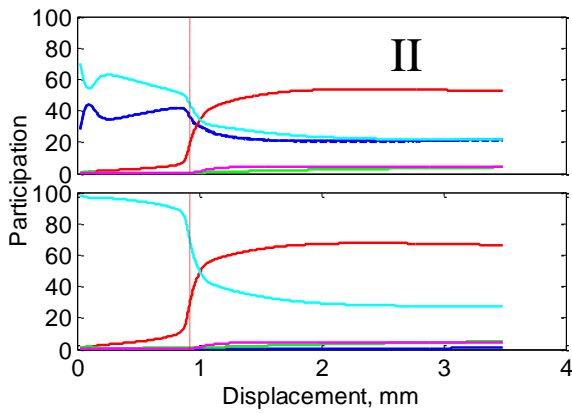
However, even in the local dominant model, if the magnitude of the distortional imperfection is large enough (case V) then both local and distortional participations are observed throughout the loading regime. Consequently, this leads to a local-distortional interacted failure at the peak strength. In the collapse regime, distortional deformations once again dominate. For all the cases studied, if end shortening ( $G4$ ) is excluded from the global buckling mode, then there are negligible global contributions during collapse.



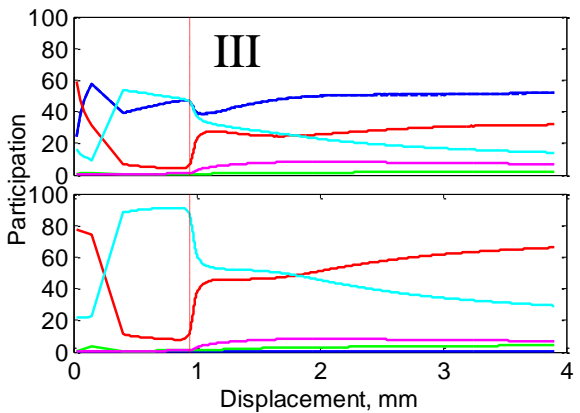
(a) load-displacement responses



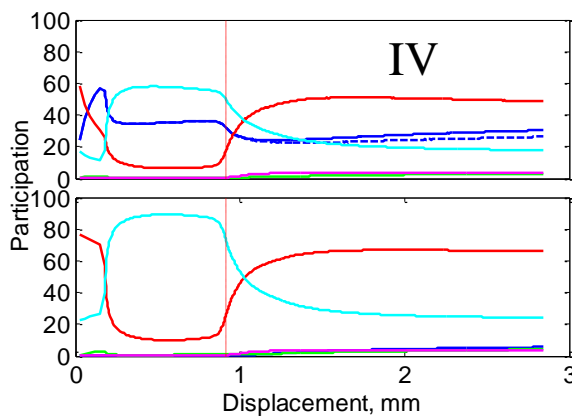
(b) no imperfections



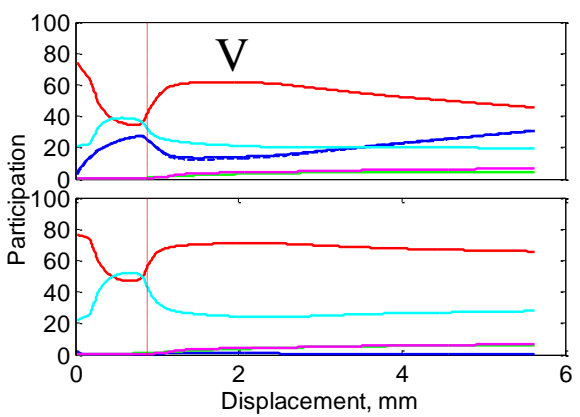
(c) local imperfections (0.1t)



(d) outward distort. imperfections (0.1t)



(e) inward distortional imperfections (0.1t)



(f) outward distort. imperfections (0.94t)

Figure 5-6 Local dominant model

### ***5.5.3.2 Distortional dominant model***

For the distortional dominant model, three imperfection schemes are studied: no imperfection (case I); local imperfections with 8 half-waves and a magnitude of 0.1t (case II); and distortional imperfections with 2 half-waves and a magnitude of 0.1t (case III). Load-displacement response and modal identification results shown throughout the nonlinear collapse analysis are provided in Figure 5-7. The distortional dominant model is far more imperfection sensitive than the local dominant model. Introduction of even a 0.1t imperfection results in peak strength decreases from the no imperfection (case I) model of 9% (below 149 kN) for the local imperfection (case II) and 14% loss for the distortional imperfection (case III). In addition, with little to no post-buckling regime before collapse the initial imperfection is more influential even in the collapse regime – as evidenced by the strongly local-distortional interacted failure that results from the local (case II) imperfection. If the imperfection matches the collapse, as in Case III, then the participation of the given mode, distortional in this case, will persist throughout the analysis. Such a “sympathetic” imperfection is likely to consistently be the most detrimental with respect to strength.

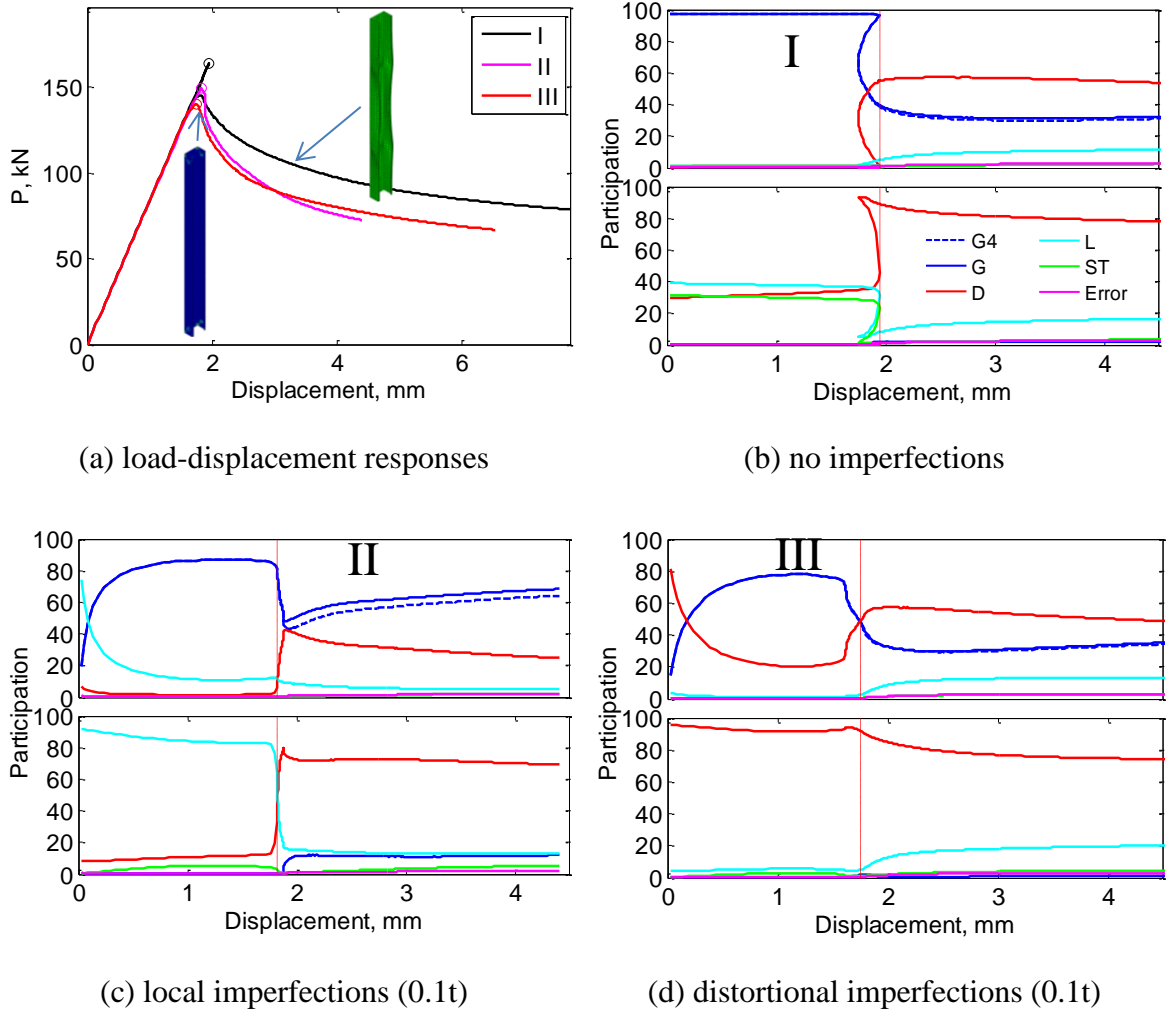


Figure 5-7 Distortional dominant model

### 5.5.3.3 Local/distortional interacted model

For the local-distortional interacted model, similar to the distortional dominant model, three imperfection schemes are studied: no imperfection (case I); local imperfections with 5 half-waves and a magnitude of 0.1t (case II); and distortional imperfections with 2 half-waves and a magnitude of 0.1t (case III). Load-displacement response and modal identification results shown throughout the nonlinear collapse analysis are provided in Figure 5-8.

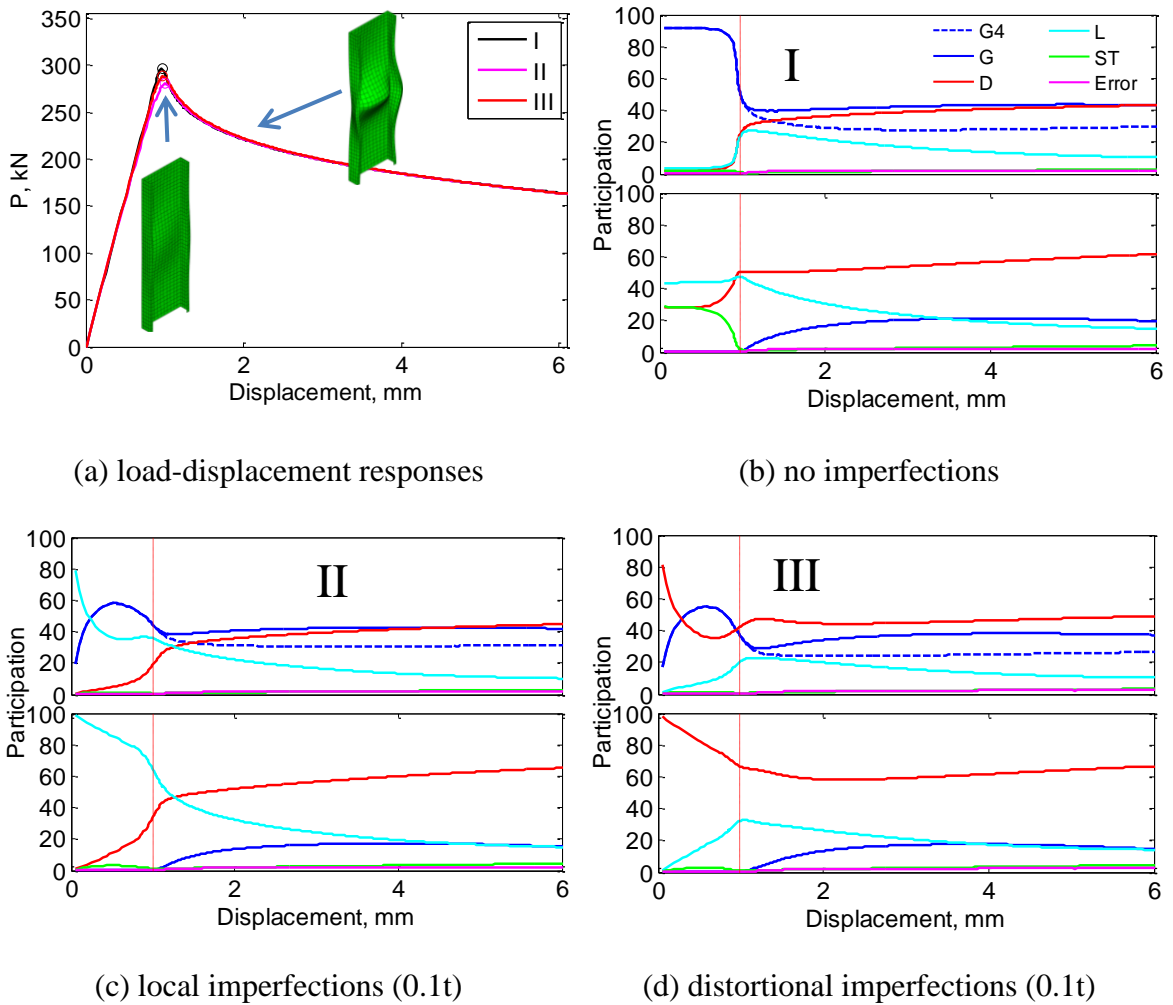


Figure 5-8 Local-distortional interacted model

In this interacted model when the imperfection matches a particular mode (e.g. local), that mode starts out as dominant (under no load), then decreases its participation under deformation as the other mode (e.g., distortional) increases. However, past peak, the distortional mode dominates and the local mode decreases its participation while a global mode (exclusive of  $G4$ ) also increases. The magnitude of the nonlinear collapse participations indicate the failure is an interaction between the two modes; however

where the eigenbuckling analysis (Table 5-1) suggests local buckling will largely control, the collapse analysis suggests distortional buckling will dominate.

## 5.6 Discussion

The examples provided herein provide proof-of-concept for the extension of modal identification, driven by *c*FSM base vectors, to nonlinear collapse analysis. A key issue that arises in the analysis that requires further study is how to handle the primary displacement associated with a given loading. In the simple loading case provided here the primary displacement was essentially coincident with the *G4* global mode, thus it was possible to consider participations both with and without this mode considered. However, for more complicated loading the separation is less clear. It is proposed that the entire linear elastic deformations associated with the applied loading on the perfect structure should be removed from the identification, but this idea needs further study.

In modal identification problems for eigenbuckling modes the necessity of shear and transverse extension (*ST*) is typically not obvious. However, consistent with observations in GBT [62] in the examples provided here *ST* has growing importance in the collapse regime, typically greater than 2% of the participation.

Though not specifically provided herein it is also worth noting that the error in the identification process is normally larger in the collapse regime due to the localization of the deformations. Potentially, this may be reduced by including base vectors with a larger number of longitudinal terms. However, the additional computational effort can be significant.

From a behavioral standpoint the dominance of distortional buckling in the post-peak regime of lipped channels, independent of the pre-peak deformations is an interesting result. Local failures, whereby local buckling dominates the response up to the peak strength are observed, but the collapse mechanisms that are triggered are typically better captured by the distortional base vectors.

Further, it is worth recalling that although the *c*FSM base vectors span a sufficient part of the FEM deformation space (and hence identification with only small errors is possible) the actual separations into the *G*, *D*, *L*, and *ST* spaces are based on linear elastic response. Specifically, when it is observed that distortional buckling dominates in the post-peak regime, what this implies is that the largely plastic deformations associated with the collapse are best described by the elastic displacements associated with distortional buckling. This extension of elastic base vectors to describe plastic deformation fields is practical, and appears potentially useful in an engineering sense, but further work is needed before such an identification could be considered rigorous.

Finally, a long term goal of this work is to connect collapse mechanisms and their related energy dissipation to the *G*, *D*, *L*, and *ST* deformation spaces. Currently, no simple means exists for predicting energy dissipation in members, and modal identification and categorization provides new information to make these connections. Future work in this direction is anticipated.

## **5.7 Summary**

A set of generalized base vectors developed from the constrained finite strip method are employed to identify the deformations of the nonlinear collapse analysis of a thin-

walled member in terms of global, distortional, local, shear, or transverse extension deformations. The applicability of the method is first demonstrated on the linear elastic static analysis. Then, the applicability is further demonstrated with numerical examples of geometrically perfect and imperfect cold-formed steel lipped channel members under uniform end shortening. The results indicate how the participation of a given deformation space evolves under load. For example, in the case of a member dominated by local buckling, the local mode has the only significant participation prior to collapse (peak strength); however, in the collapse regime distortional deformations have a large participation as they better describe the localized collapse mechanism that forms. The analysis results quantitatively demonstrate the interplay between local, distortional, and global buckling during collapse and even demonstrate the importance of shear and transverse extension (particularly during collapse). This chapter provides proof-of-concept for the extension of *c*FSM base vectors to modal identification of nonlinear collapse models and significant discussion on future work that remains in this area.

## **Chapter 6 Design applications of the finite strip method and modal identification**

### **6.1 Introduction**

In cold-formed steel member design, the elastic buckling load is a key parameter in predicting the design strength. For commonly used cold-formed steel sections, such as the C-section, Z-section, etc., the buckling loads may be categorized as local-plate, distortional, and/or global (Euler, Lateral-torsional, etc.) buckling. Finding the elastic buckling solution is a necessary first step in strength prediction.

Starting in 2004, Appendix 1 of the North American Specification for Cold-Formed Steel Structural Members (AISI-S100) introduced an alternative design method for strength prediction of beams and columns: the Direct Strength Method (DSM). The basic premise of DSM and the advantages of the method are discussed in [42]. The aforementioned elastic buckling loads are at the heart of the DSM approach. More specifically, DSM requires that the elastic buckling loads be known in local, distortional, and global buckling modes. DSM does not specify how these elastic buckling values should be calculated since numerous methods exist, as discussed in the DSM commentary found in Appendix of AISI-S100 [43].

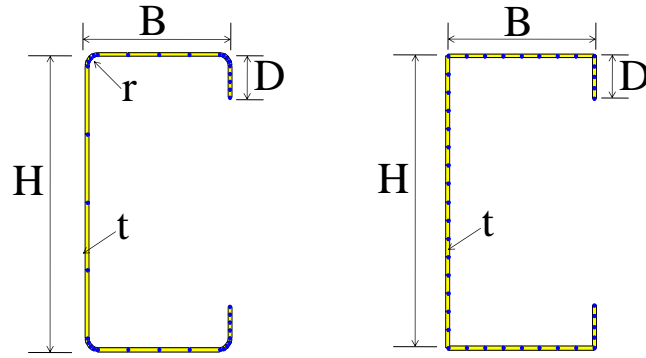
The application of the developed finite strip method (FSM) and modal identification method for finite element method (FEM) are illustrated here for elastic buckling prediction. Issues associated with the application are discussed.

## **6.2 Two step method based on signature curve**

### **6.2.1 Problem statement**

There are several issues when applying FSM solutions in the context of the Direct Strength Method, particularly when one wants to automate and generalize the process. First, DSM requires the elastic buckling loads (or moments) for all sections, thus they must be identified in all cases. Second, the treatment of the corners introduces complications in the process that must be specifically addressed.

From a strictly practical standpoint all cross sections have rounded (not sharp) corners. For stability determination in FSM such round corners can be directly handled by approximating with several (at least 4) strips in the corners, as shown in Figure 6-1(b). However, a straight-line model, ignoring the corners, as shown in Figure 6-1 (a) is useful for its simplicity and even necessary in certain cases since the modal decomposition capacity of *c*FSM cannot be fully utilized for sections with rounded corners. Of course, the rounded corner model does result in modestly different elastic stability solutions.



(a) Rounded corner model; (b) Straight-line model

Figure 6-1 Cross-section models and dimensions for use in FSM analyses

The conventional, or semi-analytical, FSM provides the most widely used approach to examine all possible instabilities in a thin-walled member under longitudinal stress (axial, bending, and/or warping torsion). If both local and distortional buckling can be uniquely determined from an FSM solution, as shown in Figure 1-4, then this is defined as a solution with “**unique minima**”. However, if either or both minima is “indistinct” the FSM solution is characterized as having “**non-unique minima**”. Studies show that the problem is a common one for SSMA stud sections [66].

*c*FSM has the capability to automatically predict the elastic buckling load (or moment) for a given buckling mode (e.g., a solution decomposed to only include distortional buckling is possible.) Thus, *c*FSM is a potential solution to the problem of non-unique minima. However, there are two basic difficulties to overcome with directly using the *c*FSM solution:

- (1) DSM’s strength expressions are calibrated to the conventional FSM minima instead of pure mode solutions from *c*FSM.

(2) *c*FSM can not handle rounded corners and still provide a meaningful separation of local and distortional buckling.

Thus, the reasoning for identifying non-unique minima *and* rounded corners as the two major hurdles in automatic identification using FSM and DSM becomes clear.

### **6.2.2 Proposed solution**

To address the problem of non-unique minima in the stability solution, and the impact of rounded corners, a two-step method is proposed here: the use of a straight-line model in *c*FSM to determine only the half-wavelength of interest in a conventional FSM analysis.

To address these issues a two-step procedure has been adopted for determining the elastic buckling loads and moments. Step 1: the analyst develops a rounded corner model of the section and runs a conventional FSM model. If unique minima exist, then stop, and use those values. Step 2: the analyst develops a straight-line model of the section and runs *c*FSM pure mode solutions for local and distortional, only for the purpose of determining the length ( $L_{cr}$ ) at which the modes occur. The elastic buckling load (or moment) is determined from the conventional FSM with round corners (Step 1) model at the  $L_{cr}$  identified in the Step 2 model. An abbreviation for this solution method is FSM@*c*FSM- $L_{cr}$ , which is illustrated for a 550S162-43 stud section under axial compression in Figure 6-2. The validity of this approach is fully explored in [66] and shown to provide consistent results.

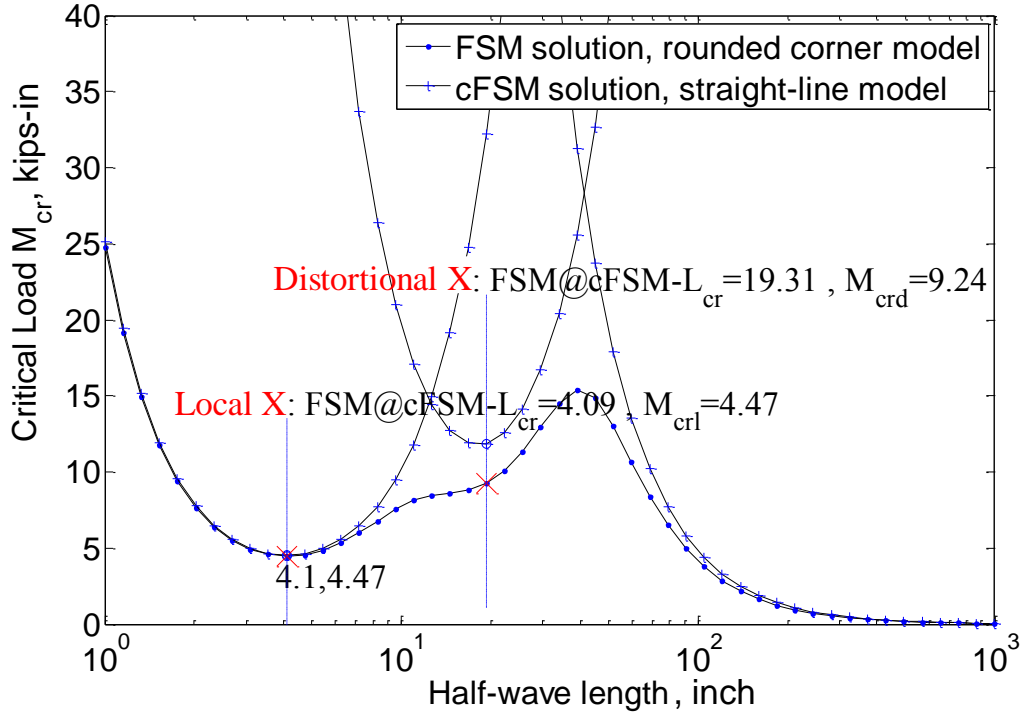


Figure 6-2 Signature curve augmented with pure mode  $c$ FSM solution and illustration of the proposed  $FSM@cFSM-L_{cr}$  solution to identifying non-unique minima

### 6.3 Method based on FSM solution of general boundary conditions

#### 6.3.1 Conventional FSM solution

Investigation of the characteristic buckling modes of an FSM solution for general boundary conditions is similar to FEM: at a physical length the higher modes provide the most direct manner for finding the  $G$ ,  $D$ , and  $L$  buckling load or moment. The first identified modes (in ascending buckling values) of  $G$ ,  $D$ , and  $L$  can be used as the needed inputs in DSM.

In particular, for FSM, the participation of longitudinal terms of the mode can be used to aid the categorization of the buckling modes in combination with the mode shapes. As discussed in Chapter 2.5, for members, if the simply supported half-

wavelengths are known for local ( $L_{cr\ell}$ ), distortional ( $L_{crd}$ ), and global buckling ( $L_{cre}$ ),  $m$  near  $L/L_{cr\ell}$ ,  $L/L_{crd}$ , and  $L/L_{cre}$  shall indicate the contribution of local, distortional, and global buckling to the buckling mode.

By utilizing the fundamental longitudinal terms, as discussed in Section 2.5, there are two distinct advantages: 1) increase the computational efficiency without significant loss of accuracy of stability solution; and 2) the stability solution is able to potentially include all the three characteristic buckling modes ( $G$ ,  $D$ , and  $L$ ) for identification.

### **6.3.2 Method with modal identification**

If  $c$ FSM is applicable (no round corners), modal identification can be performed by  $c$ FSM. Participations of  $G$ ,  $D$ ,  $L$ , and  $ST/O$  for each buckling mode can aid in categorizing the buckling modes. Thus, one can pick the first identified  $G$ ,  $D$ , and  $L$  modes based on certain exceedance rule. For most of the cases, as illustrated in Table 6-1, the participation of  $G$ ,  $D$ , or  $L$  is larger than 90% which unambiguously indicates the mode is nearly pure  $G$ ,  $D$ , or  $L$  mode. However, some of the modes are interacted with two or all of  $G$ ,  $D$ , and  $L$  modes as indicated by their significant participations; the categorization of these modes is not trivial given the coupling. The question is, how large should the participation of one characteristic mode ( $G$ ,  $D$ , or  $L$ ) be in order to be categorized that mode?

Though other rules are available, two quantification rules are explored: 75%ile exceedance and 50%ile exceedance. For each mode class ( $G$ ,  $D$ , and  $L$ ), the 1<sup>st</sup> identified modes are those of most interest. While nearly pure  $G$ ,  $D$ , or  $L$  modes (usually more than 90%ile exceedance of individual mode) are desired, buckling modes with 75%ile

exceedance of individual  $G$ ,  $D$ , or  $L$  mode already show clear dominance of one particular characteristic buckling mode. Interaction with other characteristic modes can be considered as small. With 50%ile exceedance rule, the first buckling mode that has at least 50%ile participation of individual  $G$ ,  $D$ , or  $L$  mode could be identified as a mode with dominance of one characteristic  $G$ ,  $D$ , or  $L$  mode. However, highly interacted, e.g.,  $GD$ ,  $LD$ , or  $GL$  interacted, may be selected in this case. Both rules are explored in the numerical examples presented herein.

While it is logical to pick up the modes that have the highest individual  $G$ ,  $D$ , or  $L$  participation, this may pick up higher modes with significantly larger critical loads, thus leading to unconservative prediction of the nominal strength. Further this is dependent on the number of eigen modes recovered by the solver.

### **6.3.3 Alternative way implemented by modal decomposition**

Modal decomposition in  $cFSM$  has the ability to decompose the deformation field into an individual mode or combined modes of interest. Though the critical loads of pure modes in  $cFSM$  can not be used directly with  $DSM$ , the longitudinal terms contributing most to the pure modes can be determined and these terms then used in the conventional  $FSM$  solution to force the member to buckle in the desired local or distortional buckling mode. These buckling loads may then be used as  $DSM$  inputs to predict the ultimate strength in design.

The method is quite effective especially for the local buckling mode. However, for the distortional buckling mode, depending on the member length and boundary conditions, one may need to go through many higher modes to find the distortional buckling mode even when only using the longitudinal terms suggested by pure mode (i.e.,

$m \sim L/L_{cr}$ ). This is because distortional buckling mode has an intermediate half-wavelength, and the longitudinal terms required to form the distortional buckling mode may overlap with the global buckling mode (usually longitudinal term  $m=1$ ) for a short member.

For the global buckling mode, the modal decomposition solution of  $G$  and  $ST/O$  by cFSM can provide a fairly close result compared to a conventional FSM solution. See [27] for more details about comparison between pure  $G$  modes.

#### **6.4 Method based on FEM for general boundary conditions**

As introduced in Chapter 4, the finite element method (FEM), utilizing shell elements, has become more common in analyzing the stability of thin-walled structures thanks to advances in computational power. As powerful as FEM can be, there is no modal identification and decomposition capability for stability solutions of thin-walled members. So, FE-based thin-walled design requires elastic buckling values of characteristic modes still be investigated through laborious visual examination and subjective engineering judgment. Now, with the developed modal identification method proposed in Chapter 4, quantification of buckling modes can be calculated and judgment of the buckling mode can be made based on a quantitative basis. Possible automation in the application in design can be sought with the quantitative participation of buckling modes in the FEM solution. A brief summary of methods regarding traditional observation and modal identification in applications follow.

#### 6.4.1 Traditional observation method

Finite element modeling requires some effort in initiating the model. Once the FEM model is ready, elastic buckling analysis can be performed and buckling behavior can be studied. The goal of the stability analysis for thin-walled members is to find the characteristic buckling modes:  $G$ ,  $D$ , and  $L$ .

By understanding the essential features of each characteristic buckling mode (shape, half-wavelength, etc.), appropriate categorization of the higher modes can be made through engineering judgment. The first identified modes (in ascending buckling values) of  $G$ ,  $D$ , and  $L$  can be used as the needed inputs in DSM. It is worth noting that there are possibilities that some of the interacted modes may be hard to categorize, and for short members global buckling mode is often not observed from the selected number of modes (e.g., 50 in our studies). (Note, from a practical points, if  $P_{cr}/P_y$  or  $M_{cr}/M_y$  is high enough the elastic buckling identification is unrelated, See DSM design guide [43].)

#### 6.4.2 Method with Modal identification

The proposed modal identification method of Chapter 4 provides the opportunity to quantify the buckling modes into fundamental buckling classes in terms of their participations from stability solutions of an FEM model. Therefore, a more reliable categorization can be made based on quantitative participation. However, similar to FSM, there is a question as to how large the participation of one characteristic mode should be in order to be categorized the mode.

The same quantification rules applied for FSM modal identification can be used for FEM modal identification. Therefore, two quantification rules are explored: 75%ile exceedance and 50%ile exceedance. For each mode class ( $G$ ,  $D$ , and  $L$ ), the first

identified modes are those of greatest interest. These buckling loads may then be used as DSM inputs to predict the ultimate strength in design. Both rules are illustrated in the numerical examples.

## **6.5 Numerical examples**

The numerical examples presented here are focusing on the application of FSM and FEM for general boundary conditions. Systematic studies on the two-step method by the author based on the signature curve can be found in [66]. For general boundary conditions, consider the numerical studies in Chapter 4 regarding modal identification of FEM elastic buckling analysis are considered here.

### **6.5.1 FSM-like boundary condition cases**

#### ***6.5.1.1 Elastic buckling loads of characteristic $G$ , $D$ , and $L$ buckling modes***

For the case studies with FSM-like boundary conditions, the comparison of FSM and FEM results in terms of both modal participations and critical loads show great agreement (Table 4-2). In fact, the summarized  $G$ ,  $D$ , and  $L$  modes in Table 4-2 are based on a combined investigation method involving observation, selection of reasonably high modal participation, and also mode shape matching.

With the methods established for FSM in Chapter 6, the identified characteristic  $G$ ,  $D$ , and  $L$  buckling modes are listed in Table 6-1 for conventional FSM by traditional observation and modal identification methods. Clearly, using different rules for the modal identification method, may yield different  $G$ ,  $D$ , and  $L$  characteristic buckling modes. In Table 6-1 for FSM solutions, this occurs for the characteristic distortional buckling mode of C-F. For the 3<sup>rd</sup> mode, a localized distortional buckling mode (refer to FEM buckling

mode C-F in Figure 4-2) is observed at the free end. Modal identification indicates 73% distortional buckling participation and 22% global buckling participation while the 6<sup>th</sup> mode is a more uniform distortional buckling mode (refer to FEM buckling mode C-F in Figure 4-2) with 88% *D* participation, as shown in Figure 4-8. If considering the sensitivities of modal identification, 73% may be still approximately falling into the 75%ile exceedance rule, thus 3<sup>rd</sup> mode may be the characteristic distortional buckling mode of C-F.

Similarly, Table 6-2 gives the characteristic *G*, *D*, and *L* buckling modes for FEM models with FSM-like boundary conditions. Similar to FSM solutions, different characteristic buckling modes may be identified by different methods. However, in general the results are quite robust.

Table 6-1 Characteristic buckling modes of FSM by different methods

Boundary conditions	Characteristic buckling mode	Observation		Modal identification			
		mode #	$P_{cr}$ (kN)	75%ile exceedance		50%ile exceedance	
				mode #	$P_{cr}$ (kN)	mode #	$P_{cr}$ (kN)
S-S	G	1	60.6	1	60.6	1	60.6
	D	3	156.9	3	156.9	3	156.9
	L	8	191.0	8	191.0	8	191.0
C-C	G	12	204.2	12	204.2	12	204.2
	D	1	162.8	1	162.8	1	162.8
	L	5	191.3	5	191.3	5	191.3
S-C	G	1	118.0	1	118.0	1	118.0
	D	2	158.0	2	158.0	2	158.0
	L	6	191.1	6	191.1	6	191.1
C-F	G	1	22.1	1	22.1	1	22.1
	D	3	95.8	6	161.6	3	95.8
	L	10	191.3	10	191.3	10	191.3
C-G	G	1	61.1	1	61.1	1	61.1
	D	3	157.8	3	157.8	3	157.8
	L	7	191.1	7	191.1	7	191.1

Table 6-2 Characteristic buckling modes of FEM by different methods

Boundary conditions	Characteristic buckling mode	Observation		Modal identification			
		mode #	$P_{cr}$ (kN)	75% ile exceedance		50% ile exceedance	
				mode #	$P_{cr}$ (kN)	mode #	$P_{cr}$ (kN)
S-S	G	1	60.4	1	60.4	1	60.4
	D	3	160.3	3	160.3	3	160.3
	L	9	201.5	9	201.5	7 <sup>(a)</sup>	198.7
C-C	G	7	201.6	7	201.6	7	201.6
	D	1	163.7	1	163.7	1	163.7
	L	5	201.5	5	201.5	5	201.5
S-C	G	1	112.2	1	112.2	1	112.2
	D	2	159.1	2	159.1	2	159.1
	L	8	201.5	8	201.5	8	201.5
C-F	G	1	22.0	1	22.0	1	22.0
	D	3	84.8	7 <sup>(b)</sup>	163.2	3	84.8
	L	11	201.5	11	201.5	11	201.5
C-G	G	1	60.6	1	60.6	1	60.6
	D	3	163.7	3	163.7	3	163.7
	L	7	201.5	7	201.5	7	201.5
(a): 65% ile of local							
(b): 65% ile of distortional							

### 6.5.1.2 Nominal strength by Direct Strength Method

Once the needed characteristic  $G$ ,  $D$ , and  $L$  buckling modes are identified, their critical buckling loads can be used as inputs in DSM to predict the nominal strength of the member. For a column, the DSM equations are provided in Eq. (1-4) – (1-6) in Chapter 1.4. Utilizing those equations with the critical buckling loads in Table 6-1 and Table 6-2, the nominal strength of a member can be obtained based on the different methods in identifying the characteristic buckling modes, as provided in Table 6-3 and Table 6-4. Note, the yield stress is assumed to be 345 MPa. The member is considered as globally restrained. In this case it has been assumed, flexural or flexural-torsional buckling will not happen (i.e.,  $P_{cre} = \infty$ ), so the nominal strength of global buckling ( $P_{ne}$ ) can reach the squash load ( $P_y$ ).

Table 6-3 Nominal strengths of the columns by FSM solutions

Boundary conditions	global restraint?	Observation		Modal identification			
				Based on 75% ile exceedance		Based on 50% ile exceedance	
		$P_n$ (kN)	Controlled mode	$P_n$ (kN)	Controlled mode	$P_n$ (kN)	Controlled mode
<b>S-S</b>	unrestrained	53.1	G	53.1	G	53.1	G
	full restrained	121.5	D	121.5	D	121.5	D
<b>C-C</b>	unrestrained	117.1	L	117.1	L	117.1	L
	full restrained	123.4	D	123.4	D	123.4	D
<b>S-C</b>	unrestrained	92.0	G	92.0	G	92.0	G
	full restrained	121.9	D	121.9	D	121.9	D
<b>C-F</b>	unrestrained	19.4	G	19.4	G	19.4	G
	full restrained	97.8	D	123.0	D	97.8	D
<b>C-G</b>	unrestrained	53.6	G	53.6	G	53.6	G
	full restrained	121.8	D	121.8	D	121.8	D

Table 6-4 Nominal strengths of the columns by FEM solutions

Boundary conditions	global restraint?	Observation		Modal identification			
				Based on 75% ile exceedance		Based on 50% ile exceedance	
		$P_n$ (kN)	Controlled mode	$P_n$ (kN)	Controlled mode	$P_n$ (kN)	Controlled mode
<b>S-S</b>	unrestrained	53.0	G	53.0	G	53.0	G
	full restrained	122.6	D	122.6	D	122.6	D
<b>C-C</b>	unrestrained	117.4	G	117.4	G	117.4	G
	full restrained	123.6	D	123.6	D	123.6	D
<b>S-C</b>	unrestrained	89.3	G	89.3	G	89.3	G
	full restrained	122.2	D	122.2	D	122.2	D
<b>C-F</b>	unrestrained	19.3	G	19.3	G	19.3	G
	full restrained	92.3	D	123.5	D	92.3	D
<b>C-G</b>	unrestrained	53.1	G	53.1	G	53.1	G
	full restrained	123.6	D	123.6	D	123.6	D

As shown in Table 6-3 and Table 6-4, nominal strength predicted by the FSM solution and FEM solutions is very close. If the member is not globally restrained, the strength is controlled by the global buckling mode. The only exception is for C-C, with a lower critical local buckling load predicted by the FSM solution compared to the FEM solution, the strength is controlled by local buckling though distortional buckling has the lowest critical load as shown in Table 6-1 (actually, local/global buckling interaction has been taken into consideration through Eq. (1-5)). Once the member is globally restrained, the member strength is controlled by distortional buckling.

For this member (Figure 4-1) with the boundary conditions studied here, based on different categorization methods, the predicted nominal strengths are the same for nearly all cases. However, differences are observed for the globally restrained case with C-F boundary conditions. Based on the 50%ile exceedance rule, the 3<sup>rd</sup> mode, a distortional/global interacted mode with much lower critical load, is identified as characteristic distortional buckling mode (see Table 6-1 and Table 6-2), thus leads to a much smaller nominal (more conservative) strength (Table 6-3 and Table 6-4).

## **6.5.2 Partially-restrained beam cases**

### ***6.5.2.1 Elastic buckling loads of characteristic buckling modes***

For all the three cases in Chapter 4.6, the characteristic buckling modes are identified based on the two methods for the FEM solution. The identified characteristic buckling modes are provided in Table 6-5.

For distinct modes, such as  $G$  in beams without springs or with weak springs and  $D$  in all three cases, the identified buckling modes are the same by both observation and modal identification methods. The dominance of these distinct modes is obvious, as suggested by 75%ile exceedance and confirmed by the buckling mode shapes in Figure 4-41. In fact, the contribution is more than 90% for these distinct modes, as shown in Figure 4-38 - Figure 4-40.

However, the local buckling mode for the beam models is less distinct. Significant engineering judgment is needed for the local buckling mode when investigating the buckling modes by observation, because of the mode interaction. Without springs, the 20<sup>th</sup> mode shows the dominance of local buckling with 78%ile exceedance while the 18<sup>th</sup> mode has 71%ile exceedance of the local buckling mode. However, with practical springs,

no buckling mode has 75%ile exceedance of local buckling in the first 50 modes. The observed local buckling mode (36<sup>th</sup> mode) in Table 6-5 is a very subjective choice. Modal identification indicates 53% local participation. The 1<sup>st</sup> buckling mode with 50%ile exceedance of local buckling is the 28<sup>th</sup> mode with 51% participation, which indicates the mode is highly coupled with other buckling modes (in this case, it is distortional).

In addition, for beams with practical springs, the global buckling mode is greatly restrained. No distinct global buckling mode is found in the first 50 modes based on observation and 75% exceedance rule. Further, the 1<sup>st</sup> distinct global buckling is the 68<sup>th</sup> mode at a critical moment of  $M_{cr} = 37.8$  kN-m. However, based on the 50% exceedance rule, the 32<sup>nd</sup> mode indicates an interacted mode with obvious feature of flexural buckling in major-axis bending with 50%ile exceedance interweaving with local and distortional buckling, as shown in Figure 4-41(c). Note, in fact, if  $M_{cre}$  is bigger than 2.78, no need to worry about global buckling.

Table 6-5 Identified characteristic buckling modes for all three cases

Characteristic buckling mode		Beam w/o springs			Beam w/ weak springs			Beam w/ practical springs		
		Observation	Modal Identification		Observation	Modal Identification		Observation	Modal Identification	
			75%ile	50%ile		75%ile	50%ile		75%ile	50%ile
G	Mode #	1	1	1	8	8	8	n/a <sup>(a)</sup>	n/a	32
	$P_{cr}$ (kN-m)	5.8	5.8	5.8	11.5	11.5	11.5			22.7
D	Mode #	2	2	2	1	1	1	1	1	1
	$P_{cr}$ (kN-m)	7.8	7.8	7.8	7.8	7.8	7.8	8.9	8.9	8.9
L	Mode #	20	20	18	28	37	18	36 <sup>(b)</sup>	n/a	28
	$P_{cr}$ (kN-m)	18.2	18.2	18.0	19.3	19.9	18.1	23.2		21.9
(a): observation is made in the first 50 modes										
(b): approximately based on engineering judgment										

### 6.5.2.2 Nominal strength by Direct Strength Method

Once the needed characteristic  $G$ ,  $D$ , and  $L$  buckling modes are identified, their critical buckling loads can be used as inputs in DSM to predict the nominal strength of

the member. For the beam, the DSM equations are provided in Eq. (1-8) – (1-10) in Chapter 1.4. Utilizing those equations with the critical buckling loads in Table 6-5, the nominal strength of the member can be obtained based on the different methods in identifying the characteristic buckling modes, as provided in Table 6-6. Note, for characteristic buckling mode identified as ‘n/a’ in Table 6-5, the critical moments are assumed to be large enough that this mode will not control the strength prediction.

Table 6-6 Nominal strengths of the beams

	Beam w/o springs			Beam w/ weak springs			Beam w/ practical springs		
	Observation	Modal Identification		Observation	Modal Identification		Observation	Modal Identification	
		Based on 75%ile exceedanc	Based on 50%ile exceedanc		Based on 75%ile exceedanc	Based on 50%ile exceedanc		Based on 75%ile exceedanc	Based on 50%ile exceedanc
Controlled mode	G	G	G	D	D	D	D	D	D
$P_{cr}$ (N-m)	4.7	4.7	4.7	5.0	5.0	5.0	5.3	5.3	5.3

As shown in Table 6-6, the predicted strengths are the same for all the three beam cases regardless of the different categorization methods.

## 6.6 Discussions

Though it is premature to make a conclusion as to which rule should be used for the modal identification method, it is safe to say that the 50%ile exceedance rule gives a lower bound prediction, although applying critical loads of interacted modes into DSM equations warrants further investigation. In particular, the examples presented here are always dominated by the distinct modes ( $G$ , or  $D$ ) that have lower critical loads though certain modes (e.g.,  $L$ ) are found as a coupled mode. Examples where the critical loads are coupled modes are necessary. In addition, more systematic study in design applications is needed for the proposed rule of modal identification.

Though not mentioned previously, the modal identification based on the FSM solution of general boundary conditions and FEM solution is only applicable to straight-line model (without corners) due to the fact that *c*FSM can not handle rounded corner. More study is needed to handle the corners based on these solutions.

## **6.7 Summary**

In this chapter, the application of the finite strip method and the finite element method with modal identification are presented with numerical examples and the Direct Strength Method. A two-step method is proposed based on the signature curve to overcome the indistinct minima and handle the corners of the members. Different methods of identifying the characteristic buckling modes are discussed for the finite strip method of general boundary conditions. Applications with the Direct Strength Method are illustrated with emphasis on utilizing the modal identification results. Similar applications for FEM solution are also discussed.

## **Chapter 7 Summary and recommendations**

### **7.1 Summary**

This dissertation presents a comprehensive set of research efforts on the numerical modeling of thin-walled structures, in particular cold-formed steel members, with an emphasis on the development of a new conventional and constrained finite strip method for elastic buckling analysis of members with general end boundary conditions, and an automated modal identification method for the shell finite element method to identify the characteristic buckling modes in elastic buckling analysis and to categorize the failure modes in nonlinear collapse analysis.

A new conventional finite strip method is explicitly derived, implemented and validated to account the general end boundary conditions: pin-pin, fixed-fixed, fixed-pin, fixed-free, and fixed-guided. The elastic and geometric stiffness matrices based on the specially selected longitudinal shape functions are provided in a general form with only specific integrals remaining boundary condition dependent. The validation studies show excellent agreement between eigenbuckling solutions by FSM and shell FEM with general end boundary conditions. However, one must take care to insure enough (or the proper) longitudinal terms are included in the series to capture all buckling modes of interest. For any end boundary condition other than simple supports, multiple longitudinal half-waves participate in the solution, even when simple buckling patterns

may be visually identified. The relationship between signature curves and general FSM solutions reveals the buckling characteristics of local, distortional, and global modes. Longitudinal terms of greatest interest included in the buckling analysis are then recommended as an approximation to increase the computational efficiency. Springs are appropriately accounted for in the FSM modeling. Verification studies show excellent agreement with an analytical solution for global buckling. However, pre-buckling stress in FSM is different from that in an FEM model with springs, especially for beam members, resulting in different buckling prediction. The analyst should be aware of this difference. As demonstrated herein the boundary conditions should not be mixed in the same FSM model.

Based on the new conventional finite strip method, the existing *c*FSM solutions for pin-pin boundary conditions are recast into a new generalized notation for general end boundary conditions; specifically the constraint matrices for the global, distortional, local, and other deformation spaces are written in the generalized notation. The theoretical background of the method for general boundary conditions is shown, and the procedure for defining the pure buckling modes (in the natural basis) is explicitly presented. Two ways to define the other modes are provided as either Shear (*S*) and transverse extension (*T*) modes, or the more mathematical notion (*O*) of the null of the *GDL* space and related options are discussed. With the natural basis in place, the modal basis (axial or applied) is defined by solving the constrained eigenvalue problem within each space. Coupled and uncoupled bases are accordingly presented. Summary of the available bases and normalization is discussed. The modal decomposition solution is presented using the developed *c*FSM methodology for general end boundary conditions

and compared with Generalized Beam Theory (GBT). In addition, modal identification is studied for FSM stability modes for general end boundary conditions. For application purpose, recommendations for basis, normalization of the base vectors, normalization of the participation results, and selection of the  $ST$  or  $O$  space are made for the user of  $c$ FSM.

In Chapter 4, the modal identification method for shell finite element method eigenbuckling analysis is proposed by employing the base vectors from the constrained finite strip method for general end boundary conditions. Necessary extrapolation of the base functions to finite element context is provided and minimization problem required is shown. *Associated* base functions, where the  $c$ FSM and FEM end boundary conditions correspond, are shown to provide modal identification in agreement with existing  $c$ FSM implementations, and with traditional visual observation for modal identification. *Generalized* base functions, generated from a subset of the new  $c$ FSM base vectors, are proposed, which are intended for arbitrary end boundary conditions. Modal identification utilizing *generalized* base vectors is shown to be in good agreement with those utilizing the *associated* base vectors. In addition, numerical studies of semi-rigid and mixed end boundary conditions demonstrate the applicability of the *generalized* base vectors to modal identification with arbitrary end boundary conditions. Moreover, studies on partially restrained beam indicate the applicability of modal identification for member with intermediate restraints. Furthermore, exact match of the finite element and finite strip models in terms of meshing is demonstrated to be not necessary. Extrapolation of the  $c$ FSM base functions is able to provide close modal identification solution. This enables the applicability of modal identification on member with geometrical change

along the length such as holes and tapers. Numerical study on modal identification with holes shows the method provides reasonable quantitative classification of buckling modes that are far laborious to identify by observation.

For nonlinear collapse analysis in Chapter 5, the modal identification method follows the same procedure as for elastic buckling analysis in Chapter 4, except that the modal identification is performed on the general displacement vector instead of buckling mode vector and the displacement vector need be corrected by the imperfection in the model. The method is first demonstrated capturing the behavior correctly on the linear elastic static analysis that associates with the *GD* deformation. Then, the applicability of the method is further demonstrated with numerical examples of geometrically perfect and imperfect cold-formed steel lipped channel members under uniform end shortening. The results indicate how the participation of a given deformation space evolves under load. Results show that the failure mode at the peak is sensitive to both the cross section and the imperfection in the model. In the collapse regime distortional deformations have a large participation as they better describe the localized collapse mechanism that forms. The analysis results quantitatively demonstrate the interplay between local, distortional, and global buckling during collapse and even demonstrate the importance of shear and transverse extension (particularly during collapse).

The application of finite strip method and finite element method in conjugate with modal identification are presented with numerical examples with direct strength method. First, based on the signature curve, a two-step method is proposed to overcome the indistinct minima and handle the corners of the members. Then, different methods of identifying the characteristic buckling modes are discussed for both the finite strip

method and finite element method. Concentration has been given on the use of modal identification solution. Applications with direct strength method illustrate the proposed exceedance rules in categorizing the characteristic buckling modes are applicable though more systematic research is needed.

Among other things, the newly developed conventional and constrained finite strip methods provide researcher and engineer a useful tool to study the behaviour of thin-walled structural member. Modal identification has the ability to categorize and reduce the complicated deformations that occur in a shell finite element model, which will ultimately aid Specification development, which must simplify complicated behaviour down to strength predictions in isolated buckling classes.

## **7.2 Recommendations for future research**

The finite strip method developed in this research is based on the Kirchhoff thin-plate theory and assume only axial edge traction. To take into consideration transverse loading, the geometric stiffness should include the potential work associated with second-order shear strains in Green-Lagrange functions. In addition, to accurately take into account shear effects, the Mindlin plate theory should be employed. Moreover, the membrane and bending coupling can be included as well by Mindlin plate theory.

The modal identification provides a method to quantitatively categorize the complex buckling behaviors. However, more systematic study in design application is needed for utilizing this modal identification solution towards an automated design procedure. For example, the proposed categorization rules for characteristic buckling modes based on the participation need further validation both numerically and experimentally.

Moreover, modal identification provides the participation of fundamental buckling mode classes for each mode. How to utilize these participation values in design requires further research. One possible way is to perform a reduction of the critical load or nominal strength based on the participation. This will provide a way to handle the interacted buckling modes.

Modal identification for nonlinear collapse analysis provided in this research is a proof-of-concept for the extension of modal identification. As discussed in Chapter 5, how to handle the primary displacement associated with a given loading requires further study. In the simple loading case provided in this research the primary displacement associated with loading was removed since it essentially coincides with the  $G4$  global mode. However, for more complicated loading the separation is less clear. It is proposed that the entire linear elastic deformations associated with the applied loading on the perfect structure should be removed from the identification, but this idea needs further study.

In addition, how to connect collapse mechanisms and their related energy dissipation to the  $G$ ,  $D$ ,  $L$ , and  $ST$  deformation spaces need further study. Currently, no simple means exists for predicting energy dissipation in members, and modal identification and categorization provides new information to make these connections. Future work in this direction is anticipated.

Finally, as discussed in Chapter 6, the modal identification is only applicable to straight-line model (without corners) due to the fact that  $c$ FSM can not handle rounded corner. More study is needed to pass the modal identification solutions of elastic buckling and nonlinear collapse analyses to models with corners.

## References

1. Yu, W.-W., *Cold-Formed Steel in Tall Buildings*. 1993: McGraw-Hill.
2. Kirkland, W.G., *Cold Roll Forming Practice in the United States*. 1966: American Iron and Steel Institute.
3. Yu, W.-W., *Cold-Formed Steel Design*. Third ed. 2000, New York: John Wiley & Sons.
4. NAS, *2007 Edition of the North American Specification for the Design of Cold-Formed Steel Structural Members*. 2007, Washington, DC: American Iron and Steel Institute.
5. *Eurocode 3: design of steel structures, part 1.3: general rules. ENV 1993-1-3*. 1996, European Committee for Standardisation (CEN).
6. AS/NZS, *Cold-formed steel structures, AS/NZS 4600*. 1996, Standards Australia/Standards New Zealand.
7. Hancock, G.J., *Design for distortional buckling of flexural members*. Thin-Walled Structures, 1997. **27**(1): p. 3-12.
8. Lau, S.C.W. and G.J. Hancock, *DISTORTIONAL BUCKLING FORMULAS FOR CHANNEL COLUMNS*. Journal of structural engineering New York, N.Y., 1987. **113**(5): p. 1063-1078.
9. Davies, J.M. and C. Jiang, *Design for distortional buckling*. Journal of Constructional Steel Research, 1998. **46**(1-3): p. 174-175.
10. Schafer, B.W. and T. Peköz, *Laterally braced cold-formed steel flexural members with edge stiffened flanges*. Journal of Structural Engineering, 1999. **125**(2): p. 118-127.
11. Cheung, Y.K. and L.G. Tham, *The Finite Strip Method*. 1997: CRC.
12. Bradford, M.A. and M. Azhari, *Buckling of plates with different end conditions using the finite strip method*. Computers & Structures, 1995. **56**(1): p. 75-83.
13. Fan, S.C., *Spline finite strip method in structural analysis, Ph.D. thesis*, in Department of Civil Engineering. 1982, University of Hongkong: Hongkong.
14. Cheung, Y.K., F.T.K. Au, and J. KONG, *Structural analysis by the finite strip method using computed shape functions*, in *Int Conf on Computational Methods in Engineering*. 1992: Singapore. p. 1140-1145.
15. Cheung, Y.K., *Finite strip method in analysis of elastic plate with two opposite simply supported ends*, in *The institution of civil engineering*. 1968. p. 1-7.
16. Cheung, Y.K., *Finite strip method analysis of elastic slabs*. Journal of the engineering mechanics, 1968. **94**(EM6): p. 1365-1378.
17. Fan, S.C. and Y.K. Cheung, *Analysis of shallow shells by spline finite strip method*. Engineering Structures, 1983. **5**(4): p. 255-263.
18. Zhu, D.S. and Y.K. Cheung, *Postbuckling analysis of shells by spline finite strip method*. Computers & Structures, 1989. **31**(3): p. 357-364.
19. Cheung, Y.K., *Analysis of box girder bridges by finite strip method, Concrete bridge design*. ACI publications SP-26, 1971: p. 357-378.

20. Cheung, Y.K., W.Y. Li, and L.G. Tham, *Free vibration analysis of singly curved shell by spline finite strip method*. Journal of Sound and Vibration, 1989. **128**(3): p. 411-422.
21. Cheung, Y.K., S.G. Hutton, and C. Kasemset, *Frequency analysis of coupled shear wall assemblies*. Earthquake Engineering & Structural Dynamics, 1977. **5**(2): p. 191-201.
22. Cheung, Y.K. and C. Kasemset, *Approximate frequency analysis of shear wall frame structures*. Earthquake Engineering & Structural Dynamics, 1978. **6**(2): p. 221-229.
23. Swaddiwudhipong, S., *A unified approximate analysis of tall building using generalized finite strip method, Ph.D. thesis*, in Department of Civil Engineering. 1979, University of Hongkong: Hongkong.
24. Hancock, G.J., *Local, Distortional, and lateral buckling of I-beams*. ASCE Journal of structural engineering, 1978. **104**(11): p. 1787-1798.
25. Schafer, B.W. and S. Adány, *Buckling analysis of cold-formed steel members using CUFSM: Conventional and constrained finite strip methods.*, in *Eighteenth International Specialty Conference on Cold-Formed Steel Structures: Recent Research and Developments in Cold-Formed Steel Design and Construction*. 2006. p. 39-54.
26. Adány, S. and B.W. Schafer, *Buckling mode decomposition of single-branched open cross-section members via finite strip method: Derivation*. Thin-Walled Structures, 2006. **44**(5): p. 563-584.
27. Adány, S. and B.W. Schafer, *Buckling mode decomposition of single-branched open cross-section members via finite strip method: Application and examples*. Thin-Walled Structures, 2006. **44**(5): p. 585-600.
28. Adány, S. and B.W. Schafer, *A full modal decomposition of thin-walled, single-branched open cross-section members via the constrained finite strip method*. Journal of Constructional Steel Research, 2008. **64**(1): p. 12-29.
29. Davies, J.M. and P. Leach, *First-order generalised beam theory*. Journal of Constructional Steel Research, 1994. **31**(2-3): p. 187-220.
30. Davies, J.M., P. Leach, and D. Heinz, *Second-order generalised beam theory*. Journal of Constructional Steel Research, 1994. **31**(2-3): p. 221-241.
31. Silvestre, N. and D. Camotim, *First-order generalised beam theory for arbitrary orthotropic materials*. Thin-Walled Structures, 2002. **40**(9): p. 755-789.
32. Silvestre, N. and D. Camotim, *Second-order generalised beam theory for arbitrary orthotropic materials*. Thin-Walled Structures, 2002. **40**(9): p. 791-820.
33. Dinis, P.B., D. Camotim, and N. Silvestre, *GBT formulation to analyse the buckling behaviour of thin-walled members with arbitrarily 'branched' open cross-sections*. Thin-Walled Structures, 2006. **44**(1): p. 20-38.
34. Basaglia, C., D. Camotim, and N. Silvestre. *Non-linear GBT for thin-walled steel frames: Formulation, implementation and application*. 2010.
35. Bebiano, R., N. Silvestre, and D. Camotim. *GBTUL - A code for the buckling analysis of cold-formed steel members*. 2008.

36. Camotim, D., C. Basaglia, and N. Silvestre, *GBT buckling analysis of thin-walled steel frames: A state-of-the-art report*. Thin-Walled Structures, 2010. **48**(10-11): p. 726-743.
37. Gonçalves, R., P. Le Grogneq, and D. Camotim, *GBT-based semi-analytical solutions for the plastic bifurcation of thin-walled members*. International Journal of Solids and Structures, 2010. **47**(1): p. 34-50.
38. Ádány, S., et al., *GBT and cFSM: two modal approaches to the buckling analysis of unbranched thin-walled members*. Advanced Steel Construction, an international journal 2009. **5**(2): p. 195-223.
39. Von Karman, T., E.E. Sechler, and L.H. Donnell, *The strength of thin plates in compression*. Transaction, ASME, 1932. **54**(APM 5405).
40. Winter, G., *Strength of thin steel compression flanges*. Transaction of ASCE, 1947. **Paper No. 2305, 112,1**.
41. Schafer, B.W. and T. Peköz. *Direct Strength Prediction of Cold-Formed Steel Members using Numerical Elastic Buckling Solutions*. in *Proceedings of the Fourteenth International Specialty Conference on Cold-Formed Steel Structures*. 1998. St. Louis, Missouri.
42. Schafer, B.W., *Review: The Direct Strength Method of cold-formed steel member design*. Journal of Constructional Steel Research, 2008. **64**(7-8): p. 766-778.
43. AISI, *Direct Strength Method Design Guide*. 2006, Washington, DC.
44. Yu, C. and B.W. Schafer, *Local buckling tests on cold-formed steel beams*. Journal of Structural Engineering, 2003. **129**(12): p. 1596-1606.
45. ABAQUS, *ABAQUS theory manual (v6.7)*. 2007, ABAQUS, Inc.
46. Li, Z. and B.W. Schafer. *Finite Strip Stability Solutions for General Boundary Conditions and the Extension of the Constrained Finite Strip Method*. in *Trends in Civil and Structural Engineering Computing*. 2009. Stirlingshire, UK: Saxe-Coburg Publications.
47. Ugural, A.C. and S.K. Fenster, *Advanced strength and applied elasticity*. 4th ed. 2008: Prentice Hall Professional.
48. Li, Z., *Buckling analysis of the finite strip method and theoretical extension of the constrained finite strip method for general boundary conditions*. 2009, Johns Hopkins University.
49. SSMA, *Product Technical Information, ICBO ER-4943P*. 2001, Steel Stud Manufacture Association.
50. Timoshenko, S.P. and J.M. Gere, *Theory of Elastic Stability*. 1961, New York McGraw-Hill Book Company.
51. Ádány, S., *Buckling mode classification of members with open thin-walled cross-sections by using the finite strip method*. 2004, Johns Hopkins University.
52. Li, Z., et al., *Impact of basis, orthogonalization, and normalization on the constrained Finite Strip Method for stability solutions of open thin-walled members*. Thin-Walled Structures, 2011. **49**(9): p. 1108-1122.
53. Li, Z. and B.W. Schafer. *The constrained finite strip method for general end boundary conditions*. 2010.

54. Li, Z. and B.W. Schafer. *Buckling analysis of cold-formed steel members with general boundary conditions using CUFSM: Conventional and constrained finite strip methods*. 2010.
55. Ádány, S. and A. Joó, *Identification of FEM buckling modes of thin-walled columns by using cFSM base functions.*, in *CIMS 2008, Fifth International Conference on Coupled Instabilities in Metal Structures*. 2008: Sydney, Australia. p. 265-272.
56. Ádány, S., A.L. Joó, and B.W. Schafer, *Buckling mode identification of thin-walled members by using cFSM base functions*. *Thin-Walled Structures*, 2010. **48**(10-11): p. 806-817.
57. Chu, X.T., J. Rickard, and L.Y. Li, *Influence of lateral restraint on lateral-torsional buckling of cold-formed steel purlins*. *Thin-Walled Structures*, 2005. **43**(5): p. 800-810.
58. Li, L.Y., *Lateral-torsional buckling of cold-formed zed-purlins partial-laterally restrained by metal sheeting*. *Thin-Walled Structures*, 2004. **42**(7): p. 995-1011.
59. Schafer, B.W., R.H. Sangree, and Y. Guan. *Floor system design for distortional buckling including sheathing restraint*. 2008.
60. Vieira Jr, L.C.M., Y. Shifferaw, and B.W. Schafer, *Experiments on sheathed cold-formed steel studs in compression*. *Journal of Constructional Steel Research*, 2011. **67**(10): p. 1554-1566.
61. Ye, Z.M., et al., *Buckling behavior of cold-formed zed-purlins partially restrained by steel sheeting*. *Thin-Walled Structures*, 2002. **40**(10): p. 853-864.
62. Silvestre, N. and D. Camotim, *Non-linear generalised beam theory for cold-formed steel members*. *International Journal of Structural Stability and Dynamics*, 2003. **3**(4): p. 461-490.
63. Schafer, B.W., Z. Li, and C.D. Moen, *Computational modeling of cold-formed steel*. *Thin-Walled Structures*, 2010. **48**(10-11): p. 752-762.
64. Schafer, B.W. and T. Peköz, *Computational modeling of cold-formed steel: Characterizing geometric imperfections and residual stresses*. *Journal of Constructional Steel Research*, 1998. **47**(3): p. 193-210.
65. Crisfield, M.A., *A fast incremental/iterative solution procedure that handles "snap-through"*. *Computers & Structures*, 1981. **13**(1-3): p. 55-62.
66. Li, Z. and B.W. Schafer, *Application of the finite strip method in cold-formed steel member design*. *Journal of Constructional Steel Research*, 2011. **66**(8-9): p. 971-980.

## Appendix A: Integrals from $I_1$ to $I_5$

$$I_1 = \int_0^a Y_{[m]} Y_{[n]} dy; I_2 = \int_0^a Y_{[m]}'' Y_{[n]} dy; I_3 = \int_0^a Y_{[m]} Y_{[n]}'' dy; I_4 = \int_0^a Y_{[m]}'' Y_{[n]}'' dy; I_5 = \int_0^a Y_{[m]}' Y_{[n]}' dy$$

where  $Y_{[m]}$  can be found in Section 2.1. The following only lists the non-zero terms.

### 1. S-S

$$I_1 = a/2; I_2 = I_3 = -\pi^2 m^2 / 2 / a; I_4 = \pi^4 m^4 / 2 / a^3; I_5 = -I_2; \text{ all for } m=n$$

### 2. C-C

$$I_1 = a/4, (m = n) \text{ except } I_1 = 3a/8, (m = n = 1), I_1 = -a/8, (|m - n| = 2);$$

$$I_2 = I_3 = -\pi^2 (m^2 + 1) / 4 / a, (m = n),$$

$$I_2 = \pi^2 (m^2 + 1) / 8 / a - \pi^2 m / 4 / a, (m - n = 2) \text{ and}$$

$$I_2 = \pi^2 (m^2 + 1) / 8 / a + \pi^2 m / 4 / a, (m - n = -2);$$

$$I_3 = \pi^2 (n^2 + 1) / 8 / a + \pi^2 n / 4 / a, (m - n = 2) \text{ and}$$

$$I_3 = \pi^2 (n^2 + 1) / 8 / a - \pi^2 n / 4 / a, (m - n = -2);$$

$$I_4 = \pi^4 \left[ (m^2 + 1)^2 + 4m^2 \right] / 4 / a^3, (m = n),$$

$$I_4 = -\pi^4 (m-1)^2 (n+1)^2 / 8 / a^3, (m - n = 2) \text{ and}$$

$$I_4 = -\pi^4 (n-1)^2 (m+1)^2 / 8 / a^3, (m - n = -2);$$

$$I_5 = \pi^2 (m+1)^2 / 4 / a, (m = n), I_5 = -\pi^2 (mn+1) / 8 / a, (|m - n| = 2)$$

### 3. S-C

$$I_1 = \left[1 + (m+1)^2 / m^2\right] a / 2, (m = n); I_1 = (m+1)a / 2 / m, (m - n = 1) \text{ and}$$

$$I_1 = (n+1)a / 2 / n, (m - n = -1);$$

$$I_2 = I_3 = -\pi^2 (m+1)^2 / a, (m = n),$$

$$I_2 = -\pi^2 (m+1)m / 2 / a, (m - n = 1) \text{ and } I_2 = -\pi^2 n(n+1) / 2 / a, (m - n = -1);$$

$$I_3 = -\pi^2 m(m+1) / 2 / a, (m - n = 1) \text{ and } I_3 = -\pi^2 (n+1)n / 2 / a, (m - n = -1);$$

$$I_4 = \pi^4 (m+1)^2 \left[ (m+1)^2 + m^2 \right] / 2 / a^3, (m = n),$$

$$I_4 = \pi^4 (m+1)m(n+1)^2 / 2 / a^3, (m - n = 1) \text{ and}$$

$$I_4 = \pi^4 (n+1)n(m+1)^2 / 2 / a^3, (m - n = -1);$$

$$I_5 = \pi^2 (m+1)^2 / a, (m = n), I_5 = \pi^2 (m+1)(n+1) / 2 / a, (|m - n| = 1);$$

#### 4. C-G

$$I_1 = a / 4, (m = n) \text{ except } I_1 = 3a / 8, (m = n = 1), I_1 = -a / 8, (|m - n| = 1);$$

$$I_2 = I_3 = -\pi^2 \left[ (m - 1/2)^2 + 1/4 \right] / 4 / a, (m = n),$$

$$I_2 = \pi^2 \left[ (m - 1/2)^2 + 1/4 \right] / 8 / a - \pi^2 (m - 1/2) / 8 / a, (m - n = 1) \text{ and}$$

$$I_2 = \pi^2 \left[ (m - 1/2)^2 + 1/4 \right] / 8 / a + \pi^2 (m - 1/2) / 8 / a, (m - n = -1);$$

$$I_3 = \pi^2 \left[ (n - 1/2)^2 + 1/4 \right] / 8 / a + \pi^2 (n - 1/2) / 8 / a, (m - n = 1) \text{ and}$$

$$I_3 = \pi^2 \left[ (n - 1/2)^2 + 1/4 \right] / 8 / a - \pi^2 (n - 1/2) / 8 / a, (m - n = -1);$$

$$I_4 = \pi^4 \left[ (m - 1/2)^2 + 1/4 \right]^2 / 4 / a^3 + \pi^4 (m - 1/2)^2 / 4 / a^3, (m = n),$$

$$I_4 = -\pi^4 n^4 / 8 / a^3, (m - n = 1) \text{ and } I_4 = -\pi^4 m^4 / 8 / a^3, (m - n = -1);$$

$$I_5 = \pi^2 (m - 1/2)^2 / 4 / a + \pi^2 / 16 / a, (m = n),$$

$$I_5 = -\pi^2 n^2 / 8/a, (m-n=1) \text{ and } I_5 = -\pi^2 m^2 / 8/a, (m-n=-1);$$

## 5. C-F

$$I_1 = 3a/2 - 2a(-1)^{m-1} / \pi / (m-1/2), (m=n),$$

$$I_1 = a - a(-1)^{m-1} / \pi / (m-1/2) - a(-1)^{n-1} / \pi / (n-1/2), (m \neq n);$$

$$I_2 = I_3 = \pi^2 (m-1/2)^2 \left[ (-1)^{m-1} / \pi / (m-1/2) - 1/2 \right] / a, (m=n),$$

$$I_2 = \pi (m-1/2) (-1)^{m-1} / a, (m \neq n) \text{ and } I_3 = \pi (n-1/2) (-1)^{n-1} / a, (m \neq n);$$

$$I_4 = \pi^4 (m-1/2)^4 / 2/a^3, (m=n); I_5 = \pi^2 (m-1/2)^2 / 2/a, (m=n)$$

## Appendix B: CUFSM v4

### B.1 Flow charts of the program

CUFSM is coded to analyze elastic buckling behavior of thin-walled members. The general procedures to perform finite strip analysis and advanced modal decomposition/modal identification analysis are illustrated in Figure B-1. For constrained finite strip method (cFSM), the procedure to generate the base vectors is shown in Figure B-2.

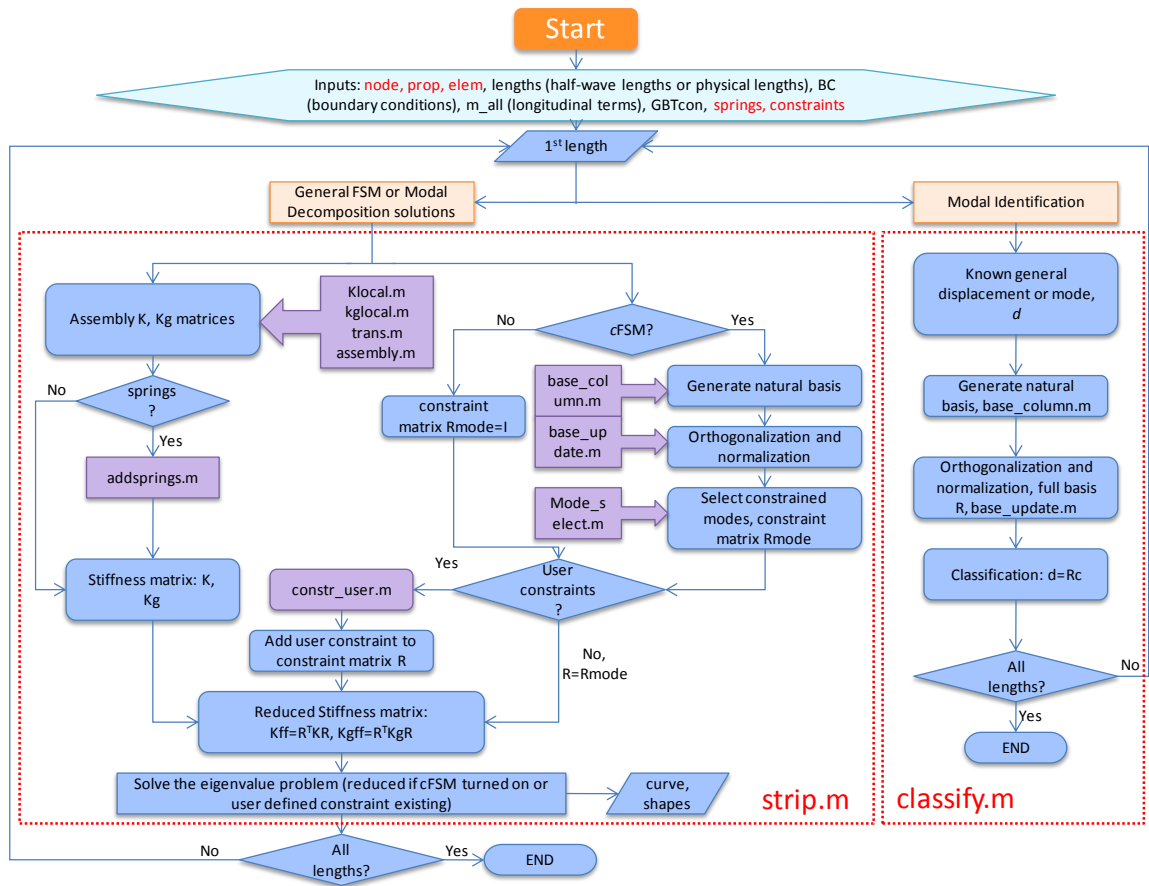


Figure B-1 Flow chart of the CUFSM code

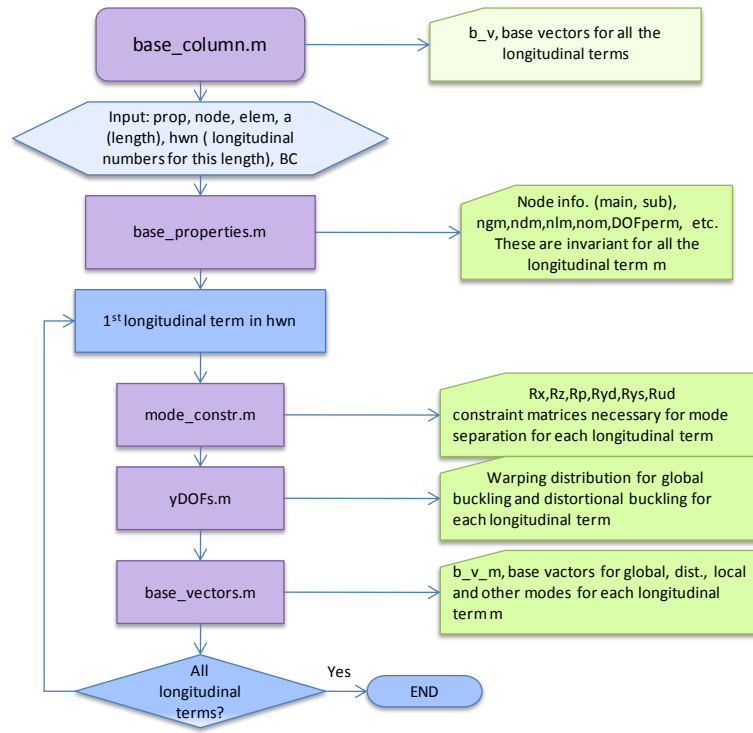


Figure B-2 Flow chart for generating the base vectors

## B.2 Screen shots of the program

An updated user-friendly interface is created for the new CUFSM version. The screen shots are provided in the following with some explanations of the menus in terms of their functionality. The intent of these screen shots is not to provide a tutorial for using the software, but rather to illustrate some of the rudimental functionalities of the software fulfilled in the interface. A comprehensive tutorial will be provided separately later.

The default screen when opening CUFSM 4 is in Figure B-3. The user can choose to load a saved data file then go to desired operation step. Or, the user can choose to input your own member data and appropriate boundary conditions.

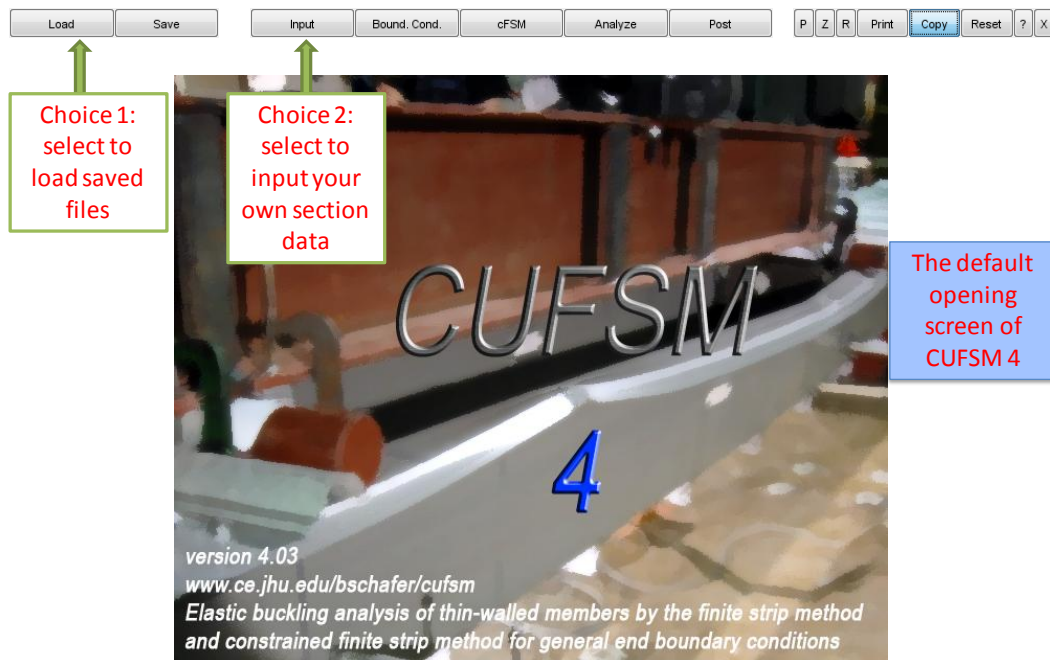


Figure B-3 Default opening screen of CUFSM 4

When getting into the input screen as shown in Figure B-4, the user need define the member in the similar fashion as the default member given. Possible spring stiffness can be added. So are any general constraints.

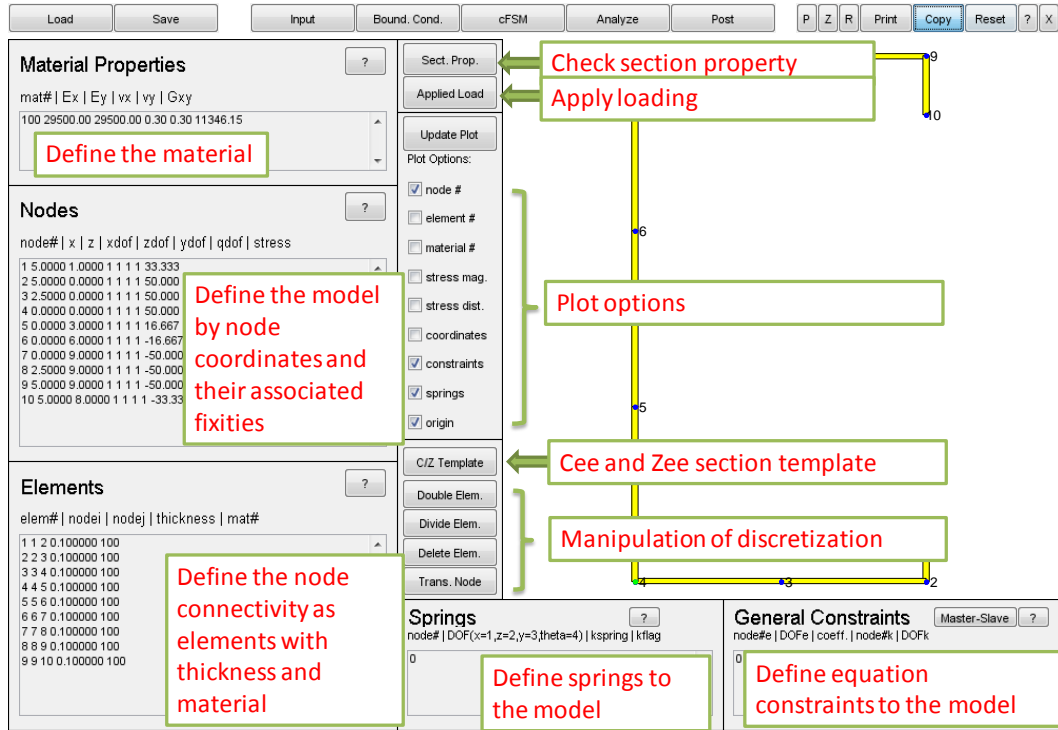
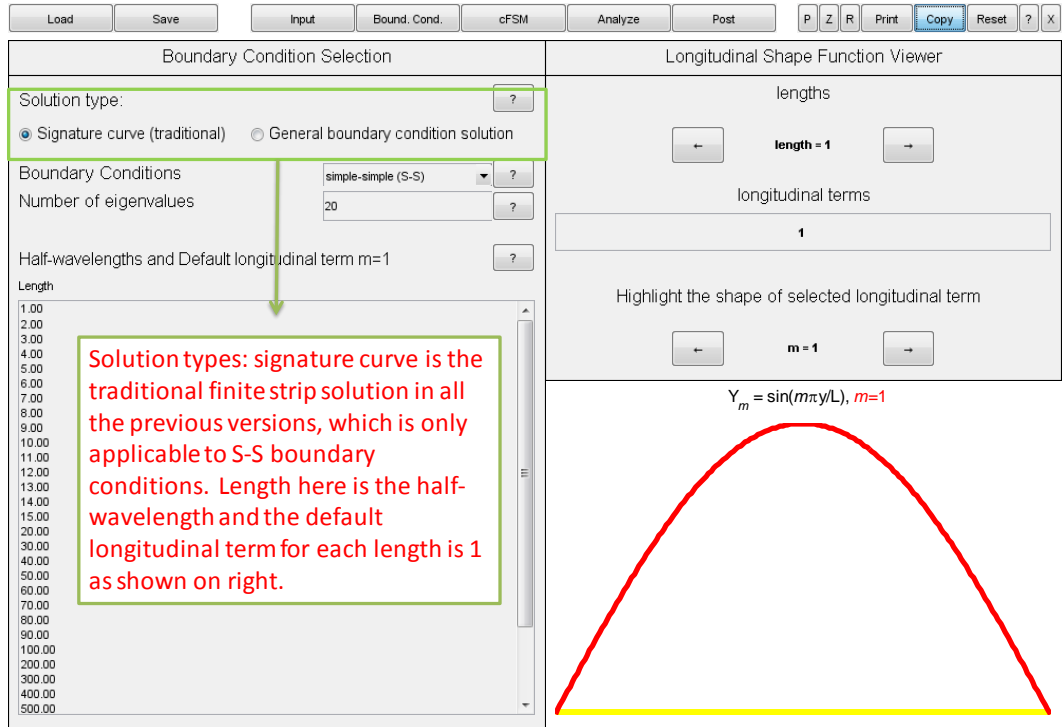
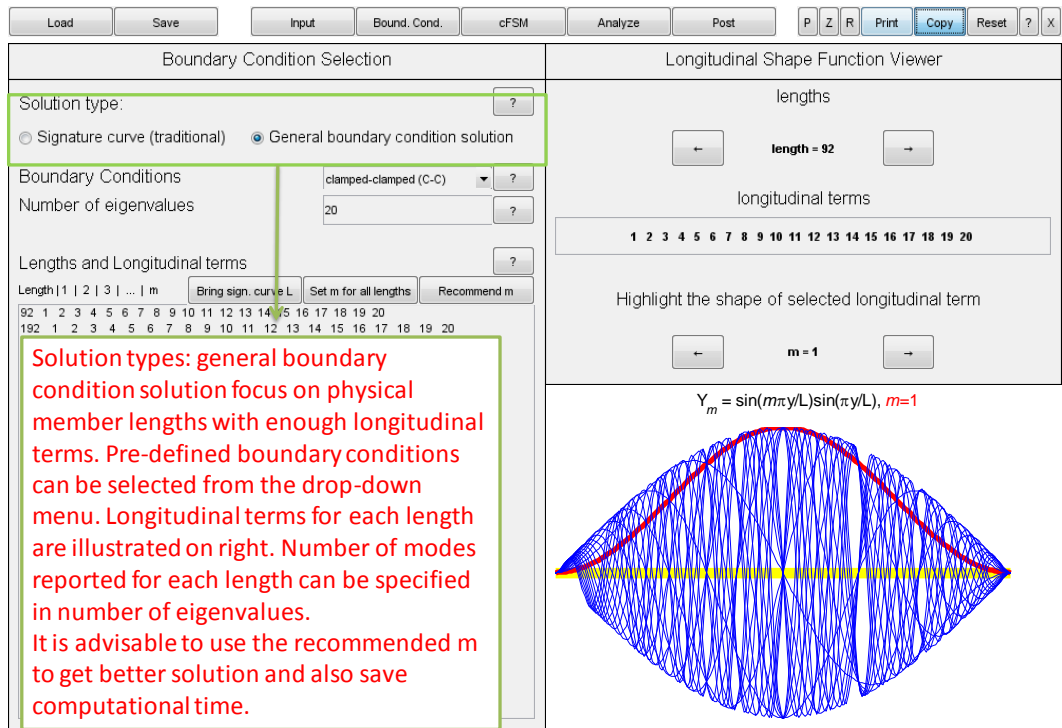


Figure B-4 Input screen of CUFSM 4

In Figure B-5, solution types are distinguished as two: 1) traditional signature curve solution; 2) general boundary condition finite strip solution. Signature curve solution is the traditional finite strip solution available in the previous CUFSM version. The solution is only applicable to simply-simply end boundary condition attribute to the orthogonal property of its associated longitudinal shape function. While for all the other boundary conditions, the loss of this orthogonality in the shape functions requires multiple longitudinal terms in the analysis. Appropriate longitudinal terms in the analysis can be recommended in Figure B-6 with enough accuracy and computational efficiency.



(a) Traditional signature curve solution



(b) General boundary condition finite strip solution

Figure B-5 Define the solution type and related boundary condition

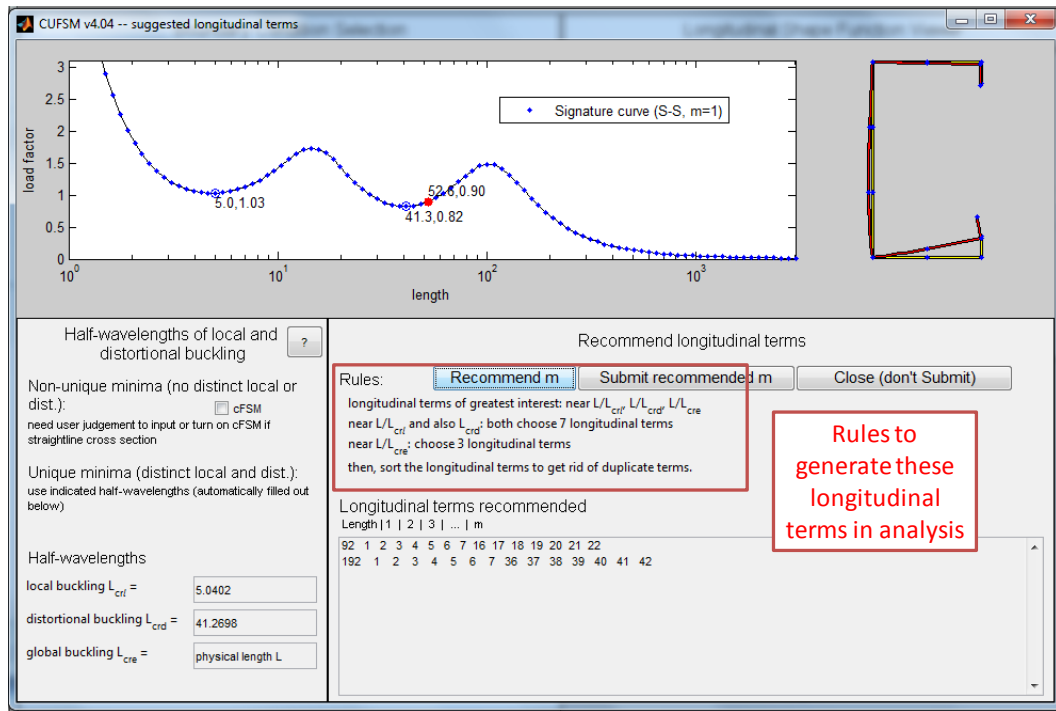


Figure B-6 Recommendation of longitudinal terms in the analysis

With constrained finite strip method in Figure B-7, we can enable the modal decomposition and identification. Different bases are available while the default one is the one the authors recommend. Base vectors are defined based on the geometry of the cross section. Combined is the original finite strip degree of freedom space. These base vectors can be viewed through the viewer provided below. Appropriately selecting the base vectors included in the analysis will turn on the modal decomposition solution. Including all the base vectors will yield the original finite strip solution but modal identification can be performed.

In Figure B-8, the similar post-processing of signature curve solution is illustrated with modal identification result. The interface is changed and improved from the previous CUFSM version.



For post-processing of general boundary condition finite strip solution in Figure B-9, we will mainly focus on the load factor of all the higher modes at the specified physical length. For each higher mode, the participation of longitudinal term relation can aid the user judge the buckling mode together with the buckling mode shape. User can also perform the constrained finite strip modal identification to quantify the buckling modes as shown in Figure B-10.

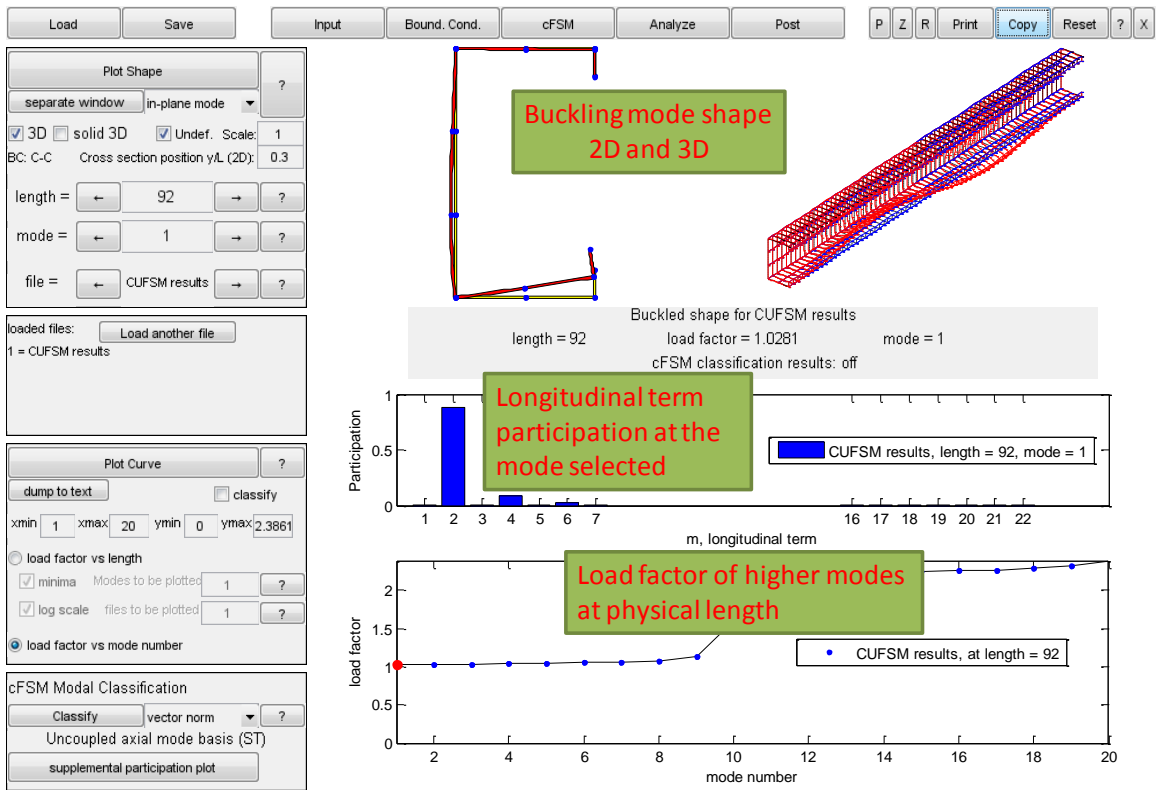


Figure B-9 Post-processing of general boundary condition solution

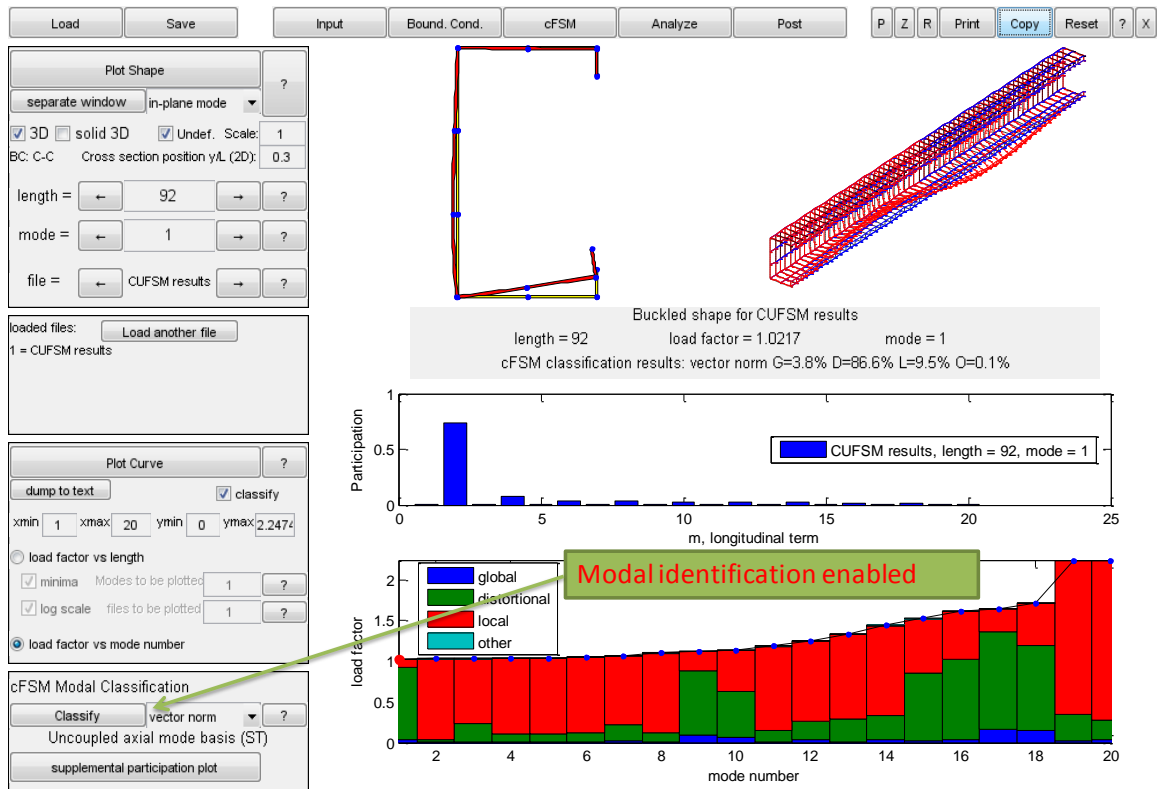


Figure B-10 Post-processing of general boundary condition solution with modal identification

### B.3 Codes

CUF5M is assembled by several subroutines written in MATLAB. The main analysis subroutine is called `strip.m`. The code of `strip.m` is given below. Full code can be found at <http://www.ce.jhu.edu/bschafer/cuf5m>.

```
function
[curve, shapes]=strip(prop,node,elem,lengths,springs,constraints,GBTcon,
BC,m_all,neigs)
%HISTORY
%June 2010, complete update to new Boundary conditions, Z. Li, B.
Schafer
%
%INPUTS
%prop: [matnum Ex Ey vx vy G] 6 x nmats
%node: [node# x z dofx dofy dofrt stress] nnodes x 8;
%elem: [elem# nodei nodej t matnum] nelems x 5;
%lengths: [L1 L2 L3...] 1 x nlengths; lengths to be analyzed
%could be half-wavelengths for signiture curve
```

```

%or physical lengths for general b.c.
%springs: [node# d.o.f. kspring kflag] where 1=x dir 2= z dir 3 = y dir
4 = q dir (twist) flag says if k is a foundation stiffness or a total
stiffness
%constraints:: [node#e dofe coeff node#k dofk] e=dof to be eliminated
k=kept dof dofe_node = coeff*dofk_nodek
%GBTcon: GBTcon.glob,GBTcon.dist, GBTcon.local, GBTcon.other vectors of
1's
% and 0's referring to the inclusion (1) or exclusion of a given mode
from the analysis,
% GBTcon.ospace - choices of ST/O mode
%     1: ST basis
%     2: 0 space (null space of GDL) with respect to K
%     3: 0 space (null space of GDL) with respect to Kg
%     4: 0 space (null space of GDL) in vector sense
% GBTcon.norm - code for normalization (if normalization is done at
all)
%     0: no normalization,
%     1: vector norm
%     2: strain energy norm
%     3: work norm
% GBTcon.couple - coupled basis vs uncoupled basis for general B.C.
especially for non-simply supported B.C.
%     1: uncoupled basis, the basis will be block diagonal
%     2: coupled basis, the basis is fully spanned
% GBTcon.orth - natural basis vs modal basis
%     1: natural basis
%     2: modal basis, axial orthogonality
%     3: modal basis, load dependent orthogonality
%BC: ['S-S'] a string specifying boundary conditions to be analyzed:
%'S-S' simply-pimply supported boundary condition at loaded edges
%'C-C' clamped-clamped boundary condition at loaded edges
%'S-C' simply-clamped supported boundary condition at loaded edges
%'C-F' clamped-free supported boundary condition at loaded edges
%'C-G' clamped-guided supported boundary condition at loaded edges
%m_all: m_all{length#}=[longitudinal_num# ...
longitudinal_num#],longitudinal terms m for all the lengths in cell
notation
% each cell has a vector including the longitudinal terms for this
length
%neigs - the number of eigenvalues to be determined at length
(default=10)

%OUTPUTS
%curve: buckling curve (load factor) for each length
%curve{1} = [ length mode#1
%           length mode#2
%           ...     ...
%           length mode#]
%shapes = mode shapes for each length
%shapes{1} = mode, mode is a matrix, each column corresponds to a mode.

%FUNCTIONS CALLED IN THIS ROUTINE
% \analysis\addspring.m : add springs to K
% \analysis\assemble.m : assemble global K, Kg

```

```

% \analysis\elemprop.m : element properties
% \analysis\kglocal.m : element kg matrix
% \analysis\klocal.m : element k matrix
% \analysis\trans.m : transform k, kg matrix
% \analysis\msort.m : clean up 0's, multiple longitudinal terms. or
out-of-order terms
% \analysis\constr_BCFlag.m : determine flags for user constraints and
internal (at node) B.C.'s
% \analysis\cFSM\base_column : cFSM base vectors (natural basis, ST)
% \analysis\cFSM\base_update.m' : cFSM base vectors with selected basis,
%                               orthogonalization, and normalization
% \analysis\cFSM\constr_user.m : user defined constraints in cFSM style
% \analysis\cFSM\mode_select.m : selection of modes for constraint
matrix R

```

```

%GUI WAIT BAR FOR FINITE STRIP ANALYSIS
wait_message=waitbar(0,'Performing Finite Strip
Analysis','position',[150 300 284 68],...
    'CreateCancelBtn',...
    'setappdata(gcbf,'canceling',1)');
setappdata(wait_message,'canceling',0)
%MATRIX SIZES
nnodes = length(node(:,1));
nelems = length(elem(:,1));
nlengths = length(lengths);

```

```

%CLEAN UP INPUT
%clean up 0's, multiple terms. or out-of-order terms in m_all
[m_all]=msort(m_all);

```

```

%DETERMINE FLAGS FOR USER CONSTRAINTS AND INTERNAL (AT NODE) B.C.'s
[BCFlag]=constr_BCFlag(node,constraints);

```

```

%GENERATE STRIP WIDTH AND DIRECTION ANGLE
[elprop]=elemprop(node,elem,nnodes,nelems);

```

```

%-----
-----

```

```

%LOOP OVER ALL THE LENGTHS TO BE INVESTIGATED
l=0; %length_index = one
while l<nlengths
    l=l+1; %length index = length index + one
    %
    %cancelled
    if getappdata(wait_message,'canceling')
        break
    end
    %length to be analyzed
    a=lengths(l);
    %longitudinal terms to be included for this length
    m_a=m_all{l};
    %

```

```

totalm=length(m_a);%Total number of longitudinal terms

%SET SWITCH AND PREPARE BASE VECTORS (R) FOR cFSM ANALYSIS
if
sum(GBTcon.glob)+sum(GBTcon.dist)+sum(GBTcon.local)+sum(GBTcon.other)>0
    %turn on modal classification analysis
    cFSM_analysis=1;
    %generate natural base vectors for axial compression loading
    [b_v_1,ngm,ndm,nlm]=base_column(node,elem,prop,a,BC,m_a);
else
    %no modal classification constraints are engaged
    cFSM_analysis=0;
end
%test the time loop to see if we need the waitbar for assembly
if length(m_a)*length(node(:,1))>=120
    wait_message_elem=waitbar(0,'Assembling stiffness
matrices','position',[150 202 284 68]);
end
%ZERO OUT THE GLOBAL MATRICES
K=sparse(zeros(4*nnodes*totalm,4*nnodes*totalm));
Kg=sparse(zeros(4*nnodes*totalm,4*nnodes*totalm));
%
%ASSEMBLE THE GLOBAL STIFFNESS MATRICES
for i=1:nelems
    %Generate element stiffness matrix (k) in local coordinates
    t=elem(i,4);
    b=elprop(i,2);
    matnum=elem(i,5);
    row=find(matnum==prop(:,1));
    Ex=prop(row,2);
    Ey=prop(row,3);
    vx=prop(row,4);
    vy=prop(row,5);
    G=prop(row,6);
    [k_1]=klocal(Ex,Ey,vx,vy,G,t,a,b,BC,m_a);
    %Generate geometric stiffness matrix (kg) in local coordinates
    Ty1=node(elem(i,2),8)*t;
    Ty2=node(elem(i,3),8)*t;
    [kg_1]=kglocal(a,b,Ty1,Ty2,BC,m_a);
    %Transform k and kg into global coordinates
    alpha=elprop(i,3);
    [k,kg]=trans(alpha,k_1,kg_1,m_a);
    %Add element contribution of k to full matrix K and kg to Kg
    nodei=elem(i,2);
    nodej=elem(i,3);
    [K,Kg]=assemble(K,Kg,k,kg,nodei,nodej,nnodes,m_a);
    %WAITBAR MESSAGE for assmebly
    if length(m_a)*length(node(:,1))>=120
        info=['Element ',num2str(i),' done.'];
        waitbar(i/nelems,wait_message_elem);
    end
end
end
if exist('wait_message_elem')==1
    if ishandle(wait_message_elem)
        delete(wait_message_elem);
    end
end

```

```

        end
    end
    %ADD SPRING CONTRIBUTIONS TO STIFFNESS
    if ~isempty(springs) %springs variable exists
        [K]=addspring(K, springs, nnodes, a, BC, m_a);
    end

    %INTERNAL BOUNDARY CONDITIONS (ON THE NODES) AND USER DEFINED
    CONSTR.
    %Check for user defined constraints too
    if BCFlag==0
        %no user defined constraints and fixities.
        Ru0=0;
        nu0=0;
    else
        %size boundary conditions and user constraints for use in R
        format
        %d_constrained=Ruser*d_unconstrained, d=nodal DOF vector (note
        by
        %BWS June 5 2006)
        Ruser=constr_user(node, constraints, m_a);
        Ru0=null(Ruser');
        %Number of boundary conditions and user defined constraints =
        nu0
        nu0=length(Ru0(1, :));
    end

    %GENERATION OF cFSM CONSTRAINT MATRIX
    if cFSM_analysis==1
        %PERFORM ORTHOGONALIZATION IF GBT-LIKE MODES ARE ENFORCED

        b_v=base_update(GBTcon.ospace, 0, b_v_l, a, m_a, node, elem, prop, ngm, ndm, nlm,
        BC, GBTcon.couple, GBTcon.orth); %no normalization is enforced: 0: m
        %assign base vectors to constraints

        b_v=mode_select(b_v, ngm, ndm, nlm, GBTcon.glob, GBTcon.dist, GBTcon.local, GB
        Tcon.other, 4*nnodes, m_a); %m
        Rmode=b_v;
        %%%%%%%%%%%%%%%%%%%%%%%%%%%%%%%%%%%%%%%%%%%%%%%%%%%%%%%%%%%%%%%%%%%%%%%%%
        %%%%%%%%%%%%%%%%%%%%%%%%%%%%%%%%%%%%%%%%%%%%%%%%%%%%%%%%%%%%%%%%%%%%%%%%%
    else
        %no modal constraints are activated therefore
        Rmode=eye(4*nnodes*totalm); %activate modal constraints
    end
    %
    %CREATE FINAL CONSTRAINT MATRIX
    %Determine the number of modal constraints, nm0
    if BCFlag==0
        %if no user defined constraints and fixities.
        R=Rmode;
    else
        %should performed uncoupled for block diagonal basis?
        if cFSM_analysis==1
            nm0=0;
            Rm0=null(Rmode');
        end
    end

```

```

        nm0=length(Rm0(1,:));
        R0=Rm0;
        if nu0>0
            R0(:,(nm0+1):(nm0+nu0))=Ru0;
        end
        R=null(R0');
    else
        R=null(Ru0');
    end
end
%
%INTRODUDCE CONSTRAINTS AND REDUCE K MATRICES TO FREE PARTS ONLY
Kff=R'*K*R;
Kgff=R'*Kg*R;

%SOLVE THE EIGENVALUE PROBLEM
%Determine which solver to use
%small problems usually use eig, and large problems use eigs.
%the eigs solver is not as stable as the full eig solver...
%LAPACK reciprocal condition estimator
rcond_num=rcond(full(Kgff\Kff));
%Here, assume when rcond_num is bigger than half of the eps, eigs
can provide
%reliable solution. Otherwise, eig, the robust solver should be
used.
if rcond_num>=eps/2
    eigflag=2;%eigs
else
    eigflag=1;%eig
end
%determine if there is a user input neigs; otherwise set it to
%default 10.
if nargin<10|isempty(neigs)
    neigs=20;
end
if eigflag==1
    [modes,lf]=eig(full(Kff),full(Kgff));
else
    options.disp=0;
    options.issym=1;
    N=max(min(2*neigs,length(Kff(1,:))),1);
    if N==1|N==length(Kff(1,:))
        [modes,lf]=eig(full(Kff),full(Kgff));
    else
        %pull out 10 eigenvalues
        [modes,lf]=eigs(full(Kgff\Kff),N,'SM',options);
    end
end
end
%CLEAN UP THE EIGEN SOLUTION
%eigenvalues are along the diagonal of matrix lf
lf=diag(lf);
%find all the positive eigenvalues and corresponding vectors,
squeeze out the rest
index=find(lf>0 & imag(abs(lf))<0.00001);
lf=lf(index);

```

```

modes=modes(:,index);
%sort from small to large
[lf,index]=sort(lf);
modes=modes(:,index);
%only the real part is of interest (eigensolver may give some small
nonzero imaginary parts)
lf=real(lf);
modes=real(modes);
%
%truncate down to reasonable number of modes to be kept
num_pos_modes=length(lf);
nummodes=min([neigs;num_pos_modes]);
lf=lf(1:nummodes);
modes=modes(:,1:nummodes);
%
%FORM THE FULL MODE SHAPE BY BRINGING BACK ELIMINATED DOF
mode=R*modes;
%
%CLEAN UP NORMALIZATION OF MODE SHAPE
%eig and eigs solver use different normalization
%set max entry (absolute) to +1.0 and scale the rest
for j=1:nummodes
    maxindex=find(abs(mode(:,j))==max(abs(mode(:,j)))));
    mode(:,j)=mode(:,j)/mode(maxindex(1),j);
end
%

%GENERATE OUTPUT VALUES
%curve and shapes are changed to cells!!
%curve: buckling curve (load factor)
%curve{1} = [ length ... length
%            mode#1 ... mode#]
%shapes = mode shapes
%shapes{1} = mode, each column corresponds to a mode.
curve{1}(1:nummodes,1)=lengths(1);
curve{1}(1:nummodes,2)=lf;
%shapes(:,1,1:min([nummodes,num_pos_modes]))=modes;
shapes{1}=mode;
%
%
%WAITBAR MESSAGE
info=['Length ',num2str(lengths(1)), ' done.'];
waitbar(1/nlengths,wait_message);
%
end
%THAT ENDS THE LOOP OVER ALL THE LENGTHS
%-----
-----
if ishandle(wait_message)
    delete(wait_message);
end
% %

```

## **Vita**

The author was born in Pingdingshan, Henan of China in November 1982 and graduated from Ye Xian High school in 2001. He subsequently enrolled in Shanghai Jiao Tong University, where he earned his Bachelor's degree in Civil Engineering in July 2005. At the same time, the author enrolled in the Shenzhen graduate school of Harbin Institute of Technology and was awarded the Master's degree in Structural Engineering in 2007.

The author was admitted as a Ph.D. student to Department of Civil Engineering at Johns Hopkins University in September 2007. He was awarded a Master of Science in Civil Engineering in 2009 and continued his Ph.D. research in finite strip modeling under the supervision of Professor Ben Schafer, completing in September 2011.